



HAL
open science

Micro-Robotic Cholesteatoma Surgery : clinical requirements analysis and image-based control under constraints

Bassem Dahroug

► **To cite this version:**

Bassem Dahroug. Micro-Robotic Cholesteatoma Surgery : clinical requirements analysis and image-based control under constraints. Automatic. Université Bourgogne Franche-Comté, 2018. English. NNT : 2018UBFCD016 . tel-01862715

HAL Id: tel-01862715

<https://theses.hal.science/tel-01862715>

Submitted on 27 Aug 2018

HAL is a multi-disciplinary open access archive for the deposit and dissemination of scientific research documents, whether they are published or not. The documents may come from teaching and research institutions in France or abroad, or from public or private research centers.

L'archive ouverte pluridisciplinaire **HAL**, est destinée au dépôt et à la diffusion de documents scientifiques de niveau recherche, publiés ou non, émanant des établissements d'enseignement et de recherche français ou étrangers, des laboratoires publics ou privés.



SPIM

Thèse de Doctorat



UFC

école doctorale **sciences pour l'ingénieur et microtechniques**
UNIVERSITÉ DE FRANCHE-COMTÉ

Micro-Robotic Cholesteatoma Surgery

clinical requirements analysis and image-based control under
constraints

■ BASSEM DAHROUG

SPIM

Thèse de Doctorat



école doctorale **sciences pour l'ingénieur et microtechniques**
UNIVERSITÉ DE FRANCHE-COMTÉ

N° X | X | X



THÈSE présentée par
BASSEM DAHROUG

pour obtenir le
Grade de Docteur de
l'Université de Bourgogne Franche-Comté

Spécialité : **Sciences pour l'ingénieur**

Micro-Robotic Cholesteatoma Surgery clinical requirements analysis and image-based control under constraints

Unité de Recherche :
Institut FEMTO-ST/AS2M

Soutenue publiquement le 16 février 2018 devant le Jury composé de :

SANDRINE VOROS	Rapporteuse	Chargée de recherche HDR, INSERM, TIMC-IMAG, Grenoble
BERNARD BAYLE	Rapporteur	Professeur des Universités, Télécom Physique Strasbourg, ICube, Strasbourg
JÉRÔME SZEWCZYK	Président du jury	Professeur des Universités, Paris Sorbonne Universités, ISIR, Paris
PHILIPPE MARTINET	Examineur	Professeur des Universités, Centrale Nantes, INRIA, Nice-Sophia-Antipolis, Nantes
STEFAN WEBER	Co-encadrant de thèse	Professeur des Universités, Universität Bern, ARTORG Center, Berne, Suisse
LAURENT TAVERNIER	Co-encadrant de thèse	Professeur des Universités - Particien Hospitalier, UBFC, CHRU, Besançon
BRAHIM TAMADAZTE	Co-encadrant de thèse	Chargé de recherche, CNRS, Institut FEMTO-ST, Besançon
NICOLAS ANDREFF	Directeur de thèse	Professeur des Universités, UBFC, Institut FEMTO-ST, Besançon

Acknowledgments

This PhD dissertation was a rich experience for me that cannot end without thanking the people who have guided me, helped me and supported me during the last three years. I would first like to thank my supervisors at FEMTO-ST, Prof. Nicolas Andreff and Dr. Brahim Tamadazte. I would like to express my gratitude to them for their support, advice, objective and constructive criticism, and for all the discussions. Thank you for trusting me, helping me and giving me the opportunity to work with you. You have been available and supportive throughout the dissertation period. Working with you has been very motivating, and especially very formative.

I would also like to thank my co-supervisors at ARTORG center and CHU Besançon, Prof. Laurent Tavernier and Prof. Stefan Weber, respectively. The first one helped me to well understand the clinical part of this thesis while the second one gave me the opportunity to test the proposed controller on ARTORG robotic system. Moreover, I thank Dr. Juan Anso, Eng. Daniel Schneider and Eng. Jan Hermann from ARTORG center for helping me to implement the proposed controller on their system.

I warmly thank the members of my jury, the reviewers Dr. Sandrine Voros and Prof. Bernard Bayle, as well as the examiners Prof. Jérôme Szweczyk and Prof. Philippe Martinet, for doing me the honour of reporting and reviewing my work and having travelled to attend my defence.

I thank all the staff of the AS2M department of the FEMTO-ST Institute for the pleasant working atmosphere and the daily exchanges.

I would like to finally thank my family for believing in me and for always supporting and encouraging me throughout my life.

Bassem Dahroug

Contents

Acronymes & Notations	xiii
General Introduction	1
Context	1
Scientific and Technical Contributions	2
1 Clinical Background	5
1.1 Anatomy and Physiology of Human Auditory System	5
1.1.1 External ear	6
1.1.2 Inner ear	9
1.1.3 Middle ear	9
1.2 Cholesteatoma	16
1.2.1 Definition of cholesteatoma	17
1.2.2 Pathology, complications and epidemiology	18
1.2.3 Diagnosis and imaging tools	21
1.2.4 Treatment	25
1.2.5 Ablation tools	27
1.3 Conclusion	30
2 Requirement Analysis for Cholesteatoma Surgery	31
2.1 Ideal Requirements for Robot-Assisted Cholesteatoma Surgery	32
2.1.1 Clinical requirements	32
2.1.2 Engineering requirements	36
2.1.3 Safety and risk analysis	40
2.2 Classification of Surgical Robotic Systems	41
2.2.1 Otologic surgical robotic systems	42
2.2.2 Non-otologic bendable surgical robotic systems	51
2.3 Guidelines for The Micro-Robot-Assisted Cholesteatoma Surgery	54
2.3.1 Clinical	54
2.3.2 Engineering	56
2.4 Conclusion	60

3	Constrained Motion Through Anatomical Structures	63
3.1	Bilateral Constrained Motion	66
3.1.1	Previous works in literature	67
3.1.2	Proposed method	70
3.2	Unilateral Constrained Motion	99
3.2.1	Previous approaches	100
3.2.2	Proposed method	101
3.3	Numerical Simulator	104
3.3.1	Validation of RCM constraints	106
3.4	Conclusion	117
4	From Pre-operative images to Motion	119
4.1	3D path following controller	120
4.1.1	Background	121
4.1.2	Proposed method	122
4.1.3	Stability condition	132
4.2	Task priority controller	133
4.2.1	Following a path under RCM constraint	135
4.2.2	Following a path under UCM constraint	136
4.3	Numerical validation	138
4.3.1	3D path following controller	140
4.3.2	Task priority controller	144
4.4	Experimental validation	153
4.4.1	Trials with a parallel robot	153
4.4.2	Toward clinical trials	163
4.5	Conclusion	166
	Conclusion and Perspectives	167
	General Conclusion	167
	Perspectives	169
	Bibliography	175

List of Figures

1	A conceptual scheme of μ RoCS system.	2
1.1	The different parts of the auditory system.	6
1.2	The carotid artery behind the auricle with the jugular vein and the parotid gland ¹	7
1.3	(a) The different parts of the inner ear, (b) the fluid path within the cochlea with its cross section.	8
1.4	The human skull ² with the anatomical direction reference.	9
1.5	(a) The different parts of tympanic membrane; (b) the three layers of tympanic membrane.	10
1.6	Comparison between two portions of human skin tissue: (a) the epidermal tissue which is the outer layer of tympanic membrane; (b) the mucous tissue which is the inner layer of tympanic membrane.	11
1.7	(a) Anterior view of the tympanic cavity with the anterior wall removed ³ , (b) lateral view of the tympanic cavity.	12
1.8	Description of the tympanic cavity walls ⁸ with the important structures which are surrounded by a rectangle.	15
1.9	The different dimensions of the auditory system.	16
1.10	A Comparison between: (a) normal tympanic membrane, and (b) infected middle ear with cholesteatoma.	17
1.11	A comparison between (a) retraction pocket disease in the tympanic membrane, and (b) tympanic membrane with perforation.	19
1.12	(a) Site of infection of cholesteatoma within the different regions of the middle ear cavity, and (b) a medial view on the mastoid bone.	19
1.13	(a) The standard position of surgeon within the operation room with a zoom of the otomicroscopy, and (b) conceptional scheme of an otomicroscopy limitation.	22
1.14	MRI images show a primary acquired cholesteatoma by the arrows [Ver-cruysse et al., 2006], where the MRI techniques are (a) echo-planar DWI, (b) T1-weight.	23

1.15	Comparison of cholesteatoma imagery [Levy et al., 2013] between fluorescence (the left image where the cholesteatoma cells are the bright grey pixels) and histological (the right image where the arrow presents a thin layer of keratin).	24
1.16	OCT image of (A) normal mucosa; (B) keratin layer (bracket) over the mucosa [Djalilian et al., 2010].	25
1.17	The endaural approach [Hildmann and Sudhoff, 2006]: (a) top view, and (b) side view.	26
1.18	The transcanal approach: (a) top view through the external ear canal [Hildmann and Sudhoff, 2006], (b) side view (the red hashed region is the bony region to be removed) [Bordure et al., 2005].	26
1.19	(a) Initial step to the postauricular approach [Hildmann and Sudhoff, 2006], and (b) the top view of the canal wall down process, where the external ear canal is removed.	27
1.20	Canal wall up process [Hildmann and Sudhoff, 2006]: (a) top view, (b) side view (the green region is the removed bony portion while the blue region is preserved).	28
1.21	Dimensions of the orifice created by the canal wall up: (a) top view, (b) side view.	28
1.22	Standard instruments used for the otological surgery [Badr-El-Dine et al., 2013].	29
1.23	(a) A conceptual scheme of the MEMS ablation tool [Gosline et al., 2012], and (b) a global view of the MEMS tool mounted on a concentric tube robot.	30
2.1	The concept scheme to use segmentation methods for generating a surface model of the auditory system.	34
2.2	μ RoCS conceptual scheme.	35
2.3	Examples of robotic platforms for minimally invasive surgery in different medical applications. (images: Bimanual endonasal [Burgner et al., 2011], PRECEYES ⁴ , ARTORG [Bell et al., 2012], μ Ralp ⁵ , Robodoc ⁶ , Mako ⁷ , Da Vinci ⁸ , Magellan ⁹ , Niobe [Carpi and Pappone, 2009], Neuromate ¹⁰)	37
2.4	Da Vinci system in the operation room during cochlear implantation surgery [Liu et al., 2014].	43
2.5	(a) Robotic system for cochlear implantation [Leinung et al., 2007]; (b) device for automated insertion of the electrode [Hussong et al., 2008].	44
2.6	The different components of ARTORG robotic system: (A) robot arm; (B) surgical driller; (C) head clamp; (D) optical tracking; (E) touch screen as the interface to the planning software [Bell et al., 2012].	45
2.7	(a) Schematic diagram of conceptual setup between the laser and the OCT [Zhang et al., 2014]; (b) experimental setup; where (1) CO ₂ laser, (2) OCT, (3) beam combiner, (4) 6-DOF parallel platform [Zhang and Worn, 2014].	45

2.8	Microtable: (a) early design concept [Labadie et al., 2009]; (b) bone-attached parallel robot with preposition frame (PPF) and automatic image-guided micro-stereotactic (AIP) frame [Kratchman et al., 2011].	47
2.9	(a) OTOBOT robotic system for mastoidectomy [Danilchenko et al., 2011]; (b) bone attached robot with the positioning frame [Dillon et al., 2014].	48
2.10	Configuration of robotic system mastoidectomy [Lim et al., 2011].	48
2.11	(a) Master-slave RobOtol surgical system, (b) experimental setup of RobOtol [Miroir et al., 2010].	49
2.12	(a) Master-slave MMS-II surgical system with forceps tool [Maier et al., 2010]; (b) master-slave MMTS surgical system, where (1) joystick console, (2) energy supply, (3) MMS, (4) active gripping adapter, (5) carrier robot, (6) patient phantom, (7) OR-table.	50
2.13	The concept of the proposed bendable endoscope.	51
2.14	(a) Global view on the Quadromanual robot, and (b) zoom on the four arms of robot [Swaney et al., 2012].	52
2.15	The ablation tool integrated with the concentric tube robot [Gosline et al., 2012].	53
2.16	(a) Global view on the different components of Sensi robotic system 910 ⁹ ; (b) the Artisan catheter and its bending angle.	53
2.17	Comparison between different imaging techniques ¹¹	55
2.18	Conceptual schema to demonstrate the required DOF for the manipulator and the end-effector.	57
2.19	Different control architectures: (a) CAS, (b) image-guided, (c) visual servoing.	59
3.1	A 3D conceptual scheme for the comparison between the movements of (a) Remote Centre of Motion (RCM), and (b) Unilaterally Constrained Motion (UCM).	64
3.2	A mathematical comparison between (a) the bilateral constraint, and (b) the unilateral constraint.	64
3.3	A 2D conceptual scheme for the comparison between the movements of (a) Remote Centre of Motion (RCM), and (b) Unilaterally Constrained Motion (UCM).	65
3.4	Examples about the special mechanisms of RCM: (a) patent by Taylor <i>et al.</i> [Taylor et al., 1995], and (b) Da-Vinci ¹² robotic manipulator.	66
3.5	A comparison between the robot control in (a) joint-space, and (b) task-space.	67
3.6	The scheme shows the different notation and vectors used to describe geometrically the RCM movement.	69
3.7	Illustration of some special conditions of [Boctor et al., 2004], where (a) $\mathbf{e}_{h_1} = \mathbf{0}$ with $\mathbf{e}_{h_2} \neq 0$, and (b) $\mathbf{e}_{h_1} \neq 0$ with $\mathbf{e}_{h_2} = 0$	70

3.8	Conceptual scheme of the system with the various reference frames (i.e., the origin points of: the world frame \mathcal{O}_w , the end-effector frame \mathcal{O}_e , the tool tip frame \mathcal{O}_t , the RCM frame \mathcal{O}_r , and the camera frame \mathcal{O}_c), and the evaluation of a curved tool to move from one point to another one under the RCM constraints.	71
3.9	Conceptual scheme of a straight tool inserted through an incision hole, and the vectors notations for describing the RCM movements.	72
3.10	The relation between the 3D RCM angular error and the angle θ which is defined between the vectors ${}^e\mathbf{y}$ and ${}^e\mathbf{u}_{er}$	73
3.11	Geometrical representation of the projection operator \mathbb{P}_\perp	74
3.12	An example of linear velocity which can be expressed in different frames.	75
3.13	A conceptual scheme to represent the different spaces and how the interaction matrix maps one space to other one.	77
3.14	The relation between the 1D RCM angular error and the angle θ which is defined between the vectors ${}^e\mathbf{y}$ and ${}^e\mathbf{u}_{er}$	81
3.15	Examples of the geometry of the RCM movements, where the desired tool tip velocity ${}^e\mathbf{v}_t$ goes in (a) the right direction, or (b) the left direction.	85
3.16	Geometric representation to deduce the end-effector angular velocity.	87
3.17	Conceptual scheme of the system with the various notations used within the equations for curved tool.	89
3.18	The geometrical description for i) projecting the incision centre point (\mathcal{O}_r) onto the curved tool, and ii) deducing analytically the linear velocity of projected point ${}^e\mathbf{p}_{t'}$ along the tool.	90
3.19	Zoom on the geometric description of the tool curve and the incision point \mathcal{O}_r at the instantaneous positions where: (a) the projected point $\mathbf{p}_{t'}$ is located between the origin of incision point and the centre of curvature circle \mathcal{O}_{ct} , and (b) the mirror condition of (a).	93
3.20	Zoom on the geometric description of the tool curve and the incision point \mathcal{O}_r at the instantaneous positions where: (a) the point \mathcal{O}_r is located between the two points $\mathbf{p}_{t'}$ and \mathcal{O}_{ct} , and (b) the mirror condition of (a).	95
3.21	Zoom on the geometric description of the tool curve and the incision point \mathcal{O}_r at the instantaneous positions where the point \mathcal{O}_{Ct} is located within the segment formed between \mathcal{O}_r and $\mathbf{p}_{t'}$	96
3.22	A comparison between the straight and curved tools.	98
3.23	Simulated motion ¹³ for visualizing the difference between: i) bilateral and unilateral constraints, and ii) the usage of straight and curved tool.	100
3.24	A geometric representation for the UCM concept.	102
3.25	The sigmoid form of the virtual spring stiffness.	103
3.26	An example of realistic simulator, where the virtual scene is consists of: i) an auditory system with cholesteatoma which is created from DICOM images, and ii) a flexible surgical tool.	104
3.27	Block diagram of the client/server communication: (a) simulated robot, and (b) real robot.	105

3.28	Testing only the RCM task with a straight tool by changing the position of the trocar point in a straight path. The test is repeated with three different values of λ .	108
3.29	Testing only the RCM task with a straight tool by changing the position of the trocar point in a spiral path.	111
3.30	Testing only the RCM task with a piecewise straight tool in a spiral path.	113
3.31	Testing only the RCM task with a curved circular tool in a spiral path.	116
4.1	The progress of Frenet frame along a Lissajous curve ¹⁴ .	120
4.2	A comparison between the performance of a path following controller (the dash blue line on the right) and a trajectory tracking controller (the dash dotted green line on the left) for the same geometric curve (the continuous brown line).	121
4.3	The concept of projecting the tool tip onto the geometric curve.	122
4.4	The progress of Frenet frame along a spiral curve ¹ .	123
4.5	Examples of different curve types, and the corresponding unit tangent vectors and the principal normal vectors.	124
4.6	The concept of projecting the tool tip onto the geometric curve.	126
4.7	The different reference frames and notions deployed for describing the path following scheme.	127
4.8	The geometric concept of the path following controller.	129
4.9	The influence of the path following error \mathbf{d}_{pf} on the control velocity of the tool tip \mathbf{v}_t , while using the gains choice (4.30).	130
4.10	(a) The controller sensitivity to the path curvature, (b) the influence of the path following error \mathbf{d}_{pf} and the path curvature \mathbf{C}_p on the control velocity of the tool tip \mathbf{v}_t , while using the gains choice (4.32).	131
4.11	The difference spaces of the projection gradient.	134
4.12	The UCM movement of the tool to follow the desired path.	137
4.13	Flowchart of the simulator to execute the desired path under the RCM/UCM constraints.	139
4.14	A straight path done by a straight tool when changing the value of β' from -0.5 to -10 .	141
4.15	The path following error during the simulated motion of the linear path while changing the value of v_{tis} .	142
4.16	A "UROCS" path done by a straight tool, while changing the value of β' from -2 to -10 .	144
4.17	The controller performances during the approach phase while varying the values of λ and γ .	145
4.18	The trial of the path following task with the RCM task while using a straight tool.	148
4.19	The trial of path following task with the RCM task while using a circular tool.	150
4.20	The trial of the path following task with the UCM task while using a circular tool.	152

4.21	Conceptual scheme of the parallel robot.	154
4.22	The different tool types, where a straight tool is located on the bottom, a piecewise straight tool is located in the middle, and a circular shape tool is located on the top.	155
4.23	The experimental setup with the different coordinate frames of the end-effector, tool tip, incision hole and camera.	155
4.24	Screen shot of the control computer, where the upper two windows are the images acquired by the visualization cameras, the lower left window is the images acquired by the control camera, and the lower right window is displaying the instantenous errors of both RCM and path following tasks.	157
4.25	The trial of path following task with the RCM task while using a straight tool.	159
4.26	The trial of path following task with the UCM task while using a straight tool.	161
4.27	The trial of the path following task with the UCM task while using a curved tool.	162
4.28	Conceptual scheme of the serial robot within the operation room.	163
4.29	The experimental setup with the robotic system of ARTORG.	164
4.30	The trial of path following task with the RCM task while using a straight tool.	165
1	The window of the proposed realistic simulator with the different options.	169
2	A tool concept for cholesteatoma removal based on concentric tube principle.	171
3	A comparison between the symmetric and the asymmetric cutouts [Swaney et al., 2017].	171
4	First prototype of bendable tool based on the model of [Swaney et al., 2017].	172
5	A secondary concept of the bendable tool.	173

List of Tables

1	Notations summary	xv
1.1	The number of cholesteatoma interventions in France, where H71: the number of patients whose had a first cholesteatoma surgery, H95.0: the number of patients whose had another intervention to remove the residual cholesteatoma, and H71+H95.0: the total number of cholesteatoma interventions in each year.	21
2.1	Summary of clinical requirements and the new surgical workflow.	33
2.2	Summary of robot data.	39
2.3	Summary of the CAS data.	40
2.4	Summary of risk analysis.	41
2.5	A comparison between the actuation sources of bendable tool. The abbreviation stand for: SMA (Shape Memory Alloy), EAP (Electric Active Ploymers),	58
2.6	Summary of essential requirements.	60
2.7	Summary of surgical robotic systems.	62
3.1	summary of different trials done with constant gain coefficients (i.e., $\lambda = 0.5$ and $T_e = 0.005$ <i>seconds</i> , whereas STD error is the standard deviation error.	116
4.1	Summary of different trials done. The following symbols mean that a trial was performed on: (\blacktriangle) the simulator, (\bullet) the parallel robot, and (\blacksquare) the serial robot. The abbreviations stand for: (PF) Path Following, (RCM) Remote Centre of Motion, and (UCM) Unilateral Central Motion.	166

Acronymes & Notations

Acronymes

CRF	<i>Coordinate Reference Frame</i>
RCM	<i>Remote Centre of Motion</i>
UCM	<i>Unilaterally Constrained Motion</i>
DOF	<i>Degree Of Freedom</i>
MEMS	<i>Micro-Electro-Mechanical System</i>

Notations

A Coordinate Reference Frame (\mathcal{R}_i) is formed by an origin point (\mathcal{O}_i) and an orthogonal basis formed by three perpendicular unit vectors (${}^i\mathbf{x}$, ${}^i\mathbf{y}$ and ${}^i\mathbf{z}$). The vectors and the points are represented by a bold lower case letters (\mathbf{v}), and a normal lower case letter is used for a scalar value (v). The homogeneous representation is used to distinct between a vector ($\mathbf{v} = [v_x; v_y; v_z; 0]$) and a point ($\mathbf{p} = [p_x; p_y; p_z; 1]$). A vector is determined by the difference between two points ($\mathbf{ab} = \mathbf{b} - \mathbf{a}$). Such a vector expressed with respect to a frame by a left superscript letter (${}^i\mathbf{ab}$). Its unit-vector and its Euclidean norm are noted (${}^i\mathbf{u}_{ab} = \frac{{}^i\mathbf{b} - {}^i\mathbf{a}}{\|{}^i\mathbf{b} - {}^i\mathbf{a}\|}$) and ($\|{}^i\mathbf{ab}\| = \sqrt{{}^iab_x^2 + {}^iab_y^2 + {}^iab_z^2}$), respectively.

Symbol	Description
\mathcal{R}_w	the world CRF and its origin point is \mathcal{O}_w ,
\mathcal{R}_e	the end-effector CRF and its origin point is \mathcal{O}_e ,
\mathcal{R}_t	the tool tip CRF and its origin point is \mathcal{O}_t ,
\mathcal{R}_r	the incision point CRF and its origin point is \mathcal{O}_r ,
${}^w\mathbf{M}_e$	the homogeneous transformation matrix that describes the pose of end-effector CRF in the world CRF,

continued on the next page

<i>continued from the previous page</i>	
Symbol	Description
${}^e\mathbf{et}$	the vector between the \mathcal{O}_e and \mathcal{O}_t , and the left superscript notes that this vector is expressed in the end-effector CRF,
${}^e\mathbf{tr}$	the vector between the \mathcal{O}_t and \mathcal{O}_r , and it is expressed in the end-effector CRF,
${}^e\mathbf{er}$	the vector between the \mathcal{O}_e and \mathcal{O}_r , and it is expressed in the end-effector CRF,
${}^e\mathbf{u}_{er}$	the unit-vector of ${}^e\mathbf{er}$ expressed in the end-effector CRF,
${}^e\mathbf{u}_{et}$	the unit-vector of ${}^e\mathbf{et}$ expressed in the end-effector CRF,
${}^e\mathbf{et}'$	the vector between the \mathcal{O}_e and $\mathbf{p}_{t'}$, and it is expressed in the end-effector CRF,
$\mathbf{p}_{t'}$	the projection point of the incision hole centre point \mathcal{O}_r onto the tool centre line,
${}^e\mathbf{u}_{et}'$	the unit-vector of ${}^e\mathbf{et}'$ expressed in the end-effector CRF,
${}^e\mathbf{y}$	the y-axis (basis vector) of the end-effector CRF,
${}^e\mathbf{I}$	an identity matrix,
\mathbf{d}_{rcm}	the lateral error of alignment task which is the perpendicular distance obtained by projecting the \mathcal{O}_r onto the tool centre line,
\mathbf{e}_{rcm*}	the angular error of alignment task which could be either $\mathbf{e}_{rcm3D} \in \mathbb{R}^{3 \times 1}$ or $e_{rcm1D} \in \mathbb{R}^{1 \times 1}$,
$\dot{\mathbf{e}}_{rcm*}$	the time-derivative of \mathbf{e}_{rcm*} ,
${}^e\dot{\mathbf{er}}$	the time-derivative of the vector \mathbf{er} ,
${}^e\dot{\mathbf{u}}_{er}$	the time-derivative of the vector ${}^e\mathbf{u}_{er}$,
${}^e\dot{\mathbf{et}}'$	the time-derivative of the vector ${}^e\mathbf{et}'$,
${}^e\dot{\mathbf{u}}_{et}'$	the time-derivative of the vector ${}^e\mathbf{u}_{et}'$,
${}^e\mathbf{v}_{r/e}$	the relative linear velocity of the incision point \mathcal{O}_r with respect to the end-effector frame (${}^e\mathbf{v}_{r/e} = {}^e\dot{\mathbf{er}}$), and it is expressed in the end-effector CRF,
${}^e\mathbf{v}_{t/e}$	the relative linear velocity of the tool tip \mathcal{O}_t with respect to the end-effector frame,
${}^e\mathbf{v}_e$	the twist velocity vector of the end-effector which gather the linear and angular velocities (${}^e\mathbf{v}_e = \begin{bmatrix} {}^e\mathbf{v}_e \\ {}^e\boldsymbol{\omega}_e \end{bmatrix} \in \mathbb{R}^{6 \times 1}$),
\mathcal{S}_t	the tool shape,
\mathbf{C}_t	the tool curvature,
s_t	the arc length of the tool,
\dot{s}_t	the curvilinear speed of the projected point ${}^e\mathbf{p}_{t'}$ along the tool shape,
${}^e\mathbf{k}_t$	the instantaneous tangential unit-vector on the tool shape,

continued on the next page

<i>continued from the previous page</i>	
Symbol	Description
$\mathbf{L}_{e_{rcm^*}}$	the interaction matrix of the alignment task, which could be either $\mathbf{L}_{e_{rcm3D}} \in \mathbb{R}^{3 \times 6}$ or $\mathbf{L}_{e_{rcm1D}} \in \mathbb{R}^{1 \times 6}$,
$\mathbf{L}_{e_{rcm^*}}^\dagger$	the inverse matrix of $\mathbf{L}_{e_{rcm^*}}$, which could be either $\mathbf{L}_{e_{rcm3D}}^\dagger \in \mathbb{R}^{6 \times 3}$,
$ker(\mathbf{L}_{e_{rcm^*}})$	the kernel matrix of $\mathbf{L}_{e_{rcm^*}}$, which could be either $ker(\mathbf{L}_{e_{rcm3D}}) \in \mathbb{R}^{6 \times 4}$ or $ker(\mathbf{L}_{e_{rcm1D}}) \in \mathbb{R}^{6 \times 5}$,
\mathcal{S}_p	the path shape,
\mathbf{C}_p	the path curvature,
s_p	the arc length of the path,
\mathbf{d}_{pf}	the projected distance of the tool tip \mathcal{O}_r onto the path shape \mathcal{S}_p ,
\mathbf{p}_p	the projection point of the tool tip \mathcal{O}_t onto the path,
\mathbf{k}_p	the instantaneous tangential unit-vector on the path shape,
\mathbf{k}'_p	the derivative of \mathbf{k}_p with respect to the arc length s_p ,
$\dot{\mathbf{k}}_p$	the time-derivative of \mathbf{k}_p ,
$\mathbf{L}_{e_{pf}}$	the interaction matrix of the path following task,
$\mathbf{L}_{e_{app}}$	the interaction matrix of the approach task,
\mathbf{e}_{app}	the linear error between the tool tip \mathcal{O}_t and the incision hole centre point \mathcal{O}_r during the approach phase where the tool is located outside the incision hole,
λ	a positive scalar gain for increasing or decreasing the velocity of the alignment task,
γ_{rot}	a positive scalar factor for increasing or decreasing the velocity along the y -axis of the end-effector frame while applying the geometric method with a straight tool,
α_{obs}	a positive scalar for the stiffness of the virtual spring,
α	a positive scalar coefficient for advancing along the path,
β	a negative scalar coefficient for returning to the path,
v_{tis}	the desired speed of the tool tip along the path,
γ	a positive gain factor which effects the approaching velocity when the tool is located outside the incision hole,

TABLE 1: Notations summary

General Introduction

Contents

Context	1
Scientific and Technical Contributions	2

Context

The auditory system is a delicate organ inside the human skull. Various infections and diseases may affect this system among which *cholesteatoma* is a frequent disease that invades the middle ear. It is an abnormal proliferation of cells that destroy the adjacent bony structures, as a consequence, a conductive hearing loss is the common complication of this disease. The infected cells may be spread all over the middle ear cavity and could cause life-threatening conditions in the long-run.

Around one new case per 10,000 citizens occur every year. In the current medical technique, the only treatment for this disease is a surgical operation. The main concern of such treatment is the high probability to be left with residual cholesteatoma, and based on the literature around 20% of patients are enduring such complications. For instance, in France through the year 2014, 7066 patients went a first cholesteatoma surgery, while 770 cases (10.9%) performed a secondary intervention (as a consequence of the residual cholesteatoma).

The rationale behind this is that the surgeon cannot remove all cholesteatoma cells during the first surgery. The residual cells develop again and the patient has to suffer another surgery, within an interval of 6 to 18 months later. The main challenges that the surgeon encounters during the operation are: i) the limited capacity to visualize the tiny and confined space of the middle ear cavity, and ii) the rigidity of the surgical tool used by the surgeon.

Therefore, the μ RoCS (MicroRobot-assisted Cholesteatoma Surgery) project was proposed (FIGURE 1) with the aim: i) to eliminate the incidence of residual cholesteatoma by removing efficiently all infected cells from the first surgery, and ii) to make a less invasive surgery. Such objectives can be achieved by providing the surgeon with an assisted

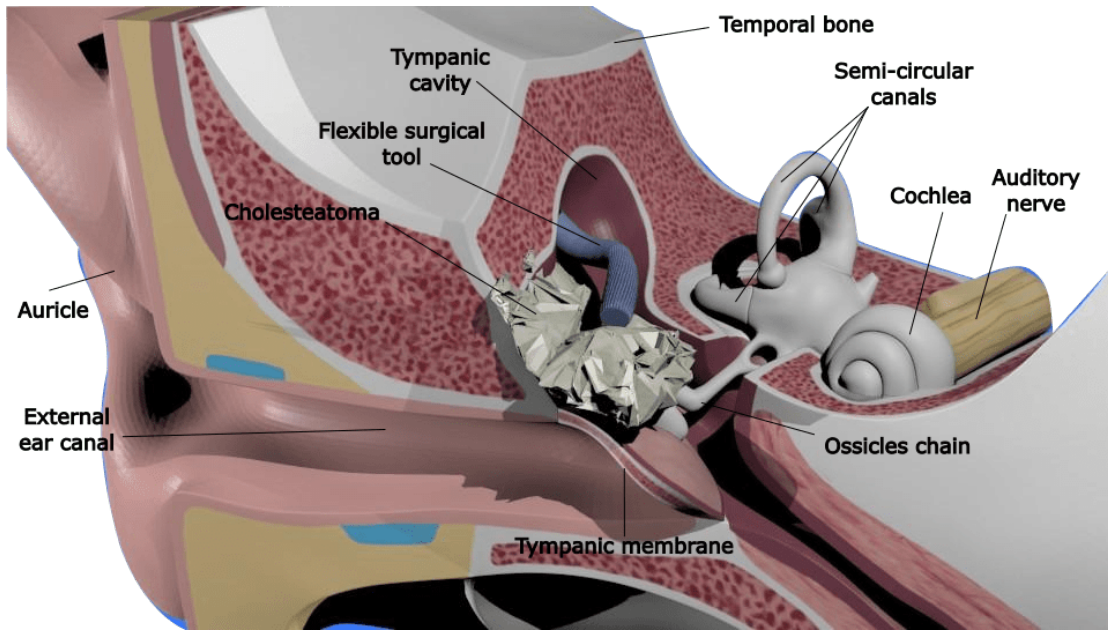


FIGURE 1: A conceptual scheme of μ RoCS system.

robot which is equipped with the latest technology. This micro-robotic system will improve the accuracy and repeatability of the surgeon's gestures. Further, the accurate selection of diseased tissues with the support of image-guided and flexible surgical robotics would improve the accessibility, and reduce the need for large incisions and bone tissues removal accordingly. As such, this would limit the invasiveness effect, as well as reducing the patient recovery time, operation time and costs. Due to the size of the auditory system and its location in the skull, the use of conventional surgical robots is impossible. This what led to our project idea which is the need to invent an unprecedented microrobot-assisted otological system.

Scientific and Technical Contributions

At FEMTO-ST Institute, France, in the AS2M (Automatique et Systèmes Micro Mécatroniques) department with the support of the MiNaRob (Micro-Nano-Robotique Biomédicale) team, this thesis was conducted. The team MiNaRob with the ENT (Ear Nose Throat) department of CHU (Centre Hospitalier Universitaire) Besançon, France, are both supporting scientific projects but this thesis marks their first collaboration in an otological application. In fact, the cholesteatoma surgery was chosen by our surgeon; since it is one of the most frequent otological pathologies that urge to enhance its treatment.

This thesis is an early stage research of μ RoCS project which was established between FEMOT-ST Institute, being a leading laboratory specializing in the fundamental and applied engineering with a focus on the micro-/nano-techniques, and the clinical part-

ner CHU Besançon. They are collaborating with ARTORG center, Universität Bern, Switzerland, which has been active in the field of computer-assisted surgery, especially with regards to the cochlear implantation procedure, and biomechanics research with a focus on the transfer of novel technology into clinical routine.

This PhD thesis focuses on the engineering discipline. However, Chapter 1 is devoted to explaining the clinical aspect whereby it describes the anatomical structure of the auditory system with a special attention to the middle ear cavity, and it sheds light also on the cholesteatoma disease from epidemiology, diagnostic and treatment perspectives.

Afterwards, the next chapters are dedicated to the engineering aspect. The purpose of Chapter 2 is to be a source of inspiration for newcomers to the field of otological surgery, and those who are concerned with the cholesteatoma treatment such as engineers, scientists and surgeons. It also aims to provide an exhaustive description of the scattered bits of investigation related to the robot-assisted cholesteatoma surgery. Thus, it starts with the introduction of the ideal requirements and specifications to reach an efficient robotic system without any constraints on the applied technology. After that, a review of the current surgical robotic systems, especially for otological surgeries, is highlighted herein with a brief on the advantages, the disadvantages and the required improvements necessary to achieve a cholesteatoma surgical robotic system.

A first step toward the ideal system is to propose a controller capable of guiding a standard/commercial surgical tool. For instance, milling a new minimally invasive tunnel, it has to guide the tool for following the milling path under the RCM (Remote Centre of Motion) constraints. The RCM movement controls the surgical tool to ensure that the tool stays always at the centre point of incision hole while performing a path following task to accomplish a resection or scanning task. Another type of constrained movement is proposed when the tool diameter is smaller than that of the entry orifice (i.e., the case when the surgeon manipulates a tool through the external ear canal). This type of movement is called UCM (Unilaterally Constrained Motion). It allows the tool moving freely within the incision hole or/and to lay on the incision wall while reaching distal targets.

Chapter 3 is dedicated to explain geometrically these two types of constrained movements (i.e., the RCM/UCM movements). It also proposes a controller to maintain these constraints on the standard rigid surgical tools. This tool could be either straight or curved. Thereafter, a proposed simulator is presented to prove the proposed control laws. Indeed, the proposed controller is formulated in the task-space which implies that the constrained motion is defined in the Cartesian space. Such formulation is used to design a modular controller which can be easily applied on different robotic structures, in case the inverse differential kinematic of the robot is known.

Chapter 4 formulates a path following controller which guides the tool tip to follow a reference curve accurately. In addition, this chapter describes a task priority controller which permits to set a hierarchy between the different tasks. This controller sets the priority between the path following task with either the RCM task or the UCM. The proposed controller is also validated numerically as presented in this chapter. Then, the proposed controller is also integrated with an exteroceptive sensor (i.e., camera) as the feedback for the control loop. Such a sensor acts as the surgeon's eyes by providing the

relative pose of the robot's end-effector with respect to the patient's head. Thereby, an image-guided controller implemented to assess experimentally the proposed control laws. These experiments were conducted on a parallel robot at FEMTO-ST and on a serial robot at ARTOG Center.

The last Chapter gives a general conclusion on our work and the different tracks for the future work.

List of publications: The contributions of this PhD thesis are summarized as:

- **Journals**

- B. Dahroug, B. Tamadazte, S. Weber, L. Tavernier, and N. Andreff, "*Review on Otological Robotic Systems: Toward Micro-Robot Assisted System for Cholesteatoma Surgery*", in *RBME* (Review on BioMedical Engineering), 2018

- **Book chapter**

- B. Dahroug, B. Tamadazte, and N. Andreff, "*Task Controller for Performing Remote Centre of Motion*", in *Lectures Notes in Electrical Engineering (LNEE)*, 2017. Selection of ICINCO 2016 to be included in the book series published by Springer.

- **Conferences ad proceedings**

- B. Dahroug, B. Tamadazte, K. Rabenorosoa, L. Tavernier, and N. Andreff, "*Towards middle ear robotic interventions: cholesteatoma removal*", in *Surgetica*, 2017
- B. Dahroug, B. Tamadazte, and N. Andreff, "*Visual Servoing Controller for Time-Invariant 3D Path Following with Remote Centre of Motion Constraint*", in *IEEE International Conference on Robotics and Automation (ICRA)*, 2017
- B. Dahroug, B. Tamadazte, and N. Andreff, "*3D Path Following with Remote Center of Motion Constraints*", in *13th International Conference on Informatics in Control, Automation and Robotics (ICINCO)*, 2016

Chapter 1

Clinical Background

Contents

1.1 Anatomy and Physiology of Human Auditory System . . .	5
1.1.1 External ear	6
1.1.2 Inner ear	9
1.1.3 Middle ear	9
1.2 Cholesteatoma	16
1.2.1 Definition of cholesteatoma	17
1.2.2 Pathology, complications and epidemiology	18
1.2.3 Diagnosis and imaging tools	21
1.2.4 Treatment	25
1.2.5 Ablation tools	27
1.3 Conclusion	30

The objective of the chapter is to present a comprehensive review of the middle ear for engineers and non-medical researchers. Section 1.1 concentrates on the clinical part in terms of: i) defining the important anatomical structures of the auditory system, and ii) presenting the medical terminology for describing the robot workspace (i.e., middle ear cavity). After that, the Section 1.2 provides a detailed description of cholesteatoma disease and its societal impact. The current diagnostic and treatment methods are also discussed.

1.1 Anatomy and Physiology of Human Auditory System

The human skull is formed by different bony portions. At the base and at the two sides of the skull is located the temporal bones which sustain the auditory systems. This system is responsible for the senses of hearing and balance. It is mainly divided in three parts, as shown in FIGURE 1.1: external ear, middle ear and inner ear.

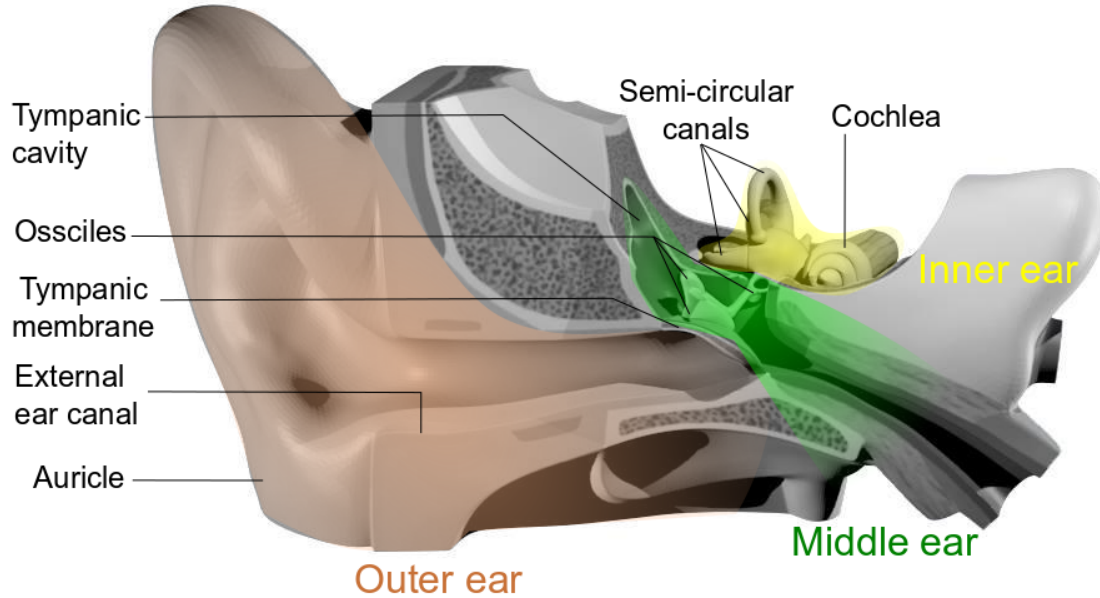


FIGURE 1.1: The different parts of the auditory system.

The sound waves are collected by the external ear, as a consequence, the ear drum (*tympanic membrane*) vibrates. These vibrations are transmitted from the middle ear to the inner ear; due to the motion of the ossicles within the tympanic cavity. The inner ear is the sensory receptor of balancing (i.e., the semi-circular canals) and hearing (i.e., the cochlea which convert the acoustic waves to nervous signals).

This section begins with the explanation of the auditory system. It also presents the description of the temporal bone which represents the robot workspace.

1.1.1 External ear

The external ear is the visible part and it consists of the pinna (or *auricle*) and the external ear canal (or *external acoustic meatus*) until the ear drum (or *tympanic membrane*).

Auricle: The main purpose of such a part is to collect and to guide the sound waves into the middle ear. It is also composed of fibro-cartilage, ligaments, muscles and skin (i.e., epidermal skin) which is continuous with the face skin [Legent et al., 1968].

The blood network around the auricle is rich. FIGURE 1.2 shows the carotid artery² that passes near the auricle and continues through the temporal bone. It also shows the dif-

¹The image is available online on: <http://slideplayer.com/slide/9202303/>

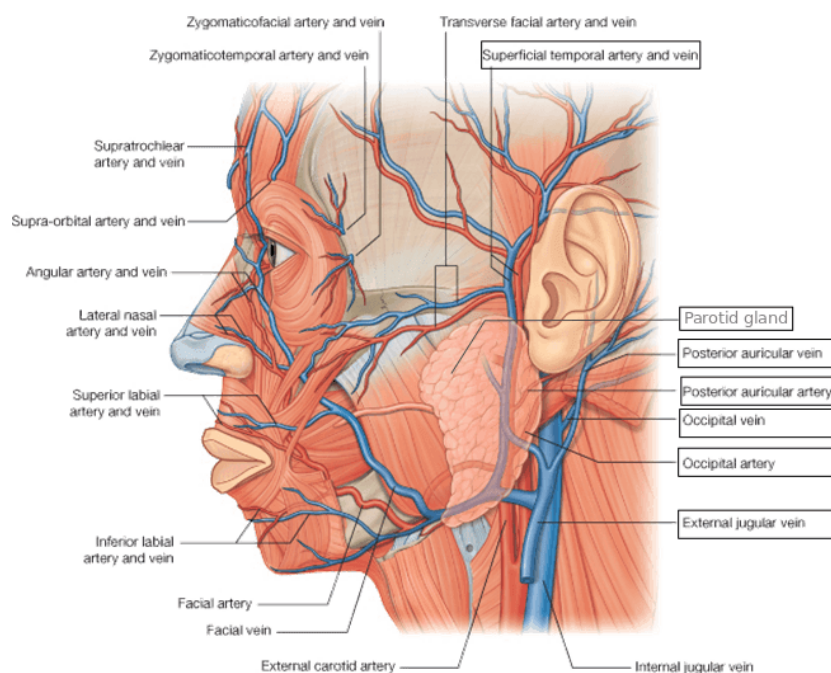


FIGURE 1.2: The carotid artery behind the auricle with the jugular vein and the parotid gland ¹.

ferent parts of the lymphatic system ³ which are located or passing near the auricle as the parotid gland and the jugular vein ⁴.

External ear canal: It is formed from two portions: i) the outer portion passes through the cartilage, and ii) the inner portion passes through the tympanic portion of the temporal bone. The skin of the outer portion is thick and covered by very fine hair. It also supports several glands, like ceruminous and sebaceous glands which are responsible to produce earwax (or *cerumen*) [Martin and Clark, 1997, Legent et al., 1968]. The skin of the inner portion is smooth, dry, adherent to the wall and much thinner when approaching to the tympanic membrane.

The canal length is about 25mm and its diameter varies approximately from 5 to 10mm . The inner bony portion represents about 16mm in length from the total canal length [Legent et al., 1968].

²Arteries carry oxygenated blood away from the heart to peripheral organs.

³It is comprising a network of lymphatic vessels that carry the lymph towards the heart and its main function is immune defence.

⁴Veins carry deoxygenated blood toward the heart.

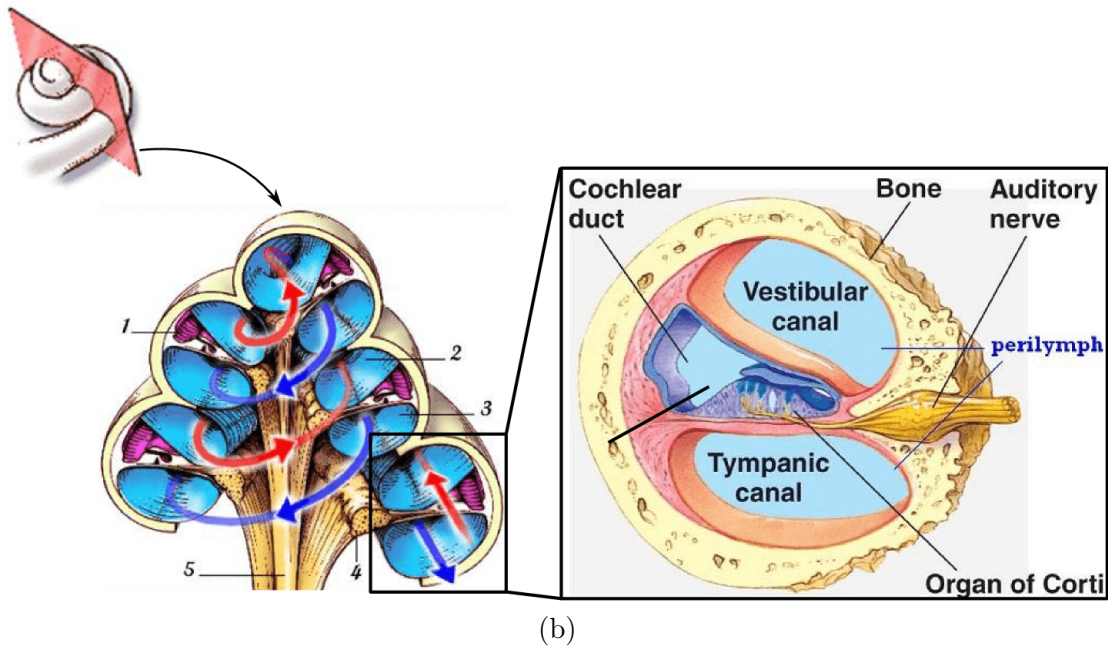
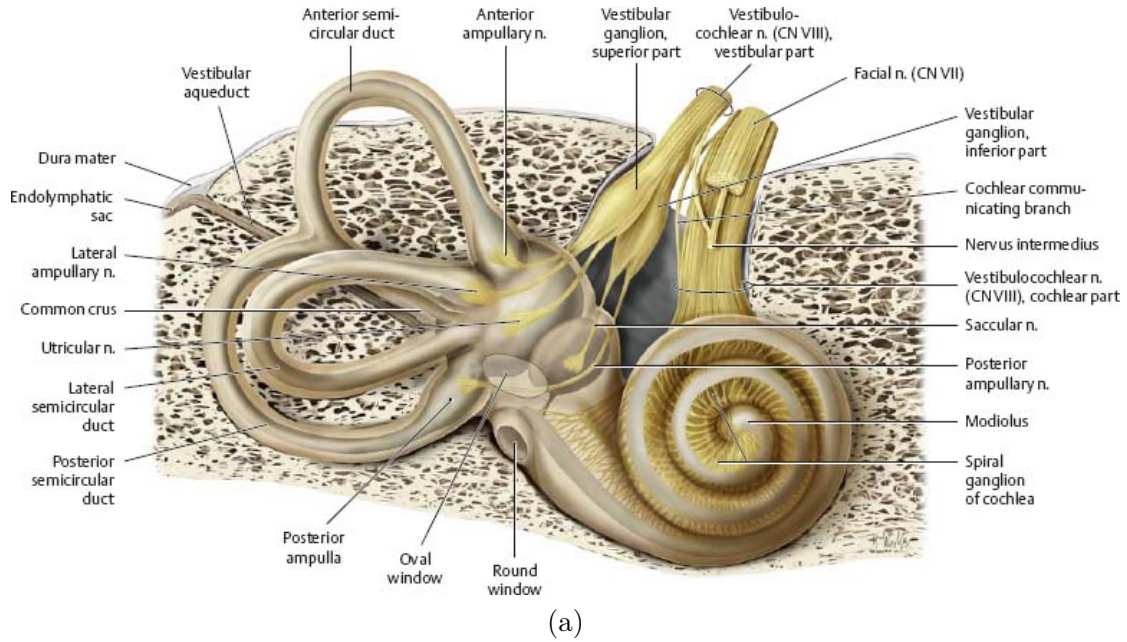


FIGURE 1.3: (a) The different parts of the inner ear, (b) the fluid path within the cochlea with its cross section.

1.1.2 Inner ear

The inner ear is responsible for the vestibular system and the auditory system (FIGURE 1.3).

Vestibular system: It contributes to the balance and it relies on the forces of gravity and inertia. It is formed by three *semicircular canals* which are filled with fluid. The movement of this fluid within these canals provides the sense of equilibrium. In fact, this system could be considered as a gyroscope sensor which provides a continuous information about the head orientation.

Auditory system: A snail-like shell named the *cochlea* is responsible for the hearing sense. Such an organ is filled with liquid that is the same as the one existing in the vestibular system. This liquid is perturbed when the stapes hummers on the oval window. This perturbation moves the liquid inside the cochlea where exists the organ of hearing (*organ of Corti*). At the surface of this organ lies hair cells that are connected to the auditory nerve. With the motion of these hair cells (*stereocilia*), the nerve cells are simulated. The hair cells themselves are about $10\mu\text{m}$ long and $1\mu\text{m}$ in diameter [Martin and Clark, 1997].

1.1.3 Middle ear

It consists of the tympanic membrane and the tympanic cavity that shields three tiny bones (i.e., *malleus*, *incus* and *stapes*, or they are called *ossicles*). Indeed, the tympanic cavity is a part of the middle ear cavity which extends in the temporal bone.

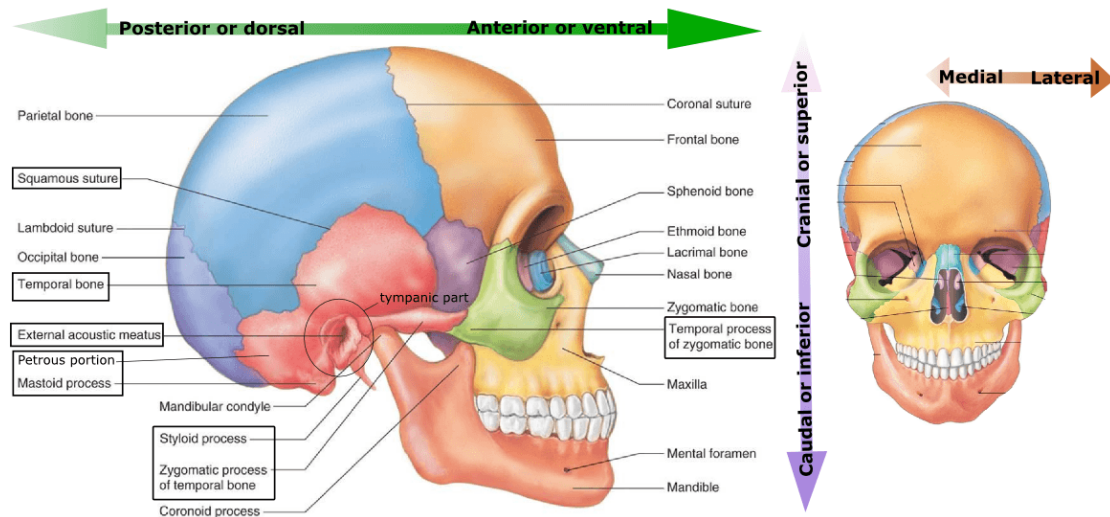


FIGURE 1.4: The human skull ⁵ with the anatomical direction reference.

Temporal bone: Such a bony portion (FIGURE 1.4) is mainly composed of five parts [Gray, 1918]:

- i) **Squamous portion:** it forms the anterior and the upper part of the bone, where its inferior boundary is connected with *zygomatic process*. Its inferior surface presents depressions corresponding to the convolutions of the temporal lobe of the brain.
- ii) **Mastoid portion:** it forms the posterior part of the temporal bone. It continues below into a conical projection, the *mastoid process*, which serves as the attachment of several muscles. A section of the mastoid process is hollowed out into a number of air spaces (i.e., *mastoid cells*).
- iii) **Petrous portion:** it contains, in its interior, the essential parts of the organ of hearing and its surfaces consist of canals, openings and grooves to transmit the facial nerve, acoustic nerve and veins.
- iv) **Tympanic part:** it is a curved plate of bone lying below the squamous portion and in front of the mastoid process. It presents a narrow furrow, which is called also the *tympanic sulcus*, and it serves as the attachment of the tympanic membrane.
- v) **Styloid process:** it serves as an anchor point for several ligaments and muscles.

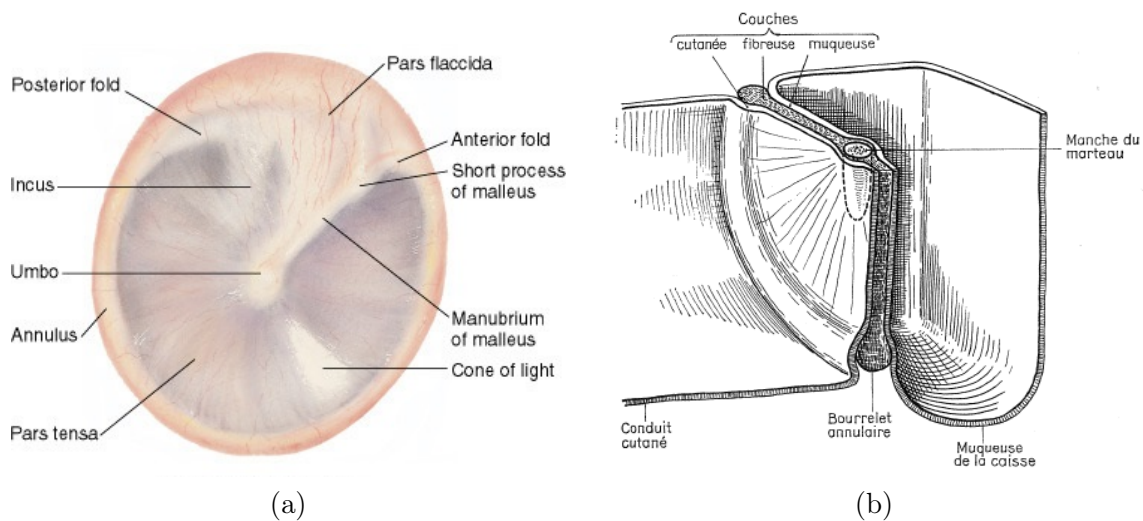


FIGURE 1.5: (a) The different parts of tympanic membrane; (b) the three layers of tympanic membrane.

Tympanic membrane: It is the border between the external ear outward and the middle ear inward, where its different parts are shown in FIGURE 1.5. It is slightly stretched into the middle ear to be pulled inward, resulting in its concave configuration. Its summit is called *umbo* (FIGURE 1.5(a)). It is held in position at the end of the

⁵The image is available online on: <http://chandlerphysicaltherapy.net/anatomy/muscular-system/head-and-neck/>

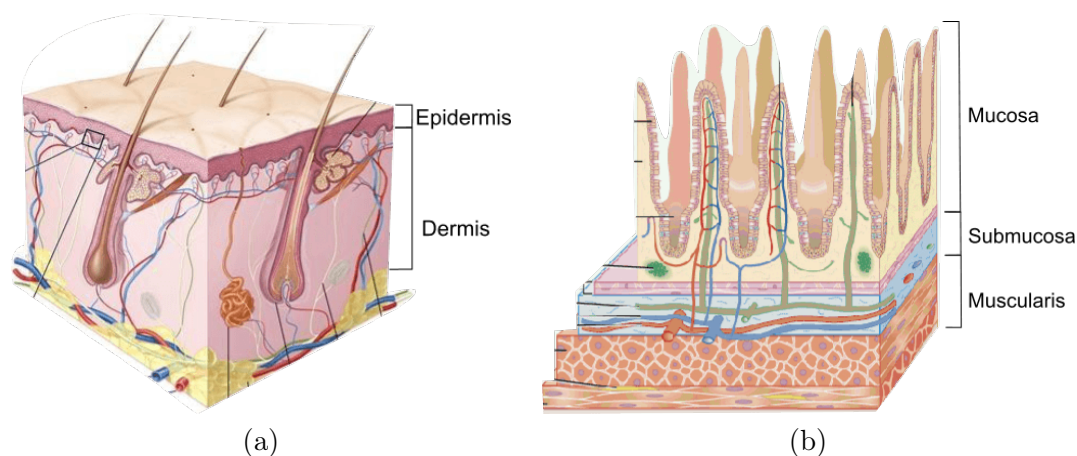


FIGURE 1.6: Comparison between two portions of human skin tissue: (a) the epidermal tissue which is the outer layer of tympanic membrane; (b) the mucous tissue which is the inner layer of tympanic membrane.

ear canal by a ring of tissue called the *tympanic annulus*. The greatest surface area of the tympanic membrane is taut (stretched) and is called the *pars tensa*. At the top of the tympanic membrane, the tissues are looser resulting in the name *pars flaccida* (or *Shrapnell's membrane*). The total area of the tympanic membrane is about 90mm^2 and its thickness varies from 0.07mm to 0.1mm [Martin and Clark, 1997].

The tympanic membrane is comprised of three layers [Legent et al., 1968] (FIGURE 1.5(b)): i) the outer layer is *epidermis*⁶ which continues directly with the skin of the external ear canal, ii) the middle layer is fibrous that composed from four types of fibres which provide some degrees of rigidity to the tympanic membrane, and iii) the internal layer is *mucosa*⁷ (FIGURE 1.6) that continues with the tympanic cavity.

Ossicular chain: The malleus bone is embedded in the tympanic membrane thanks to a fibrous layer. The incus bone connects the stapes bone, which hummers on the inner ear for transmitting the tympanic membrane vibration to the inner ear, with the malleus bone. These bones are linked together by articulations. In addition, the ossicles hold their position with muscles and ligaments (FIGURE 1.7).

The first one is *stapedius* muscle that is attached to the neck of the stapes and supplies blood to the process of the incus. It has a length of about 7mm and a diameter

⁶The outer skin of the human body is composed of three layers: epidermis is the outer layer, "epi" in Greek means "upon or over", the medial layer is dermis and the hypodermis is the last layer, also called subcutaneous. Beneath these three layers, there are fats.

⁷A membrane lining all body passages that communicate with the air, such as the respiratory and alimentary tracts and having cells and associated glands that secrete mucus. The mucus is a substance that consists chiefly of glycoproteins, water, cells, and inorganic salts and is secreted as a protective lubricant coating.

⁸The images are available online on: <http://doctorlib.info/medical/anatomy/37.html>

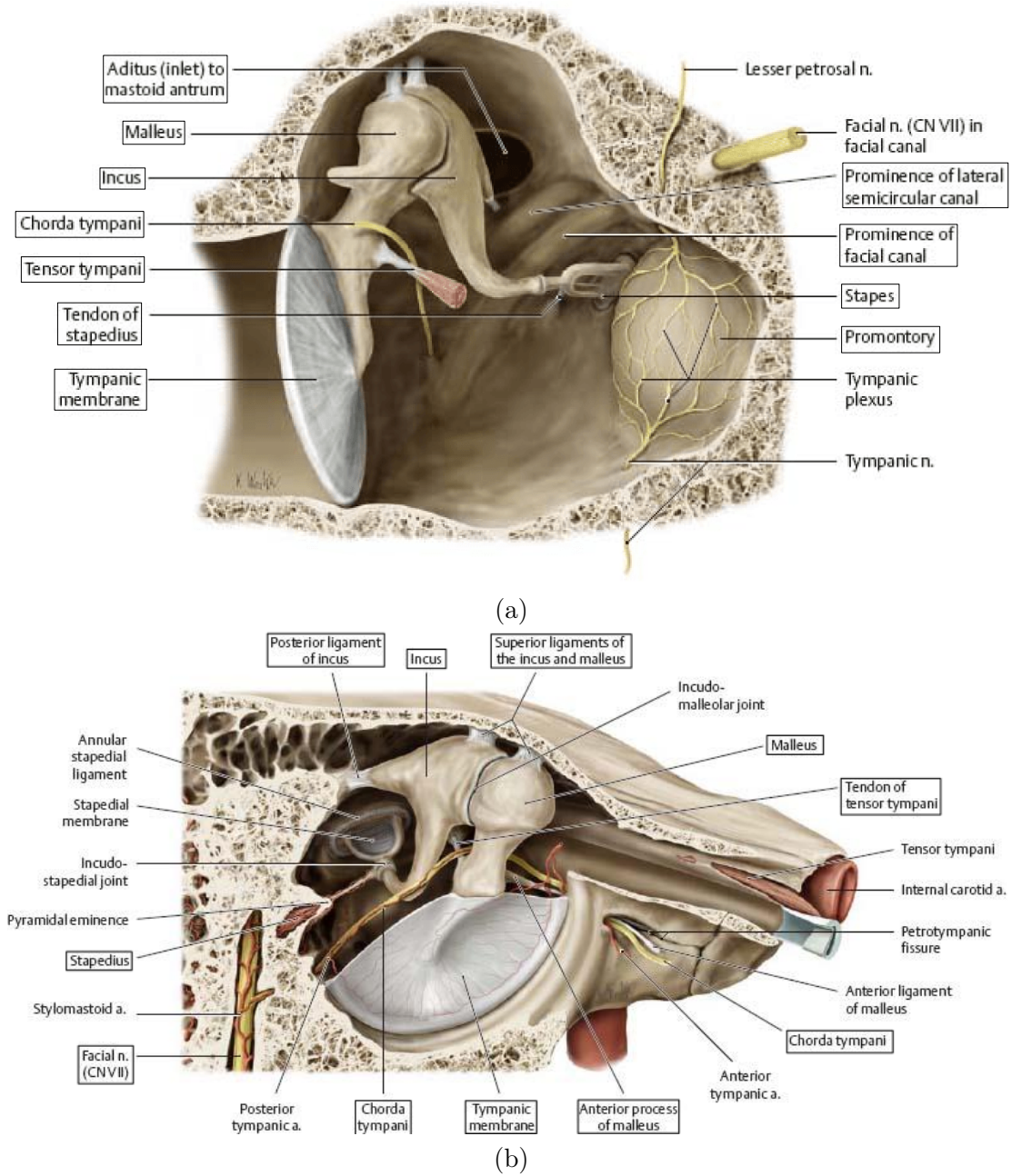


FIGURE 1.7: (a) Anterior view of the tympanic cavity with the anterior wall removed ⁸, (b) lateral view of the tympanic cavity.

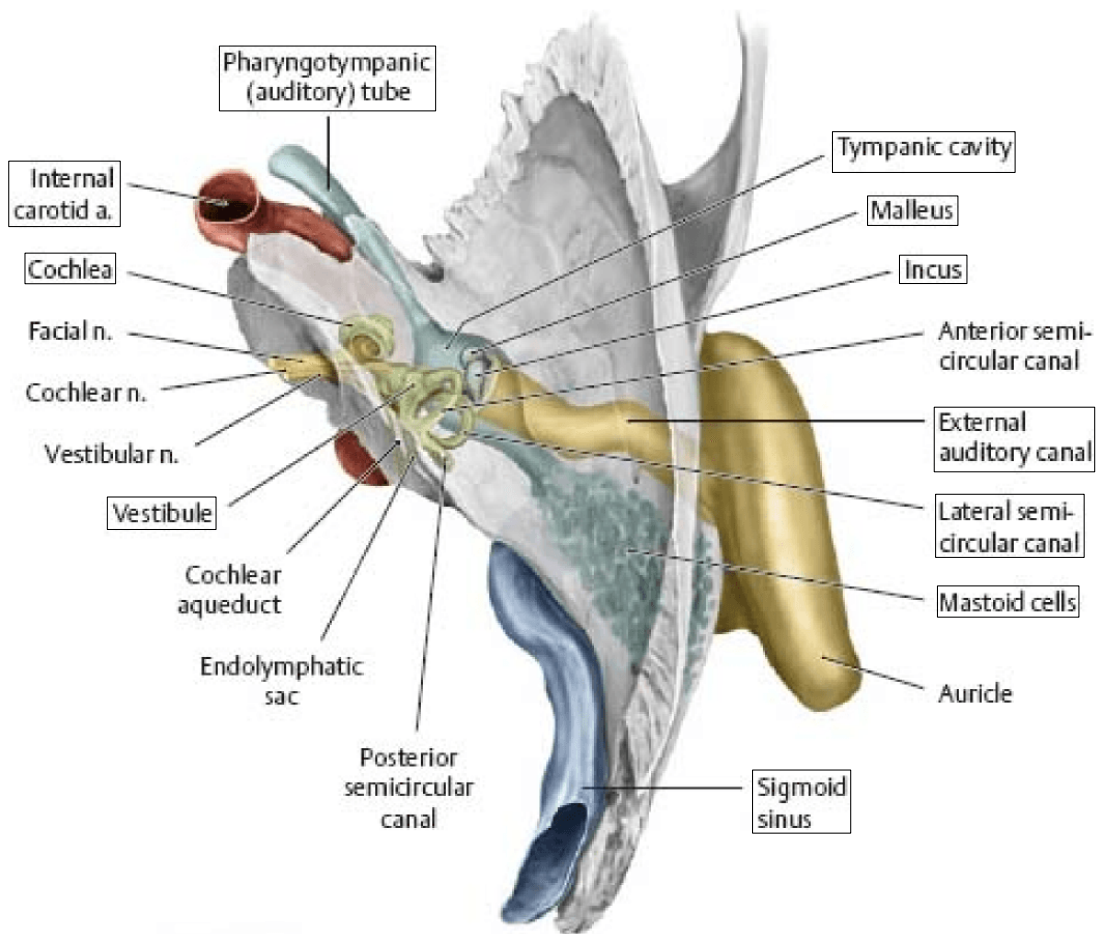
of 1.5mm^2 . The second is *tensor tympanica* muscle where its length about 25mm and its diameter 1.5mm^2 [Legent et al., 1968, Martin and Clark, 1997].

Tympanic cavity: Such a cavity has an irregular parallelepiped form. The description of each wall is as follows:

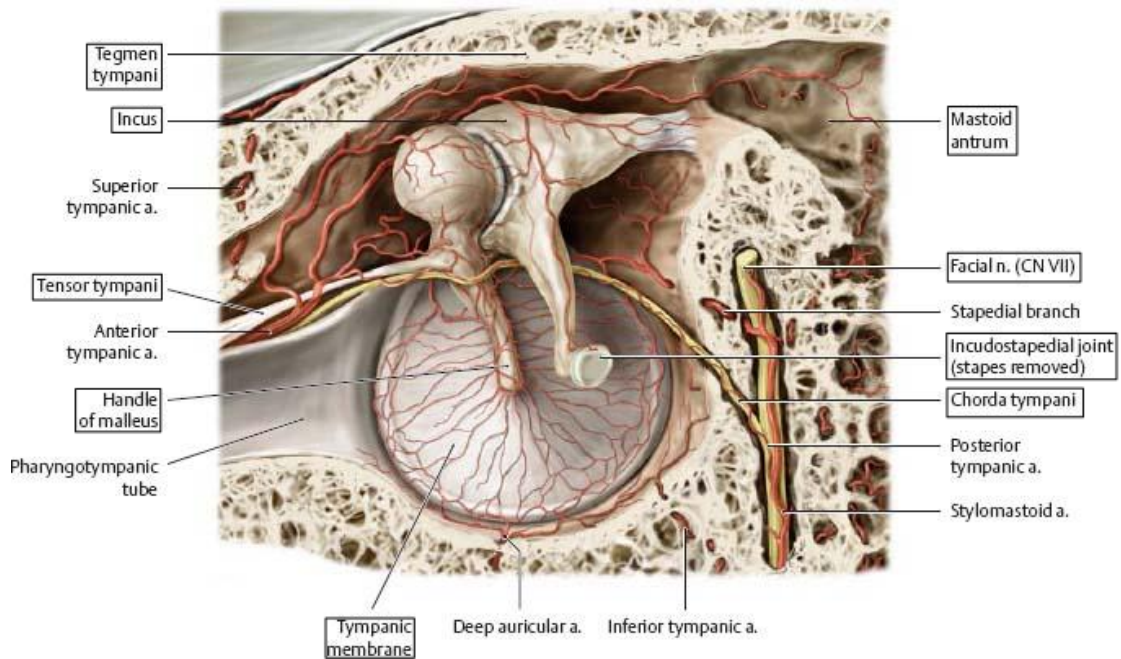
- The **superior wall** is a thin layer of bone, separating the tympanic cavity from meninges⁹, and it is called *tegmen tympani* (FIGURE 1.8(b)).
 - The space below this wall is called *epitympanic recess* or *attic*. In this region, the malleus head and the body of incus are located.
- The **inferior wall** holds the *Eustachian tube* (or pharyngotympanic tube as depicted in FIGURE 1.8(a) and (c)).
 - The space above this wall is called *hypotympanum*.
 - The Eustachian tube is a canal that connects the middle ear cavity with *Nasopharynx* (base of the nose). Its length is about 34mm [Martin and Clark, 1997]. This tube aims to balance the pressure between the external ear and the middle ear in order to maximize the mobility of the tympanic membrane.
- The **anterior wall** has an approximate height of 7mm .
 - Behind this wall passes the *carotid artery*.
- The **posterior wall** has a height of about 15mm .
 - At the top of this wall exists a hole which connects the upper region of the tympanic cavity (*epitympanic recess*) with the mastoid portion via *mastoid antrum* (FIGURE 1.8(b)).
- The **external wall** (or lateral wall) holds the tympanic membrane (FIGURE 1.8(b)).
 - The space located at the same level of the tympanic membrane is called *atrium* or *mesotympanic* which is the medial space between the epitympanic and hypotympanum. Also, the *chorda tympani*¹⁰ nerve passes through this region and it is frequently damaged by the cholesteatoma.
- The **internal wall** (or medial wall) separates the middle ear from the inner ear (FIGURE 1.8(c)). It is also called *labyrinthine* and it is divided horizontally into two portions:
 - Upper portion: the posterior region is marked by two bony projection that protects the external semi-circular canal and the facial nerve. The anterior region is a bony region that contains air cells.
 - Lower portion consists of the following regions:
 - * *Promontory* is a bony projection of cochlea.
 - * *Oval window* is a very thin layer that separates the cochlea and the stapes foot. This layer acts as a valve to prevent the liquid inside the cochlea from getting out. It has an elliptical form with a bigger diameter of about 3mm and a small diameter of around 1.5mm .

⁹The singular is meninx which is a fine membrane. The meninges are the three membranes enclosing the brain and spinal cord (i.e., dura mater, pia mater and arachnoid mater).

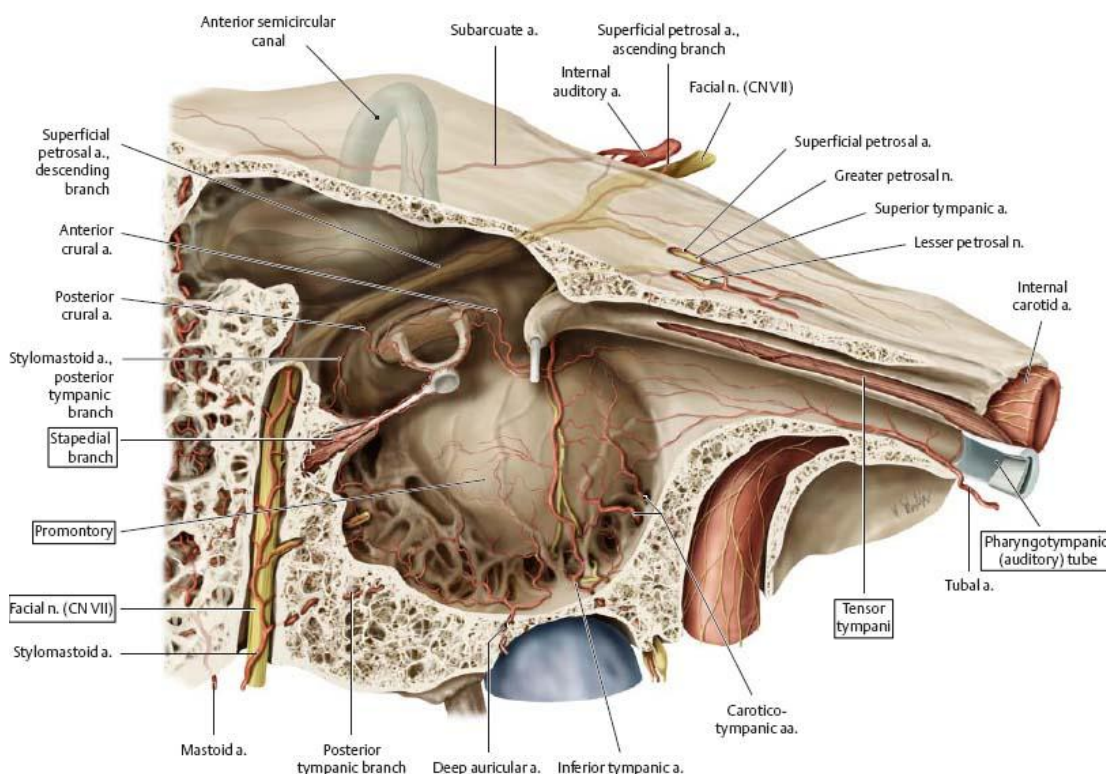
¹⁰This nerve carries information about the sensation of taste from the anterior two-thirds of one side of the tongue.



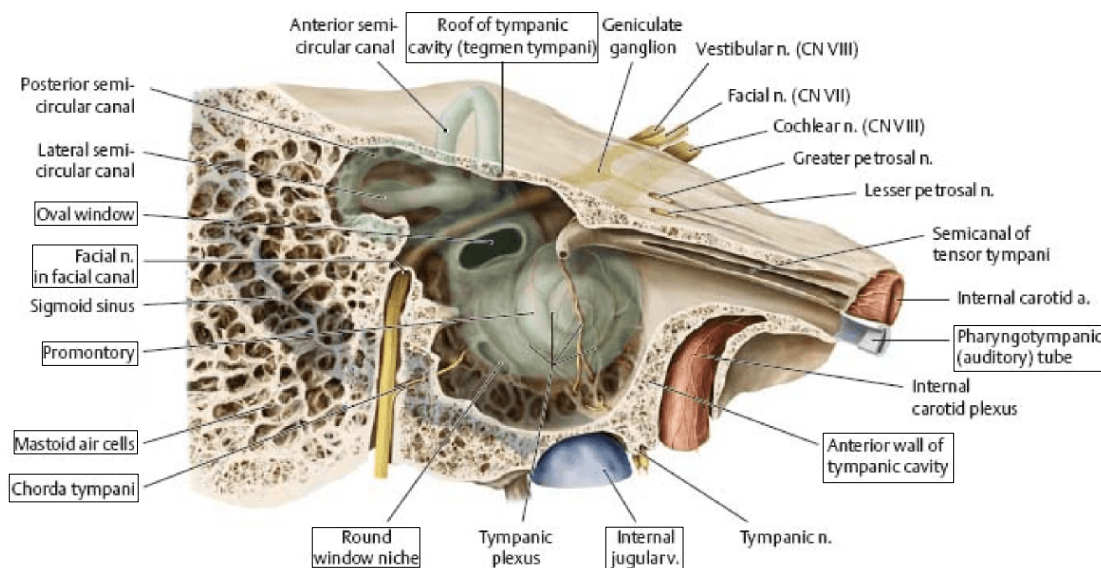
(a) inferior cross section of the tympanic cavity



(b) lateral cross section of the external wall



(c) medial cross section of the internal wall



(d) more depth in the medial direction of the internal wall

FIGURE 1.8: Description of the tympanic cavity walls ⁸ with the important structures which are surrounded by a rectangle.

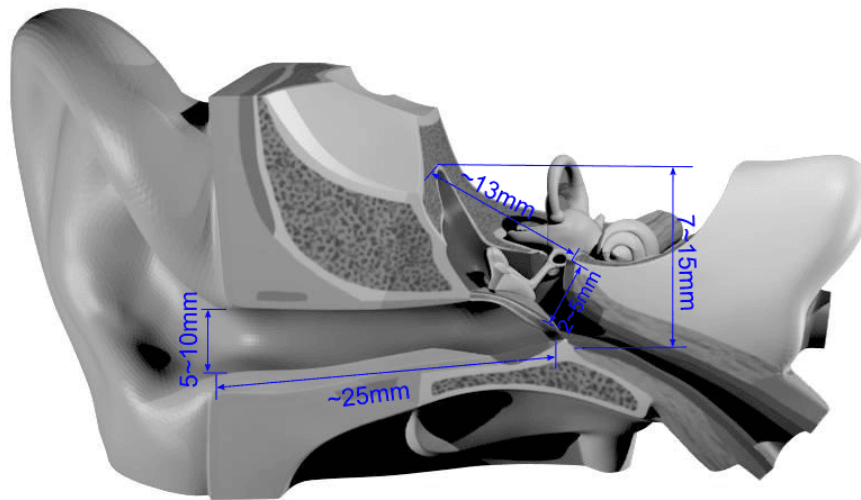


FIGURE 1.9: The different dimensions of the auditory system.

- * *Round window* is a thin layer like the oval window which compensates the vibration of the cochlear liquid that is produced by the oval window. It is also located beside promontory.
- * *Facial canal* is also called Fallopian canal and it is a protrusion on the wall where the facial nerve passes.

The length of tympanic cavity is about 13mm (anterior to posterior), its height varies from 15mm (posterior wall) to 7mm (anterior wall) and its width varies between 5mm (external) and 2mm (internal wall) [Legent et al., 1968] (FIGURE 1.9). The volume of this cavity varies from one person to another, which also increases during the individual growth periods, approximately from 452mm^3 for an infant to 640mm^3 for an adult [Abdala and Keefe, 2012]. All the internal cavities are covered by *mucous membrane*, including the tympanic cavity, the inner surface of the tympanic membrane, and the Eustachian tube [Legent et al., 1968, Martin and Clark, 1997].

1.2 Cholesteatoma

It is a disease that infects the middle ear by introducing abnormal skin in the middle ear cavity. In fact, it is due to the epidermal cells which come from the external ear canal and cover up the mucosa cells of the middle ear cavity. These cells gradually expands within the temporal bone and cause complications by destroying the adjacent bony structures. The surgical treatment is the only choice.

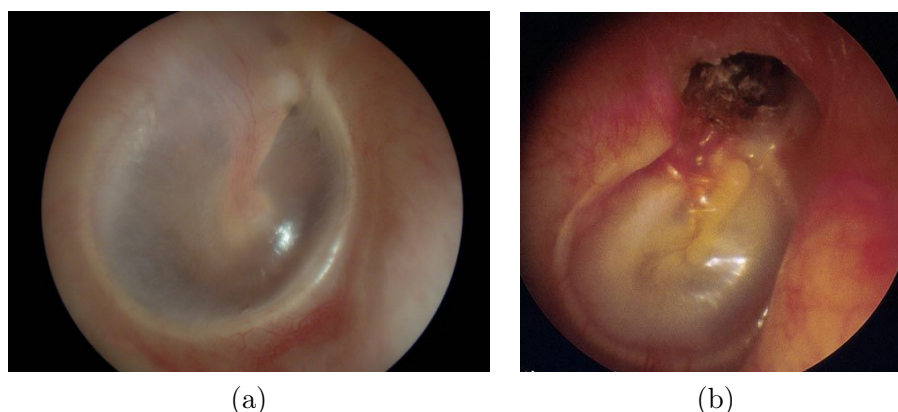


FIGURE 1.10: A Comparison between: (a) normal tympanic membrane, and (b) infected middle ear with cholesteatoma.

1.2.1 Definition of cholesteatoma

It occurs when keratinizing ¹¹ stratified squamous epithelium accumulates in the middle ear or other pneumatized portions of the temporal bone [Alper, 2004]. FIGURE 1.10 shows the difference between a normal and an infected ear.

Cholesteatoma is classically classified into three types: *congenital* and *acquired* which is divided into primary acquired and secondary acquired [Olszewska et al., 2004]. The congenital cholesteatoma occurs behind an intact tympanic membrane and it is rarer than the acquired cholesteatoma. The term "acquired" is related to an infection of the tympanic membrane. The primary acquired cholesteatoma appears locally on the pars flaccida, while the secondary acquired appears with a traumatic of pars tensa or fraction of the temporal bone.

Otitis media with cholesteatoma: Primary acquired cholesteatoma can occur in the presence of *otitis media*. This term means that the mucous membrane lining the middle ear is infected [Martin and Clark, 1997]. The general category of otitis media is frequently represented by the terms *acute* ¹², *chronic* ¹³ and *suppurative* ¹⁴. The term *acute otitis media* means the rapid onset of signs and symptoms of acute inflammation within the middle ear. If the tympanic membrane is perforated, this is known as *acute otitis media with perforation*. If there is a liquid in the middle ear, this is called *acute otitis media with effusion*. Otitis media with cholesteatoma occurs when the inflammation becomes chronic.

¹¹i.e., producing keratin which is a tough, insoluble portion substance that is the chief structural constituent of hair, nails, horns, and hooves.

¹²It means sudden rise of the disease. The disease also stays relatively for short duration compared to chronic.

¹³It means that the disease stays for long duration.

¹⁴It implies a formation or a discharge of pus. Pus is generally a viscous, yellowish-white fluid formed in infected tissue, consisting of white blood cells, cellular debris, and necrotic tissue.

1.2.2 Pathology¹⁵, complications and epidemiology¹⁶

The etiopathogenesis of cholesteatoma is still controversial [Olszewska et al., 2004]. The first description of cholesteatoma was probably given by Du Verney in 1683 as a fat mass, which he called "*steatoma*". In 1829, the French pathologist Cruveilhier redefined it as "*tumeur perlée*" or pearly tumour of the temporal bone. In 1838, the German physiologist Johannes Müller devised the term "*cholesteatoma*", by identifying a layered pearly tumour of fat. The term "cholesteatoma" must be considered a misnomer as this tumorous lesion ("-oma") contains neither cholesterol ("chol-") nor fat ("-stea-").

The origin of cholesteatoma has been subject to extensive debates. On one hand, the origin of congenital cholesteatoma is remnants of epithelial tissue behind an intact tympanic membrane. On the other hand, there is evidence for at least four different mechanisms for the development of acquired cholesteatoma, or a possible combination of these theories [Alper, 2004, Olszewska et al., 2004, Bordure et al., 2009]:

- *Squamous metaplasia*¹⁷ theory: the earliest observations suggest the transformation of middle ear skin to epidermal due to inflammation and infection.
- *Basal hyperplasia*¹⁸ theory: the epithelial cells from the keratinizing epithelium of the pars flaccida could invade into the subepithelial space and form an attic cholesteatoma. In other words, it is a rapid infection of the upper portion of the tympanic membrane and it spreads the upper region of the tympanic cavity.
- *Immigration or invasion theory*: the squamous epithelium migrates from the margin of a tympanic membrane perforation into the middle ear spaces. FIGURE 1.11(b) shows the tympanic membrane perforation.
- *Retraction pocket or invagination theory*: this theory is the most widely supported. The pars flaccida, or occasionally the pars tensa, of the tympanic membrane retracts into the middle ear due to negative pressure, inflammation or both. The retention of keratin accumulating within the deep retraction pocket establishes cholesteatoma.
 - *Retraction pocket disease*: FIGURE 1.11(a) presents the tympanic membrane with retraction pocket. The process is initiated by malfunctioning of the Eustachian tube, leading to impaired ventilation of middle ear and mastoid. The inadequate ventilation results in negative pressure in the middle ear, which leads to the tympanic membrane becoming flaccid (or retracted) accompanied by inflammation. As the pocket deepens, desquamated debris cannot be cleared, and cholesteatoma results.

Another classification of cholesteatoma is based on the infection site which is an important factor for the surgical procedure. This classification distinguishes between

¹⁵Pathology studies the disease from different aspects: etiology (cause), pathogenesis (development mechanisms), morphologic (structural alterations of cells) and clinical manifestation (consequences of changes).

¹⁶Epidemiology is the medical branch that deals with the incidence and prevalence of the disease in large population.

¹⁷Normal transformation of tissue from one type to another, as in the ossification of cartilage to form bone, or transformation of cells from a normal to an abnormal state.

¹⁸An abnormal increase in the number of cells in an organ or a tissue with consequent enlargement.

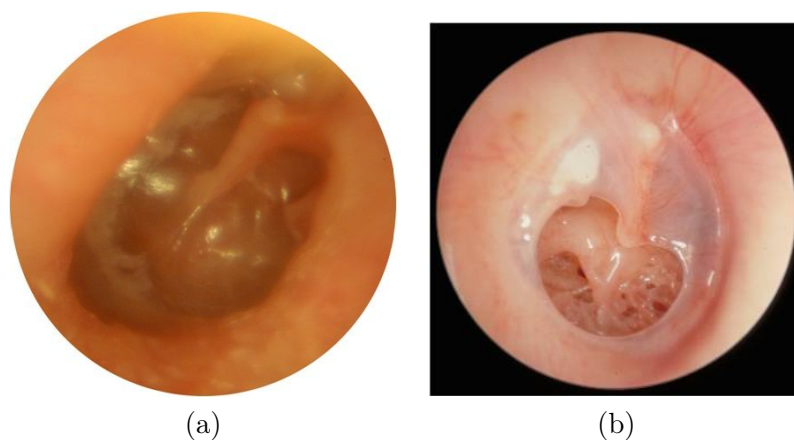


FIGURE 1.11: A comparison between (a) retraction pocket disease in the tympanic membrane, and (b) tympanic membrane with perforation.

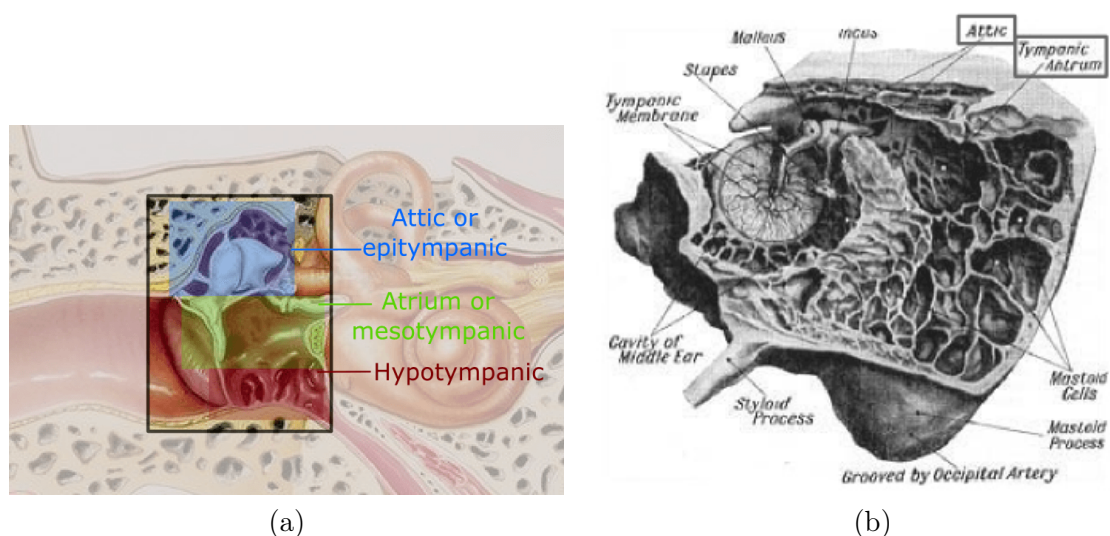


FIGURE 1.12: (a) Site of infection of cholesteatoma within the different regions of the middle ear cavity, and (b) a medial view on the mastoid bone.

several sites (FIGURE 1.12): the attic and antrum, tympanic cavity, mastoid, Eustachian tube and labyrinth (semi-canal projection) [Olszewska et al., 2004].

Complications of cholesteatoma: The evolution of the disease is life-threatening on the long run. The complications can be classified as follows [Alper, 2004, Bordure et al., 2009]:

- *Destruction of the ossicular chain* which leads to a conductive hearing loss.

- *Facial paralysis* due to the erosion of the fallopian canal which expands to the facial nerve.
- *Labyrinthitis* due to the erosion of the bony skeleton of the inner ear (vestibular with an erosion of the lateral semi-circular canal which leads to balance disorders, and rarer cochlea with an invasion of the oval window).
- Extracranial complications (or intratemporal):
 - *Mastoiditis* due to the invasion of the mastoid air cells.
 - Erosion of the tympanic membrane.
 - Erosion of the bony wall between the external ear canal and the mastoid, especially the attic area.
- Intracranial complications:
 - *Meningitis* is an inflammation of meninges that protects the brain and spinal cord.
 - *Subdural empyema* (infection of subdural space).
 - *Dural sinus thrombosis* is a blood clot in the vein which drains blood from the brain.
 - Erosion of the bony covering of the sigmoid (lateral) sinus.
 - *Brain Abscess* is an abscess (a collection of pus that has built up) caused by the infection of brain tissue.

Epidemiology: There are many studies that describe the frequency and distribution of cholesteatoma in a defined human population. Most of the literature consists of hospital-based data, case series of specialized centres and specialized ear surgeons. Each year, around 10 new cases per 100,000 inhabitants are infected by cholesteatoma. It affects also men more than women and children less than adults [Kemppainen et al., 1999, Djurhuus et al., 2010, Fiedler et al., 2013].

Since the only treatment in the current medical practice is a surgical intervention, approximately ten to thirty percent of cholesteatoma operations are unsuccessful with some residual or recurrent cholesteatoma cells, and it is higher in children than adults [Sheehy et al., 1977, Aquino et al., 2011, Djurhuus et al., 2015]. Recurrent cholesteatoma means that the disease grows again after the ablation process, while residual cholesteatoma refers to the cells that have been left behind by the surgeon. In both cases, an MRI (Magnetic Resonance Imaging) revision is performed (two to three times with an interval of six months between each time). This revision has the objectives to: i) visualize and observe the evolution of the cholesteatoma cells aggregation, ii) determine if it is necessary to perform a secondary procedure (also known as "second-look"). TABLE 1.1 shows recent French statistics from ATIH¹⁹ that represent the total number of cholesteatoma interventions.

¹⁹ ATIH: Agence Technique de l'Informatique sur l'Hospitalisation (French healthcare database). [online] <http://www.atih.sante.fr/statistiques-par-ghm-0>

Year	H71	H95.0 (H71%)	Total (H71+H95.0)
2012	7355	766 (10.4%)	8121
2013	7214	835 (11.6%)	8049
2014	7066	770 (10.9%)	7836

TABLE 1.1: The number of cholesteatoma interventions in France, where H71: the number of patients whose had a first cholesteatoma surgery, H95.0: the number of patients whose had another intervention to remove the residual cholesteatoma, and H71+H95.0: the total number of cholesteatoma interventions in each year.

1.2.3 Diagnosis and imaging tools

As far as the diagnosis is concerned, an HR-CT (High-Resolution Computer Tomography) and an MRI are widely used in the pre- and post-operative cholesteatoma assessments [De Foer et al., 2015]. These methods are considered as the standard pre-operative imaging techniques.

Throughout the intra-operative phase, the surgeon uses a standard otomicroscopy (FIGURE 1.13(a)). It is useful for visualizing the big debris of cholesteatoma cells. However, it is characterized by a restricted field of view, especially for visualizing the lateral region within the middle ear cavity as depicted (FIGURE 1.13(b)). As a result the probability of leaving cholesteatoma cells behind is high.

The surgeon may also use an otoendoscopy besides the otomicroscopy for providing a larger field of view during the intra-operative phase [Bordure et al., 2005, Ayache et al., 2008, Marchioni et al., 2011, Hanna et al., 2014]. Indeed, the endoscope is based on a fibre-optics technology, where their diameter may vary from 2.2mm to 0.3mm as reported in [Karhuketo et al., 1988]. In addition, it grants a minimally invasive procedure during the second surgery and it may reduce the rate of residual cholesteatoma during the primary operation [Thomassin et al., 1993, Badr-el Dine, 2002, Sajjadi, 2013]. However, its use is not ergonomic and it makes the surgeon to lose a hand to hold it. Moreover, it is not reliable because it is based on white-light imaging is based on white-light imaging and does not allow for a clear distinction of small cholesteatoma cells.

Other imaging techniques are still in the research developments, for instance, ultrasound, fluorescence and OCT (Optical Coherence Tomography). The usage of these research imaging techniques are beneficial; since it can provide an optical biopsy (real-time imaging modalities with micro-metric resolution and some depth) during the intra-operative phase.

Standard diagnostic imaging: On the one side, CT provides good information about the ossicles and the bony structures. On the other side, MRI is useful for characterizing soft tissues, such as cholesteatoma. The actual technology of MRI cannot detect the cholesteatoma cells that are smaller than 3mm. Consequently, the diagnosis of residual cholesteatoma is often difficult which explains the need for a second-look in too many cases [Kösling and Bootz, 2001, McJunkin and Chole, 2014, De Foer et al., 2015].

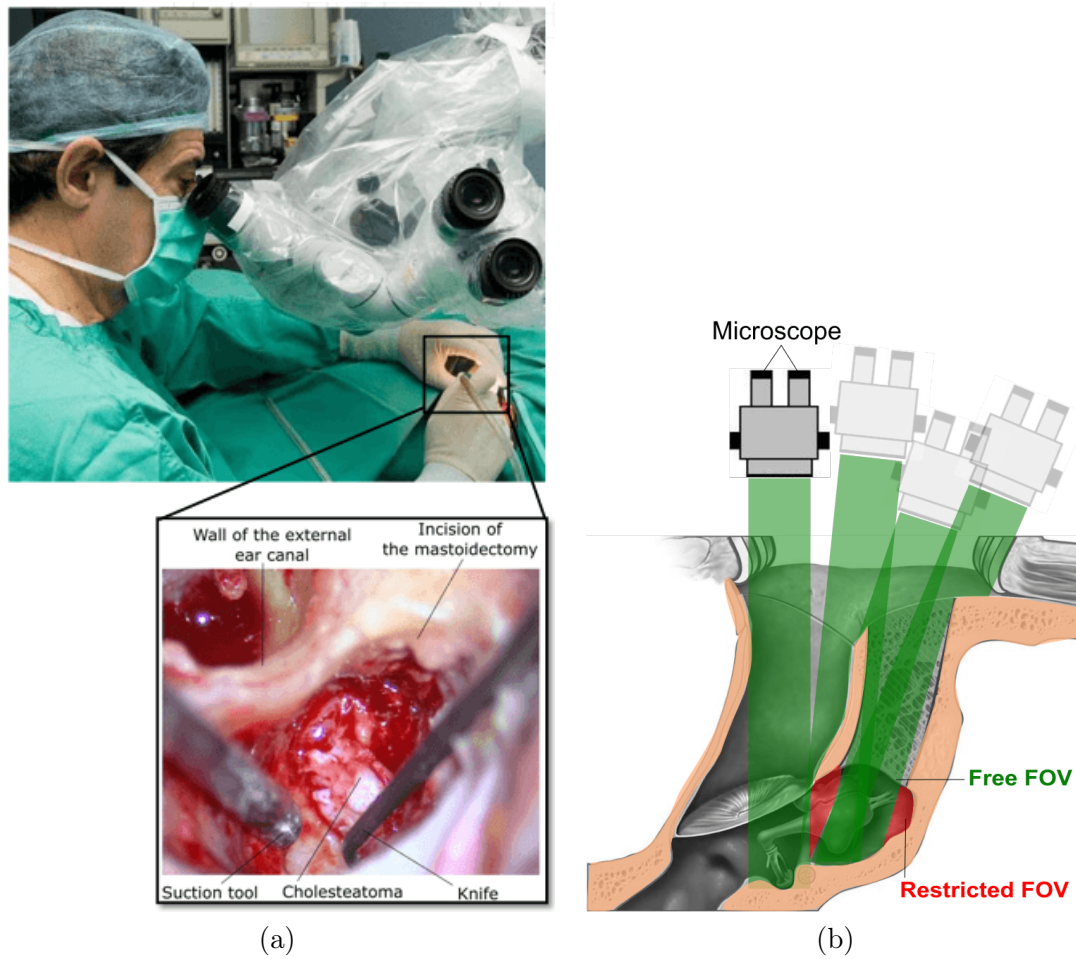


FIGURE 1.13: (a) The standard position of surgeon within the operation room with a zoom of the otomicroscopy, and (b) conceptual scheme of an otomicroscopy limitation.

This also urge for developing intra-operative diagnosis tools, able to detect individual cholesteatoma cells.

There are different techniques to detect cholestesatoma by applying the MRI, such as a delay contrast-enhanced T1-weight and an echo-planar diffusion-weighted. The latter technique showed more reliable results [Vercruysse et al., 2006, Frickmann and Zautner, 2012] (FIGURE 1.14). Vercruysse *et al.* [Vercruysse et al., 2006] performed a study to assess an echo-planar diffusion-weighted MRI for detecting the primary acquired (55 patients) and the residual cholesteatoma (45 patients). In the first group, the diffusion-weight imaging (DWI) method detected 89% of cases with sensitivity and specificity values²⁰ of 81% and 100%, respectively. In the second group, only one of seven surgically

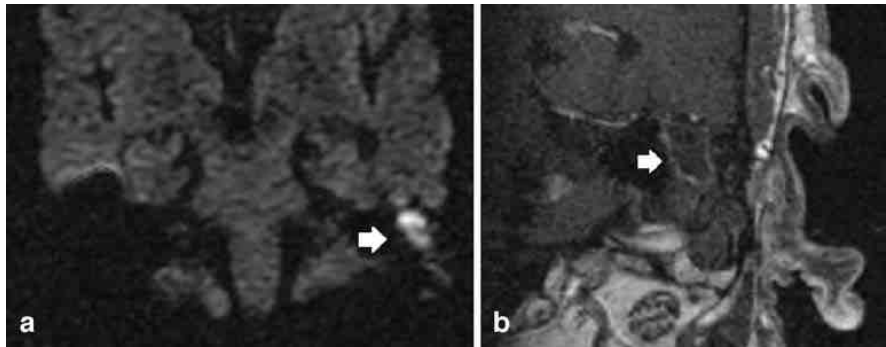


FIGURE 1.14: MRI images show a primary acquired cholesteatoma by the arrows [Ver-cruysse et al., 2006], where the MRI techniques are (a) echo-planar DWI, (b) T1-weight.

verified residual cases were correctly diagnosed using DWI, with sensitivity and specificity values of 12.5% and 100%, respectively.

As a conclusion, the latest technology of MRI has difficulties to identify the residual cholesteatoma which is even almost impossible during the intra-operation phase. Thus, it is required an innovative imaging tool able to go to the problem source.

Research diagnostic imaging: The real problem that faces the surgeon during the intra-operative phase is to detect the cholesteatoma cells, where it is difficult to visualize the lateral cavity of the middle ear cavity by using a standard otomicroscope. In addition, the otoendoscopy and the MRI cannot detect residual cholesteatoma cells. Therefore, one of the following methods can be used during the intra-operative phase to detect the residual cells in real-time with good reliability.

Ultrasound imaging: It is a mature field that has many applications for medical [Fenster et al., 2001] and non-medical applications [Awad et al., 2012]. It is useful to scan a region of interest [Fenster et al., 2001] and to remove tissues too [Haar and Coussios, 2007]. It is widely used in intravascular [Nissen and Yock, 2001] and ophthalmic imaging [Silverman, 2009]. This method has not yet been applied for cholesteatoma biopsy, based on our knowledge, but it was involved in other otological applications.

The authors in [Brown et al., 2009] proposed a high-frequency ultrasound system for imaging the auditory system. They obtained 3D images of the ossicles and the tympanic membrane by using a 6mm diameter probe. They also gathered 2D images of the cochlea through the round window membrane. The ex-vivo experiments showed that the axial resolution was around $50\mu\text{m}$, while the lateral resolution varied from $80\mu\text{m}$ to $130\mu\text{m}$ over a 5.12mm scan depth.

²⁰Related to medical diagnostics, sensitivity and specificity are statistical measures of the performance of a binary classification test, where i) sensitivity measures the proportion of positives that are correctly identified (e.g. the percentage of sick people who are correctly identified as having the condition), and ii) specificity measures the proportion of negatives that are correctly identified (e.g. the percentage of healthy people who are correctly identified as not having the condition)

The authors in [Torbatian et al., 2009] succeeded to miniaturize the probe diameter to 1mm . They reclaimed that the system showed a better resolution than both the MRI and the CT. However, it is required to inject water into the tympanic cavity for the acoustic coupling sake.

Fluorescence imaging: It is also known as *confocal imaging* which is based on distinguishing the wavelength of the light emitted by different substances [Muldoon et al., 2007, Orosco et al., 2013]. This method is applied to locate the remaining cholesteatoma cells during the surgery as reported in [Levy et al., 2013, Bradley et al., 2013]. They conducted the ex-vivo experiments by using a fibre-optic endoscope that has a diameter of 1mm . The experiments indicated that the mean accuracy, sensitivity and specificity were 95%, 98% and 92%, respectively (FIGURE 1.15). However, the tympanic cavity surface should be stained with a contrast agent (e.g., proflavine) before taking images in order to discriminate normal and infected epithelial tissues.

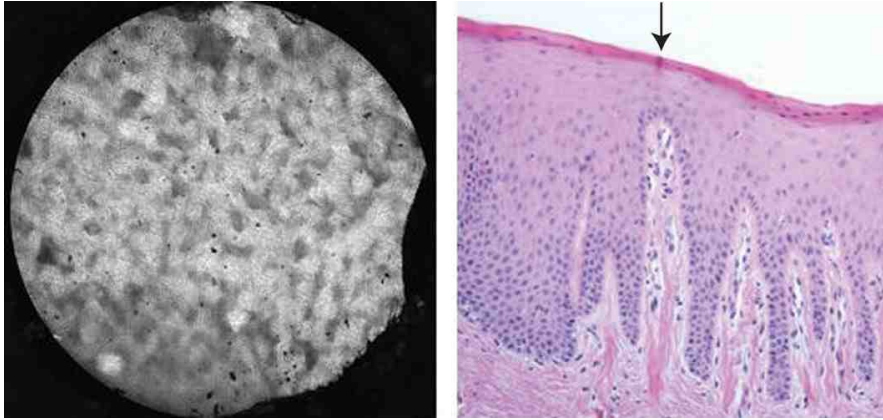


FIGURE 1.15: Comparison of cholesteatoma imagery [Levy et al., 2013] between fluorescence (the left image where the cholesteatoma cells are the bright grey pixels) and histological (the right image where the arrow presents a thin layer of keratin).

Optical Coherence Tomography: OCT is a modern imaging method [Fercher, 1996, Fercher et al., 2003, Gora et al., 2017], where its operating principle is similar to that of ultrasound but it replaces sound waves with light waves. It has many applications in diagnostic of cancer mucosa [Sergeev et al., 1997], ophthalmology [Budenz et al., 2007], cardiac [Brezinski et al., 1997, Patwari et al., 2000, Jang et al., 2002] and otology imaging. The OCT demonstrated that its resolution is better than the ultrasound [Brezinski et al., 1997, Patwari et al., 2000, Jang et al., 2002] for visualizing a coronary artery. It showed also a better imaging of skin structure compared to the fluorescence technique [Lademann et al., 2007].

There are many designs of endoscopic OCT that have been proposed in order to visualize a sub-structure inside cavities and hollow organs [Tran et al., 2004, Burkhardt et al., 2012]. Indeed, there are many works that deal with OCT for imaging various features within the middle ear, for instance, anatomical structures [Heermann et al.,

2002, Pitris et al., 2011], motion of ossicles [Subhash et al., 2012], chronic otitis media [Nguyen et al., 2012a, Djalilian et al., 2008].

A clinical study was done for imaging the cholesteatoma cells by using an OCT scanner and comparing the obtained results with the conventional observations by the binocular microscopy and histology [Djalilian et al., 2010]. The authors performed the in-vivo experiments on 10 patients (5 males and 5 females). The OCT probe was inserted into the tympanic cavity under a microscopic guidance, after a surgical exposure. The resultant OCT images showed the difference in signal intensity between normal tissue and those infected (FIGURE 1.16). The cross-section resolution was about $10\mu\text{m}$ and the penetration depth was around 1mm . The probe had a 2.7mm diameter and it was too large to inspect certain areas (e.g., the posterior superior quadrant of the middle ear) because the probe may injure the stapes.

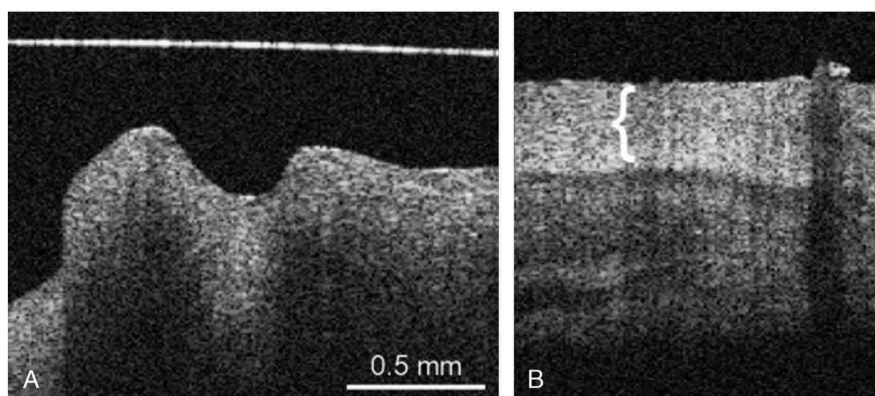


FIGURE 1.16: OCT image of (A) normal mucosa; (B) keratin layer (bracket) over the mucosa [Djalilian et al., 2010].

1.2.4 Treatment

The definitive and the only treatment of cholesteatoma is a surgery. The main surgical objective is the cholesteatoma removal and the secondary objectives are the reconstruction of ear function and repair of what the disease destroyed. This secondary phase of cholesteatoma intervention is often done by a *stapedectomy procedure* which consists of replacing the damaged ossicles by an artificial prosthesis. However, this thesis does not concentrate on this secondary phase since the surgeon can easily do it through the external auditory canal. Indeed, this thesis is dedicated to the primary phase where the surgeon usually leaves behind some residual cholesteatoma cells. In case that the residual cholesteatoma is suspected, an additional "*second-look*" procedure is performed 6 to 18 months later to inspect the mastoid and middle ear [Alper, 2004].

There are different techniques to gain access to the middle ear which depends on the infection site. In general, there are three ways to enter into the tympanic cavity, which are the endaural approach, transcanal approach, and the postauricular approach [Bordure et al., 2005, Hildmann and Sudhoff, 2006].

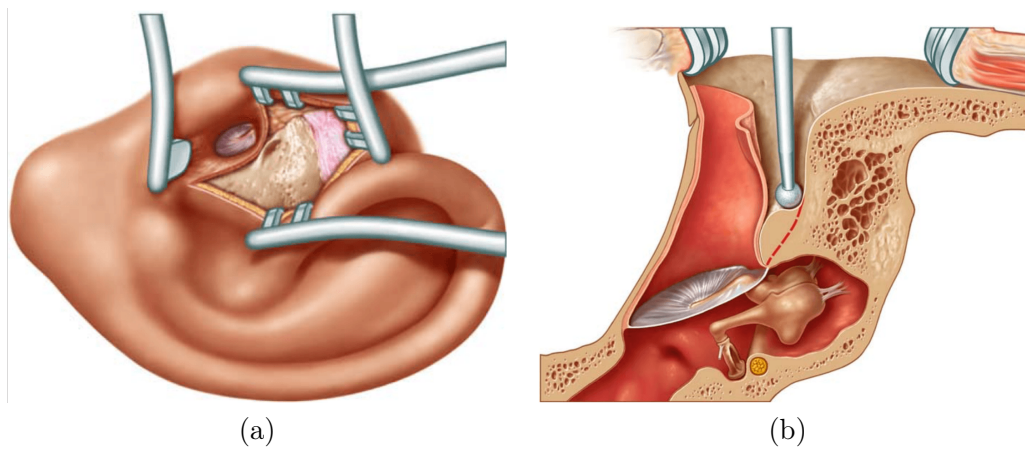


FIGURE 1.17: The endaural approach [Hildmann and Sudhoff, 2006]: (a) top view, and (b) side view.

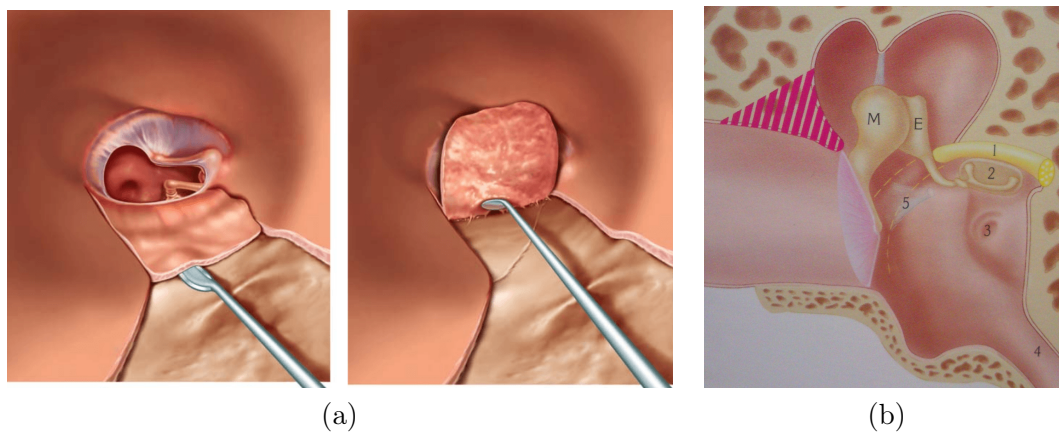


FIGURE 1.18: The transcanal approach: (a) top view through the external ear canal [Hildmann and Sudhoff, 2006], (b) side view (the red hashed region is the bony region to be removed) [Bordure et al., 2005].

Endaural approach: This technique enters the middle ear through the posterior and superior portion of external ear canal (FIGURE 1.17). It is applied by the surgeon when the cholesteatoma cells are concentrated in the attic region of the tympanic cavity.

Transcanal approach: This method is less invasive than the previous one and it is used when the cholesteatoma cells are trapped between the attic and atrium regions of the tympanic cavity. Indeed, it reaches the middle ear cavity by removing the bone at the end of the external ear canal (FIGURE 1.18).

Postauricular approach: This technique is applied by the surgeon when the cholesteatoma cells are propagated from the attic region to the mastoid portion. This approach is also

called *mastoidectomy* and it consists of creating a big hole behind the auricle (FIGURE 1.19(a)). Indeed, this category is divided into two types: *canal wall down* and *canal wall up*.

Canal wall down: This technique is too invasive and it creates a big orifice within the mastoid portion. It also sacrifices the posterior portion of the external ear canal (FIGURE 1.19(b)). In fact, this approach is an old fashion technique and surgeons rarely use it. Its advantages are that: i) it is technically far easier to eradicate disease, and ii) any disease that recurs will be visible and not trapped in a closed cavity. The disadvantages are that: i) it is not always possible to create a trouble-free cavity, and ii) it is very difficult to reconstruct a functioning sound-conducting ossicular system [Alper, 2004].

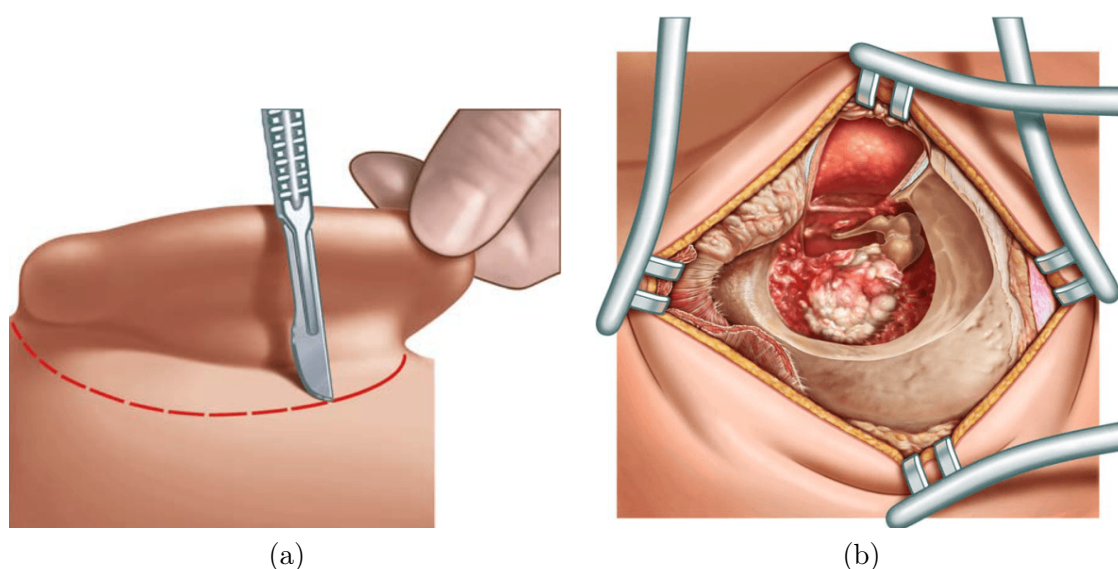


FIGURE 1.19: (a) Initial step to the postauricular approach [Hildmann and Sudhoff, 2006], and (b) the top view of the canal wall down process, where the external ear canal is removed.

Canal wall up: This method is less invasive than the previous one because the surgeon conserves the posterior portion of the external ear canal (FIGURE 1.20). The size of the created orifice is also presented in FIGURE 1.21. This mastoidectomy type is indeed the most used technique and its advantages are the potential for a reconstruction (preserving or restoring hearing) and a better chance of having a trouble-free ear as regards infection. The disadvantages are the greater degree of technical skill required and, because of this, the potential for leaving behind some infected cells is high [Alper, 2004].

1.2.5 Ablation tools

The excision of cholesteatoma cells requires high expertise, since it may appear either as i) a beaded appearance, or ii) a uniform layer above the middle ear mucosa [Bordure

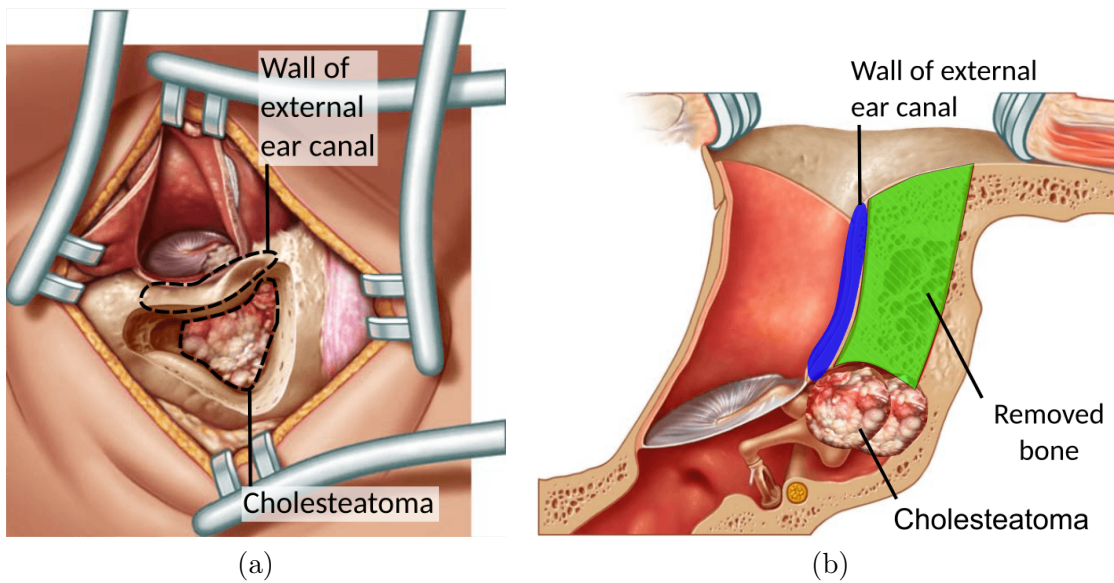


FIGURE 1.20: Canal wall up process [Hildmann and Sudhoff, 2006]: (a) top view, (b) side view (the green region is the removed bony portion while the blue region is preserved).

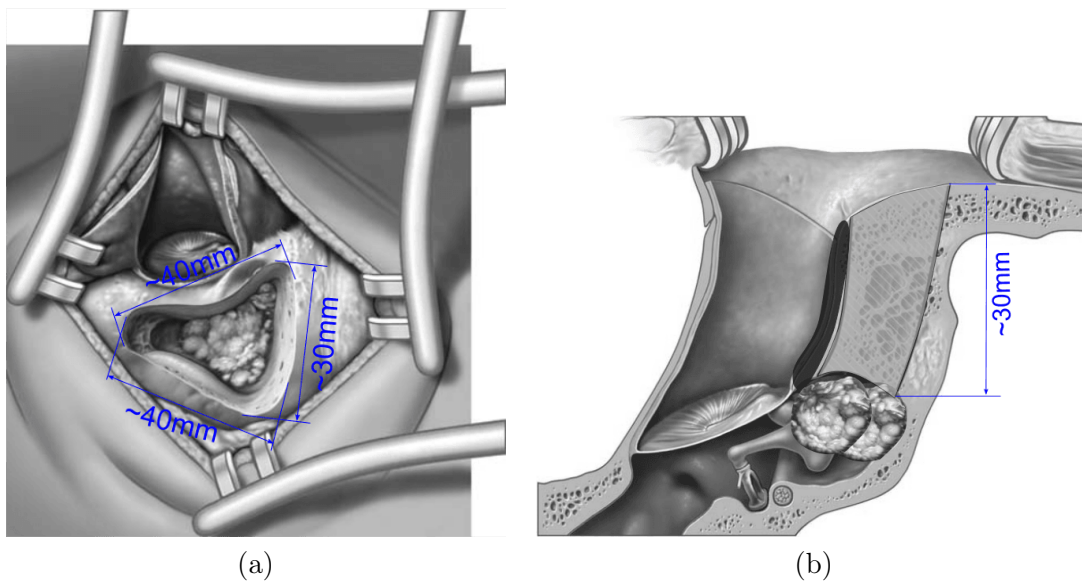


FIGURE 1.21: Dimensions of the orifice created by the canal wall up: (a) top view, (b) side view.

et al., 2009]. Therefore, the surgeon should be equipped with adequate instruments (FIGURE 1.22) and the latest technology of ablation tools. Such a tool could be a laser, an ultrasound or a MEMS (Micro-Electro-Mechanical System). A possible solution is

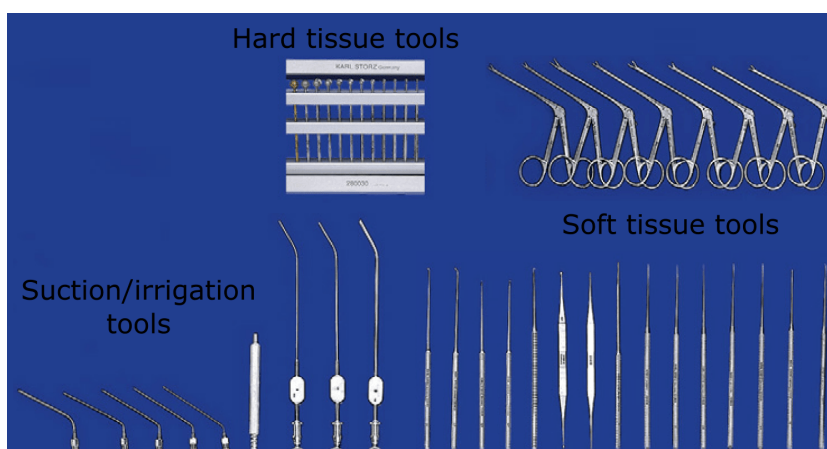


FIGURE 1.22: Standard instruments used for the otological surgery [Badr-El-Dine et al., 2013].

using a micro-tool to scatter and suck out the big debris of epithelium cells, then a laser or an ultrasound tool is used for burning the residual cells.

Laser tool: In otological surgery, the laser is a powerful tool for removing soft and hard tissues. It is already commercially available, for instance, the *BeamPath* CO₂ laser system developed by OmniGuide Surgical²¹ allows to perform laser otosclerosis surgery [Lesinski and Giesken, 2008] and ablation of cholesteatoma.

A study was conducted to assess the use of a solid-state potassium titanyl phosphate (KTP) laser for reducing the rate of residual cholesteatoma [Hamilton, 2005]. The study demonstrated that this rate was significantly reduced, where 1 out of 36 cases had residual cholesteatoma after laser surgery, and 10 out of 33 cases without laser treatment.

A laser treatment was also proposed in [Caffier et al., 2008] in order to destroy the cholesteatoma cells based on the information obtained from a fluorescence imaging. The objective of in-vitro experiments was the characterization of the photodynamic effect on cholesteatoma tissue and the different absorption enhancements. The proposed system showed the ability to destroy up to 92% of cholesteatoma cells.

Ultrasound tool: The High-Intensity Focused Ultrasound (HIFU) is used to target diseased or damaged tissue within the human body, such as eye²², prostate²³, or breast. However, this technique is not yet applied to destroy cholesteatoma.

The ultrasound technology can remove soft tissue but it can also cut out hard tissue. The piezosurgery device (Mectron Medical Technology²⁴) is a new ablation tool which allows removing the bone while keeping the soft tissues intact. Such a device is useful for

²¹omniGuide Surgical [online]. <http://www.omni-guide.com>

²²Imasonic Medical Transducer [online]. <http://www.imasonic.com/Medical/Medical.php>

²³Sonacare Medical [online]. <http://sonacaremedical.com>

²⁴Mectron Medical Technology [online]. <http://medical.mectron.com/>

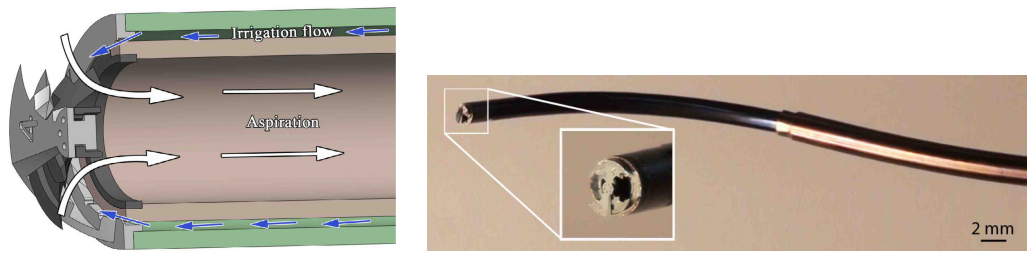


FIGURE 1.23: (a) A conceptual scheme of the MEMS ablation tool [Gosline et al., 2012], and (b) a global view of the MEMS tool mounted on a concentric tube robot.

otologic operation since it performs a mastoidectomy while preserving the facial nerve [Salami et al., 2009].

MEMS tool: A cutting tool can be manufactured using a metal MEMS process. Such systems are not yet applied for otological application but it is used for cardiac application [Gosline et al., 2012]. For instance, the researchers in Harvard Medical School implemented a tissue removal tool by applying MEMS technology [Gosline et al., 2012]. The tool consists of three main parts: an inner aspiration tube, an outer irrigation canal and a MEMS cutting tool. The outer diameter of the irrigation tube is 3 mm. The irrigation canal is formed by the gap between the inner aspiration tube and the outer diameter. The cutting tool is held on the outer and it has a stator/rotor geometry for producing a scissoring action on the tissue (FIGURE 1.23).

1.3 Conclusion

This chapter showed the challenges of middle ear surgery which is the only treatment for cholesteatoma due to the need to make a direct contact for extracting the infected cells.

A road map was established about: i) the location of cholesteatoma cells within the middle ear, and ii) the standard surgical techniques to reach such cells. However, the surgeon cannot remove all the infected cells from the first operation.

The main challenges, that face the surgeon during the operation, are mainly: i) the limited field of view, ii) the rigidity of surgical tool, and iii) the tiny workspace. In fact, the surgeon cannot verify the lateral region hidden by the incision wall due to the use of the standard optical microscope and the rigid surgical instruments. Therefore, a bendable (i.e., flexible and actuated) micro-tool would be beneficial to overcome the previous challenges. Moreover, this bendable tool will hold a fibre-optic which can be used as an OCT (imaging tool) and/or a laser (ablation tool) in order to remove efficiently the residual cholesteatoma cells. Thereby, the next chapters aim to study a novel concept for a robot-assisted cholesteatoma surgery. Such a system will be ergonomic and improve the surgeon's dexterity by automating the tool movements while keeping the surgeon's supervision. The next chapter will study the first step toward the implementation of the required system.

Chapter 2

Requirement Analysis for Cholesteatoma Surgery

Contents

2.1	Ideal Requirements for Robot-Assisted Cholesteatoma Surgery	32
2.1.1	Clinical requirements	32
2.1.2	Engineering requirements	36
2.1.3	Safety and risk analysis	40
2.2	Classification of Surgical Robotic Systems	41
2.2.1	Otologic surgical robotic systems	42
2.2.1.1	Inner ear surgery	42
2.2.1.2	Middle ear surgery	47
2.2.2	Non-otologic bendable surgical robotic systems	51
2.3	Guidelines for The Micro-Robot-Assisted Cholesteatoma Surgery	54
2.3.1	Clinical	54
2.3.2	Engineering	56
2.4	Conclusion	60

The previous chapter demonstrated the challenging problems of cholesteatoma in terms of diagnostic and ablation. Thereby, this chapter starts by describing the ideal requirements for implementing a futuristic surgical robotic system to perform a minimal invasive cholesteatoma surgery. The ideal requirements are presented in Section 2.1 and they do not take into account the available technology constraints. This section discusses also the new surgical protocol which modifies the standard procedure for cholesteatoma intervention. These modifications are the result of applying the proposed assistant robotic system.

After that, a review of the otological robotic systems is presented in Section 2.2. The review shows the current state of research in the field and what is missing. Indeed, these

systems show a good basis of work for developing a futuristic robotic system dedicated to cholesteatoma surgery. Afterwards, the section shows additional systems which are used in other surgery types. These systems apply the latest technology in different fields and it is required to adapt this technology for cholesteatoma surgery. For each system is also presented its advantages, disadvantages, as well the needed improvements for reaching the ideal requirements.

In the end, Section 2.3 shows the possible solutions, in terms of the actual technology, in order to reach an efficient and reliable surgical robotic system for treating cholesteatoma. Thus this section could be a source of inspiration for a newcomer to the field of cholesteatoma surgery, and those concerned in cholesteatoma treatment as engineers, scientists, and surgeons.

2.1 Ideal Requirements for Robot-Assisted Cholesteatoma Surgery

This section presents the futuristic requirements and specifications which are needed to implement an ideal system. A novel surgical workflow is thus proposed here in order to satisfy the clinical demands. In addition, the engineering requirements are also discussed to design the different components of the desired system. Safety and risk analysis are also discussed within this section.

2.1.1 Clinical requirements

Micro-surgery of middle ear demands a well-trained surgeon to overcome the clinical challenges which can be summarized as:

- i) the movements within the tiny space of the middle ear cavity while preserving the critical anatomical structures (e.g., ossicles chain, facial nerve and chorda tympani nerve),
- ii) the limited FOV (Field Of Vision) and the use of rigid surgical instruments for inspecting and manipulating within the middle ear cavity.

Therefore, the ideal system should be ergonomic for the surgeon for reducing his/her strain, and hence reducing the hand tremor and increasing the precision (e.g., [Rothbaum et al., 2002]). The system should also aid the surgeon in performing dexterous micro-movements, and provide a visual feedback and/or an automated control based on the pre- and intra-operative images. TABLE 2.1 shows the important clinical needs.

Clinical Requirements

- **Residual cholesteatoma** should be remove efficiently from the first surgery,
- **Imaging & ablation tools** must be capable to detect/remove the tiny residual cells,

- **Bendable tool**, which is flexible and actuated, combines imaging and ablation tools,
- **Mechatronics device** exchanges easily between the driller and the other tool types,
- **Become less invasive**,
- **New protocol**: the clinical requirements imply a new workflow during the surgery.
 - **Pre-operative phase**:
 - * placement of fiducial markers,
 - * pre-operative imaging with CT and MRI imaging devices,
 - * (semi)automatic segmentation of patient's auditory system,
 - * (semi)automatic localization of cholesteatoma cells,
 - * construction a 3D surface/numerical model,
 - * plan the middle ear access tunnel (its diameter around $2 - 3mm$) for the drilling phase,
 - * plan the removal phase of cholesteatoma cells,
 - * produce a manual incision either in the external ear canal, in the auricle or behind the ear, or a combination of both.
 - **Intra-operative phase**:
 - * automatic/manual registration of pre-operative plan to patient,
 - * bone ablation for creating the access tunnel (its depth $25 - 30mm$),
 - * visualize the critical structure to the surgeon with the imaging tool (its outer diameter around $0.5 - 2mm$) and determine the boundary of cholesteatoma region,
 - * automatic/cooperative cholesteatoma removal from the middle ear cavity and/or the ossicles with the ablation tool (its outer diameter $< 2mm$),
 - * diagnostic in real-time of the middle ear cavity for localizing the residual cholesteatoma cells,
 - * execute the excision of residual cholesteatoma.
- **Risk analysis**: sterilization, bio-compatible of end-effector material, infection risk, safety in surgeon/patient robot interface, risk during surgery and other specification by laws (e.g., CE approval),
- **Reducing intervention time and cost**.

TABLE 2.1: Summary of clinical requirements and the new surgical workflow.

New surgical workflow: The new procedure begins by fixing fiducial markers onto the patient skull during the pre-operative phase (see TABLE 2.1). These markers are useful for the segmentation and the registration processes; since they will appear in the pre-operative images as reference points with respect to the target anatomy structures.

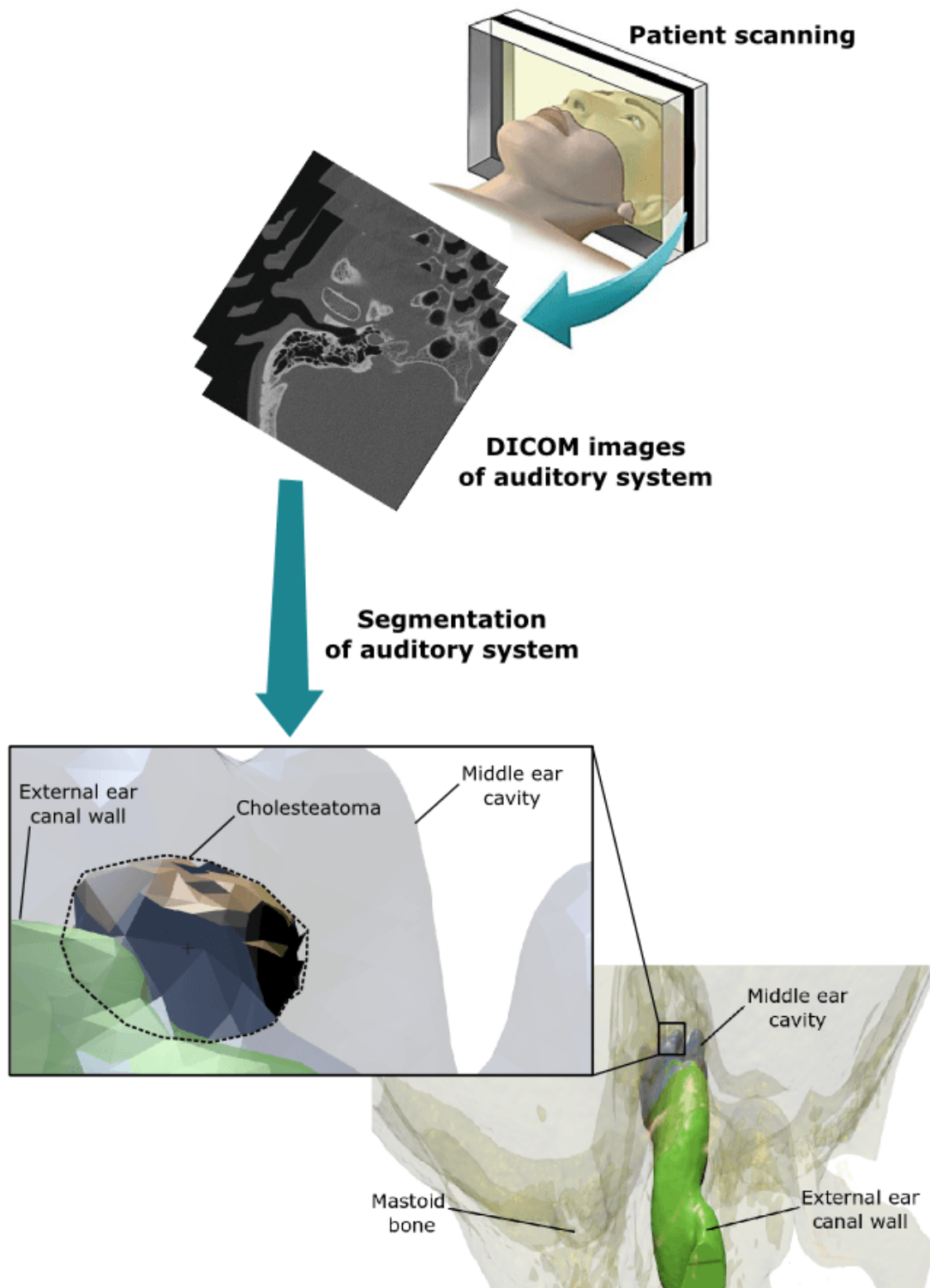


FIGURE 2.1: The concept scheme to use segmentation methods for generating a surface model of the auditory system.

The images with the CT allows identifying the bony structures, while that with the MRI is useful to locate the soft tissue and the cholesteatoma cells.

The *segmentation process* [Pham et al., 2000a] collects the pre-operative slice images of CT and/or MRI in order to form a 3D surface model (FIGURE 2.1). Based on this model, the surgeon plans a safe access tunnel from the mastoid surface to the middle ear cavity. The tunnel location should be optimized in order to drill the minimal distance for reaching the cholesteatoma cells. The tunnel diameter should be less invasive, compared to the standard mastoidectomy procedure, and its diameter should be reduced to be around $2mm$.

The *registration process* [Peters, 2006, Cleary and Peters, 2010] is performed at the beginning of intra-operative phase for calibrating the image-guided robotic system. Such a process often consists of bringing the coordinate reference frames of the patient pre-operative images with the patient actual pose on the operation table. The calibration between the robot and the patient is a very important step and it will affect directly the system accuracy during the intra-operation phase. All previous steps are performed with the help of planning software throughout the pre-operative phase (e.g., [Gerber et al., 2014]).

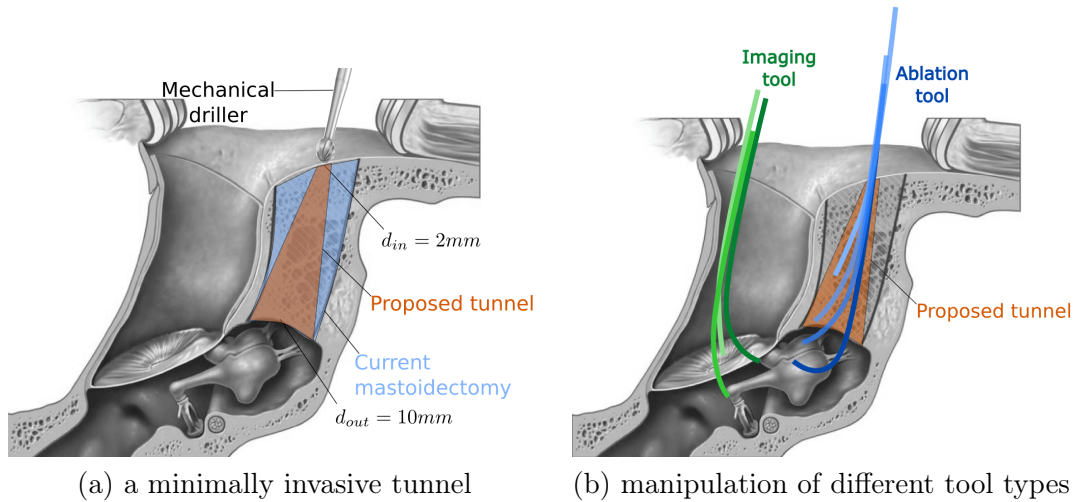


FIGURE 2.2: μ RoCS conceptual scheme.

Through the intra-operation phase, a navigation software is responsible to:

- i) drill the planned tunnel in the temporal bone to reach the middle ear cavity,
- ii) insert the surgical tool within the middle ear cavity for inspecting the suspected region while avoiding the other anatomical structures,
- iii) remove efficiently the cholesteatoma cells.

There are various possibilities to achieve the previous steps. Thus, a new minimally invasive tunnel is proposed in order to reach the tympanic cavity through the mastoid bone as depicted in FIGURE 2.2(a)). Such a conical tunnel has a small diameter of $2mm$ at its base, which is located at the external surface of the mastoid bone behind the

auricle, and then the tunnel expands gradually until it reaches its maximum diameter at its end. This new tunnel has the advantage for the patient to reduce the risk of anatomical lesions and recovery time. Moreover, the surgeon can manipulate his/her tools through this new tunnel, and of course, the way through the external ear canal is available. This concept of bi-manipulation (i.e., manipulating two tools simultaneously, see FIGURE 2.2(b)) is hence possible and it is already applied by the surgeon while using his/her hands during the operation.

During ablation, the first manipulator drills the new tunnel through the mastoid portion. However, the route between the mastoid surface until the tympanic cavity could contain infected cells. Thus, a novel mechatronics device is required for an easy and fast exchange between the different tool types (i.e., ablation and imaging tools). This device is a useful feature to the surgeon for disinfecting the mastoid portion.

The second manipulator could pass from another tunnel or from the external ear canal. It is equipped with an imaging probe to provide real-time 3D images (i.e., 3D optical biopsy) with micro-scale resolution. Such images are ideal to find out with great precision the location of cholesteatoma cells within the tympanic cavity. The OCT tool keeps the infected cells within its field of view and it guides automatically the ablation tool to scatter and suck out the infected cells.

2.1.2 Engineering requirements

Minimally invasive robotic platforms [Vitiello et al., 2013, Burgner-Kahrs et al., 2015] are gaining more usage in the operating room (FIGURE 2.3) since they offer the latest engineering technology in the surgeon's hand. Beside that surgeons are always searching for new techniques to enhance outcomes for patients by making procedures less invasive, safer and more effective. In fact, a surgeon could be considered as a flight pilot [Weber et al., 2017]. In the pilot cabin, the cockpit contains flight instruments which provide the pilot with control instruments and essential information about the plane and its surrounding environment. In a similar way, the surgeon should be equipped with instruments which allow controlling precisely the surgical robot and supply information about the patient and the robot status. Such instruments are important to increase the situation awareness in order that the surgeon/pilot could take the right decision; since an error in such domain could cost the lives of other persons.

¹PRECEYES platform [online]. <http://www.preceyes.nl/>

² μ RALP (Micro-technologies and Systems for Robot-Assisted Laser Phonomicrosurgery). [online]. <http://www.microralp.eu/>

³Robodoc platform is commercialized by Curexo Technology Corp. [online]. http://www.robodoc.com/professionals_howitworks.html

⁴Mako platform is commercialized by MAKO Surgical Corp. [online]. <https://www.stryker.com/content/stryker/us/en/joint-replacement/systems/mako-robotic-arm-assisted-surgery.html>

⁵Da Vinci platform is commercialized by Intuitive Surgical, Inc. [online]. http://www.intuitivesurgical.com/products/davinci_surgical_system/davinci_surgical_system_si/

⁶Magellan platform is commercialized by Hansen Medical [online]. <http://www.hansenmedical.com/us/en>

⁷Neuromate platform is commercialized by Renishaw [online]. <http://www.renishaw.com/en/neuromate-stereotactic-robot--10712>

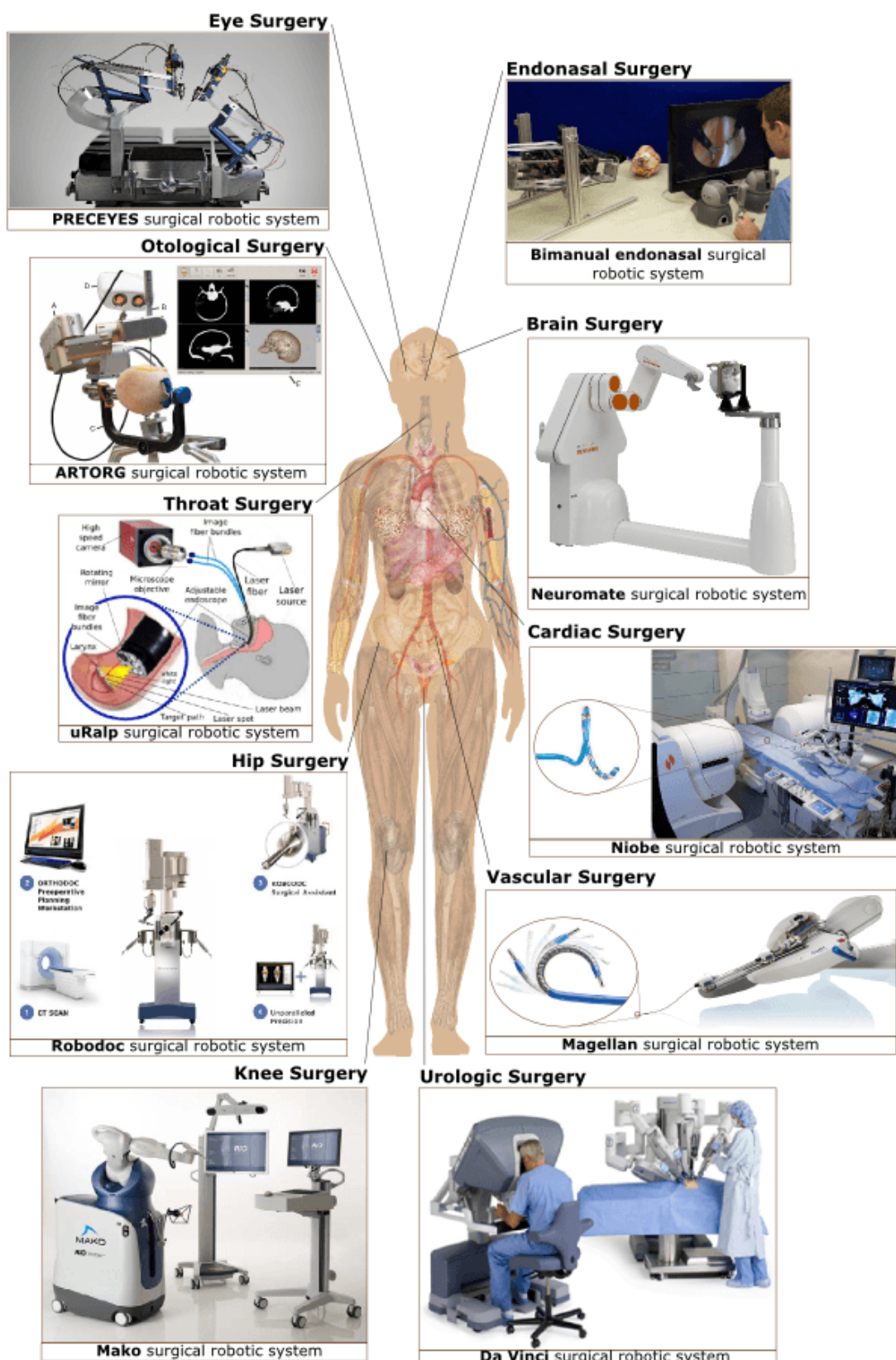


FIGURE 2.3: Examples of robotic platforms for minimally invasive surgery in different medical applications. (images: Bimanual endonasal [Burgner et al., 2011], PRECEYES ¹, ARTORG [Bell et al., 2012], μ Ralp ², Robodoc ³, Mako ⁴, Da Vinci ⁵, Magellan ⁶, Niobe [Carpi and Pappone, 2009], Neuromate ⁷)

A surgical robotic system is generally divided into two main parts: i) the robot structure, and ii) the software assisting the surgeon. There are various reviews that present the historical development of such systems and describe their various components [Davies, 2000, Taylor and Stoianovici, 2003, Pott et al., 2005, Dogangil et al., 2009]. The assistance software is often named *Computer-Assisted Surgery* (CAS) software, and ideally allows to improve the accuracy and the repeatability of a medical robotic system.

Robot structure: A classic robot structure consists mainly of its manipulator and its end-effector. On one side, the robot manipulator is classified on various criteria [Spong et al., 2006], such as the kinematic structure or the actuation source. The kinematic structure of the manipulator depends on how its joints are arranged together, for instance, an open-loop manipulator (serial robot, e.g., SCARA or 6R) [Khalil and Dombre, 2002] or a closed-loop manipulator (parallel robot, e.g., delta or hexapod) [Siciliano and Khatib, 2008]. The actuation of the manipulator's joints is typically done either by an electrical, a hydraulic or a pneumatic actuator.

On the other side, the robot end-effector holds the surgical instrument that satisfies the surgeon needs (e.g., forceps, ablation tool, suction/irrigation tool or imaging tool). The end-effectors are mainly divided into two categories:

- i) *rigid end-effector*: when it enters a minimal invasive incision, its workspace has a cone form because the centre line of the tool body should be coincident with the centre point of the incision hole. Such a pivoted movement is named *fulcrum effect* or *Remote Centre of Motion*⁸ (RCM) [Kuo et al., 2012, Dahroug et al., 2016] which is applied during different surgical intervention types (e.g., eye [Ida et al., 2012] and abdominal [Osa et al., 2010] surgeries).
- ii) *bendable end-effector*: its workspace is more complex than the rigid one. It can also provide more dexterity and flexibility for avoiding obstacles [Loeve et al., 2010, Vitiello et al., 2013]. There are various types of actuator to steer the distal tip of end-effector, for instance cable-driven [Camarillo et al., 2008], concentric tubes [Webster and Jones, 2010, Dupont et al., 2010], magnetic fields [Carpi and Pappone, 2009] or smart materials (e.g., piezoelectric, conducting polymers [Shoa et al., 2008] or shape memory alloy).

The design requirements of the robot kinematic structure are summarized in TABLE 2.2.

Robot Requirements

- **Macro-manipulator:**
 - large workspace (around $1000mm \times 1000mm \times 500mm$),
 - range (around $500mm$).
- **Bendable micro-end-effector characteristics:**

⁸see Chapter 3 for more details about the constrained motion.

- actuation type (concentric tube, tendon-driven, smart material or magnetic field),
- small workspace (around $5mm \times 15mm \times 15mm$),
- range (15mm),
- number of segments (1 and/or 2),
- hollow segments,
- outer diameter ($0.5 - 2mm$ [Djalilian et al., 2010, Fichera et al., 2017]),
- length ($> 30mm$ [Bell et al., 2012, Fichera et al., 2017]),
- bending radius ($< 3mm$),
- bending angle ($\geq 90^\circ$ [Fichera et al., 2017]),
- resolution ($< 0.02mm$ [Miroir et al., 2010]),
- force ($\leq 5N$ [Miroir et al., 2010]),
- payload (few grams).
- **Modelling and control**
 - adaptability to patient variability and safety
 - accuracy (100% of the above characteristic) and response time ($< 0.1s$)
- **Fabrication:** bio-compatibility, environmentally friendly and low cost

TABLE 2.2: Summary of robot data.

CAS Requirements

- **Exteroceptive sensors**
 - optical tracking: accuracy (around $0.05mm$),
 - micro-fibre-optic imaging probe:
 - * resolution ($\leq 10m$),
 - * depth ($\geq 10m$),
 - * FOV (around 90° [Fichera et al., 2017]),
 - * frequency of image acquisition (around $30Hz$ [Fichera et al., 2017]).
- **Pre-operative planning software**
 - segmentation: yes (semi or fully automated),
 - 3D reconstruction of anatomical structures: yes,
 - registration: accuracy ($< 0.15mm$ [Gerber et al., 2014]),
 - access tunnel and ablation path planning: yes.
- **Intra-operative control software**
 - real-time navigation control

- **Surgeon-robot interface:** interface software, simulator, co-manipulation (hand tremor, semi-automated), fully automated, virtual reality and learning

TABLE 2.3: Summary of the CAS data.

Computer-assisted surgery software: The design requirements of the CAS software were summarized in TABLE 2.3. The CAS software is important to improve the accuracy and the repeatability of a medical robotic system. It commonly consists of proprioceptive and exteroceptive sensors, controllers and robot-surgeon interfaces (i.e., a communication interface that help the user to control the robot easily). The interaction between these components contributes to guide and track the robot either in a semi-automated (tele-operative) or in a fully automated mode. A planning software should be used as the first step before the intra-operative phase to achieve three functions:

- segmenting the pre-operative images to create a 3D surface model,
- optimizing the drilling path from the temporal bone surface to the middle ear cavity while avoiding the damage of critical structures,
- registering the robot pose (position and orientation) with respect to the patient's body.

The fully automated mode performs some pre-programmed movements defined by the surgeon. However, the tele-operative mode provides the surgeon with a continuous control in order to imitate the surgeon's movements (the master) by moving the slave robot so that large movements of the master will result in micro-motions, with small forces, applied by the slave. This mode is also named *master-slave* control which allows improving the surgery efficiency by eliminating the hand tremor and providing a scaled motion. The master movements could be acquired by the system via various methods, for instance moving a joystick, drawing the path on a tactile tablet, tracking the surgeon's hand [Mitra and Acharya, 2007] (optical tracking [Rautaray and Agrawal, 2012]), executing the surgeon's voice commands (voice recognition, e.g., [Yokoyama et al., 2003]), or even using the surgeon's brain signals (e.g., [Carmena et al., 2003, Millan et al., 2004, Donoghue et al., 2007]). This kind of system could also be equipped with a more complex feature which is the *haptic sensation* [Barbé et al., 2007, Bolopion and Régnier, 2013]. This feature mimics the sense of touch by supplying a feedback force to the master and hence to the surgeon.

2.1.3 Safety and risk analysis

While designing and working with a medical robotic system, the safety occupies an important aspect [Howe and Matsuoka, 1999, Nathoo et al., 2005, Kettenbach et al., 2008]. TABLE 2.4 shows some primary risks which could be produced by the robot or by the CAS software. However, a comprehensive study is needed to determine the potential hazard which may produce by the robot on the patient and the medical staff (e.g., [Fei

et al., 2001, Korb et al., 2005]). Undesirable situations (e.g., unexpected system failure or sudden movement) should be avoided by applying the adequate hardware and software protections. Such protections should ensure that the tool tip does not hit the critical structures within the patient's body. It is also essential to pull out the robot easily during the unwanted situations. In addition, the robot part(s) that make(s) contact with the patient's body should be sterilized. The material of such part(s) should be bio-compatible too. Finally, the imaging system has a great impact on the safety because the image quality assists to construct the 3D surface model of patient's anatomy, to localize the infected cells and to guide the robot. Consequently, its accuracy influences the treatment outcomes and the robotic system accuracy.

Risk Analysis (*risk level*, and *risk impact*)

- **Robot structure**
 - access to some anatomical locations may be infeasible due to insufficient degrees of freedom of the micro-robotic tool (*low level*, and *medium impact*)
 - the required bending angle or radius of curvature is high to reach the entire workspace (*low level*, and *medium impact*)
 - pull out the robot from the patient body in case of system failure without damaging critical structures (*low level*, and *high impact*)
- **CAS software**
 - critical structures are not visible in the available image data due to factors such as insufficient contrast or spatial resolution (*medium level*, and *medium impact*)
 - unable to plan a safe trajectory due to space between critical anatomy with the required drill diameter (*low level*, and *high impact*)
 - accuracy of the robotic system is insufficient (*low level*, and *high impact*)
 - insufficient image quality for accurate image guidance (*medium level*, and *high impact*)

TABLE 2.4: Summary of risk analysis.

2.2 Classification of Surgical Robotic Systems

The presented classification in this section arranges the medical robotics systems into two main groups, according to the surgical applications. The first group is devoted to the otologic surgery. It presents the current robotic systems that are applied to inner and middle ear surgeries. The second group shows some examples of the technology used in different surgical applications which are helpful in the middle ear surgery. In fact, the surgical tool rigidity is a major issue that troubles the control of the tool during the

operation. Therefore, the second group focuses on flexible robots (or continuum robots) which are developed to increase the tool manoeuvrability. The strengths and weaknesses of each system are shown. Besides that, the needed improvements towards an efficient cholesteatoma surgery are suggested.

2.2.1 Otologic surgical robotic systems

In the literature, there are two reviews which discuss the previous works done for otologic robotic systems [Tabrizi et al., 2017, Dahroug et al., 2018], where [Dahroug et al., 2018] is dedicated to cholesteatoma surgery. The stapedectomy surgery was the first application in the field of otologic robotic systems (e.g., [Brett et al., 1995, Rothbaum et al., 2002]). The objective of this surgery is to replace the stapes bone by an artificial prosthesis to treat conductive hearing loss. This surgery type reaches the middle ear through the external ear canal.

However, a large number of otological robotic systems are dedicated to cochlear implantation for treating a sensorineural hearing loss. The surgery task is mainly composed of two stages:

- i) the first one is to create a tunnel to the inner ear, and
- ii) the second one is to insert an electrode into the cochlea (e.g., [Clark et al., 2012, Pile and Simaan, 2014]).

The first stage could be done either by performing mastoidectomy or cochleostomy procedures. The cochleostomy creates a tunnel which begins at the outer surface of the mastoid, passes through the facial recess and terminates in the middle ear nearby the region of the round window. Such a procedure may be achieved by a robotic system (e.g., [Brett et al., 2007, Klenzner et al., 2009]). The aim of the latter systems is to reduce the size of the tunnel created by the mastoidectomy to a tunnel just larger than the inserted electrode (which its diameter is around $1.5 \sim 2\text{mm}$) for reaching the inner ear.

To the best of our knowledge, there is not a robotic system that is dedicated to cholesteatoma surgery. However, the applied technology in the following systems can be helpful to implement our required system. The following otological robotic systems are divided into two categories:

- i) the first category deals with the inner ear to perform a cochleostomy, and
- ii) the second one deals with the middle ear to execute a mastoidectomy or a stapedectomy.

2.2.1.1 Inner ear surgery

Some researchers from Johns Hopkins University, USA, used the Da Vinci surgical system⁹ for conducting a cochlear implantation surgery [Liu et al., 2014] (FIGURE 2.4). Note that this commercial system was originally dedicated to urologic surgery. However, the researchers adapted it for performing mastoidectomy and guiding the electrode insertion based on images acquired from pre-operative CT images and a stereo-endoscope. A special tool adaptor is fabricated to hold an 8mm drilling tool and to shift its axis by 30° in order to be paralleled with the endoscope axis. In fact, it is beneficial to use

Strengths: The master console provides a planning software and 3D environment reconstruction. This study extends its capacity by adding augmented reality for helping the surgeon. The tele-operated slave robot has a good accuracy for tool positioning.

Weaknesses: This system is very expensive and its size is huge for executing small movements within the middle ear.

Improvements: Reduce size and costs. Add adequate tools for middle ear surgery.



FIGURE 2.4: Da Vinci system in the operation room during cochlear implantation surgery [Liu et al., 2014].

the different components of this commercial system, as its master console, its slave robot with four arms (which equipped with a driller, a 3D stereo-endoscope, and a suction/irrigation tool), a CT scanner, and its planning software. The system was tested on ex-vivo experimentations. The operation was performed in two cases: i) the first one was done on a left temporal bone, and ii) the second one was done with augmented reality on right temporal bone. The test was finished without any violation of critical structures and each side took around 160 minutes. For comparison, the current surgical intervention of cholesteatoma takes around 120 minutes by a senior surgeon, while it may take around 240 minutes by a junior surgeon. However, this system is too expensive and bulky. This is why dedicated robots were developed as shown below.

At Hannover University, Germany, another robotic system for cochlear implantation [Leinung et al., 2007, Majdani et al., 2009, Baron et al., 2010] was developed. An industrial robot (KUKA KR3) with 6-DOF is deployed to drill a tunnel through the facial recess (FIGURE 2.5(a)). The system is also equipped with a flat-panel volume CT and a commercial planning software iPlan 2.6 (BrainLAB AG, Feldkirchen, Germany). The planning software is used to segment the CT images with the help of five fiducial markers which are attached to the patient's skull. The planning software is also used to plan the optimal trajectory to reach the inner ear. During the operation, the system applies an image-guided control software. The navigation system detects the robot pose with the help of three markers which are attached to the robot end-effector. The star marker consists of spheres, which reflect the infrared light, and they are detected via a stereovision system with an error less than $0.35mm$. The proposed system was tested on ten human cadaveric temporal bones. The results showed that nine out of ten procedures were completed without complications. The experimental tests indicated that the targeting mean deviation error was about $0.5mm$, essentially due to the calibration errors. Finally, a mechatronic device was proposed [Hussong et al., 2008] to insert automatically

⁹Intuitive Surgical, Inc. [online]. http://www.intuitivesurgical.com/products/davinci_surgical_system/davinci_surgical_system_si/

Strengths: the system consists of planning software, image-guided control, optical navigation system, milling tool and insertion control of electrode

Weaknesses: Industrial robot is good for testing the control laws but it is not compatible with the clinical applications. The system is only equipped with a hard tissue ablation tool. The targeting error is too large.

Improvements: Reduce the robot size and increase its resolution. Develop a soft tissue ablation tool and a control software for guiding the ablation tool inside the patient body. Also, it is necessary to increase the accuracy of a navigation system, and reduce the targeting error by half its current value.



(a)



(b)

FIGURE 2.5: (a) Robotic system for cochlear implantation [Leinung et al., 2007]; (b) device for automated insertion of the electrode [Hussong et al., 2008].

the electrode array inside the inner ear (FIGURE 2.5(b)). Other systems similar to this one are also proposed (e.g., [Zhang et al., 2006, Zhang et al., 2008]).

The next robotic platform [Bell et al., 2012] will overcome the drawbacks of the previous system [Baron et al., 2010] by: i) implementing a robot structure suitable for clinical applications, and ii) reducing the optical tracking accuracy and the targeting error.

At ATORG centre, Switzerland, a prototype robotic system [Bell et al., 2012, Gerber et al., 2014] for stereotactic cochlear electrode implantation is developed. A mechanical driller executes a $1.8 \sim 2\text{mm}$ tunnel from the surface of the mastoid, passing through the facial recess, to reach the cochlear. The different components of the system are shown in FIGURE 2.6. A custom-built serial robot with 5-DOF is attached to the OR (Operation Room) table due to its light weight (5.5kg). The patient's head is fixed with a non-invasive head clamp which is also attached to the OR table. A high accuracy optical tracking system ($< 0.05\text{mm}$) is deployed to register a pre-operative plan to the patient and to control the tool position. A planning software is also used to perform a semi-automatic segmentation of the mastoid bone, the surrounding critical anatomical structures and the target structures. In addition, it detects the registration of fiducials with sub-pixel accuracy (around 0.1mm). The system estimates the tool position continuously based on the relation between the force applied by the driller and the bone density [Williamson et al.,] during the drilling stage in order to add additional safety

Strengths: The robotic system is suitable for realistic clinical applications, especially for creating a tunnel to the tympanic cavity. It also presents a good optical tracking accuracy and targeting error.

Weaknesses: The system is not prepared for performing the second phase of cholesteatoma surgery. It is missing soft tissue cutting tool, bendable end-effector, imaging tool for detecting cholesteatoma and control software for guiding the robot during the second phase.

Improvements: Bendable ablation tool for removing soft tissue and imaging tool should be added. A mechatronics device for exchanging between tools would be beneficial.

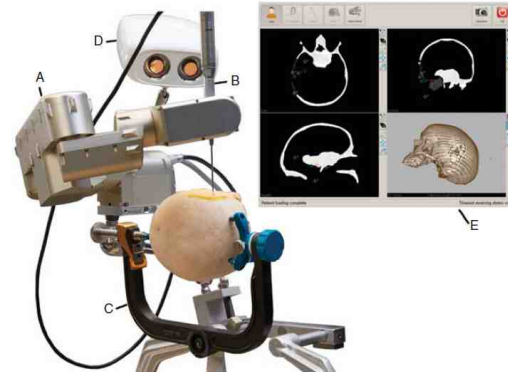
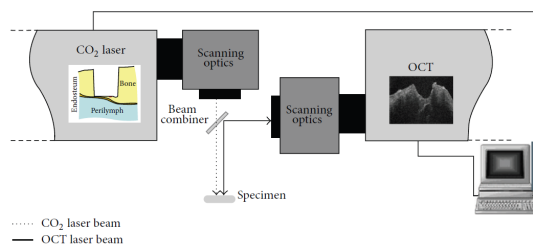


FIGURE 2.6: The different components of ARTORG robotic system: (A) robot arm; (B) surgical driller; (C) head clamp; (D) optical tracking; (E) touch screen as the interface to the planning software [Bell et al., 2012].

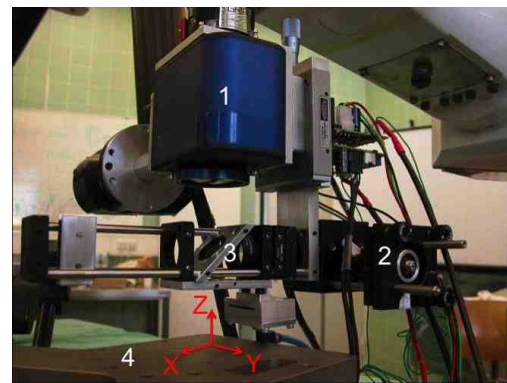
Strengths: Proof of concept to perform a laser bone removal guided by an OCT imaging system. The system accuracy is good. Notable patient tracking system by using OCT.

Weaknesses: The system setup has a big size and it is difficult to use in real clinical applications. For creating the tunnel to the tympanic cavity would take too long by using laser, but it is good for targeting small areas with high accuracy.

Improvements: The laser and OCT tools should be integrated into a bendable end-effector for increasing the system dexterity.



(a)



(b)

FIGURE 2.7: (a) Schematic diagram of conceptual setup between the laser and the OCT [Zhang et al., 2014]; (b) experimental setup; where (1) CO₂ laser, (2) OCT, (3) beam combiner, (4) 6-DOF parallel platform [Zhang and Worn, 2014].

criteria. The monitoring of facial nerve [Ansó et al., 2014] is also employed to ensure its safety during the drilling stage. This robotic system was tested on eight human head and the experiments showed $0.18mm$ mean accuracy [Bell et al., 2013].

Furthermore, at the Karlsruhe Institute of Technology, Germany, a study was conducted [Zhang et al., 2014] [Zhang and Worn, 2014] to perform a laser cochleostomy ablation guided by an OCT. The laser advantage is to provide a clean cut on the bone with no significant thermal injury to the surrounding tissue. The laser allows also a contactless removal of the bone tissue in the absence of any mechanical stress onto the fragile structures, compared to the conventional surgical burrs. It is also considered to be safer for the patient by generating much less bone-debris and reducing the risk of inflammatory tissue. However, the surgical burr drill is quicker to execute a large hole compared to the laser.

In fact, an OCT is located coaxially to the laser tool in order to detect the laser spot position. The system setup is shown in FIGURE 2.7. This special setup is arranged in this configuration in order to overlap the working space of both systems (i.e., OCT and laser) with the help of beam combiner. It is also helpful to control the laser ablation and the OCT scanning simultaneously: the laser pulses is guided according to the thickness of the residual bone layer above the critical structure. A novel tracking system is proposed by locating small laser-ablated landmarks surrounding the cochlea. Such a tracking system is used to track the small displacements of the patient head during the intervention. An ex-vivo experimental evaluation on cadaver cochleas was achieved. The preliminary measurements in OCT scans indicated that the mean absolute accuracy of tunnel shape was around $20\mu m$.

At Vanderbilt University, USA, a robotic system, named *Microtable* (FIGURE 2.8(a)), was proposed for executing cochleostomy. The *Microtable* was designed to be attached to the patient's head and it is customized for each patient based on the planned trajectory. Therefore, this new strategy is good; since the patient tracking error will be eliminated. In addition, the advantage of this modality is achieved due to the rapid prototyping fabrication technique. The fabrication of the template is quick, takes around six minutes, then the template is sterilized. A custom planning software is applied to define the drilling trajectory. It also collects the pre-operative CT images for an automatic segmentation process with an accuracy of approximately 2 voxels [Noble et al., 2008] (for image resolution around $0.3 \times 0.3 \times 0.4mm^3$). The mean error to identify temporal bone anatomy varies $0.5 \sim 0.3mm$ [Noble et al., 2009]. The software is also used to optimize the linear trajectory. Some tests were performed on a phantom model and the results showed a mean drilling accuracy to reach the target of $0.37 \pm 0.18mm$.

The concept of *Microtable* was extended to perform automatic percutaneous cochlear implantation [Kratchman et al., 2011] with a parallel robot (FIGURE 2.8(b)). In-vitro and ex-vivo experiments were conducted and the targeting error is $0.2 \pm 0.07mm$ and $0.38mm$, respectively.

Strengths: The system provides good targeting error. The robot attached to the bone eliminates all the needs to track patient's movements.

Weaknesses: The system segmentation error is quite high. Soft tissue ablation tool, diagnostic imaging tool and bendable end-effector are missing. It would be difficult to exchange between the different tools with the current configuration.

Improvements: Add adequate tools for middle ear surgery, as imaging, biopsy and soft tissue cutting tools. It is also helpful to modify the current design to easily exchange between the different tools.

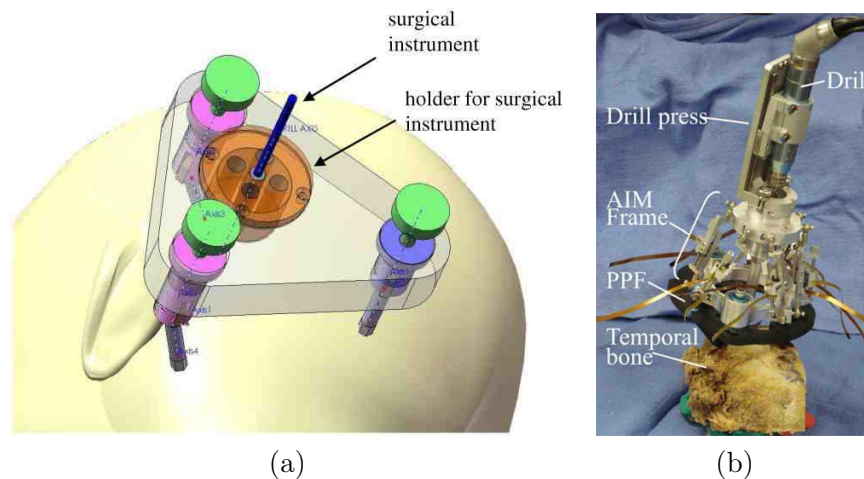


FIGURE 2.8: Microtable: (a) early design concept [Labadie et al., 2009]; (b) bone-attached parallel robot with preposition frame (PPF) and automatic image-guided microstereotactic (AIP) frame [Kratchman et al., 2011].

2.2.1.2 Middle ear surgery

At Vanderbilt University, USA, two robotic systems were proposed to perform mastoidectomy [Danilchenko et al., 2011, Dillon et al., 2014]. Both systems are equipped with a CT scanner and a planning software for segmentation of anatomical structures and registration procedure. On one side, the proposed system in [Danilchenko et al., 2011] is named *OTOBOT*. It consists of an industrial robot (Mitsubishi RV-3S) and a custom-built end-effector to hold the surgical driller. It is also equipped with an optical tracking system to measure the current pose of both the robot and the patient. The optical markers are fixed on the end-effector and on the patient (FIGURE 2.9(a)). The accuracy of the tracking system is around 0.25mm [Baron et al., 2010]. Ex-vivo experiments were conducted to evaluate the system performances on three temporal bones. The results showed 0.6mm maximum error and the percentage of removed volume on each temporal bone were 97.7%, 99.99% and 96.05% of the planned volume, respectively.

On the other side, the proposed system in [Dillon et al., 2014] used a different strategy to execute the mastoidectomy. This strategy is similar to Microtable, where a custom-built 4-DOF serial robot is attached to the temporal bone. This robotic configuration eliminates the need for optical tracking system (FIGURE 2.9(b)). An in-vitro test was

Strengths: The bone-attached robot [Dillon et al., 2014] does not require an optical tracking system.

Weaknesses: Only the bone ablation tool is available in both systems. The components of [Danilchenko et al., 2011] are not adapted to clinical applications and the tracking error is relatively large. The system [Dillon et al., 2014] cannot manipulate tools in the middle ear through the external ear canal.

Improvements: Add soft tissue ablation tool for both systems. Reduce the size of optical marker of system [Danilchenko et al., 2011] and the tracking error.

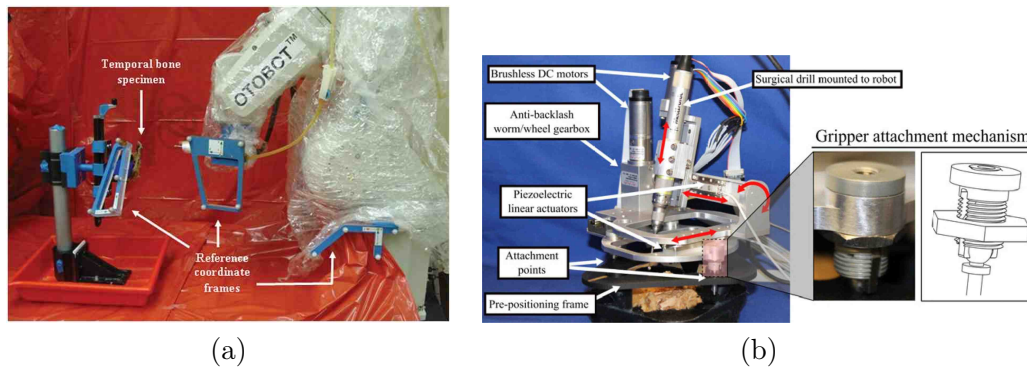


FIGURE 2.9: (a) OTOBOT robotic system for mastoidectomy [Danilchenko et al., 2011]; (b) bone attached robot with the positioning frame [Dillon et al., 2014].

Strengths: Significant kinematic structure for RCM. Cooperative control for eliminating the hand tremor.

Weaknesses: The system does neither have soft tissue cutting tool nor cholesteatoma imaging tool.

Improvements: Add the required tools and a mechatronics device for exchanging between tools. A planning software is necessary to carry out automatically the mastoidectomy. In the end, the collaborative control would be useful during the cholesteatoma removal process.

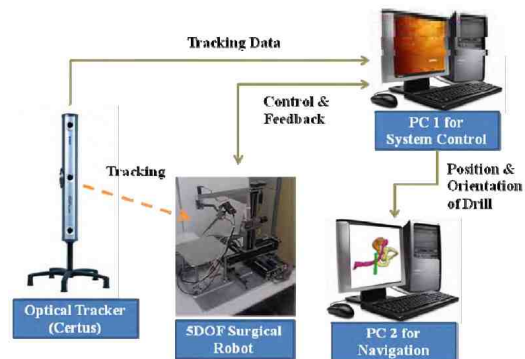


FIGURE 2.10: Configuration of robotic system mastoidectomy [Lim et al., 2011].

done on a phantom model and the drilling test showed 0.5mm mean accuracy.

At Hanyang University, South Korea, another image-guided robotic system was proposed to perform mastoidectomy [Lim et al., 2011]. A special kinematic structure of 5-DOF serial robot (FIGURE 2.10) was introduced in order to impose physical constraints on the surgical tool (i.e., the fulcrum effect). An optical tracker and a navigation soft-

ware are also used. Such a software provides a warning mode when the driller approaches critical structures (e.g., the facial nerve). The safe margin was set to 3mm which is relatively large with respect to the target application. The system allows also a human-robot collaboration control to compensate the hand tremor.

Strengths: Good tools for middle ear surgery, as micro-scissor or laser, driller and endoscope. A specific kinematic structure that allows manipulating tools within the middle ear through the natural orifice of the external ear canal. Tele-operated robot allows eliminating the surgeon's hand tremor.

Weaknesses: The rigid tools are ideal to work in the middle region of tympanic cavity (i.e., atrium/mesotympanic) but they cannot reach the upper or lower regions (i.e., attic/epitympanic recess or hypotympanic) where cholesteatoma often develops.

Improvements: The end-effector has to gain some bending characteristics in order to reach the different regions of tympanic cavity and avoid the critical anatomical structures. Adding the possibility to get into the middle ear through the temporal bone and a planning software is needed. Adequate tool for cholesteatoma ablation is also required and the control software for its navigation and its automated guidance.

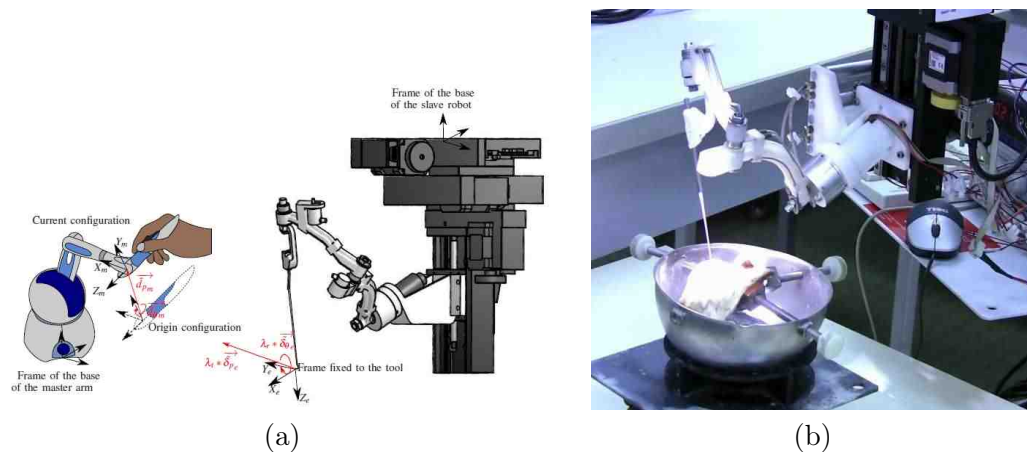


FIGURE 2.11: (a) Master-slave RobOtol surgical system, (b) experimental setup of RobOtol [Miroir et al., 2010].

At ISIR (Institut des Systèmes Intelligents et Robotique), France, a tele-operated robotic system was proposed for carrying out a stapedectomy surgery through the external ear canal [Miroir et al., 2008, Miroir et al., 2010, Nguyen et al., 2012b]. *RobOtol* is the name of this assistant system and it consists of a slave robotic arm and a master joystick (FIGURE 2.11). The system is designed to use three robotic arms simultaneously, whereby each arm has 6-DOF and its dimensions are optimized for middle ear surgery. The special kinematic structure of each arm allows enhancing the field of vision provided to the surgeon for performing more complex gestures. These arms are moved by the surgeon via the joystick, while the surgeon looks to middle ear structures by using either a conventional otomicroscopy or a 4mm endoscope. During the procedure, the surgeon

removes the stape bone and drills a hole of 0.5mm into the incus bone. Afterwards, the surgeon attaches the prosthesis between the incus bone and the round window of the inner ear. Such a procedure requires a force that varies between 0.7N to 3N .

Strengths: MMS could exchange between the standard surgical tools, while MMTS could switch between endoscope, driller or MMS. Coupling between coarse and fine motions is a good feature for achieving a wide workspace with precise displacements.

Weaknesses: MMTS is not precise without MMS which provides rigid tools. Planning, tracking and navigation software are missing.

Improvements: Increase the accuracy of macro-manipulator of MMTS in order to drill the tunnel to middle ear with high precision. A planning software is also required. Add bendable cholesteatoma ablation and imaging tools, and its guidance control software.

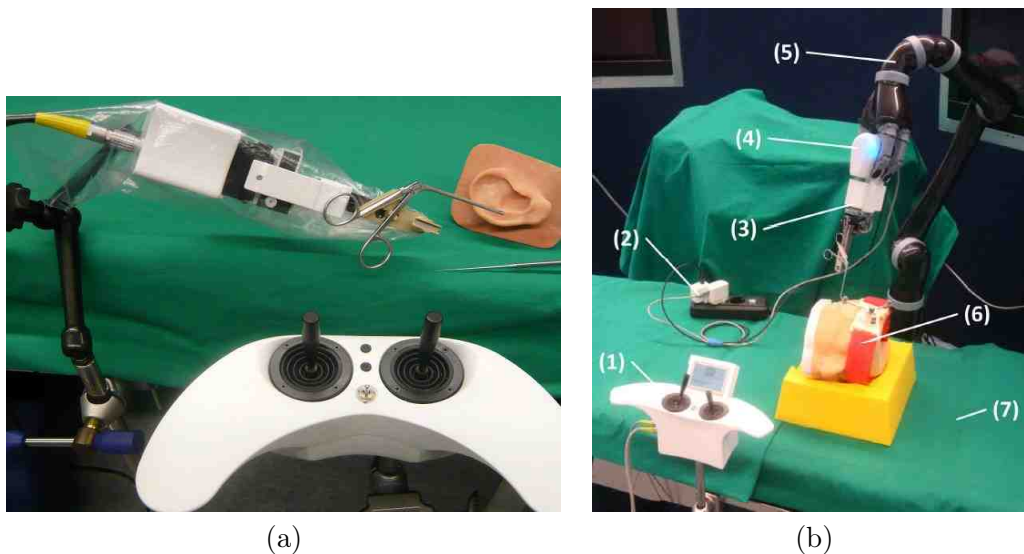


FIGURE 2.12: (a) Master-slave MMS-II surgical system with forceps tool [Maier et al., 2010]; (b) master-slave MMTS surgical system, where (1) joystick console, (2) energy supply, (3) MMS, (4) active gripping adapter, (5) carrier robot, (6) patient phantom, (7) OR-table.

At München University, Germany, another tele-operated system was developed for stapedectomy, named Micromanipulator System (*MMS-II*) [Maier et al., 2010]. *MMS-II* allows the surgeon to manipulate standard surgical instruments within the middle ear. It consists of a small manipulator with 4-DOF and a control console with two joysticks (FIGURE 2.12(a)). It provides also a measuring feature to determine exactly the distance between the stapes and the incus for deciding the required prosthesis length [Maier et al., 2011]. In fact, the surgeon needs to touch both anatomical structures by using the micro-instrument, then the system calculates and visualizes their relative distance. The system standard deviation error to position the tool-tip is around $\pm 0.02\text{mm}$.

Another system was proposed to enhance the workspace and the features of the MMS-II system, and it named Micro-Macro Telemanipulation System (*MMTS*) [Entsfellner et al., 2013] (FIGURE 2.12(b)). This new version consists of: i) a joystick console which is fixed on the operation table, ii) a macro-manipulator arm (i.e., 6-DOF with 1.6mm positioning accuracy) for large displacement, and iii) robotic fingers which hold the gripping adaptor. Such adaptor is designed for gripping different tools (e.g., micro-manipulator MMS-II for fine movement, endoscope or driller). In addition, the system is equipped with four force sensors for measuring the applied force at the instrument tip.

the Robotic Ear Nose and Throat Microsurgery System (*REMS*) [Olds et al., 2014], which is similar to MMS-II and MMTS, was also proposed to manipulate standard rigid tool during an otolaryngologic procedure. All previous systems are good for manipulating the standard surgical tools but their rigidity represents a challenging problem for the surgeon to reach the lateral region within the middle ear cavity through the small entry orifice.

To overcome this problem, a bendable endoscope was in [Fichera et al., 2017], at Vanderbilt University, USA, to visualize the cholesteatoma within the middle ear cavity. The proposed system was originally implemented for the eye surgery [He et al., 2015, York et al., 2015]. However, the novel wrist consists of a nitinol tube with several asymmetric cutouts (FIGURE 2.13). The tube bends with the actuation of a single tendon (i.e., the angle θ in FIGURE 2.13). The tube can also translate along one axis and it rotates about its central axis. The outer diameter can be miniaturized below 2mm . A phantom model of the middle ear cavity was fabricated by a 3D printer. The experimental work showed that the proposed bendable endoscope increased the visibility of sinus tympani region by 74.16%, compared with a straight endoscope which has a visibility of the same region by 6.9%.

The next part shows some additional examples from other surgical applications which apply bendable tools throughout the interventions.

Strengths: A bendable actuated endoscope. The outer diameter of the tube and its curvature are relatively small.

Weaknesses: The ablation tools and the planning software are missing.

Improvements: Integrating a planning software and some ablation tools for the hard and soft tissue. A mechatronics device is needed to facilitate the exchange between the imaging and the ablation tool. Try to reduce the tube curvature by modifying the cutouts shape.

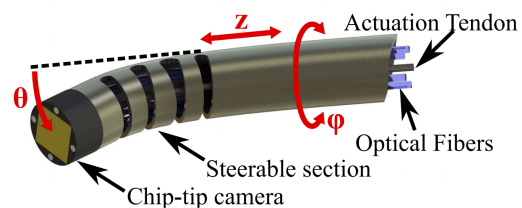


FIGURE 2.13: The concept of the proposed bendable endoscope.

2.2.2 Non-otologic bendable surgical robotic systems

The main purpose of the following robotic systems is to perform minimally invasive surgeries by using a bendable distal tool. The continuum robotics is a vast and an active

research topic [Webster and Jones, 2010, Walker, 2013, Burgner-Kahrs et al., 2015], especially during the last two decades. Therefore, this part presents some examples for the most frequent actuation sources (i.e., concentric tubes and tendon-driven) used in non-otological surgeries. In fact, the technologies used by these systems are useful to develop a suitable system for the middle ear surgery.

Strengths: Concentric tube configuration increases the surgical instrument dexterity. The system supply various tool types, as suction/irrigation tool and endoscope.

Weaknesses: The tube curvature is too large with respect to the ear dimensions. The actuation unit is bulky. The ablation tool for hard and soft tissues are missing.

Improvements: The end-effector diameter and its curvature should be reduced, and the forceps replaced by an adequate ablation tool. The actuation unit must be shrunk. The end-effector should be mounted on a robotic manipulator to increase its workspace.

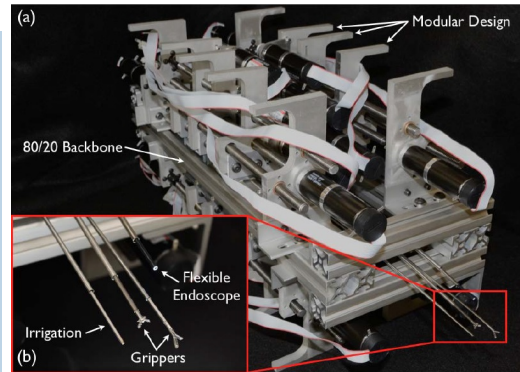


FIGURE 2.14: (a) Global view on the Quadromanual robot, and (b) zoom on the four arms of robot [Swaney et al., 2012].

Endonasal surgery: A bendable end-effector was proposed for endonasal surgery [Burgner et al., 2011, Swaney et al., 2012]. The structure of flexible tool is based on concentric tube configuration. The idea of concentric tube is to arrange elastic tubes in a telescopic manner. The base tube should be a straight one and the others are pre-curved. By sliding and/or rotating the last tubes with respect to the base tube, the tool tip could reach different positions in the space. The proposed system in [Swaney et al., 2012] has four arms. One arm holds a camera, two arms manipulate forceps tools and the last arm is dedicated to the suction/irrigation tool (FIGURE 2.14). Each arm had an outer diameter of $4mm$. The robot is designed to reach a velocity of $4cm/second$ with $0.7N$ maximum force and $0.25Nm$ maximum torque.

Cardiac surgery: This surgery type is widely investigated by research works, as well as by the commercial systems. The available cardiac surgical robots are characterized by a high flexibility and the latest ablation tools technology. The following systems provide a good inspiration for designing the required system.

On the research side, a novel tele-operated robotic tool was proposed to enable a tissue removal from inside the beating heart [Gosline et al., 2012] (FIGURE 2.15). The MEMS (Micro Electro Mechanical System) tool is described early in Section 1.2.5. However,

Strengths: The robot has a bendable end-effector (concentric tube configuration) and a remarkable ablation tool for soft tissue.

Weaknesses: The end-effector is not equipped with a hard tissue removal tool nor with an imaging tool. The tool outer diameter and its curvature are large. A planning software is not mentioned.

Improvements: Miniaturization of the end-effector is needed. Adding a planning and a navigation software are required.

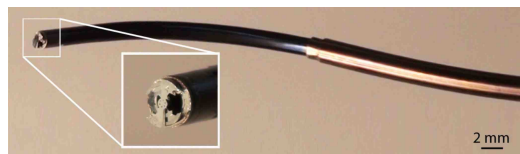


FIGURE 2.15: The ablation tool integrated with the concentric tube robot [Gosline et al., 2012].

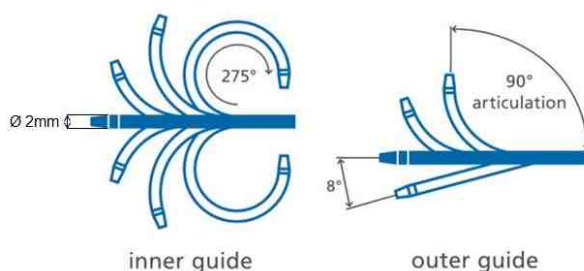
Strengths: The robot structure is compact and flexible in the operation room. The end-effector is actuated by a cable-driven and it has a small outer diameter. The master console also supplies the surgeon with a planning and navigation software.

Weaknesses: The inner catheter is not hollow and it cannot hold some tools, for instance fibre-based imaging system (e.g., OCT or confocal probe), driller, suction/irrigation or laser tools. The bending radius is large which is not compatible with the middle ear cavity dimensions.

Improvements: Modify the end-effector and integrate an adequate tool for cholesteatoma surgery, such as ablation tool and imaging tool. Reduce the bending radius.



(a)



(b)

FIGURE 2.16: (a) Global view on the different components of Sensi robotic system ¹⁰; (b) the Artisan catheter and its bending angle.

this tool is integrated with a steerable concentric tube robot which has a single tube driven by a 2-DOF stage (i.e., one rotation and one translation).

On the commercial side, Hansen Medical ¹⁰, USA, has developed a robotic catheter system named *Sensi* [Riga et al., 2011]. It is incorporated with a flexible and cable-driven catheter called *Artisan* [Camarillo et al., 2008]. The system is also equipped with a master-slave electromechanical mechanism, as well as a planning and navigation software. The workstation console allows the surgeon to guide and visualize the robotic catheter (FIGURE 2.16(a)). The integrated *Artisan* control catheter comprises an inner and an outer guide catheters which create a sharp bending radius of 10mm (FIGURE 2.16(b)).

Indeed, the inner guide is steerable and it is characterized by a diameter of $2mm$ and a 270° bending angle, while the outer guide is passive with a maximum bending angle 90° .

2.3 Guidelines for The Micro-Robot-Assisted Cholesteatoma Surgery

The current state of otologic robotic systems, as well as the ideal requirements and specifications for micro-robotic assisted cholesteatoma surgery are presented in the above sections. Consequently, this section shows the guidelines, based on the current technology, for designing and implementing the required system.

2.3.1 Clinical

The required robotic system must offer an accurate diagnostic and perform a minimally invasive surgery. Consequently, the treatment outcome must be amplified by:

- i) reducing the time, cost and hospitalization stay, and
- ii) eliminating the second-look operation.

The patient's safety occupies the first priority during the design process of the desired medical robotic system. Therefore, a detailed study about the danger that may happen during the operation is mandatory.

Imaging tool: The imaging tools play an important role during the diagnostic and the treatment phases, especially for detecting the residual cholesteatoma cells. It is indeed required to remove completely these cells during the first intervention. The standard otological microscopy is not a good visual tool throughout the intra-operative phase due to its restricted FOV. In fact, it is unable to visualize the lateral cavities of the middle ear. Therefore, the use of endoscope reduces the percentage of residual cholesteatoma [Sajjadi, 2013]. Still, the surgeon cannot visualize all the hidden infected cells by using the previous visual tools due to the lack of controllability.

CT and MRI are non-invasive techniques which are essential during the pre-operative phase for differentiating between tissue types. They are also helpful to reconstruct a 3D surface model of the patient's middle ear. However, CT is not suitable for guiding a tool in real-time during the intra-operative phase due to its radiation hazard [Maurin et al., 2004]. In fact, CT is useful for imaging hard tissues but MRI is a functional tool for detecting soft tissues (i.e., cholesteatoma cells) [Kösling and Bootz, 2001]. Despite that, MRI is not useful during the intra-operative phase because it cannot detect cholesteatoma cell aggregates that are smaller than $3mm$ [McJunkin and Chole, 2014]. FIGURE 2.17 demonstrates that the CT and MRI cannot satisfy the latter criteria while the confocal microscope (fluorescence imaging) has the best resolution compared to the others methods.

¹⁰Sensei and Magellan robotic systems, Hansen Medical [online]. <http://www.hansenmedical.com/us/en>

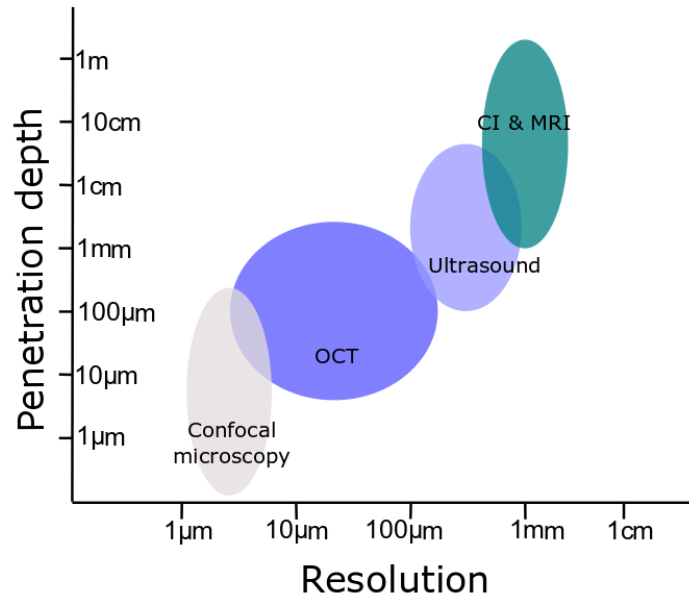


FIGURE 2.17: Comparison between different imaging techniques ¹¹.

The fluorescence technique could also reach a very small diameter (e.g., the commercial confocal endomicroscopy *Cellvizio* ¹²). It provides yet a 2D image in real-time with few micro-meters in depth. The tympanic cavity should also be stained with a contrast agent for distinguishing between cells types [Levy et al., 2013].

A 3D image in real-time with a micro-scale resolution could be obtained by OCT or ultrasound. These two technologies are promising imaging techniques for otological applications. On the one side, the ultrasound needs a coupling medium (e.g., fill out the tympanic cavity with water [Brown et al., 2009]) to improve the wave propagation. Moreover, its technology needs to be pushed up for achieving a small probe diameter (i.e., its diameter around 1mm [Torbatian et al., 2009] or even smaller). On the other side, fibre-based OCT can easily attain small diameter. Both techniques (i.e., OCT and ultrasound) need although an additional micro-system for sweeping and constructing the region of interest.

Ablation tool: A standard driller is needed to create the tunnel through the mastoid bone to reach the middle ear cavity. However, the new excision tool must be flexible enough to solve the rigidity issue of the standard ablation tools. It should reach the different regions within the middle ear without the need to become invasive.

¹¹ CS Betz, V Volgger, SM Silverman, M Rubinstein, M Kraft, C Arens, BJJ Wong. *Clinical optical coherence tomography in head and neck oncology: overview and outlook*. 2013. [online]. <http://www.oapublishinglondon.com/article/419>

¹²More information about Cellvizio is available online. <http://www.maunakeatech.com/en/cellvizio>

The MEMS technology could produce a micro-cutting tool for extracting the majority of cholesteatoma debris (e.g., [Gosline et al., 2012]) while the laser or ultrasound is useful for removing the small residual cells of cholesteatoma. However, it is difficult to achieve a flexible probe based on ultrasound. On the contrary, a laser ablation tool for cholesteatoma already exists commercially¹³.

At the end, an optimal solution could use a fibre-optic cable which integrates imaging and ablation characteristics which has the advantages to reduce the exchange time between the different tools. The laser cable used to remove the tiny residual cells. The same cable can be used to combine an OCT and fluorescence in order to achieve a good resolution with enough depth for detecting the residual cells.

2.3.2 Engineering

Robot structure: The robotic structure is mainly composed of two sub-parts: i) the manipulator, and ii) the end-effector.

Robot's manipulator: It holds the end-effector and it provides a large (macro) displacement. The manipulator could be semi or fully automated. Thus, an important feature is that the surgeon can use the otological microscope while the robot is performing a task (e.g., [Miroir et al., 2010]). The manipulator structure should also have at least 4-DOF to execute a task through the incision hole (i.e., to achieve the RCM constraints). Indeed, if the structure has additional DOF, it leads to redundancy [Maciejewski and Klein, 1985, Siciliano, 1990]. The redundant manipulator occurs when its joints number (joints DOF) is greater than those required to execute a given task. Such a task could be any kinematic or dynamic goal. The advantage of redundancy is to increase the manipulator dexterity which is helpful to avoid singularities, joints limits, workspace obstacles and optimize performance (e.g., by minimizing joint torque or energy).

The manipulator workspace should be optimized (e.g., [Faraz and Payandeh, 1997]) in order to conclude the reachable and the dexterous workspaces. On the one side, the reachable workspace is defined as the set that collects all points attained by the end-effector in a 3D space. On the other side, the dexterous workspace is the set of points that could be reached by the end-effector with various orientations.

Robot's end-effector: It grips the surgical tool (i.e., the ablation and imaging tools) and it provides a fine (micro) displacement. Therefore, it must be hollow to allow passing through the different instruments (e.g., suction, irrigation, laser or OCT). Moreover, the end-effector must be flexible enough (i.e., at least two rotations and one translation, for instance [Fichera et al., 2017]) to navigate within the middle ear cavity as shown in FIGURE 2.18. Indeed, a 3-DOF flexible robot can reach the different points within a convex cavity. A convex region is defined as a space where every point within this space set can be connected to the other points with a straight line and this line is included in the space set, while a non-convex region is the space that does not satisfy the latter condition and a portion of the straight line does not include within the space set. For instance, the point **a** in FIGURE 2.18 can reach any other point within the light

¹³More information about omniGuide Surgical is available online. <http://www.omni-guide.com>

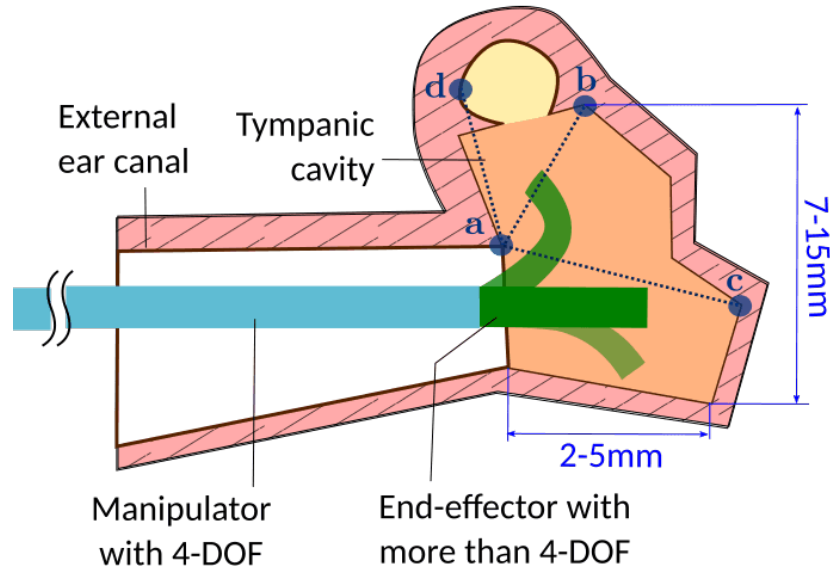


FIGURE 2.18: Conceptual schema to demonstrate the required DOF for the manipulator and the end-effector.

orange region which is convex. If the latter region is unified with the light yellow region in FIGURE 2.18, the resultant region becomes non-convex, where the point **a** cannot be connected with the point **d** with a straight. Thereby, additional DOFs are required for the flexible robot in order to overcome the difficulties within a non-convex region.

The actuation sources for the distal tool tip are many. They could be classified as either intrinsic or extrinsic types [Burgner-Kahrs et al., 2015]. Intrinsic actuators are embedded within the end-effector structure, for instance pneumatic [Chen et al., 2008], hydraulic [Ikuta et al., 2006, De Volder and Reynaerts, 2010], smart material or magnetic fields [Carpi and Pappone, 2009, Clark et al., 2012]. On the contrary, extrinsic actuators are outside the structure and the actuator force should be transmitted through mechanical components, such as cable-driven [Camarillo et al., 2008] or concentric tube [Webster and Jones, 2010]. TABLE 2.5 summarized the different actuation sources applied for a flexible robot. However, this table should be completed in the future work in order to be more specific.

The available technology of pneumatic or hydraulic actuators is characterized by a large diameter compared to the required dimensions for the middle ear. In fact, more research efforts are needed to reach smaller dimensions.

The family of smart materials is wide and it contains of various subtypes (e.g., piezoelectric [Gu et al., 2016], Shape Memory Alloy (SMA) [Kruevitch et al., 1996, Jani et al., 2014], and Electro-Active Polymers (EAP) [Shoa et al., 2008, Chikhaoui, 2016]). Piezoelectric actuators operate with a very high voltage in order to achieve very small deformations. It has also fast response time but it is crucial during the control to eliminate both vibration and hysteresis effects. SMA actuators can support heavy payload

	Actuation type	Generated Force	Radius of Curvature	Deformation	Response time	Operating Voltage	Specific Parameters	Advantage	Disadvantage
Fluid	Pneumatic	big	big	-	-	-	chambers of pressure, valves & pressure regulator	big generated forces	too many components for regulating the pressure
	Hydraulic	very big	big	-	-	-	chambers of pressure, valves & pressure regulator	big generated forces	too many components for regulating the pressure
Smart materials	Piezoelectric	-	very big	very small	fast	very big (~100v)	-	-	vibrations & hysteresis effects
	SMA	big	medium	medium (~8%)	~ 0.01second	small (~2v)	material selection & fabrication procedure	big generated forces	generated heat & hysteresis effect
	EAP	small	small	big	-	-	material selection & fabrication procedure	small generated forces	small curvature radius
	Cable-Driven	medium	medium	medium	-	-	tube stiffness & number of sections	reach small outer diameter	the cable characterization parameters change with the usage & prevent the tendon slack
	Concentric tube	medium	big	medium	-	-	tube stiffness & number of sections	reach small outer diameter	friction between tubes results snapping
	Magnetic	big	small	big	fast	-	the generated magnetic field	contactless actuation	risky when exposed to a high magnetic field (> 4T)

TABLE 2.5: A comparison between the actuation sources of bendable tool. The abbreviation stand for: SMA (Shape Memory Alloy), EAP (Electric Active Ploymers),

and can be miniaturized. However, their main drawbacks are: i) the generated heat during the operation, and ii) the fabrication of required end-effector is not an easy task. EAP actuators consume less operation voltage compared to SMA actuators and their deformation is also larger.

Concentric tube robots have two main problems: i) a high bending radius, and ii) the snapping effect [Kim et al., 2014, Gilbert et al., 2016] which is not desirable within the tiny space of middle ear. The snapping problem occurs when the tube actuator accumulates a torsion energy due to the friction between the actuated tubes, then this accumulated energy is suddenly released which causes the robot to snap to a remote position.

Cable-driven actuator could achieve high bending angles (e.g., [Camarillo et al., 2008, He et al., 2015, York et al., 2015]), despite the fact that the cables occupy space within the hollow shaft. As a result, they reduce the space for inserting a tool through the hollow shaft. It is also necessary to prevent tendon slack during the control.

Magnetic actuation had the advantage to manipulate the end-effector without contact (e.g., [Carpi and Pappone, 2009, Clark et al., 2012]). Consequently, the end-effector distal tip should be made of a ferromagnetic material or consist of a permanent magnet. A separate study should also be conducted for the electro-magnetic design, modelling and control; since it is risky that the patient exposed to a high magnetic field (> 4T) [Schenck, 1992].

There is a trade-off between the actuator choice for the end-effector and the design requirements. A possible solution is to combine two actuation types, for instance cable-driven to achieve some flexibility in the middle ear cavity, while magnetic fields to attain more flexibility within the tympanic cavity with small shaft diameter.

Finally, the structure of the flexible robot should be optimized (e.g., [Xu and Zheng, 2012, Burgner et al., 2013]). Such a study will allow determining the optimal number of DOF and the catheter optimal length.

Computer-assisted surgery: The CAS software consists of proprioceptive and exteroceptive sensors, controllers and communication interface. The proprioceptive sensors (e.g., joint and/or force sensors) collect data about the internal state of the robot. The

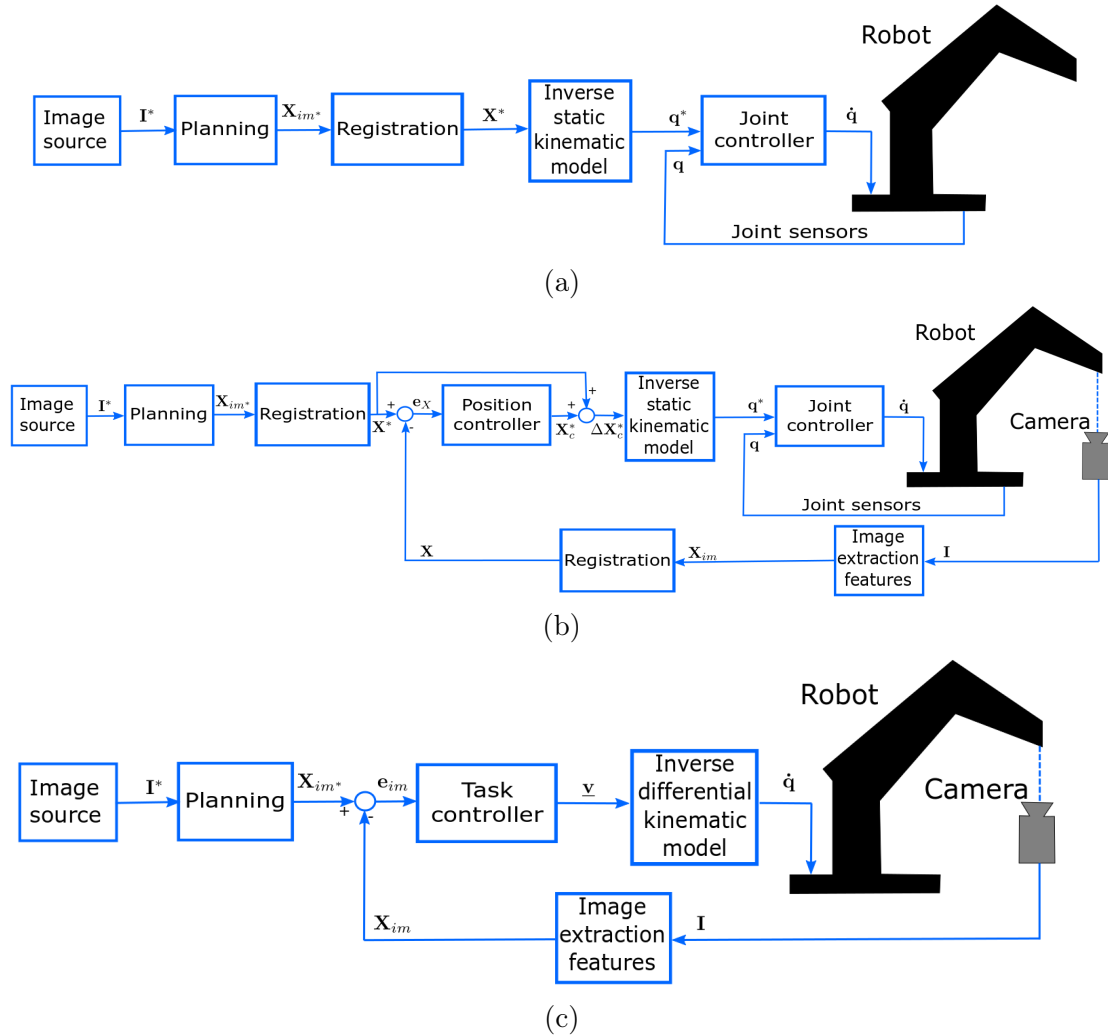


FIGURE 2.19: Different control architectures: (a) CAS, (b) image-guided, (c) visual servoing.

absolute pose (position and orientation) of the tool tip could be estimated from this data. FIGURE 2.19(a) shows the control approach which uses the proprioceptive sensors. Such a controller is implemented in the joint-space which represents the low-level robot control for solving the inverse kinematic issue. However, this approach cannot take into account the environment uncertainty, whereas the robot works blindly because it depends only on its proprioceptive sensors.

Another approach is the image-guided control [Peters, 2006, Cleary and Peters, 2010] which uses an imaging source for comparing the reference images with the acquired ones, as the surgeon perception sense (FIGURE 2.19(b) and (c)). The imaging source (e.g., CT [Maurin et al., 2004], MRI [Greigarn and Çavuşoğlu, 2014], OCT [Zhang et al., 2014],

Requirements	Specifications
Accuracy	a dozen micrometers
Dexterity	4-DOF outside the ear and at least 3-DOF inside the ear
Actuation	cable-driven, magnetic field or concentric tube
Imaging source	OCT, fluorescence or ultrasounds
Innovative tool	alternating between ablation and imaging

TABLE 2.6: Summary of essential requirements.

ultrasound [Vitrani et al., 2005] and/or camera(s)) acts as an exteroceptive sensor which provides informations about the external environment. The exteroceptive sensing allows knowing the relative pose of the tool tip with respect to the organ, which is more useful than to know the absolute pose. However, the control approach of FIGURE 2.19(b) consumes time due to the registration process which is essential to correlate the pre-operative images with the patient on the operation table. This process is used when the exteroceptive sensor is not compatible for real-time control applications (e.g., MRI or CT). This control strategy is often named "*look-then-move*" and it is usually used for a stereotactic surgery. Besides that, the image-guided approach can combine different imaging modality in order to visualize various data for the surgeon with the help of virtual reality and 3D rendering. These advanced techniques require a huge computational capacity and time.

The usage of a visual servoing control approach [Hutchinson et al., 1996, Chaumette and Hutchinson, 2006] eliminates the need for the registration process because it uses directly the images information in the feedback loop (FIGURE 2.19(c)). Indeed, the exteroceptive sensor is compatible for real-time applications (e.g., camera, endoscope, OCT, etc.), where the control strategy is often called "*look-and-move*". Further, this approach is only prone to the velocity errors in the control forward path which are compensated by the image-based feedback loop. Therefore, the registration errors are eliminated and the cycle time is noteworthy reduced. Consequently, a visual servoing control scheme is a good candidate to guide the robot's movements.

2.4 Conclusion

To the best of our knowledge, there is not a robotic system that is capable to perform cholesteatoma surgery. The implementation of an efficient and reliable assisted micro-robotic system dedicated to cholesteatoma surgery is not an easy task. It indeed requires expertise in various domains; since it is an interdisciplinary research topic.

On the clinical side, the chapter begun by providing a detailed information about the cholesteatoma disease, its diagnostics, as well as its treatment which is a surgical procedure. As a result, an investigation on the diagnostics imaging technique which is applicable during the intra-operative phase is needed. This imaging tool is necessary to detect the residual cholesteatoma cells. A separate study is also required to study in details the safety of the new clinical protocol on the patient and the surgical staff. It

is also needed a separate study in order to determine exactly the values of the required accuracy, velocity and forces.

On the engineering side, the miniaturization issue is a big scientific and technical challenge, especially for a tiny workspace as the middle ear cavity. Consequently, the chapter presented the different robotic systems dedicated to the inner ear and the middle ear. It also showed some medical robotic systems from other surgical applications, the technology of which could be used, with some adaptations, for the middle ear surgery. These systems are summarized in TABLE 2.7. In short, the new robotic system should be ergonomic and overcome the rigidity problem by designing a flexible micro-tool (TABLE 2.6). This flexible robot provides various functions in order to alternate between: i) the ablation task (i.e., hard tissue during the tunnel drilling and soft tissues during the cholesteatoma excision), and ii) the imaging task (i.e., scan the surrounding environment, search for cholesteatoma cells and guide the excision process). A good control strategy of the tool tip with a high accuracy and dexterity is also needed for increasing the visibility within the middle ear cavity. This high-level control is the link between the robot structure and the user.

Thereby, the remaining of the manuscript is dedicated to the control issues. Nowadays, there are various manipulators that are available commercially with their low-level controller. Such a controller allows transforming the control position or velocity from the Cartesian-space into the control commands for the manipulator's joints (i.e., the classical robotic problem of inverse kinematics, from the task-space to the joint-space). However, a high-level controller for performing some complex surgical tasks is not well defined by means that the realization of trajectories under the anatomical constraints. Therefore, the next chapter begins by describing geometrically these constraints.

TABLE 2.7: Summary of surgical robotic systems. The abbreviations stand for: Kinematic structure (**S**erial/**P**arallel/**S**pecial **S**tructure), Actuation source (**P**assive/**A**ctive), Rigid tool (**S**traight/**C**urved), Bendable tool (**C**ontinuous/**D**iscrete), Actuation type (**M**agnetic/**C**able-**D**riven/**C**oncentric **T**ube), Tool type (**D**riller/**F**orces/**E**lectrode/**L**aser), Proprioceptive sensor (**J**oint Sensors/**F**orce Sensor), Extroceptive sensor (**S**tereo-**C**amera/**E**ndoscope/**S**tandard **O**tomicroscope), Degree of Autonomy (**C**o-**O**perative/**S**emi **A**utomated/**F**ully **A**utomated).

No.	Previous works	Applications	Status	Robot structure										CAS software			Tool type	Proprioceptive sensor	Extroceptive sensor	Degree of Autonomy		
				Robot's manipulator					Robot's end-effector					Segmentation	Planning	Navigation						
				Kinematic structure	Degree of freedom	Actuation source	Rigid tool	Bendable tool	Number of Sections	Degree of freedom	Actuation type	Tool exchanger										
1	[Brett et al., 1995]	Stapedectomy	Prototype	-	-	-	-	S	-	-	-	-	-	-	-	-	-	√	D	FS	-	CO
2	[Rothbaum et al., 2002]	Stapedectomy	Prototype	-	-	-	-	S	-	-	-	-	-	-	-	-	-	√	D	FS	-	CO
3	[Brett et al., 2007]	Cochleostomy	Prototype	S	-	P	-	S	-	-	-	-	-	-	-	-	-	√	D	FS	-	FA
4	[Klenzer et al., 2009]	Cochleostomy	Prototype	S/P	6	A	-	S	-	-	-	-	-	-	-	-	√	-	√	D	-	SA
5	(Hannover Univ., Germany) [Baron et al., 2010]	Cochleostomy	Prototype	S	6	A	-	-	-	-	-	-	-	-	√	√	√	D/E	-	CT/SC	SA	
6	Microtable (Vanderbilt Univ., USA) [Kratzman et al., 2011]	Cochleostomy	Prototype	P	6	A	-	-	-	-	-	-	-	√	√	√	D/E	-	CT	SA		
7	Otobot (Vanderbilt Univ., USA) [Danilchenko et al., 2011]	Mastoidectomy	Prototype	S	6	A	S	-	-	-	-	-	-	√	√	√	D	-	CT/SC	SA		
8	(Hanyang Univ., South Korea) [Lim et al., 2011]	Mastoidectomy	Prototype	SS	5	A	S	-	-	-	-	-	-	√	√	√	D	-	CT/SC	CO		
9	MMS (TUM, Germany) [Maier et al., 2011]	Stapedectomy	Prototype	S	4	P	S	-	-	-	-	-	-	-	-	-	D/F/E	FS	-	CO		
10	RobOtol (IRIS, France) [Nguyen et al., 2012b]	Stapedectomy	Experimental	SS	6	A	S	-	-	-	-	-	-	-	-	-	D/F	-	SO	CO		
11	[Clark et al., 2012]	Cochleostomy	Prototype	-	-	-	-	C	1	2	M	-	-	-	-	√	E	FS	-	SA		
12	MMTS (TUM, Germany) [Entsfehlner et al., 2013]	Stapedectomy	Prototype	S	6	A	S	-	-	-	-	-	-	-	-	-	D/F	-	-	CO		
13	[Pile and Simaan, 2014]	Cochleostomy	Prototype	P	6	A	-	-	-	-	-	-	-	-	-	√	E	FS	-	SA		
14	(Vanderbilt Univ., USA) [Dillon et al., 2014]	Mastoidectomy	Prototype	P	6	A	S	-	-	-	-	-	-	√	√	√	D	-	CT	SA		
15	(KIT, Germany) [Zhang and Worn, 2014]	Cochleostomy	Prototype	-	-	P	-	-	-	-	-	-	-	-	-	√	L	-	OCT	SA		
16	Da Vinci (JHU, USA) [Liu et al., 2014]	Mastoidectomy electrode insertion	Experimental	S	-	A	-	-	-	-	-	-	-	√	√	√	D/E	JS/FS	CT/E	CO		
17	(Vanderbilt Univ., USA) [Fichera et al., 2017]	Cholesteatoma	Prototype	-	-	-	-	C	1	3	CD	-	-	-	√	-	-	-	E	FA		
18	(ARTORG, Swiss) [Weber et al., 2017]	Cochleostomy	Experimental	S	5	A	S	-	-	-	-	-	-	√	√	√	D	JS/FS	CT/SC	SA		
19	Quadromanual (Vanderbilt Univ., USA) [Swaney et al., 2012]	Endonasal	Prototype	-	-	-	-	C	3	6	CT	-	-	-	-	-	F	-	E	CO		
20	(Harvard Medical School, USA) [Swaney et al., 2012]	Cardiac	Prototype	-	-	-	-	C	3	6	CT	-	-	-	-	-	MEMS	-	-	SA		
21	Sensei (Hansen Medical, USA) ¹⁰	Vascular and cardiac	Commercial	S	-	-	-	C	1	6	CD	-	√	√	√	F	JS/FS	CT/E	CO			

Chapter 3

Constrained Motion Through Anatomical Structures

Contents

3.1	Bilateral Constrained Motion	66
3.1.1	Previous works in literature	67
3.1.2	Proposed method	70
3.1.2.1	Straight tool movement	71
3.1.2.2	Curved tool movement	89
3.2	Unilateral Constrained Motion	99
3.2.1	Previous approaches	100
3.2.2	Proposed method	101
3.2.2.1	Rigid tool movement	102
3.3	Numerical Simulator	104
3.3.1	Validation of RCM constraints	106
3.4	Conclusion	117

Minimal invasive surgical robotic systems enter the human body either from a natural orifice or a created orifice. In both cases, the robot must avoid any damage to the incision walls and the anatomical structures within the patient body.

The majority of medical applications (e.g., laparoscopic [Osa et al., 2010, Dalvand and Shirinzadeh, 2012] and eye [Fleming et al., 2008, Ida et al., 2012] surgeries) consider that the incision hole size has almost the same diameter as that of surgical tool. Consequently, the tool linear motion is restricted along the two axes that span the plane surface formed at the incision point (FIGURE 3.1(a)). The instrument can rotate around the incision point (or *trocar point*) and can translate only along the penetration axis that is perpendicular on the plane surface (i.e. the y-axis as depicted in FIGURE 3.1(a)). This constrained motion is referred as RCM (*Remote Centre of Motion*), *bilateral constraints*

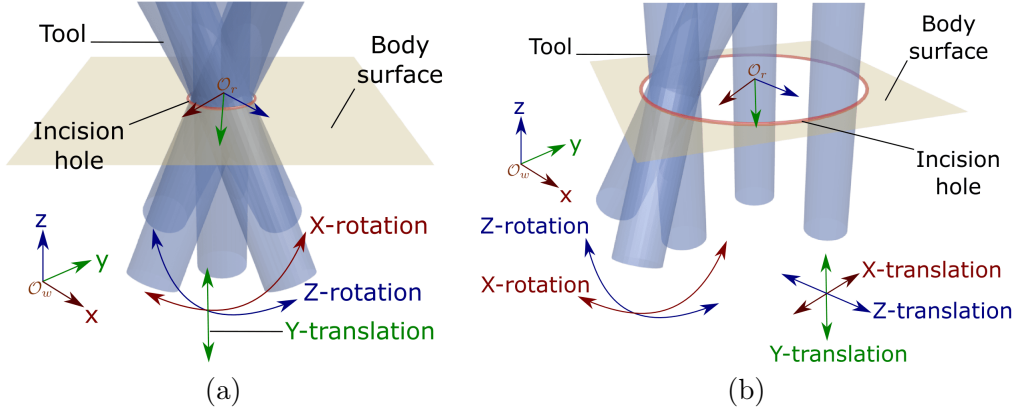


FIGURE 3.1: A 3D conceptual scheme for the comparison between the movements of (a) Remote Centre of Motion (RCM), and (b) Unilaterally Constrained Motion (UCM).

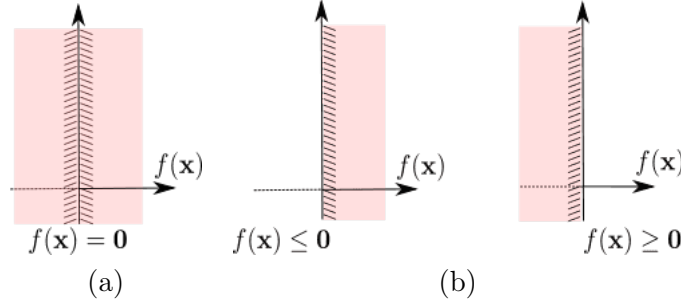


FIGURE 3.2: A mathematical comparison between (a) the bilateral constraint, and (b) the unilateral constraint.

or *fulcrum effect*. Nevertheless, the bilateral assumption is not valid during others surgeries types (e.g., nose [Swaney et al., 2012] and ear [Miroir et al., 2010, Entsfellner et al., 2013] surgeries) where the orifice size is bigger than the tool size and it forms a cylinder around the instrument. In this case, the tool can translate into the hole before it hits the orifice wall (FIGURE 3.1(b)). We will refer to this restricted motion as UCM (*Unilaterally Central Motion*).

From a mathematical point of view, the unilateral constraint is considered as a system of linear/non-linear inequalities, where the system function should be positive or negative (i.e., $f(\mathbf{x}) \leq 0$ or $f(\mathbf{x}) \geq 0$, see FIGURE 3.2(b)). On the opposite, the bilateral constraint is considered as a system of linear/non-linear equalities, where the system function must be equal to zero (i.e., $f(\mathbf{x}) \leq 0$ and $f(\mathbf{x}) \geq 0 \Leftrightarrow f(\mathbf{x}) = 0$, see FIGURE 3.2(a)).

By applying the previous concept on the RCM/UCM movements, the system transfer function is defined as the linear distance ($\mathbf{f}(\mathbf{x}) = \mathbf{d}({}^w\mathbf{M}_e)$) which depends on the tool pose (${}^w\mathbf{M}_e$). As shown in FIGURE 3.3(a), the distance (\mathbf{d}_{max}) represents the length between the incision wall and its centre point. The RCM constraints should satisfy both conditions: $\mathbf{d} \leq \mathbf{d}_{max}$ and $\mathbf{d} \geq \mathbf{d}_{max} \Leftrightarrow \mathbf{d} = \mathbf{d}_{max}$. On the contrary, FIGURE 3.3(b)

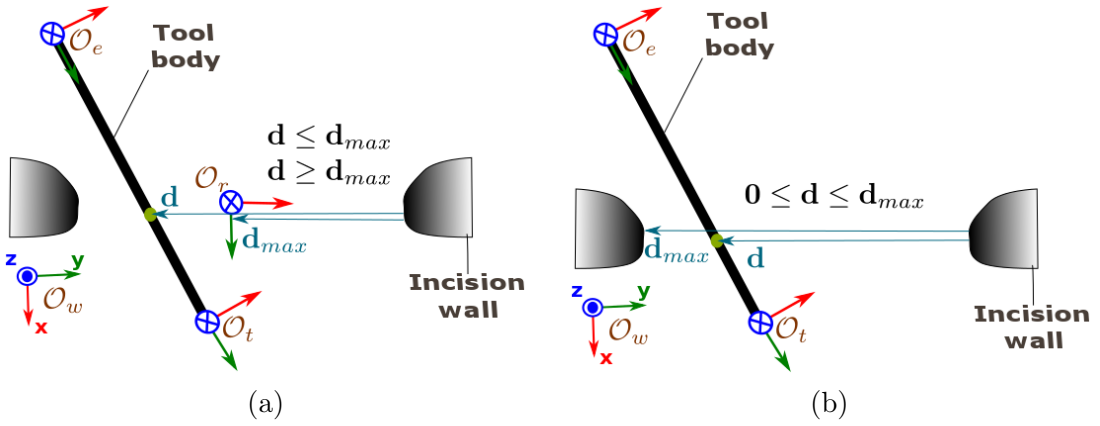


FIGURE 3.3: A 2D conceptual scheme for the comparison between the movements of (a) Remote Centre of Motion (RCM), and (b) Unilaterally Constrained Motion (UCM).

represents the distance \mathbf{d}_{max} as the length between two opposite points onto the incision wall. The UCM constraints must satisfy that $\mathbf{0} \leq \mathbf{d} \leq \mathbf{d}_{max}$.

In clinical applications, the surgical task is a complex job (e.g., suturing a wound, scanning a region of interest or excising some tissues). One way to define a complex surgical task is by assembling several subtasks. The notation subtask (or a small task) is used to indicate that the task DOF (Degree Of Freedom) is smaller than the DOF provided by the robot kinematic structure. For instance, the RCM subtask needs 4-DOF while a general purpose robot has a 6-DOF. Thereby, the redundancy paradigm [Maciejewski and Klein, 1985, Siciliano, 1990] and the task priority technique [Nakamura et al., 1987] are raised. Such topics are detailed in the next Chapter 4, along with the description of other subtasks (i.e., 3D path following scheme). In other words, the global objective is performing the RCM or the UCM movements which represent the first subtask. The latter subtask should be accomplished alongside a secondary subtask (i.e., 3D path following control) in order to finish the complex surgical task.

Therefore, this chapter is dedicated to describe the RCM and the UCM subtasks which are discussed in Sections 3.1 and 3.2, respectively. The proposed solution does not impose a special structure for the robot structure. Indeed, the proposed software controller restricts the motion of a general purpose robot (i.e., a serial or a parallel robot). In addition, the proposed controller is formulated in the task-space (or Cartesian-space) which is helpful to be easily integrated with different robotic systems; since it uses an exteroceptive sensor for determining the relative pose of robot's end-effector with respect to the target object, and then it sends the control velocity to the robot's low level controller. Such a low-level controller allows mapping the task control velocity to the joint-space. This mapping is a classical robotic issue and it is defined by the robot's manufacturer. The proposed controller guides also a rigid surgical tool which could be either a straight or a curved one. At the end of this chapter, Section 3.3 presents the developed numerical simulator in order to validate the proposed controller.

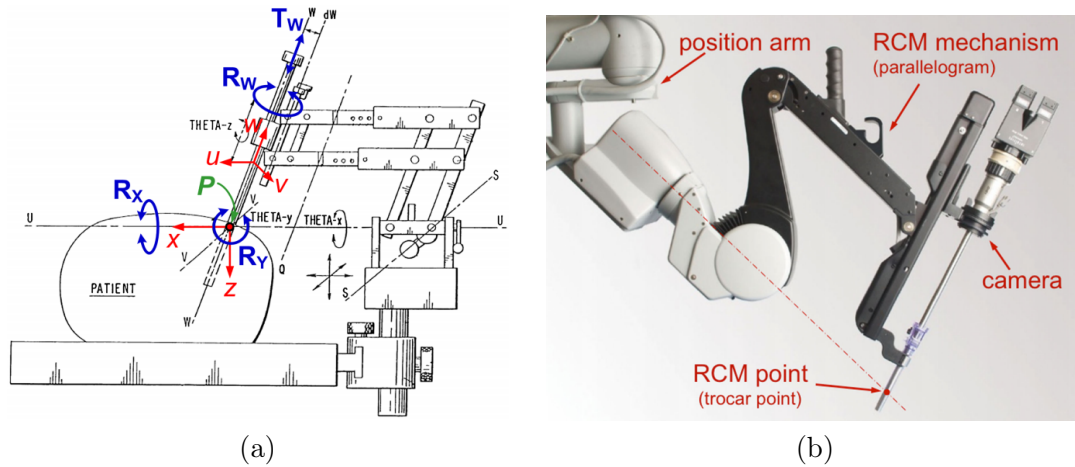


FIGURE 3.4: Examples about the special mechanisms of RCM: (a) patent by Taylor *et al.* [Taylor *et al.*, 1995], and (b) Da-Vinci¹ robotic manipulator.

3.1 Bilateral Constrained Motion

In the literature, there are a lot of works which demonstrate how to achieve the RCM movements by constructing a specific kinematic structure (FIGURE 3.4). The authors in [Kuo *et al.*, 2012] discussed the kinematics considerations that should be taken into account during the design process of an RCM mechanism. The latter mechanism has the advantage of protecting the incision wall from any sudden lateral hits; since the kinematic structure constrains the physical motion in order to be pivoted about the incision point. However, it does not provide enough flexibility to change the location of penetration point. In addition, the control software formulates the RCM constraints in the joint-space which is particular for the robot structure.

This section is concerned to achieve the RCM movement with an alternative solution. Such a solution is based on the implementation of an accurate and a repeatable software controller for performing the RCM movement without the need for a specific kinematic structure. This complex controller has the advantage of modifying the robot motion in order to follow the trocar point with a high flexibility. The proposed controller is also formulated in the task-space which can be applied on different robots, regardless their structure (e.g., serial [Osa *et al.*, 2010] or parallel [Dalvand and Shirinzadeh, 2012] robot). The essential condition is that the robot DOF should be equal or greater than 4-DOF. Additionally, the proposed controller is formulated by two methods: i) a geometric method which is applicable to a straight tool, while ii) an algebraic method is usable for straight or curved tools. Section 3.1.2 will detail the proposed controller but let us begins first by the previous works in literature.

¹ Intuitive Surgical, Inc., <http://www.intuitivesurgical.com/>

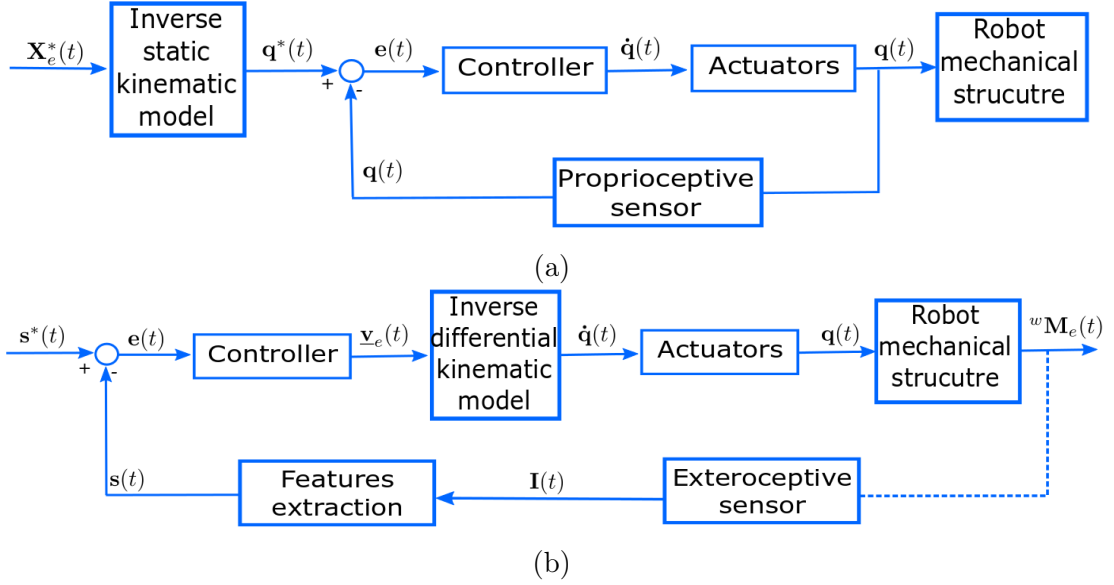


FIGURE 3.5: A comparison between the robot control in (a) joint-space, and (b) task-space.

3.1.1 Previous works in literature

There are different reported methods in the literature to formulate a RCM controller as: i) an extended Jacobian with quadratic optimization [Funda et al., 1996], ii) a so-called artificial intelligence based heuristic search [Boctor et al., 2004], iii) an analytical solution based on trocar modelling with Euler angle representation [Mayer et al., 2004], iv) a gradient projection approach in closed-loop form [Azimian et al., 2010], v) a dual quaternion-based kinematic controller [Marinho et al., 2014], and vi) a constrained Jacobian based on Lie algebra [Pham et al., 2015].

The previous techniques are used to maintain the RCM task and additional tasks are added to extend the robot functionality (i.e., a trajectory tracking task or point-to-point task). Beside that the majority of these methods [Funda et al., 1996, Azimian et al., 2010, Aghakhani et al., 2013, Marinho et al., 2014, Pham et al., 2015] constrain the kinematic Jacobian matrix of their robot (\mathbf{J}). Indeed, the forward kinematic model of a robot is often defined as:

$$\mathbf{v}_e = \mathbf{J}(\mathbf{q})\dot{\mathbf{q}}. \quad (3.1)$$

The kinematic Jacobian matrix $\mathbf{J} \in \mathbb{R}^{6 \times n}$ is a transformation that maps the free joints vector variable ($\mathbf{q} \in \mathbb{R}^{n \times 1}$) into the twist vector ($\mathbf{v}_e = \begin{bmatrix} \mathbf{v} \\ \boldsymbol{\omega} \end{bmatrix} \in se(3)$). In other words, this function $\mathbf{J}(\mathbf{q})$ is the velocities transformation from the joint-space (i.e., the space that gathers the speed of the robot joints) into the task-space (i.e., the linear and angular velocity of the end-effector in the Cartesian space).

The previous methods constrained this kinematic Jacobian matrix $\mathbf{J}_{con}(\mathbf{q})$. Thus, the motion control problem consists of eliminating the error between the measured value of the joint variables and the desired ones (i.e., $\mathbf{e} = \mathbf{q} - \mathbf{q}^*$), and the control joint velocity variables is deduced as ($\dot{\mathbf{q}} = \mathbf{J}_{con}^\dagger \mathbf{v}_e$). FIGURE 3.5(a) shows this concept of the joint-space controller, where a proprioceptive sensor is usually used for measuring the actual value of the joint variables. In fact, the joint-space control needs a precise knowledge of the robot kinematic model. In case that the inverse static model is not accurate, it will introduce an additional error in the control loop. Consequently, the controller would not be able to detect and fix this additional error since the robot model is located outside of the control loop (FIGURE 3.5(a)). Further, this type of controller is specific to the robot structure because the kinematic Jacobian matrix is specific for each robotic structure. Furthermore, the robot works blindly, if the patient moves during the time, the controller cannot detect this error and hence cannot compensate it.

Therefore, the usage of an exteroceptive sensor is beneficial since it imitates the surgeon's eyes. It provides also a "super-human" perception thanks to the variety of available sensors (e.g., endoscope, OCT, fluorescence, ultrasound). In fact, the exteroceptive sensor provides a measured signal which is processed to extract the desired information ($\mathbf{s} \in \mathbb{R}^{m \times 1}$). For instance, a camera gives a measured image which is processed for extracting the desired visual features \mathbf{s} (e.g., the image coordinates of some points of interest, the image coordinates of the centroid of an object or the pose estimation of an object).

The controller sensor-based (FIGURE 3.5(b)) does not need an accurate knowledge about the robot kinematic model because the inverse differential kinematic model of the robot is included within the control loop. However, if the exteroceptive sensor is not accurate, the controller cannot eliminate the error between the measured value and the desired one (i.e., $\mathbf{e} = \mathbf{s} - \mathbf{s}^*$). Thereby, there is a trade-off between the accuracy of the robot mathematical model and that of the sensor. The general differential model of an exteroceptive sensor is defined as:

$$\dot{\mathbf{s}} = \mathbf{L}(\mathbf{s})\mathbf{v}_e \quad (3.2)$$

where ($\dot{\mathbf{s}}$) is the time-derivative of the measured features, and ($\mathbf{L}(\mathbf{s}) \in \mathbb{R}^{m \times 6}$) is the interaction matrix which relates the velocity of features $\dot{\mathbf{s}}$ and the velocity of a robot's end-effector \mathbf{v}_e .

By imposing the RCM constraints on the interaction matrix, as proposed in [Mayer et al., 2004, Boctor et al., 2004, Osa et al., 2010], the controller will be more generic to perform the fulcrum task and it is not limited to a specific robotic structure. However, the Euler angle representation used in [Mayer et al., 2004] is mathematically heavy to formulate the RCM constraints in the task-space. An easier method was proposed in [Boctor et al., 2004] to define the RCM constraints by applying a geometric vector form. The authors used a method with two heuristic functions for solving the problem. The first heuristic function is an error which is intended to measure the alignment of the tool with the desired tool configuration, where the tool body passes through the trocar and the tool tip is on the reference trajectory. The first function is evaluated by a cross

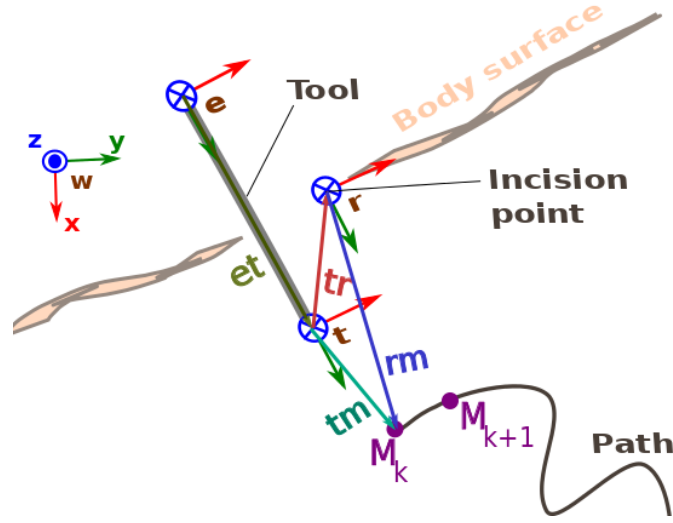


FIGURE 3.6: The scheme shows the different notation and vectors used to describe geometrically the RCM movement.

product (\times) as:

$$\mathbf{e}_{h_1} = \mathbf{et} \times \mathbf{rm}. \quad (3.3)$$

The first function reduces the angular error between the vectors (\mathbf{et} and \mathbf{rm}), as depicted in FIGURE 3.6. The vector \mathbf{et} is determined by the distance from the tool base (\mathbf{e}) to its tip (\mathbf{t}), while the vector \mathbf{rm} is formed between the trocar point (\mathbf{r}) and a target point on the reference trajectory (\mathbf{m}). The second heuristic function is used to reduce the tracking error between the tool tip \mathbf{t} and the target point on the reference trajectory \mathbf{m} as:

$$\mathbf{e}_{h_2} = \mathbf{t} - \mathbf{m}. \quad (3.4)$$

The choice of first heuristic function is not so precise because the angular alignment error \mathbf{e}_{h_1} couples the tool body, the trocar point and the target point. It should be simpler by treating the error between the tool body and the trocar point independently from the reference trajectory. In addition, the heuristic functions are not arranged in a hierarchical form. Consequently, the controller does not guarantee to converge to a solution that fulfils the two conditions together.

For instance, the controller may reach its local optimal solution when both vectors \mathbf{et} and \mathbf{rm} are parallel (i.e., $\mathbf{e}_{h_1} = \mathbf{0}$ as shown in FIGURE 3.7(a)) while the tool tip does not reach the desired point on the trajectory (i.e., $\mathbf{e}_{h_2} \neq 0$). On the opposite, the controller reaches a local minimum when the tool tip is coincident with the desired point on the trajectory (i.e., $\mathbf{e}_{h_2} = 0$ as depicted in FIGURE 3.7(b)) but the vector \mathbf{et} does not aligned with the vector \mathbf{rm} (i.e., $\mathbf{e}_{h_1} \neq 0$). The RCM constraint is only satisfied when both heuristic functions are zero. If, for some reason (and many of them can occur when controlling a robot in the real world), one of the two heuristics cannot be satisfied then unacceptable efforts may be applied to the tissues around the insertion point.

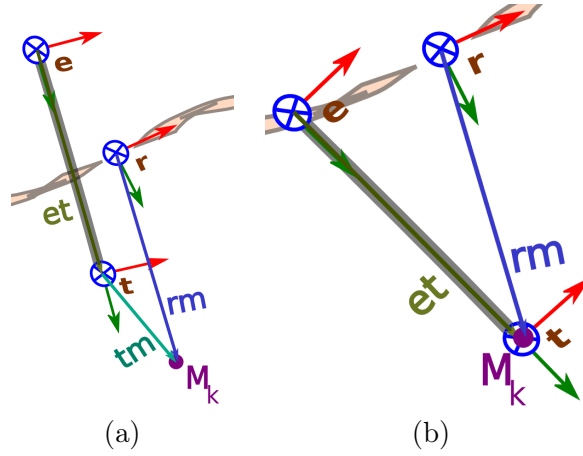


FIGURE 3.7: Illustration of some special conditions of [Boctor et al., 2004], where (a) $e_{h_1} = \mathbf{0}$ with $e_{h_2} \neq 0$, and (b) $e_{h_1} \neq 0$ with $e_{h_2} = 0$.

Another method was reported in [Osa et al., 2010] for describing the RCM constraint in the task-space. The proposed IBVS (Image-Based Visual Servoing) controller relates explicitly the relation between the velocity vector of the trocar point and that of the instrument. Such a choice is better than that made in [Boctor et al., 2004] because it formulates the RCM constraints independently from other tasks. Indeed, the linear velocity of trocar point is converted into an angular velocity which is applied to a straight tool. However, this solution is not applicable to a curved tool. Beside that this solution treats only the condition when the incision point r is located within the tool segment $[e, t]$ and outside this segment the system behaviour is unknown.

Our proposed formulation is intrinsic to the RCM task and it decorrelates the RCM task from the other tasks (i.e., contrary to [Boctor et al., 2004], the tool tip target point (m) does not appear in the error). In addition, it allows regulation the alignment error even when the tool is located outside the incision hole before that it is inserted through the incision. In case that the rigid tool has a straight form, our proposed eliminates the need to compute the projection of the incision hole centre point r onto the tool body $[e, t]$, which is necessary for other methods [Osa et al., 2010, Azimian et al., 2010].

3.1.2 Proposed method

This part formulates the RCM constraints in the task-space. An analytical solution was proposed for this new geometric formulation. Such a solution reduces the computational time since it eliminates the need for the heavy computational methods (e.g., Moore-Penrose inverse method) to estimate the inverse of the RCM interaction matrix.

The formulation is extended to describe the motion of a rigid curved tool under the RCM constraints (FIGURE 3.8). However, it is not easy to find out an analytical solution for the extended geometric formulation. Thus, a numerical method is applied to find out

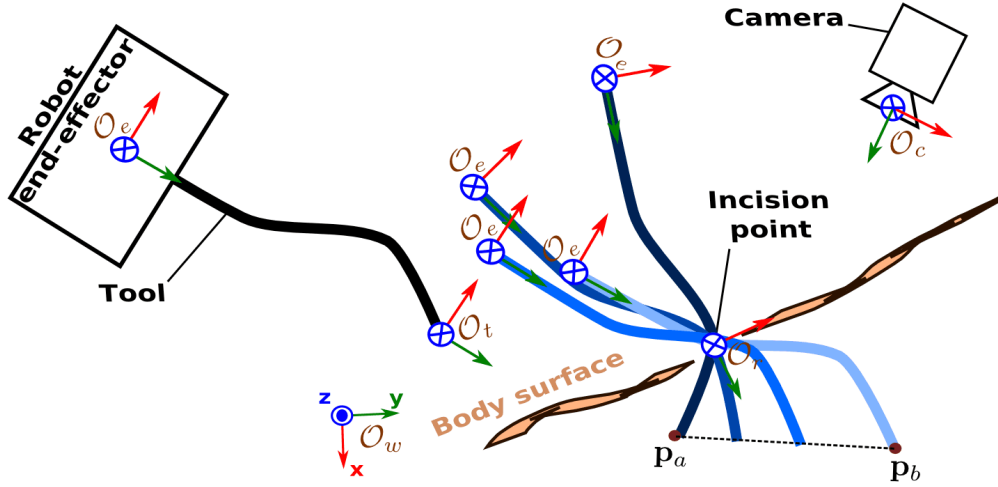


FIGURE 3.8: Conceptual scheme of the system with the various reference frames (i.e., the origin points of: the world frame \mathcal{O}_w , the end-effector frame \mathcal{O}_e , the tool tip frame \mathcal{O}_t , the RCM frame \mathcal{O}_r , and the camera frame \mathcal{O}_c), and the evaluation of a curved tool to move from one point to another one under the RCM constraints.

the inverse solution. Consequently, a velocity controller is proposed to impose the RCM constraints either on a straight tool or a curved tool.

Problem statement: FIGURE 3.8 shows a general view on the various reference frames associated to the essential parts of the system. The fulcrum effect restricts locally two dimensions of the tool linear motion (i.e., the translation along the x - and z -axes of trocar point frame \mathcal{R}_r) and it allows only one translation along the penetration axis (i.e., the y -axis of frame \mathcal{R}_r). In other words, the tool centre line should always be coincident with the incision hole centre point, while the tool tip can move freely within a cavity (FIGURE 3.8). Therefore, the RCM task must ensure that the misalignment error between the tool centre line and the incision hole centre point is null. Thus, the problem comes to deduce the adequate velocity which is applied at the end-effector (or the tool base) for eliminating the misalignment error and executing the desired linear velocity at the tool tip.

3.1.2.1 Straight tool movement

This part begins by presenting the geometric model which describes the RCM movement with a straight tool. Such a method will be extended in the next part to include the RCM movement with a curved tool.

RCM lateral error: It is defined as the vector distance (\mathbf{d}_{rcm} as depicted in FIGURE 3.9), which is obtained by projecting the incision hole centre point (\mathcal{O}_r) onto the

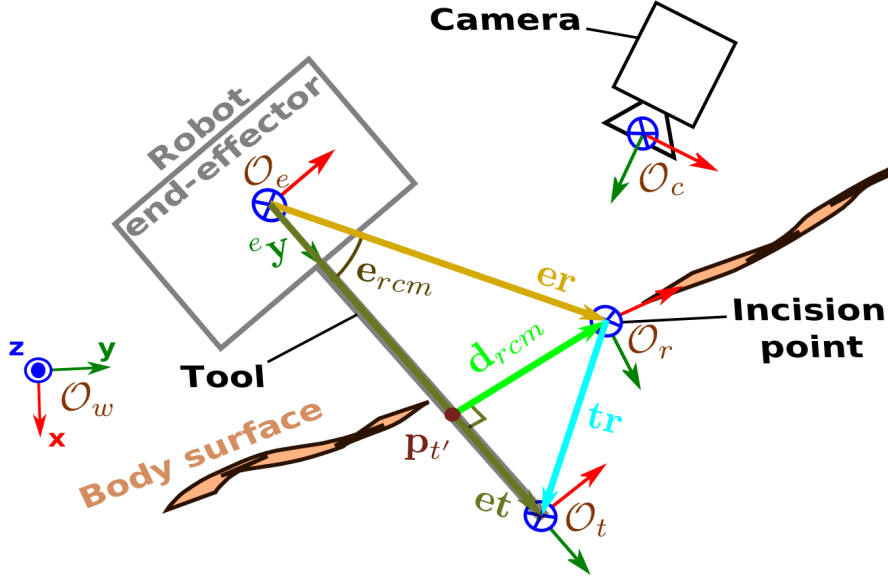


FIGURE 3.9: Conceptual scheme of a straight tool inserted through an incision hole, and the vectors notations for describing the RCM movements.

tool centre line (${}^e\mathbf{et}$). The RCM lateral error \mathbf{d}_{rcm} is thus computed as:

$$\mathbf{d}_{rcm} = {}^e\mathbf{er} - \underbrace{{}^e\mathbf{u}_{et} \underbrace{{}^e\mathbf{u}_{et}^T}_{=\|\mathbf{et}'\|} {}^e\mathbf{er}}_{= {}^e\mathbf{et}'}, \quad (3.5)$$

$$\mathbf{d}_{rcm} = (\mathbf{I}_{3 \times 3} - {}^e\mathbf{u}_{et} \underbrace{{}^e\mathbf{u}_{et}^T}_{= {}^e\mathbf{et}'}) {}^e\mathbf{er} \quad (3.6)$$

whereby the $(\mathbf{I}_{3 \times 3})$ is an identity matrix, $({}^e\mathbf{er})$ is the vector between the end-effector frame \mathcal{O}_e and the trocar point \mathcal{O}_r , $({}^e\mathbf{u}_{et})$ is the unit-vector of ${}^e\mathbf{et}$ which is formed between the tool base \mathcal{O}_e and its distal tip \mathcal{O}_t , and $({}^e\mathbf{et}')$ is the vector formed between the tool base \mathcal{O}_e and the projected point $\mathbf{p}_{t'}$.

3-Dimensional RCM angular error:

Choice of error: The RCM angular error ($\mathbf{e}_{rcm3D} \in \mathbb{R}^{3 \times 1}$) is determined by the cross-product (\times) between the vectors ${}^e\mathbf{et}$ and ${}^e\mathbf{er}$ as [Dahroug et al., 2016]:

$$\mathbf{e}_{rcm3D} = {}^e\mathbf{et} \times {}^e\mathbf{er}. \quad (3.7)$$

In fact, this error is basically the geodesic error between the two vectors. In case that the vector \mathbf{et} is not aligned with the vector \mathbf{er} , then the vector \mathbf{et} rotates in order to eliminate the angular error with the other vector (FIGURE 3.9). When both vectors are

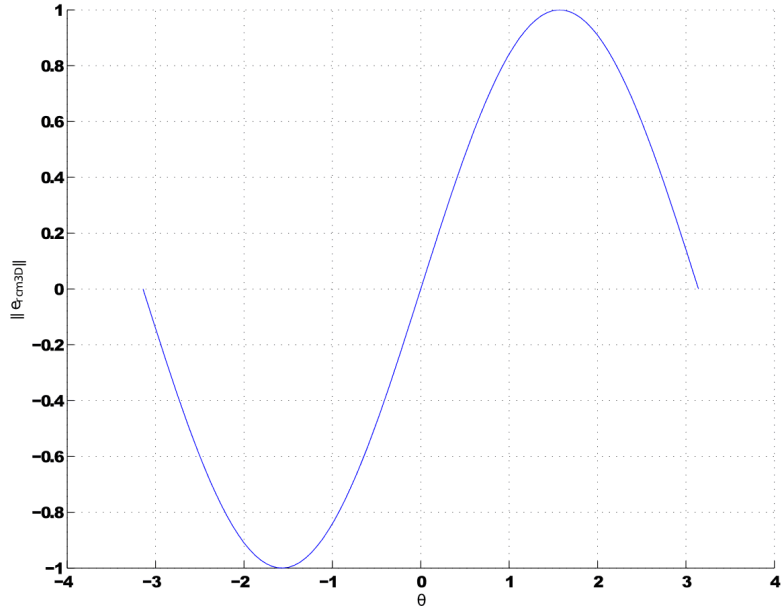


FIGURE 3.10: The relation between the 3D RCM angular error and the angle θ which is defined between the vectors ${}^e\mathbf{y}$ and ${}^e\mathbf{u}_{er}$.

parallel, the latter error becomes zero (i.e., $\mathbf{e}_{rcm3D} = \mathbf{0}$), which implies that the three points \mathcal{O}_e , \mathcal{O}_r and \mathcal{O}_t are aligned.

Since the projection of the incision hole centre point onto the tool body is not needed, the unit-vector of both vectors is applied, where the unit-vector of ${}^e\mathbf{et}$ is the same as the constant y -component of the end-effector frame (i.e., ${}^e\mathbf{y} = [0; 1; 0]$, see FIGURE 3.9). The angular RCM error is thus deduced as:

$$\mathbf{e}_{rcm3D} = {}^e\mathbf{y} \times {}^e\mathbf{u}_{er}. \quad (3.8)$$

Note that the Euclidean norm of the latter equation could be determined as:

$$\|\mathbf{e}_{rcm3D}\| = \|{}^e\mathbf{y}\| \|{}^e\mathbf{u}_{er}\| \sin(\theta) \quad (3.9)$$

whereby $\|{}^e\mathbf{y}\| = 1$, $0 \leq \|{}^e\mathbf{u}_{er}\| \leq 1$, and θ is the angle between both vectors ${}^e\mathbf{y}$ and ${}^e\mathbf{u}_{er}$.

FIGURE 3.10 shows the variation of the angle $-\pi \leq \theta \leq \pi$, and its influence on the RCM angular error. This graph is also obtained by fixing $\|{}^e\mathbf{u}_{er}\| = 1$ in the latter equation. The amplitude of $\|\mathbf{e}_{rcm3D}\|$ is reduced when the $\|{}^e\mathbf{u}_{er}\|$ is decreased.

Differential kinematics of the error: The time-derivative of the RCM angular error is evaluated as:

$$\dot{\mathbf{e}}_{rcm3D} = {}^e\mathbf{y} \times {}^e\dot{\mathbf{u}}_{er} + \underbrace{{}^e\dot{\mathbf{y}} \times {}^e\mathbf{u}_{er}}_{=0} \quad (3.10)$$

The unit-vector of ${}^e\mathbf{er}$ and its time-derivative are calculated, respectively, as:

$${}^e\mathbf{u}_{er} = \frac{{}^e\mathbf{er}}{\|{}^e\mathbf{er}\|} \quad (3.11)$$

$${}^e\dot{\mathbf{u}}_{er} = \frac{\|{}^e\mathbf{er}\| {}^e\dot{\mathbf{er}} - {}^e\mathbf{er} \frac{d\|{}^e\mathbf{er}\|}{dt}}{\|{}^e\mathbf{er}\|^2}. \quad (3.12)$$

The Euclidean norm of the vector ${}^e\mathbf{er}$ is determined as, where $({}^e\mathbf{er}^T)$ is the transpose of vector ${}^e\mathbf{er}$:

$$\|{}^e\mathbf{er}\| = \sqrt{{}^e\mathbf{er}^T {}^e\mathbf{er}}, \quad (3.13)$$

and its time-derivative as:

$$\frac{d\|{}^e\mathbf{er}\|}{dt} = \frac{{}^e\mathbf{er}^T {}^e\dot{\mathbf{er}}}{\sqrt{{}^e\mathbf{er}^T {}^e\mathbf{er}}} = \frac{{}^e\mathbf{er}^T {}^e\dot{\mathbf{er}}}{\|{}^e\mathbf{er}\|}. \quad (3.14)$$

By injecting (3.14) in (3.12), the unit-vector ${}^e\dot{\mathbf{u}}_{er}$ is simplified as:

$$\begin{aligned} {}^e\dot{\mathbf{u}}_{er} &= \frac{{}^e\dot{\mathbf{er}}}{\|{}^e\mathbf{er}\|} - \frac{{}^e\mathbf{er} {}^e\mathbf{er}^T {}^e\dot{\mathbf{er}}}{\|{}^e\mathbf{er}\|^3} \\ &= \left(\frac{\mathbf{I}_{3 \times 3}}{\|{}^e\mathbf{er}\|} - \frac{{}^e\mathbf{u}_{er} {}^e\mathbf{u}_{er}^T}{\|{}^e\mathbf{er}\|} \right) {}^e\dot{\mathbf{er}} \end{aligned} \quad (3.15)$$

$${}^e\dot{\mathbf{u}}_{er} = \frac{1}{\|{}^e\mathbf{er}\|} \underbrace{(\mathbf{I}_{3 \times 3} - {}^e\mathbf{u}_{er} {}^e\mathbf{u}_{er}^T)}_{=:\mathbb{P}_{\perp u_r}} {}^e\dot{\mathbf{er}}. \quad (3.16)$$

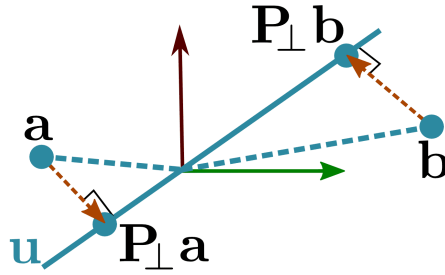


FIGURE 3.11: Geometrical representation of the projection operator \mathbb{P}_{\perp} .

The term $(\mathbb{P}_{\perp u_r} = \mathbf{I}_{3 \times 3} - {}^e\mathbf{u}_{er} {}^e\mathbf{u}_{er}^T)$ in the latter equation represents the projection operator onto the vector ${}^e\mathbf{u}_{er}$. Indeed, this operator is a linear transformation that maps an element from a vector space into its self. For instance, assume that the line \mathbf{u} and both points \mathbf{a} and \mathbf{b} are in the space \mathbb{R}^2 , as depicted in FIGURE 3.11. The projector operator \mathbb{P}_{\perp} maps the points \mathbf{a} and \mathbf{b} onto the line \mathbf{u} (FIGURE 3.11).

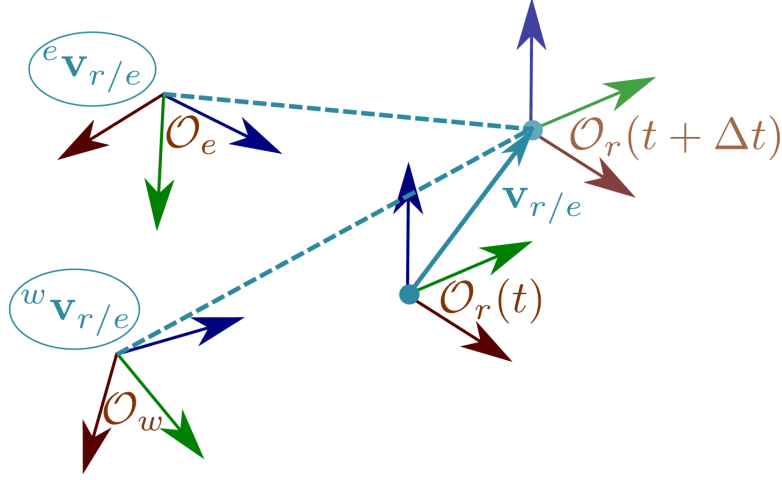


FIGURE 3.12: An example of linear velocity which can be expressed in different frames.

The term $({}^e\dot{\mathbf{r}})$ represents the linear velocity of the incision point \mathcal{O}_r with respect to the end-effector frame (i.e., ${}^e\dot{\mathbf{r}} = {}^e\mathbf{v}_{r/e}$). This velocity can be expressed with respect to different frames. For instance, FIGURE 3.12 shows the incision point \mathcal{O}_r moved during a finite time with a certain velocity with respect to the end-effector $\mathbf{v}_{r/e}$. This velocity can also be observed from the world frame ${}^w\mathbf{v}_{r/e}$, where a left superscript is added to note the reference frame.

By choosing the end-effector frame, the trocar velocity ${}^e\mathbf{v}_{r/e}$ is formulated in terms of the end-effector twist velocity as:

$$\begin{aligned} {}^e\mathbf{v}_{r/e} &= {}^e\mathbf{v}_{e/e} + {}^e\omega_{e/e} \times {}^e\mathbf{er} \\ &= \underbrace{[\mathbf{I}_{3 \times 3} \quad -[{}^e\mathbf{er}]_{\times}]}_{\mathbf{L}_{v_r}} \underbrace{\begin{bmatrix} {}^e\mathbf{v}_{e/e} \\ {}^e\omega_{e/e} \end{bmatrix}}_{{}^e\underline{\mathbf{v}}_{e/e}} \end{aligned} \quad (3.17)$$

whereby $([{}^e\mathbf{er}]_{\times})$ is the anti-symmetric matrix of the vector ${}^e\mathbf{er}$.

To simplify the notations, when the velocity frame is represented in its bases, for instance ${}^e\mathbf{v}_{e/e}$, it is simplified as ${}^e\mathbf{v}_e$. Indeed, the term $({}^e\underline{\mathbf{v}}_e)$ is the twist vector of end-effector which gathers the linear (${}^e\mathbf{v}_e$) and angular (${}^e\omega_e$) velocities.

The trocar point \mathcal{O}_r is also moving in an opposite direction of that end-effector to ensure that the misalignment error remains null. As a consequence, a negative sign is added to the latter equation (3.17), and it becomes as:

$${}^e\mathbf{v}_{r/e} = -\mathbf{L}_{v_r} {}^e\underline{\mathbf{v}}_e. \quad (3.18)$$

By putting (3.18) in (3.16), the unit-vector ${}^e\dot{\mathbf{u}}_{er}$ is reformulated as:

$${}^e\dot{\mathbf{u}}_{er} = \frac{-1}{\|{}^e\mathbf{er}\|} \underbrace{\left(\underbrace{\mathbf{I}_{3 \times 3} - {}^e\mathbf{u}_{er} {}^e\mathbf{u}_{er}^T}_{\mathbb{P}_{\perp u_r}} \right)}_{\mathbf{L}_{u_r}} \underbrace{\left(\mathbf{I}_{3 \times 3} - [{}^e\mathbf{er}]_{\times} \right)}_{\mathbf{L}_{v_r}} \underbrace{\begin{bmatrix} {}^e\mathbf{v}_e \\ {}^e\boldsymbol{\omega}_e \end{bmatrix}}_{{}^e\mathbf{v}_e} \quad (3.19)$$

The time-derivative of the RCM angular error is thus redefined by substituting (3.19) in (3.10), and it equals to:

$$\dot{\mathbf{e}}_{rcm3D} = \underbrace{[{}^e\mathbf{y}]_{\times} \mathbf{L}_{u_r}}_{\mathbf{L}_{e_{rcm3D}}} {}^e\mathbf{v}_e \quad (3.20)$$

where $(\mathbf{L}_{e_{rcm3D}} \in \mathbb{R}^{3 \times 6})$ is the interaction matrix of the alignment task. This matrix describes how the error $\dot{\mathbf{e}}_{rcm3D}$ is modified when the end-effector frame is moving with a velocity ${}^e\mathbf{v}_e$.

Control of the error: For reducing exponentially the RCM angular error, a proportional controller is applied as:

$$\dot{\mathbf{e}}_{rcm3D} = -\lambda \mathbf{e}_{rcm3D}. \quad (3.21)$$

The latter equation represents the exponential decay behaviour, where (λ) is a positive scalar gain for the alignment task. By increasing λ , the system tends to reduce quickly the error \mathbf{e}_{rcm3D} . In opposite condition, the reduction of λ will affect the system by taking more time to eliminate the error.

The controller should deduce the control twist velocity of end-effector in equation (3.20). By replacing the (3.21) in (3.20), it becomes as:

$$\mathbf{L}_{e_{rcm3D}} {}^e\mathbf{v}_e = -\lambda \mathbf{e}_{rcm3D}, \quad (3.22)$$

and the control velocity of end-effector is evaluated as, where $(\mathbf{L}_{e_{rcm3D}}^{\dagger})$ is the inverse matrix of $\mathbf{L}_{e_{rcm3D}}$:

$${}^e\mathbf{v}_e = -\lambda \mathbf{L}_{e_{rcm3D}}^{\dagger} \mathbf{e}_{rcm3D}. \quad (3.23)$$

The inversion of $\mathbf{L}_{e_{rcm3D}}$ is not guarantee (i.e., a non-invertible matrix) because it is not a square matrix and its rank could be deficient. The Moore-Penrose inverse method (or pseudo-inverse method, where $\mathbf{L}_{e_{rcm3D}}^{\dagger} \mathbf{L}_{e_{rcm3D}} = \mathbf{I}_{6 \times 6}$) is a useful technique to estimate the inverse for this type of matrix (i.e., a non-invertible matrix). It can be computed by the SVD (Singular Value Decomposition), LU (Lower Upper) or QR factorization techniques [Strang et al., 1993, Hogben, 2006].

Since there is not an exact solution for (3.22), a least-square solution is applied to find out the optimal solution of (3.23). Such a solution space has a subspace which corresponds to the null-space (or it called Kernel [Strang et al., 1993, Lay, 2012]). The kernel of $\mathbf{L}_{\mathbf{e}_{rcm3D}}$ is a set of vectors ${}^e\mathbf{v}_e \in \mathbb{R}^6$ that satisfy:

$$\mathbf{L}_{\mathbf{e}_{rcm3D}} {}^e\mathbf{v}_e = \mathbf{0} \quad (3.24)$$

FIGURE 3.13 intuitively shows this set as an ellipse within the space of ${}^e\mathbf{v}_e$. The blue dots in the latter figure represent some non-zero solutions in the ${}^e\mathbf{v}_e$ space, then they are mapped to the zero set within the \mathbf{e}_{rcm3D} space. As many numerical tool boxes do, we will use the operator $ker(\mathbf{L}_{\mathbf{e}_{rcm3D}})$ ² to manipulate the kernel of $\mathbf{L}_{\mathbf{e}_{rcm3D}}$

Compute the kernel of the interaction matrix: The matrix $ker(\mathbf{L}_{\mathbf{e}_{rcm3D}})$ can be determined by an analytical method, without the need to apply the heavy computational methods (i.e., pseudo-inverse or SVD). It is formed indeed by the combinations of column vectors, where the multiplication of each column vector by the interaction matrix leads to a zero column vector. It is also necessary that the columns of the kernel matrix are orthogonal to each other, and their Euclidean norms equal to unity. Therefore, the kernel matrix is determined as:

$$ker(\mathbf{L}_{\mathbf{e}_{rcm3D}}) = \begin{bmatrix} {}^e\mathbf{u}_{er} & \mathbf{0}_{3 \times 1} & \frac{\|{}^e\mathbf{er}\|}{n_{c3}} ({}^e\mathbf{u}_{er} \times \mathbf{u}_{\mathbf{e}_{rcm3D}}) & \frac{-\|{}^e\mathbf{er}\|}{n_{c4}} \mathbf{u}_{\mathbf{e}_{rcm3D}} \\ \mathbf{0}_{3 \times 1} & {}^e\mathbf{u}_{er} & \frac{1}{n_{c3}} \mathbf{u}_{\mathbf{e}_{rcm3D}} & \frac{1}{n_{c4}} ({}^e\mathbf{u}_{er} \times \mathbf{u}_{\mathbf{e}_{rcm3D}}) \end{bmatrix} \quad (3.25)$$

whereby $ker(\mathbf{L}_{\mathbf{e}_{rcm3D}}) \in \mathbb{R}^{6 \times 4}$, $(\mathbf{u}_{\mathbf{e}_{rcm3D}})$ is the unit-vector of \mathbf{e}_{rcm3D} , $(\mathbf{0}_{3 \times 1})$ is a column vector of zeros, (n_{c3}) and (n_{c4}) are the Euclidean norms of the third and the fourth columns of the kernel matrix, respectively.

Indeed, they are calculated as:

$$n_{c3} = \sqrt{\|{}^e\mathbf{er}\|^2 \underbrace{({}^e\mathbf{u}_{er} \times \mathbf{u}_{\mathbf{e}_{rcm3D}})^T ({}^e\mathbf{u}_{er} \times \mathbf{u}_{\mathbf{e}_{rcm3D}})}_{=1} + \underbrace{\mathbf{u}_{\mathbf{e}_{rcm3D}}^T \mathbf{u}_{\mathbf{e}_{rcm3D}}}_{=1}} \quad (3.26)$$

$$= \sqrt{\|{}^e\mathbf{er}\|^2 + 1}$$

$$n_{c4} = \sqrt{\|{}^e\mathbf{er}\|^2 \underbrace{\mathbf{u}_{\mathbf{e}_{rcm3D}}^T \mathbf{u}_{\mathbf{e}_{rcm3D}}}_{=1} + \underbrace{({}^e\mathbf{u}_{er} \times \mathbf{u}_{\mathbf{e}_{rcm3D}})^T ({}^e\mathbf{u}_{er} \times \mathbf{u}_{\mathbf{e}_{rcm3D}})}_{=1}} \quad (3.27)$$

$$= \sqrt{\|{}^e\mathbf{er}\|^2 + 1}.$$

²This operator gives a matrix whose columns form an orthogonal basis of the kernel of $\mathbf{L}_{\mathbf{e}_{rcm3D}}$.

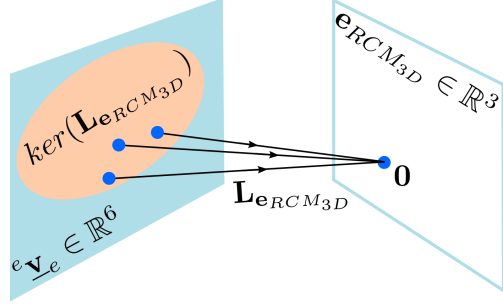


FIGURE 3.13: A conceptual scheme to represent the different spaces and how the interaction matrix maps one space to other one.

Proof of the analytical kernel matrix: The multiplication of the interaction matrix $\mathbf{L}_{e_{rcm3D}}$ by the column vector of $\ker(\mathbf{L}_{e_{rcm3D}})$ should equal to null. The first column of (3.25) multiplied by $\mathbf{L}_{e_{rcm3D}}$, the resultant is:

$$\begin{aligned}
\mathbf{L}_{e_{rcm3D}} \begin{bmatrix} {}^e\mathbf{u}_{er} \\ \mathbf{0}_{3 \times 1} \end{bmatrix} &= \frac{-1}{\|{}^e\mathbf{er}\|} [{}^e\mathbf{y}]_{\times} (\mathbf{I} - {}^e\mathbf{u}_{er} {}^e\mathbf{u}_{er}^T) [\mathbf{I} - [{}^e\mathbf{er}]_{\times}] \begin{bmatrix} {}^e\mathbf{u}_{er} \\ \mathbf{0}_{3 \times 1} \end{bmatrix} \\
&= \frac{-1}{\|{}^e\mathbf{er}\|} [{}^e\mathbf{y}]_{\times} (\mathbf{I} - {}^e\mathbf{u}_{er} {}^e\mathbf{u}_{er}^T) ({}^e\mathbf{u}_{er} + \mathbf{0}) \\
&= \frac{-1}{\|{}^e\mathbf{er}\|} [{}^e\mathbf{y}]_{\times} ({}^e\mathbf{u}_{er} - \underbrace{{}^e\mathbf{u}_{er} {}^e\mathbf{u}_{er}^T {}^e\mathbf{u}_{er}}_{=\|{}^e\mathbf{u}_{er}\|^2=1}) \\
&= \frac{-1}{\|{}^e\mathbf{er}\|} [{}^e\mathbf{y}]_{\times} \underbrace{({}^e\mathbf{u}_{er} - {}^e\mathbf{u}_{er})}_{=0} = \mathbf{0}.
\end{aligned} \tag{3.28}$$

The term ${}^e\mathbf{u}_{er}^T {}^e\mathbf{u}_{er}$ equals to one since the Euclidean norm of a unit-vector is always equaled to one.

The second column of (3.25) multiplied by $\mathbf{L}_{e_{rcm3D}}$, the resultant is:

$$\begin{aligned}
\mathbf{L}_{e_{rcm3D}} \begin{bmatrix} \mathbf{0}_{3 \times 1} \\ {}^e\mathbf{u}_{er} \end{bmatrix} &= \frac{-1}{\|{}^e\mathbf{er}\|} [{}^e\mathbf{y}]_{\times} (\mathbf{I} - {}^e\mathbf{u}_{er} {}^e\mathbf{u}_{er}^T) [\mathbf{I} - [{}^e\mathbf{er}]_{\times}] \begin{bmatrix} \mathbf{0}_{3 \times 1} \\ {}^e\mathbf{u}_{er} \end{bmatrix} \\
&= \frac{-1}{\|{}^e\mathbf{er}\|} [{}^e\mathbf{y}]_{\times} (\mathbf{I} - {}^e\mathbf{u}_{er} {}^e\mathbf{u}_{er}^T) (\mathbf{0} - \underbrace{{}^e\mathbf{er} \times {}^e\mathbf{u}_{er}}_{=0}) = \mathbf{0}.
\end{aligned} \tag{3.29}$$

The term ${}^e\mathbf{er} \times {}^e\mathbf{u}_{er}$ is null because both vectors are parallel.

The third column of (3.25) multiplied by $\mathbf{L}_{e_{rcm3D}}$, which gives:

$$\begin{aligned}
\mathbf{L}_{e_{rcm3D}} \begin{bmatrix} \frac{\|{}^e\mathbf{er}\|}{n_{c3}} ({}^e\mathbf{u}_{er} \times \mathbf{u}_{e_{rcm3D}}) \\ \frac{1}{n_{c3}} \mathbf{u}_{e_{rcm3D}} \end{bmatrix} \\
&= \frac{-1}{\|{}^e\mathbf{er}\|} [{}^e\mathbf{y}]_{\times} (\mathbf{I} - {}^e\mathbf{u}_{er} {}^e\mathbf{u}_{er}^T) [\mathbf{I} - [{}^e\mathbf{er}]_{\times}] \begin{bmatrix} \frac{\|{}^e\mathbf{er}\|}{n_{c3}} ({}^e\mathbf{u}_{er} \times \mathbf{u}_{e_{rcm3D}}) \\ \frac{1}{n_{c3}} \mathbf{u}_{e_{rcm3D}} \end{bmatrix} \\
&= \frac{-1}{\|{}^e\mathbf{er}\|} [{}^e\mathbf{y}]_{\times} (\mathbf{I} - {}^e\mathbf{u}_{er} {}^e\mathbf{u}_{er}^T) \left(\frac{1}{n_{c3}} (\underbrace{\|{}^e\mathbf{er}\| {}^e\mathbf{u}_{er}}_{={}^e\mathbf{er}} \times \mathbf{u}_{e_{rcm3D}}) - \frac{1}{n_{c3}} ({}^e\mathbf{er} \times \mathbf{u}_{e_{rcm3D}}) \right) \\
&= \frac{-1}{\|{}^e\mathbf{er}\|} [{}^e\mathbf{y}]_{\times} (\mathbf{I} - {}^e\mathbf{u}_{er} {}^e\mathbf{u}_{er}^T) \underbrace{\left(\frac{1}{n_{c3}} ({}^e\mathbf{er} \times \mathbf{u}_{e_{rcm3D}}) - \frac{1}{n_{c3}} ({}^e\mathbf{er} \times \mathbf{u}_{e_{rcm3D}}) \right)}_{=0} = \mathbf{0}.
\end{aligned} \tag{3.30}$$

Recall that a vector triple product is evaluated as:

$$\mathbf{a} \times (\mathbf{b} \times \mathbf{c}) = \mathbf{b}\mathbf{a}^T\mathbf{c} - \mathbf{c}\mathbf{a}^T\mathbf{b}. \tag{3.31}$$

The fourth column of (3.25) multiplied by $\mathbf{L}_{e_{rcm3D}}$, the resultant is:

$$\begin{aligned}
& \mathbf{L}_{e_{rcm3D}} \begin{bmatrix} \frac{-\|e_{er}\|}{n_{c4}} \mathbf{u}_{e_{rcm3D}} \\ \frac{1}{n_{c4}} ({}^e \mathbf{u}_{er} \times \mathbf{u}_{e_{rcm3D}}) \end{bmatrix} \\
&= \frac{-1}{\|e_{er}\| n_{c4}} [{}^e \mathbf{y}]_{\times} (\mathbf{I} - {}^e \mathbf{u}_{er} {}^e \mathbf{u}_{er}^T) [\mathbf{I} - [{}^e \mathbf{er}]_{\times}] \begin{bmatrix} -\|e_{er}\| \mathbf{u}_{e_{rcm3D}} \\ {}^e \mathbf{u}_{er} \times \mathbf{u}_{e_{rcm3D}} \end{bmatrix} \\
&= \frac{-1}{\|e_{er}\| n_{c4}} [{}^e \mathbf{y}]_{\times} (\mathbf{I} - {}^e \mathbf{u}_{er} {}^e \mathbf{u}_{er}^T) \left(-\|e_{er}\| \mathbf{u}_{e_{rcm3D}} - \underbrace{{}^e \mathbf{er} \times ({}^e \mathbf{u}_{er} \times \mathbf{u}_{e_{rcm3D}})}_{= {}^e \mathbf{u}_{er} {}^e \mathbf{er}^T \mathbf{u}_{e_{rcm3D}} - \mathbf{u}_{e_{rcm3D}} \underbrace{{}^e \mathbf{er}^T {}^e \mathbf{u}_{er}}_{=\|e_{er}\|}} \right) \\
&= \frac{-1}{\|e_{er}\| n_{c4}} [{}^e \mathbf{y}]_{\times} \left(\underbrace{-\|e_{er}\| \mathbf{u}_{e_{rcm3D}}}_{\text{blue}} - \underbrace{{}^e \mathbf{u}_{er} {}^e \mathbf{er}^T \mathbf{u}_{e_{rcm3D}}}_{\text{green}} + \underbrace{\|e_{er}\| \mathbf{u}_{e_{rcm3D}}}_{\text{blue}} \right. \\
&\quad \left. + \underbrace{\|e_{er}\| {}^e \mathbf{u}_{er} {}^e \mathbf{u}_{er}^T \mathbf{u}_{e_{rcm3D}}}_{\text{red}} + \underbrace{{}^e \mathbf{u}_{er} \underbrace{{}^e \mathbf{u}_{er}^T {}^e \mathbf{u}_{er}}_{=1} {}^e \mathbf{u}_{er}^T \mathbf{u}_{e_{rcm3D}}}_{\text{green}} \right. \\
&\quad \left. - \underbrace{\|e_{er}\| {}^e \mathbf{u}_{er} {}^e \mathbf{u}_{er}^T \mathbf{u}_{e_{rcm3D}}}_{\text{red}} \right) = 0.
\end{aligned} \tag{3.32}$$

The terms with the same color of under-brace are eliminated together, and thus the latter equation equals null. This completes the proof of the kernel matrix.

There are varies conditions which should be checked to validate the analytical kernel matrix during the computation program. The first condition is that:

$$(\mathbf{I} - \mathbf{L}_{e_{rcm3D}}^\dagger \mathbf{L}_{e_{rcm3D}}) = \ker(\mathbf{L}_{e_{rcm3D}}) \ker(\mathbf{L}_{e_{rcm3D}})^T. \tag{3.33}$$

The second condition is that:

$$\ker(\mathbf{L}_{e_{rcm3D}})^T \ker(\mathbf{L}_{e_{rcm3D}}) = \mathbf{I}_{4 \times 4}, \tag{3.34}$$

$$\begin{aligned}
& \begin{bmatrix} {}^e \mathbf{u}_{er}^T & \mathbf{0}_{3 \times 1}^T \\ \frac{\|e_{er}\|}{n_{c3}} ({}^e \mathbf{u}_{er} \times \mathbf{u}_{e_{rcm3D}})^T & \frac{1}{n_{c3}} \mathbf{u}_{e_{rcm3D}} \\ \frac{-\|e_{er}\|}{n_{c4}} \mathbf{u}_{e_{rcm3D}} & \frac{1}{n_{c4}} ({}^e \mathbf{u}_{er} \times \mathbf{u}_{e_{rcm3D}})^T \end{bmatrix} \begin{bmatrix} {}^e \mathbf{u}_{er} & \mathbf{0}_{3 \times 1} & \frac{\|e_{er}\|}{n_{c3}} ({}^e \mathbf{u}_{er} \times \mathbf{u}_{e_{rcm3D}}) & \frac{-\|e_{er}\|}{n_{c4}} \mathbf{u}_{e_{rcm3D}} \\ \mathbf{0}_{3 \times 1} & {}^e \mathbf{u}_{er} & \frac{1}{n_{c3}} \mathbf{u}_{e_{rcm3D}} & \frac{1}{n_{c4}} ({}^e \mathbf{u}_{er} \times \mathbf{u}_{e_{rcm3D}}) \end{bmatrix} = \\
& \begin{bmatrix} \underbrace{{}^e \mathbf{u}_{er}^T {}^e \mathbf{u}_{er} + 0}_{=1} & 0 + 0 & \frac{\|e_{er}\|}{n_{c3}} \underbrace{{}^e \mathbf{u}_{er}^T ({}^e \mathbf{u}_{er} \times \mathbf{u}_{e_{rcm3D}}) + 0}_{=0} & \frac{-\|e_{er}\|}{n_{c4}} \underbrace{{}^e \mathbf{u}_{er}^T \mathbf{u}_{e_{rcm3D}} + 0}_{=0} \\ 0 + 0 & 0 + \underbrace{{}^e \mathbf{u}_{er}^T {}^e \mathbf{u}_{er}}_{=1} & 0 + \underbrace{{}^e \mathbf{u}_{er}^T \mathbf{u}_{e_{rcm3D}}}_{=0} & 0 + \frac{1}{n_{c4}} \underbrace{{}^e \mathbf{u}_{er}^T ({}^e \mathbf{u}_{er} \times \mathbf{u}_{e_{rcm3D}})}_{=0} \\ \frac{\|e_{er}\|}{n_{c3}} \underbrace{({}^e \mathbf{u}_{er} \times \mathbf{u}_{e_{rcm3D}})^T {}^e \mathbf{u}_{er} + 0}_{=0} & 0 + \underbrace{\mathbf{u}_{e_{rcm3D}}^T {}^e \mathbf{u}_{er}}_{=0} & \frac{\|e_{er}\|^2}{n_{c3}^2} \underbrace{({}^e \mathbf{u}_{er} \times \mathbf{u}_{e_{rcm3D}})^T ({}^e \mathbf{u}_{er} \times \mathbf{u}_{e_{rcm3D}})}_{=1} + \frac{1}{n_{c3}} \underbrace{\mathbf{u}_{e_{rcm3D}}^T \mathbf{u}_{e_{rcm3D}}}_{=1} & \frac{-\|e_{er}\|^2}{n_{c3} n_{c4}} \underbrace{({}^e \mathbf{u}_{er} \times \mathbf{u}_{e_{rcm3D}})^T \mathbf{u}_{e_{rcm3D}}}_{=0} + \frac{1}{n_{c3} n_{c4}} \underbrace{\mathbf{u}_{e_{rcm3D}}^T ({}^e \mathbf{u}_{er} \times \mathbf{u}_{e_{rcm3D}})}_{=0} \\ \frac{-\|e_{er}\|}{n_{c4}} \underbrace{\mathbf{u}_{e_{rcm3D}}^T {}^e \mathbf{u}_{er} + 0}_{=0} & 0 + \underbrace{({}^e \mathbf{u}_{er} \times \mathbf{u}_{e_{rcm3D}})^T {}^e \mathbf{u}_{er}}_{=0} & \frac{-\|e_{er}\|^2}{n_{c3} n_{c4}} \underbrace{\mathbf{u}_{e_{rcm3D}}^T ({}^e \mathbf{u}_{er} \times \mathbf{u}_{e_{rcm3D}})}_{=0} + \frac{1}{n_{c3} n_{c4}} \underbrace{({}^e \mathbf{u}_{er} \times \mathbf{u}_{e_{rcm3D}})^T \mathbf{u}_{e_{rcm3D}}}_{=0} & \frac{-\|e_{er}\|^2}{n_{c4}^2} \underbrace{\mathbf{u}_{e_{rcm3D}}^T \mathbf{u}_{e_{rcm3D}}}_{=1} + \frac{1}{n_{c4}^2} \underbrace{({}^e \mathbf{u}_{er} \times \mathbf{u}_{e_{rcm3D}})^T ({}^e \mathbf{u}_{er} \times \mathbf{u}_{e_{rcm3D}})}_{=1} \end{bmatrix}.
\end{aligned} \tag{3.35}$$

The element (3,1) of the latter matrix is null because the resultant from the cross-product of the term $({}^e \mathbf{u}_{er} \times \mathbf{u}_{erm3D})$ is perpendicular on the vector ${}^e \mathbf{u}_{er}$, then the dot product of the term $({}^e \mathbf{u}_{er} \times \mathbf{u}_{erm3D})^T {}^e \mathbf{u}_{er}$ is null. This case is similar to the elements (4,2), (1,3), (4,3) and (3,4). Since the vectors in the latter matrix are unit-vectors, then their dot product with themselves are equal to one, as the elements (1,1), (2,2), (3,3) and (4,4). Recall that the scalars $n_{c3} = n_{c4} = \sqrt{\|{}^e \mathbf{er}\|^2 + 1}$, then the element (3,3) is simplified to $\frac{\|{}^e \mathbf{er}\|^2 + 1}{n_{c3}^2} = 1$, and the element (4,4) is also simplified to $\frac{\|{}^e \mathbf{er}\|^2 + 1}{n_{c4}^2} = 1$. This completes the proof by obtaining the identity matrix for the latter condition. \square

1-Dimensional RCM angular error:

Choice of error: The previous 3-dimensional misalignment error (3.8) imposes three equations to formulate the RCM movement. Indeed, the dimension of the interaction matrix \mathbf{L}_{erm3D} is 3×6 which implies that there are three equations to find out the six variables in (3.20). It means that the three equations constrain the three components of linear velocity of the end-effector, while the three components of angular velocity of the end-effector are free to be chosen.

The form (3.36) reduces the dimension of (3.20) to one. It offers the advantage to liberate more DOF that will be used later to satisfy another task (e.g., the path following task). The following 1-dimensional RCM angular error is thus formulated as [Dahroug et al., 2017b]:

$$e_{rcm1D} = 1 - {}^e \mathbf{y}^T {}^e \mathbf{u}_{er}. \quad (3.36)$$

The new formulation offers a numerical stability compared to the previous one. In case that the vector \mathbf{u}_{erm3D} tends to zero, its direction becomes numerically ill-defined, where its sign could oscillate between positive and negative values. This behaviour is eliminated with the new formulation of the RCM angular error because the e_{rcm1D} is always positive (FIGURE 3.14 compared to FIGURE 3.10). Note that this dot product in (3.36) could be reformulated as:

$$e_{rcm1D} = 1 - (\|{}^e \mathbf{y}\| \|{}^e \mathbf{u}_{er}\| \cos(\theta)). \quad (3.37)$$

FIGURE 3.14 shows that the e_{rcm1D} is positive when the angle varies $-\pi \leq \theta \leq \pi$. This graph is also obtained by fixing $\|{}^e \mathbf{u}_{er}\| = 1$ in the latter equation. The amplitude of e_{rcm1D} is reduced when the $\|{}^e \mathbf{u}_{er}\|$ is decreased.

Differential kinematics of the error: The time-derivative of misalignment error (3.36) between the tool centre line and the trocar point is evaluated as:

$$\dot{e}_{rcm1D} = - {}^e \mathbf{y}^T {}^e \dot{\mathbf{u}}_{er}. \quad (3.38)$$

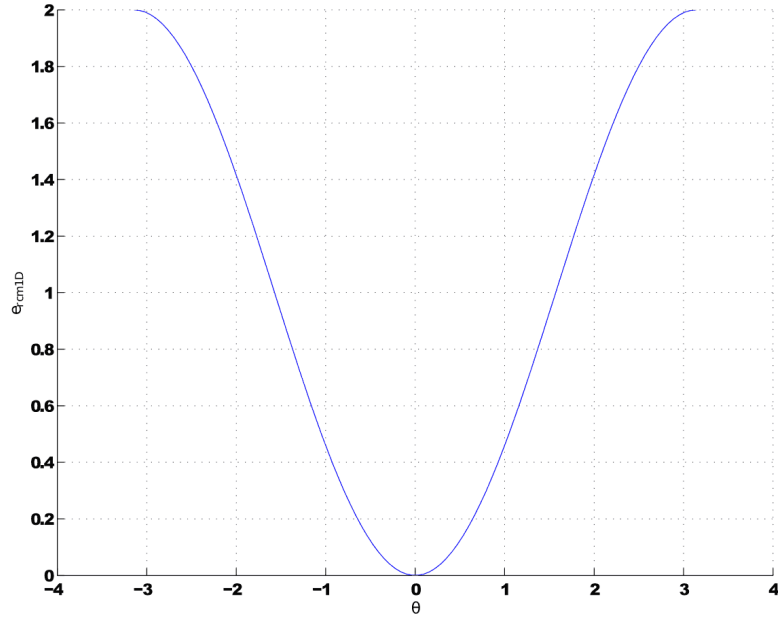


FIGURE 3.14: The relation between the 1D RCM angular error and the angle θ which is defined between the vectors ${}^e\mathbf{y}$ and ${}^e\mathbf{u}_{er}$.

By substituting the unit-vector ${}^e\dot{\mathbf{u}}_{er}$ of (3.19) in the latter equation (3.38), the time-derivative of misalignment error is reformulated as:

$$\dot{e}_{rcm1D} = \underbrace{-{}^e\mathbf{y}^T \mathbf{L}_{u_r}}_{\mathbf{L}_{e_{rcm1D}}} {}^e\mathbf{v}_e \quad (3.39)$$

whereby ($\mathbf{L}_{e_{rcm1D}} \in \mathbb{R}^{1 \times 6}$) is the interaction matrix of the misalignment error.

Control of the error: A proportional controller is also used to deduce the control twist velocity of end-effector as:

$$\begin{aligned} \dot{e}_{rcm1D} &= -\lambda e_{rcm1D}, \\ \mathbf{L}_{e_{rcm1D}} {}^e\mathbf{v}_e &= -\lambda e_{rcm1D}, \end{aligned} \quad (3.40)$$

$${}^e\mathbf{v}_e = -\lambda e_{rcm1D} \mathbf{L}_{e_{rcm1D}}^\dagger. \quad (3.41)$$

Such a controller will reduce the error e_{rcm1D} exponentially. A numerical estimation could be done to invert the interaction matrix $\mathbf{L}_{e_{rcm1D}}$.

Compute the kernel of the interaction matrix: An analytical method is carried out to determine the kernel of $\mathbf{L}_{e_{rcm1D}}$ which is computed as:

$$\ker(\mathbf{L}_{e_{rcm1D}}) = \begin{bmatrix} {}^e\mathbf{u}_{er} & {}^e\mathbf{y} \times {}^e\mathbf{u}_{er} & \mathbf{0}_{3 \times 1} & \mathbf{0}_{3 \times 1} & \frac{\|{}^e\mathbf{er}\|}{n_{c5}} ({}^e\mathbf{u}_{er} \times ({}^e\mathbf{y} \times {}^e\mathbf{u}_{er})) \\ \mathbf{0}_{3 \times 1} & \mathbf{0}_{3 \times 1} & {}^e\mathbf{u}_{er} \times ({}^e\mathbf{y} \times {}^e\mathbf{u}_{er}) & {}^e\mathbf{u}_{er} & \frac{1}{n_{c5}} ({}^e\mathbf{y} \times {}^e\mathbf{u}_{er}) \end{bmatrix}. \quad (3.42)$$

Where $\ker(\mathbf{L}_{e_{rcm1D}}) \in \mathbb{R}^{6 \times 5}$, (n_{c5}) is the Euclidean norm of the fifth column of the kernel matrix.

This norm is determined as:

$$\begin{aligned} n_{c5} &= \sqrt{\|{}^e\mathbf{er}\|^2 \underbrace{({}^e\mathbf{u}_{er} \times ({}^e\mathbf{y} \times {}^e\mathbf{u}_{er}))^T ({}^e\mathbf{u}_{er} \times ({}^e\mathbf{y} \times {}^e\mathbf{u}_{er}))}_{=1} + \underbrace{({}^e\mathbf{y} \times {}^e\mathbf{u}_{er})^T ({}^e\mathbf{y} \times {}^e\mathbf{u}_{er})}_{=1}} \\ &= \sqrt{\|{}^e\mathbf{er}\|^2 + 1}. \end{aligned} \quad (3.43)$$

Proof of the analytical kernel matrix: The first column of (3.42) multiplied by $\mathbf{L}_{e_{rcm1D}}$, then the resultant is:

$$\begin{aligned} \mathbf{L}_{e_{rcm1D}} \begin{bmatrix} {}^e\mathbf{u}_{er} \\ \mathbf{0}_{3 \times 1} \end{bmatrix} &= \frac{1}{\|{}^e\mathbf{er}\|} {}^e\mathbf{y}^T (\mathbf{I} - {}^e\mathbf{u}_{er} {}^e\mathbf{u}_{er}^T) [\mathbf{I} - [{}^e\mathbf{er}]_{\times}] \begin{bmatrix} {}^e\mathbf{u}_{er} \\ \mathbf{0}_{3 \times 1} \end{bmatrix} \\ &= \frac{1}{\|{}^e\mathbf{er}\|} {}^e\mathbf{y}^T (\mathbf{I} - {}^e\mathbf{u}_{er} {}^e\mathbf{u}_{er}^T) ({}^e\mathbf{u}_{er} + \mathbf{0}) \\ &= \frac{-1}{\|{}^e\mathbf{er}\|} {}^e\mathbf{y}^T ({}^e\mathbf{u}_{er} - \underbrace{{}^e\mathbf{u}_{er} {}^e\mathbf{u}_{er}^T {}^e\mathbf{u}_{er}}_{=\|{}^e\mathbf{u}_{er}\|^2=1}) \\ &= \frac{1}{\|{}^e\mathbf{er}\|} {}^e\mathbf{y}^T \underbrace{({}^e\mathbf{u}_{er} - {}^e\mathbf{u}_{er})}_{=0} = \mathbf{0}. \end{aligned} \quad (3.44)$$

Recall that a scalar triple product is evaluated as:

$$\mathbf{a} \cdot (\mathbf{b} \times \mathbf{c}) = \mathbf{b} \cdot (\mathbf{c} \times \mathbf{a}) = \mathbf{c} \cdot (\mathbf{a} \times \mathbf{b}). \quad (3.45)$$

The second column of (3.42) multiplied by $\mathbf{L}_{e_{rcm1D}}$, then the resultant is:

$$\begin{aligned}
\mathbf{L}_{e_{rcm1D}} \begin{bmatrix} {}^e\mathbf{y} \times {}^e\mathbf{u}_{er} \\ \mathbf{0}_{3 \times 1} \end{bmatrix} &= \frac{1}{\|{}^e\mathbf{er}\|} {}^e\mathbf{y}^T (\mathbf{I} - {}^e\mathbf{u}_{er} {}^e\mathbf{u}_{er}^T) [\mathbf{I} - [{}^e\mathbf{er}]_{\times}] \begin{bmatrix} {}^e\mathbf{y} \times {}^e\mathbf{u}_{er} \\ \mathbf{0}_{3 \times 1} \end{bmatrix} \\
&= \frac{1}{\|{}^e\mathbf{er}\|} {}^e\mathbf{y}^T (\mathbf{I} - {}^e\mathbf{u}_{er} {}^e\mathbf{u}_{er}^T) ({}^e\mathbf{y} \times {}^e\mathbf{u}_{er} + \mathbf{0}) \\
&= \frac{1}{\|{}^e\mathbf{er}\|} {}^e\mathbf{y}^T \left({}^e\mathbf{y} \times {}^e\mathbf{u}_{er} - \underbrace{{}^e\mathbf{u}_{er} {}^e\mathbf{u}_{er}^T ({}^e\mathbf{y} \times {}^e\mathbf{u}_{er})}_{= {}^e\mathbf{u}_{er} \cdot ({}^e\mathbf{y} \times {}^e\mathbf{u}_{er})} \right) \\
&= \frac{1}{\|{}^e\mathbf{er}\|} {}^e\mathbf{y}^T \left({}^e\mathbf{y} \times {}^e\mathbf{u}_{er} - \underbrace{{}^e\mathbf{u}_{er} \underbrace{{}^e\mathbf{u}_{er} \cdot ({}^e\mathbf{y} \times {}^e\mathbf{u}_{er})}_{= {}^e\mathbf{y} \cdot ({}^e\mathbf{u}_{er} \times {}^e\mathbf{u}_{er})}}_{=0} \right) \\
&= \frac{1}{\|{}^e\mathbf{er}\|} \underbrace{{}^e\mathbf{y}^T ({}^e\mathbf{y} \times {}^e\mathbf{u}_{er})}_{= {}^e\mathbf{y} \cdot ({}^e\mathbf{y} \times {}^e\mathbf{u}_{er})} \\
&= \frac{1}{\|{}^e\mathbf{er}\|} {}^e\mathbf{u}_{er} \cdot \underbrace{({}^e\mathbf{y} \times {}^e\mathbf{y})}_{=0} = \mathbf{0}.
\end{aligned} \tag{3.46}$$

The third column of (3.42) multiplied by $\mathbf{L}_{e_{rcm1D}}$, which gives:

$$\begin{aligned}
\mathbf{L}_{e_{rcm1D}} \begin{bmatrix} {}^e\mathbf{u}_{er} \times ({}^e\mathbf{y} \times {}^e\mathbf{u}_{er}) \\ \mathbf{0}_{3 \times 1} \end{bmatrix} &= \frac{1}{\|{}^e\mathbf{er}\|} {}^e\mathbf{y}^T (\mathbf{I} - {}^e\mathbf{u}_{er} {}^e\mathbf{u}_{er}^T) [\mathbf{I} - [{}^e\mathbf{er}]_{\times}] \begin{bmatrix} {}^e\mathbf{u}_{er} \times ({}^e\mathbf{y} \times {}^e\mathbf{u}_{er}) \\ \mathbf{0}_{3 \times 1} \end{bmatrix} \\
&= \frac{1}{\|{}^e\mathbf{er}\|} {}^e\mathbf{y}^T (\mathbf{I} - {}^e\mathbf{u}_{er} {}^e\mathbf{u}_{er}^T) \left(\mathbf{0} + \left(\underbrace{({}^e\mathbf{er} \times {}^e\mathbf{u}_{er})}_{=0} \times ({}^e\mathbf{y} \times {}^e\mathbf{u}_{er}) \right) \right) \\
&= \mathbf{0}.
\end{aligned} \tag{3.47}$$

The fourth column of (3.42) multiplied by $\mathbf{L}_{e_{rcm1D}}$, which provides:

$$\begin{aligned}
\mathbf{L}_{e_{rcm1D}} \begin{bmatrix} \mathbf{0}_{3 \times 1} \\ e_{\mathbf{u}_{er}} \end{bmatrix} &= \frac{1}{\|e_{\mathbf{er}}\|} e_{\mathbf{y}}^T (\mathbf{I} - e_{\mathbf{u}_{er}} e_{\mathbf{u}_{er}}^T) [\mathbf{I} - [e_{\mathbf{er}}]_{\times}] \begin{bmatrix} \mathbf{0}_{3 \times 1} \\ e_{\mathbf{u}_{er}} \end{bmatrix} \\
&= \frac{1}{\|e_{\mathbf{er}}\|} e_{\mathbf{y}}^T (\mathbf{I} - e_{\mathbf{u}_{er}} e_{\mathbf{u}_{er}}^T) (\mathbf{0} + e_{\mathbf{u}_{er}}) \\
&= \frac{-1}{\|e_{\mathbf{er}}\|} e_{\mathbf{y}}^T (e_{\mathbf{u}_{er}} - \underbrace{e_{\mathbf{u}_{er}} e_{\mathbf{u}_{er}}^T e_{\mathbf{u}_{er}}}_{=\|e_{\mathbf{u}_{er}}\|^2=1}) \\
&= \frac{1}{\|e_{\mathbf{er}}\|} e_{\mathbf{y}}^T \underbrace{(e_{\mathbf{u}_{er}} - e_{\mathbf{u}_{er}})}_{=0} = \mathbf{0}.
\end{aligned} \tag{3.48}$$

The fifth column of (3.42) multiplied by $\mathbf{L}_{e_{rcm1D}}$, which equals:

$$\begin{aligned}
\mathbf{L}_{e_{rcm1D}} \begin{bmatrix} \frac{\|e_{\mathbf{er}}\|}{n_{c5}} (e_{\mathbf{u}_{er}} \times (e_{\mathbf{y}} \times e_{\mathbf{u}_{er}})) \\ \frac{1}{n_{c5}} (e_{\mathbf{y}} \times e_{\mathbf{u}_{er}}) \end{bmatrix} \\
&= \frac{1}{\|e_{\mathbf{er}}\| n_{c5}} e_{\mathbf{y}}^T (\mathbf{I} - e_{\mathbf{u}_{er}} e_{\mathbf{u}_{er}}^T) [\mathbf{I} - [e_{\mathbf{er}}]_{\times}] \begin{bmatrix} \|e_{\mathbf{er}}\| e_{\mathbf{u}_{er}} \times (e_{\mathbf{y}} \times e_{\mathbf{u}_{er}}) \\ e_{\mathbf{y}} \times e_{\mathbf{u}_{er}} \end{bmatrix} \\
&= \frac{1}{\|e_{\mathbf{er}}\| n_{c5}} e_{\mathbf{y}}^T (\mathbf{I} - e_{\mathbf{u}_{er}} e_{\mathbf{u}_{er}}^T) \left(\underbrace{\|e_{\mathbf{er}}\| e_{\mathbf{u}_{er}}}_{=e_{\mathbf{er}}} \times (e_{\mathbf{y}} \times e_{\mathbf{u}_{er}}) - e_{\mathbf{er}} \times (e_{\mathbf{y}} \times e_{\mathbf{u}_{er}}) \right) \\
&= \mathbf{0}.
\end{aligned} \tag{3.49}$$

This completes the proof of the kernel matrix. The last check test is to verify that:

$$ker(\mathbf{L}_{e_{rcm1D}})^T ker(\mathbf{L}_{e_{rcm1D}}) = \mathbf{I}_{5 \times 5}, \tag{3.50}$$

$$\begin{bmatrix} e_{\mathbf{u}_{er}}^T & \mathbf{0}_{3 \times 1}^T \\ (e_{\mathbf{y}} \times e_{\mathbf{u}_{er}})^T & (e_{\mathbf{u}_{er}} \times (e_{\mathbf{y}} \times e_{\mathbf{u}_{er}}))^T \\ \mathbf{0}_{3 \times 1}^T & e_{\mathbf{u}_{er}}^T \\ \frac{\|e_{\mathbf{er}}\|}{n_{c5}} (e_{\mathbf{u}_{er}} \times (e_{\mathbf{y}} \times e_{\mathbf{u}_{er}}))^T & \frac{1}{n_{c5}} (e_{\mathbf{y}} \times e_{\mathbf{u}_{er}})^T \end{bmatrix} \begin{bmatrix} e_{\mathbf{u}_{er}} & e_{\mathbf{y}} \times e_{\mathbf{u}_{er}} & \mathbf{0}_{3 \times 1} & \mathbf{0}_{3 \times 1} \frac{\|e_{\mathbf{er}}\|}{n_{c5}} (e_{\mathbf{u}_{er}} \times (e_{\mathbf{y}} \times e_{\mathbf{u}_{er}})) \\ \mathbf{0}_{3 \times 1} & \mathbf{0}_{3 \times 1} & e_{\mathbf{u}_{er}} \times (e_{\mathbf{y}} \times e_{\mathbf{u}_{er}}) & e_{\mathbf{u}_{er}} \frac{1}{n_{c5}} (e_{\mathbf{y}} \times e_{\mathbf{u}_{er}}) \end{bmatrix} = \mathbf{I}_{rcm1D}. \tag{3.51}$$

In fact, the latter check test is similar to (3.35). For instance, the element (4,1) of \mathbf{I}_{rcm1D} is computed as:

$$\frac{\|e_{\mathbf{er}}\|}{n_{c5}} (e_{\mathbf{u}_{er}} \times (e_{\mathbf{y}} \times e_{\mathbf{u}_{er}}))^T e_{\mathbf{u}_{er}} + \mathbf{0}. \tag{3.52}$$

The resultant vector from the term $(e_{\mathbf{u}_{er}} \times (e_{\mathbf{y}} \times e_{\mathbf{u}_{er}}))$ is perpendicular to the vector $e_{\mathbf{u}_{er}}$, thus the dot product is null. Recall that $n_{c5} = \sqrt{\|e_{\mathbf{er}}\|^2 + 1}$, then the

element (4,4) of \mathbf{I}_{rcm1D} is evaluated as:

$$\begin{aligned} & \frac{\|{}^e \mathbf{er}\|^2}{n_{c5}^2} \underbrace{({}^e \mathbf{u}_{er} \times ({}^e \mathbf{y} \times {}^e \mathbf{u}_{er}))^T ({}^e \mathbf{u}_{er} \times ({}^e \mathbf{y} \times {}^e \mathbf{u}_{er}))}_{=1} + \frac{1}{n_{c5}^2} \underbrace{({}^e \mathbf{y} \times {}^e \mathbf{u}_{er})^T ({}^e \mathbf{y} \times {}^e \mathbf{u}_{er})}_{=1} = \\ & \frac{\|{}^e \mathbf{er}\|^2 + 1}{n_{c5}^2} = 1. \end{aligned} \quad (3.53)$$

This completes the proof. \square

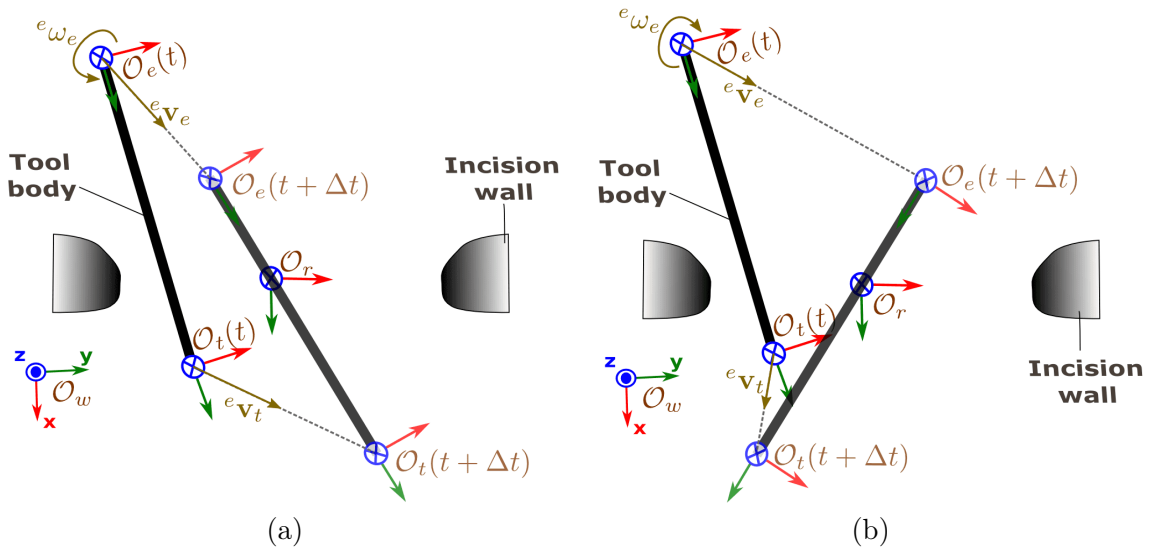


FIGURE 3.15: Examples of the geometry of the RCM movements, where the desired tool tip velocity ${}^e \mathbf{v}_t$ goes in (a) the right direction, or (b) the left direction.

Geometrical solution when the tool is inside the incision hole: Throughout such situation, the tool tip should be capable to move in any direction within a cavity according to a desired velocity. Beside that the tool centre line should also be coincident with the centre point of the incision hole. FIGURE 3.15 demonstrates the tool movements to achieve the desired velocity under the RCM constraints, where the tool should execute the desired velocity \mathbf{v}_t while correcting the misalignment error with the incision point \mathcal{O}_r . Thus, this paragraph shows how to deduce the control twist vector ${}^e \underline{\mathbf{v}}_e$ in a geometric way for performing such a constrained motion.

The surgeon defines the required linear velocity of the tool tip (\mathbf{v}_t). Then, this velocity can be expressed with respect to any desired frame. The end-effector frame is chosen because it is required to deduce the control twist vector ${}^e \underline{\mathbf{v}}_e$. Thus, the tool tip velocity expressed with respect to the end-effector frame (${}^e \mathbf{v}_{t/e}$) is defined as:

$${}^e \mathbf{v}_{t/e} = {}^e \mathbf{v}_e + {}^e \omega_e \times {}^e \mathbf{et}. \quad (3.54)$$

Recall that the relative velocity of the incision point with respect to the end-effector was defined in (3.17) as:

$${}^e\mathbf{v}_{r/e} = {}^e\mathbf{v}_e + {}^e\omega_e \times {}^e\mathbf{er}. \quad (3.55)$$

It is required to relate between ${}^e\mathbf{v}_{t/e}$ and ${}^e\mathbf{v}_{r/e}$. Thereby, the linear velocity of the incision hole is reformulated by replacing the end-effector velocity ${}^e\mathbf{v}_e$ in the latter equation by that comes from (3.54). This reformulation is represented as:

$${}^e\mathbf{v}_{r/e} = {}^e\mathbf{v}_{t/e} + {}^e\omega_e \times \underbrace{{}^e\mathbf{er} - {}^e\mathbf{et}}_{= {}^e\mathbf{tr}} \quad (3.56)$$

whereby (${}^e\mathbf{tr}$) is the distance vector from the tool tip frame \mathcal{O}_t to the RCM frame \mathcal{O}_t , and it is expressed in the end-effector frame.

Although, the RCM constraints permit a linear motion along the y -component of end-effector frame, while the angular velocity is free. Therefore, the linear velocity of RCM frame must satisfy the following condition [Dahroug et al., 2017a]:

$$\boxed{{}^e\mathbf{v}_{r/e} = -\gamma_{rot} {}^e\mathbf{y}} \quad (3.57)$$

The term (γ_{rot}) is a positive scalar factor for increasing or decreasing the velocity along the y -axis of the end-effector frame. The negative sign appeared in the latter equation because the velocity of the incision point ${}^e\mathbf{v}_{r/e}$ has an opposite direction to the end-effector velocity ${}^e\mathbf{v}_e$. In other words, if we observe the tool motion from a global view (world frame, see FIGURE 3.15), we can consider that the incision frame is fixed in the space, while the end-effector frame is moving with a certain velocity vector toward the incision frame. However, we can assume an opposite view where the end-effector frame is fixed, while the incision frame is moving with a certain velocity (i.e., the same magnitude of the previous case but in opposite direction) toward the end-effector frame. This is why the negative sign is added to (3.57).

By equating both (3.56) and (3.57), the angular velocity of end-effector could be deduced as:

$${}^e\mathbf{v}_{t/e} + {}^e\omega_e \times {}^e\mathbf{tr} = -\gamma_{rot} {}^e\mathbf{y}, \quad (3.58)$$

$${}^e\omega_e \times {}^e\mathbf{tr} = -\underbrace{({}^e\mathbf{v}_{t/e} + \gamma_{rot} {}^e\mathbf{y})}_{= {}^e\mathbf{v}_{Res}}. \quad (3.59)$$

In case that both vector ${}^e\mathbf{tr}$ and ${}^e\mathbf{v}_{Res}$ are not perpendicular, there is not an exact solution. However, a solution can be found by projecting the velocity ${}^e\mathbf{v}_{Res}$ onto the vector ${}^e\mathbf{tr}$, as depicted in FIGURE 3.16:

$${}^e\omega_e \times {}^e\mathbf{tr} = \underbrace{(\mathbf{I}_{3 \times 3} - \frac{{}^e\mathbf{tr} {}^e\mathbf{tr}^T}{\|{}^e\mathbf{tr}\|^2})}_{= {}^e\mathbf{v}_{Res}^\perp} {}^e\mathbf{v}_{Res}, \quad (3.60)$$

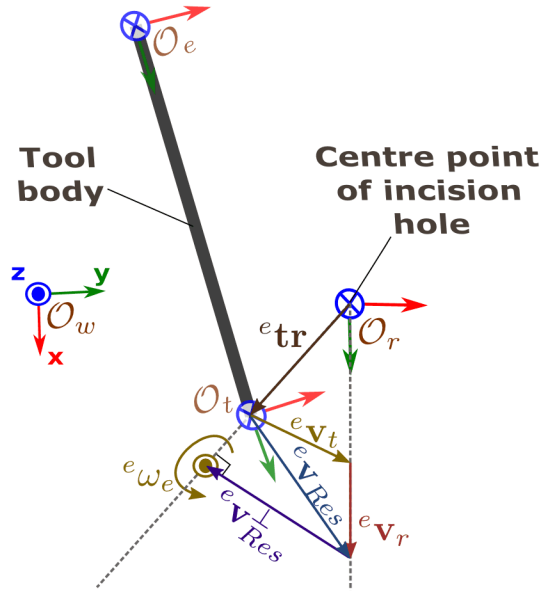


FIGURE 3.16: Geometric representation to deduce the end-effector angular velocity.

with the assumption that the angular velocity of end-effector equals to:

$${}^e\omega_e = \frac{{}^e\mathbf{tr} \times {}^e\mathbf{v}_{Res}}{\|{}^e\mathbf{tr}\|^2} + \mu {}^e\mathbf{tr}. \quad (3.61)$$

The second term in the right hand side of equation (3.61) is an additional component to represent the tool rotation around its centre line (i.e., the y -axis), where μ is a gain parameter for increasing or decreasing the weight factor of this rotation. This term can be neglected in case that the surgical tool (e.g., a laser or ultrasound ablation tools) used by the surgeon not required this additional DOF. This term is also neglected to simplify the calculation.

In order to verify that the previous assumption of the end-effector angular velocity (3.61) is good, the assumed velocity vector of (3.61) multiplied by the vector ${}^e\mathbf{tr}$ must be equal to the left hand side of (3.59). This check test is formulated as:

$$\begin{aligned} {}^e\omega \times {}^e\mathbf{tr} &= \frac{{}^e\mathbf{tr} \times {}^e\mathbf{v}_{Res}}{\|{}^e\mathbf{tr}\|^2} \times {}^e\mathbf{tr} \\ &= \frac{1}{\|{}^e\mathbf{tr}\|^2} [({}^e\mathbf{v}_{t/e} + \gamma_{rot} {}^e\mathbf{y}) \times {}^e\mathbf{tr}] \times {}^e\mathbf{tr} \\ &= \frac{-1}{\|{}^e\mathbf{tr}\|^2} \underbrace{{}^e\mathbf{tr}}_a \times \left[\underbrace{({}^e\mathbf{v}_{t/e} + \gamma_{rot} {}^e\mathbf{y}) \times {}^e\mathbf{tr}}_b \right] \times \underbrace{{}^e\mathbf{tr}}_c. \end{aligned} \quad (3.62)$$

Recall that a vector triple product could be evaluated as:

$$\mathbf{a} \times (\mathbf{b} \times \mathbf{c}) = \mathbf{a}\mathbf{c}^T\mathbf{b} + \mathbf{b}\mathbf{a}^T\mathbf{c}. \quad (3.63)$$

By applying the previous formula, the equation (3.62) is redefined as:

$$\begin{aligned} {}^e\omega_e \times {}^e\mathbf{tr} &= \frac{-1}{\|{}^e\mathbf{tr}\|^2} \left[{}^e\mathbf{tr} {}^e\mathbf{tr}^T ({}^e\mathbf{v}_t + \gamma_{rot} {}^e\mathbf{y}) + ({}^e\mathbf{v}_t + \gamma_{rot} {}^e\mathbf{y}) \underbrace{{}^e\mathbf{tr}^T {}^e\mathbf{tr}}_{=\|{}^e\mathbf{tr}\|^2} \right] \\ &= \frac{-1}{\|{}^e\mathbf{tr}\|^2} {}^e\mathbf{tr} {}^e\mathbf{tr}^T ({}^e\mathbf{v}_t + \gamma_{rot} {}^e\mathbf{y}) - ({}^e\mathbf{v}_t + \gamma_{rot} {}^e\mathbf{y}). \end{aligned} \quad (3.64)$$

The first term in the right hand side of (3.64) should be eliminated in order to achieve the equality between both equations (3.64) and (3.59). As a result, this term should be null as:

$${}^e\mathbf{tr}^T ({}^e\mathbf{v}_t + \gamma_{rot} {}^e\mathbf{y}) = 0 \quad (3.65)$$

Consequently, the gain factor γ_{rot} is defined, to satisfy the latter condition, as:

$${}^e\mathbf{tr}^T {}^e\mathbf{v}_t + \gamma_{rot} {}^e\mathbf{tr}^T {}^e\mathbf{y} = 0 \quad (3.66)$$

$$\gamma_{rot} = -\frac{{}^e\mathbf{v}_t^T {}^e\mathbf{tr}}{{}^e\mathbf{y}^T {}^e\mathbf{tr}} \quad (3.67)$$

By replacing (3.67) in (3.64), it becomes as:

$$\begin{aligned} {}^e\omega_e \times {}^e\mathbf{tr} &= \frac{-1}{\|{}^e\mathbf{tr}\|^2} \left(\underbrace{{}^e\mathbf{tr} {}^e\mathbf{tr}^T {}^e\mathbf{v}_t - \frac{{}^e\mathbf{v}_t^T {}^e\mathbf{tr}}{{}^e\mathbf{y}^T {}^e\mathbf{tr}} {}^e\mathbf{tr} {}^e\mathbf{tr}^T {}^e\mathbf{y}}_{=0} \right) - ({}^e\mathbf{v}_t + \gamma_{rot} {}^e\mathbf{y}) \\ &= -({}^e\mathbf{v}_t + \gamma_{rot} {}^e\mathbf{y}). \end{aligned} \quad (3.68)$$

Such a result proves that the assumption of ${}^e\omega_e$ (3.61) and the choice of γ_{rot} (3.67) are well done. By substituting (3.67) in (3.61), the control angular velocity of end-effector is determined. Finally, the resultant of this substitution replaces the angular velocity in (3.54) for deducing the control linear velocity of the end-effector. The control twist velocity of end-effector is thus formulated as:

$$\mathbf{v}_e = \begin{bmatrix} {}^e\mathbf{v}_e \\ {}^e\omega_e \end{bmatrix} = \begin{bmatrix} {}^e\mathbf{v}_t - {}^e\omega_e \times {}^e\mathbf{tr} \\ \frac{1}{\|{}^e\mathbf{tr}\|^2} ({}^e\mathbf{v}_t + \gamma_{rot} {}^e\mathbf{y}) \times {}^e\mathbf{tr} \end{bmatrix} \in \mathbb{R}^{6 \times 1}. \quad (3.69)$$

Differential kinematics of error: The unit-vector ${}^e\dot{\mathbf{u}}_{er}$ was calculated previously in (3.19), while the unit-vector ${}^e\dot{\mathbf{u}}_{et'}$ is deduced as:

$${}^e\dot{\mathbf{u}}_{et'} = \frac{1}{\|{}^e\dot{\mathbf{e}}\mathbf{t}'\|} [\mathbf{I}_{3 \times 3} - {}^e\mathbf{u}_{et'} {}^e\mathbf{u}_{et'}^T] {}^e\dot{\mathbf{e}}\mathbf{t}'. \quad (3.72)$$

The vector ${}^e\dot{\mathbf{e}}\mathbf{t}'$ represents the velocity of projection point ${}^e\mathbf{p}_{t'}$ along the tool shape ($\mathcal{S}_t(s_t)$) which is a function of the curve arc length (s_t). The vector ${}^e\dot{\mathbf{e}}\mathbf{t}'$ is thus evaluated as:

$${}^e\dot{\mathbf{e}}\mathbf{t}' = \frac{\partial {}^e\mathbf{e}\mathbf{t}'}{\partial s_t} \frac{ds_t}{dt} = {}^e\mathbf{k}_t \dot{s}_t \quad (3.73)$$

whereby (\dot{s}_t) is the curvilinear speed of the projected point ${}^e\mathbf{p}_{t'}$ along the tool shape, and (${}^e\mathbf{k}_t$) is the instantaneous tangential unit-vector on the tool shape.

Such a shape is approximated by the tool curvature ($\mathbf{C}_t(s_t)$) which is defined by a radius of curvature (\mathbf{r}_{C_t}) and its centre point (\mathcal{O}_{C_t}), as depicted in FIGURE 3.18, while the unit-vector ${}^e\mathbf{k}_t$ is defined by two consecutive sample points on the tool body as:

$${}^e\mathbf{k}_t = \frac{{}^e\mathbf{p}_{t_{i-1}} - {}^e\mathbf{p}_{t_i}}{\|{}^e\mathbf{p}_{t_{i-1}} - {}^e\mathbf{p}_{t_i}\|} \quad (3.74)$$

The problem now is how to deduce the curvilinear speed in equation (3.73) in order to calculate the time-derivative of the unit-vector ${}^e\mathbf{u}_{et'}$. Therefore, a reference frame is placed at the centre point \mathcal{O}_{C_t} and its basis are formed by $\{{}^e\mathbf{k}_t, {}^e\mathbf{j}_t, {}^e\mathbf{i}_t\}$, where ${}^e\mathbf{j}_t$ and ${}^e\mathbf{i}_t$ are determined as:

$${}^e\mathbf{j}_t = \frac{\mathbf{r}_{C_t}}{\|\mathbf{r}_{C_t}\|}, \quad \text{and} \quad {}^e\mathbf{i}_t = {}^e\mathbf{j}_t \times {}^e\mathbf{k}_t. \quad (3.75)$$

Thus, the radius of curvature \mathbf{r}_{C_t} is in the same direction as the basis ${}^e\mathbf{j}_t$ (FIGURE 3.18) and it is determined as:

$$\mathbf{r}_{C_t} = r_{C_t} {}^e\mathbf{j}_t, \quad \text{with} \quad r_{C_t} = \|\mathbf{r}_{C_t}\| \in \mathbb{R}^+. \quad (3.76)$$

The projected distance \mathbf{d}_{rcm} is also collinear with the basis ${}^e\mathbf{j}_t$, and it can be decomposed as:

$$\mathbf{d}_{rcm} = {}^e\mathbf{p}_{t'} - {}^e\mathcal{O}_r \quad (3.77)$$

However, the direction of vector \mathbf{d}_{rcm} can vary from that of the basis ${}^e\mathbf{j}_t$ (i.e., in the same or the opposite direction). To determine the direction sign of the vector \mathbf{d}_{rcm} with respect to the basis ${}^e\mathbf{j}_t$, it is calculated as:

$$\mathbf{d}_{rcm} = d_{rcm} {}^e\mathbf{j}_t, \quad (3.78)$$

$$\text{with} \quad d_{rcm} = \mathbf{d}_{rcm}^T {}^e\mathbf{j}_t = \frac{\mathbf{d}_{rcm}^T \mathbf{r}_{C_t}}{\|\mathbf{r}_{C_t}\|} \in \mathbb{R}. \quad (3.79)$$

Furthermore, the curvature vector $\mathbf{C}_t(s_t)$ is in the same direction as the basis \mathbf{i}_t , since:

$$\begin{aligned} \mathbf{C}_t(s_t) \times \mathbf{r}_{C_t} &= {}^e\mathbf{k}_t, \\ \text{and } \|\mathbf{C}_t(s_t)\| &= \frac{1}{\|\mathbf{r}_{C_t}\|} = C_t \in \mathbb{R}^+, \end{aligned} \quad (3.80)$$

then,

$$\mathbf{C}_t(s_t) = C_t {}^e\mathbf{i}_t. \quad (3.81)$$

Therefore, the instantaneous curvature is deduced analytically by substituting the basis \mathbf{i}_t (3.75) in the latter equation as:

$$\begin{aligned} \mathbf{C}_t(s_t) &= C_t ({}^e\mathbf{j}_t \times {}^e\mathbf{k}_t), \\ \mathbf{C}_t(s_t) &= \frac{1}{\|\mathbf{r}_{C_t}\|} \left(\frac{\mathbf{r}_{C_t}}{\|\mathbf{r}_{C_t}\|} \times {}^e\mathbf{k}_t \right), \end{aligned} \quad (3.82)$$

$$\mathbf{C}_t(s_t) = \frac{\mathbf{r}_{C_t} \times {}^e\mathbf{k}_t}{\|\mathbf{r}_{C_t}\|^2}. \quad (3.83)$$

Consider a finite displacement applied to the incision centre point \mathcal{O}_r at a velocity ${}^e\mathbf{v}_{r/e}$ during a small period Δt . In fact, the resultant displacement from the linear velocity of RCM frame $\Delta t {}^e\mathbf{v}_{r/e}$ is decomposed into (FIGURE 3.18):

- i) the first component ($\Delta t {}^e\mathbf{k}_t {}^e\mathbf{k}_t^T {}^e\mathbf{v}_{r/e}$) represents the projected component of ${}^e\mathbf{v}_{r/e}$ onto the vector ${}^e\mathbf{k}_t$ and it effects the progress of $\mathbf{p}_{t'}$ along the tool shape,
- ii) the second component ($\Delta t (\mathbf{I} - {}^e\mathbf{k}_t {}^e\mathbf{k}_t^T) {}^e\mathbf{v}_{r/e}$) is the complement of the first component and it affects the distance \mathbf{d}_{rcm} .

The first component of the linear velocity $\Delta t {}^e\mathbf{v}_{r/e}$ is thus more important than the second one, because it is used directly to deduce analytically the curvilinear speed \dot{s}_t by applying *Thales* theorem. Consequently, the second component is removed from FIGURE 3.19.

The position of projected point $\mathbf{p}_{t'}(t + \Delta t)$ is found by the intersection of the radial line passing through the vector $(\mathcal{O}_{c_t}, \mathcal{O}_r + \Delta t {}^e\mathbf{k}_t {}^e\mathbf{k}_t^T {}^e\mathbf{v}_{r/e})$, as depicted in FIGURE 3.19. Therefore, the two triangles $(\mathcal{O}_{c_t}, \mathcal{O}_r, \mathcal{O}_r + \Delta t {}^e\mathbf{k}_t {}^e\mathbf{k}_t^T {}^e\mathbf{v}_{r/e})$ and $(\mathcal{O}_{c_t}, \mathbf{p}_{t'}(t), \mathbf{p}_{t'}(t + \Delta t))$ are similar (FIGURE 3.19) under the condition that $\Delta t \ll 1$. *Thales* theorem states that:

$$\frac{\Delta t \dot{s}_t}{\Delta t {}^e\mathbf{k}_t^T {}^e\mathbf{v}_{r/e}} = \frac{\mathbf{r}_{C_t}^T {}^e\mathbf{j}_t}{{}^e\mathbf{r}_{C_t}^T \mathbf{j}_t - \mathbf{d}_{rcm}^T {}^e\mathbf{j}_t}, \quad (3.84)$$

by eliminating Δt from the left hand side of the latter equation, and from the right hand side replacing the vectors \mathbf{r}_{C_t} and \mathbf{d}_{rcm} as in (3.76) and (3.78), respectively:

$$\begin{aligned} \frac{\dot{s}_t}{{}^e\mathbf{k}_t^T {}^e\mathbf{v}_{r/e}} &= \frac{r_{C_t} {}^e\mathbf{j}_t^T {}^e\mathbf{j}_t}{r_{C_t} {}^e\mathbf{j}_t^T {}^e\mathbf{j}_t - d_{rcm} \underbrace{{}^e\mathbf{j}_t^T {}^e\mathbf{j}_t}_{=1}} \\ &= \frac{r_{C_t}}{r_{C_t} - d_{rcm}}. \end{aligned} \quad (3.85)$$

The speed along the arc length \dot{s}_t is thus deduced by multiplying the right hand side of the latter equation by the inverse of r_{C_t} as:

$$\begin{aligned}\dot{s}_t &= \frac{1}{1 - \frac{d_{rcm}}{r_{C_t}}} {}^e\mathbf{k}_t^T {}^e\mathbf{v}_{r/e} \\ &= \frac{1}{1 - d_{rcm}C_t} {}^e\mathbf{k}_t^T {}^e\mathbf{v}_{r/e}.\end{aligned}\quad (3.86)$$

The term $(d_{rcm}C_t)$ in the latter equation does not take in account the direction of the vector \mathbf{C}_t ; since $C_t = \|\mathbf{C}_t(s_t)\| \in \mathbb{R}^+$. Therefore, the magnitude of curvature C_t could be reformulated by using equation (3.81) as:

$$\begin{aligned}C_t &= \mathbf{C}_t(s_t)^T {}^e\mathbf{i}_t \\ &= \mathbf{C}_t(s_t)^T ({}^e\mathbf{j}_t \times {}^e\mathbf{k}_t) \\ &= -\mathbf{C}_t(s_t)^T ({}^e\mathbf{k}_t \times {}^e\mathbf{j}_t) \\ &= -(\mathbf{C}_t(s_t) \times {}^e\mathbf{k}_t)^T {}^e\mathbf{j}_t \in \mathbb{R}.\end{aligned}\quad (3.87)$$

By combining the latter equation with (3.79), the term $(d_{rcm}C_t)$ is redefined into:

$$\begin{aligned}d_{rcm}C_t &= -\mathbf{d}_{rcm}^T {}^e\mathbf{j}_t (\mathbf{C}_t(s_t) \times {}^e\mathbf{k}_t)^T {}^e\mathbf{j}_t \\ &= -\mathbf{d}_{rcm}^T (\mathbf{C}_t(s_t) \times {}^e\mathbf{k}_t) \underbrace{{}^e\mathbf{j}_t^T {}^e\mathbf{j}_t}_{=1} \\ &= -\mathbf{d}_{rcm}^T (\mathbf{C}_t(s_t) \times {}^e\mathbf{k}_t).\end{aligned}\quad (3.88)$$

In order to verify that the new definition of term $(d_{rcm}C_t)$ is correct, the resultant vector from the term $(\mathbf{C}_t(s_t) \times {}^e\mathbf{k}_t)$ in the latter equation has an opposite direction to the basis ${}^e\mathbf{j}_t$ and its magnitude equals to C_t . Thus, the term $(d_{rcm}C_t)$ is replaced by $(-C_t\mathbf{j}_t)$ in the latter equation, and it becomes as:

$$\begin{aligned}d_{rcm}C_t &= -d_{rcm} {}^e\mathbf{j}_t^T (-C_t\mathbf{j}_t) \\ &= d_{rcm}C_t \underbrace{{}^e\mathbf{j}_t^T {}^e\mathbf{j}_t}_{=1}.\end{aligned}\quad (3.89)$$

Such a result proves that the new definition (3.88) is good. It is then used in equation (3.86) in order to deduce the speed along the arc length \dot{s}_t as:

$$\dot{s}_t = \frac{{}^e\mathbf{k}_t^T {}^e\mathbf{v}_{r/e}}{1 + \mathbf{d}_{rcm}^T (\mathbf{C}_t(s_t) \times {}^e\mathbf{k}_t)}.\quad (3.90)$$

This solution is valid when the projected distance \mathbf{d}_{rcm} is smaller than the radius ${}^e\mathbf{r}_{C_t}$ (FIGURE 3.19) because the *Thales* theorem cannot be used directly to formulate similar triangles. Therefore, it is important to satisfy the condition that $(\mathbf{p}_{t'} \in [\mathcal{O}_r, \mathcal{O}_{C_t}])$

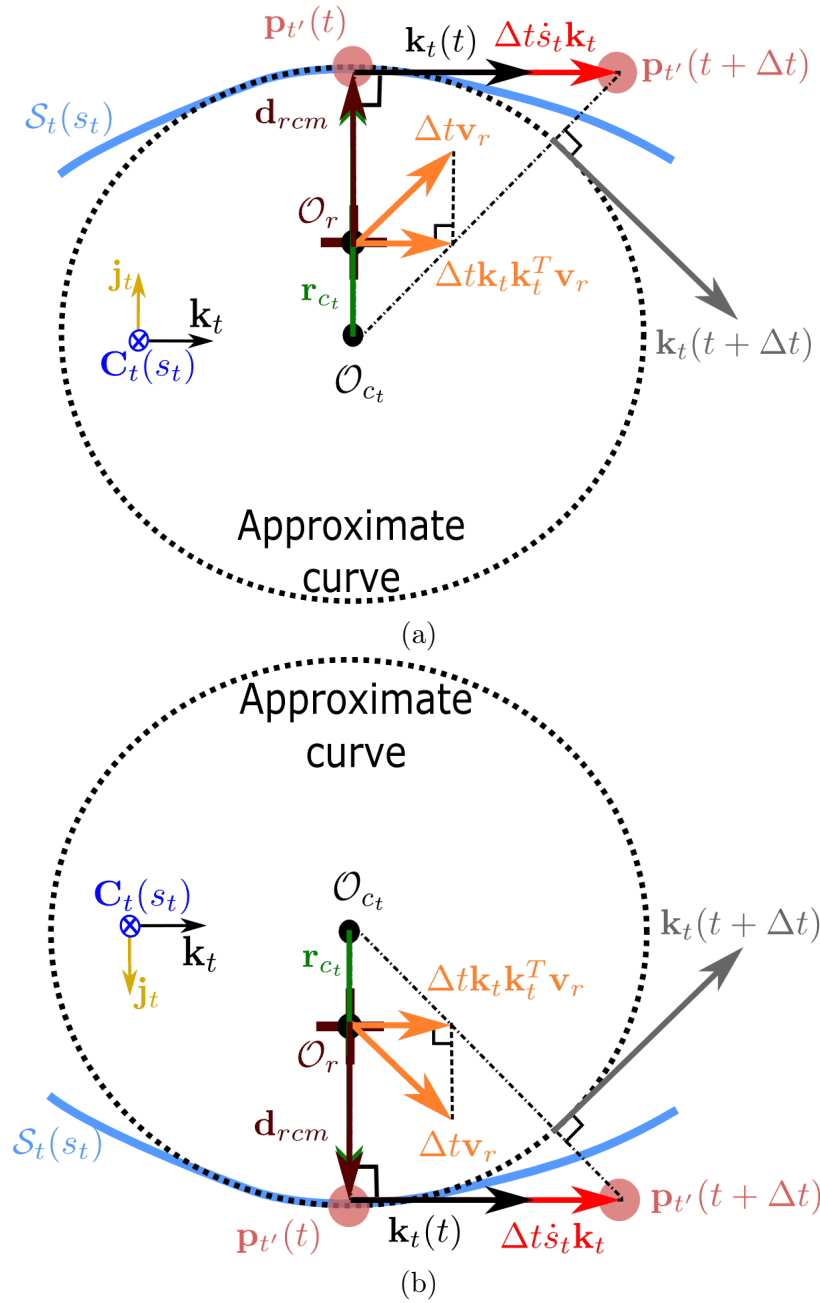


FIGURE 3.20: Zoom on the geometric description of the tool curve and the incision point \mathcal{O}_r at the instantaneous positions where: (a) the point \mathcal{O}_r is located between the two points $\mathbf{p}_{t'}$ and \mathcal{O}_{c_t} , and (b) the mirror condition of (a).

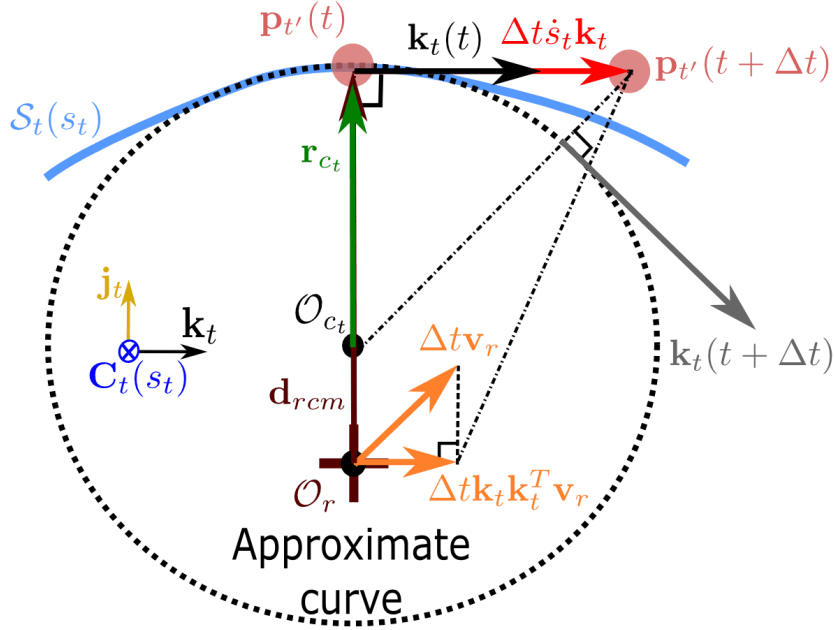


FIGURE 3.21: Zoom on the geometric description of the tool curve and the incision point \mathcal{O}_r at the instantaneous positions where the point \mathcal{O}_{C_t} is located within the segment formed between \mathcal{O}_r and $\mathbf{p}_{t'}$.

and $\mathbf{d}_{rcm} \in \mathbb{R}^-$, see FIGURE 3.19) or $(\mathcal{O}_r \in [\mathbf{p}_{t'}, \mathcal{O}_{C_t}])$ and $\mathbf{d}_{rcm} \in \mathbb{R}^+$, see FIGURE 3.20). In case that $\mathbf{d}_{rcm} = \mathbf{r}_{C_t}$, there is a numerical singularity because the right hand side of (3.85) is divided by zero. Thereby, the implementation of RCM controller should take into account this singular case.

Another special case could also occur, when $\mathcal{O}_{C_t} \in [\mathcal{O}_r, \mathbf{p}_{t'}]$ and $\mathbf{d}_{rcm} > \mathbf{r}_{C_t}$, as shown in FIGURE 3.21. There is not a simple geometric construction to find out an analytical expression for deducing the speed along the arc length \dot{s}_t during this special case; since the formulation of similar triangles cannot be identified to apply the *Thales* theorem. In fact, this special case which uses a highly curved tool is not treated with the proposed controller because it requires a specific numerical solution. As a result, it is not acceptable to use a tool with a very small curvature radius. For instance, if the vector distance \mathbf{d}_{rcm} is around $1mm$, to satisfy the special case, the curvature radius \mathbf{r}_{C_t} is less than $1mm$.

Compute the interaction matrix: After the formulation of the curvilinear speed \dot{s}_t is determined in (3.90), the velocity of projected point ${}^e \dot{\mathbf{e}}_{t'}$ is redefined by replacing (3.90) in (3.73), and it becomes equal to:

$${}^e \dot{\mathbf{e}}_{t'} = \frac{{}^e \mathbf{k}_t {}^e \mathbf{k}_t^T}{1 + \mathbf{d}_{rcm}^T (\mathbf{C}_t(s_t) \times {}^e \mathbf{k}_t)} {}^e \mathbf{v}_{r/e}. \quad (3.91)$$

From the latter equation, the speed of projected point ${}^e\dot{\mathbf{e}}\mathbf{t}'$ depends on: i) the projected distance \mathbf{d}_{rcm} , ii) tool curvature $\mathbf{C}_t(s_t)$, and iii) the velocity of RCM frame ${}^e\mathbf{v}_{r/e}$. By injecting (3.91) in (3.72), the rate of change of ${}^e\dot{\mathbf{u}}_{et'}$ is thus derived as:

$${}^e\dot{\mathbf{u}}_{et'} = \frac{1}{\|{}^e\mathbf{e}\mathbf{t}'\|} [\mathbf{I} - {}^e\mathbf{u}_{et'} {}^e\mathbf{u}_{et'}^T] \frac{{}^e\mathbf{k}_t {}^e\mathbf{k}_t^T}{1 + \mathbf{d}_{rcm}^T (\mathbf{C}_t(s_t) \times {}^e\mathbf{k}_t)} {}^e\mathbf{v}_{r/e}. \quad (3.92)$$

By replacing the linear velocity of RCM frame ${}^e\mathbf{v}_{r/e}$ by equation (3.17), the latter equation turns into:

$${}^e\dot{\mathbf{u}}_{et'} = \underbrace{\frac{1}{\|{}^e\mathbf{e}\mathbf{t}'\|} [\mathbf{I} - {}^e\mathbf{u}_{et'} {}^e\mathbf{u}_{et'}^T] \frac{{}^e\mathbf{k}_t {}^e\mathbf{k}_t^T}{1 + \mathbf{d}_{rcm}^T (\mathbf{C}_t(s_t) \times {}^e\mathbf{k}_t)}}_{\mathbf{L}_{u_{et'}}} \underbrace{[\mathbf{I} - [{}^e\mathbf{e}\mathbf{r}]_{\times}]}_{\mathbf{L}_{e_{\omega_e}}} \underbrace{\begin{bmatrix} {}^e\mathbf{v}_e \\ {}^e\omega_e \end{bmatrix}}_{{}^e\mathbf{v}_e}. \quad (3.93)$$

Finally, the rate of change of the alignment task $\dot{\mathbf{e}}_{rcm3D}$ is obtained by substituting the unit-vectors ${}^e\dot{\mathbf{u}}_{er}$ and ${}^e\dot{\mathbf{u}}_{et'}$, (3.19) and (3.93) respectively, in (3.71). The resultant is formulated as:

$$\dot{\mathbf{e}}_{rcm3D} = \underbrace{\left([{}^e\mathbf{u}_{er}]_{\times} \mathbf{L}_{u_{et'}} + [{}^e\mathbf{u}_{et'}]_{\times} \mathbf{L}_{u_{er}} \right)}_{\mathbf{L}_{e_{rcm3D}}} \underbrace{\begin{bmatrix} {}^e\mathbf{v}_e \\ {}^e\omega_e \end{bmatrix}}_{{}^e\mathbf{v}_e}. \quad (3.94)$$

Control of the error: In order to reduce exponentially the alignment task, a simple proportional controller is applied as:

$$\dot{\mathbf{e}}_{rcm3D} = \mathbf{L}_{e_{rcm3D}} {}^e\mathbf{v}_e = -\lambda \mathbf{e}_{rcm3D}. \quad (3.95)$$

The latter equation represents the alignment task with bilateral constraints which is used for a curved tool. Thereby, the control twist velocity of end-effector is determined as:

$${}^e\mathbf{v}_e = -\lambda \mathbf{L}_{e_{rcm3D}}^\dagger \mathbf{e}_{rcm3D} \quad (3.96)$$

1-Dimensional RCM angular error:

Choice of error: In a similar way, the 1-dimensional RCM error for curved tool is obtained by modifying (3.36), and it is calculated as:

$$e_{rcm1D} = 1 - {}^e\mathbf{u}_{et'}^T {}^e\mathbf{u}_{er}. \quad (3.97)$$

The time-derivative of the latter equation is formulated as:

$$\dot{e}_{rcm1D} = - \left({}^e\mathbf{u}_{et'}^T {}^e\dot{\mathbf{u}}_{er} + {}^e\dot{\mathbf{u}}_{et'}^T {}^e\mathbf{u}_{er} \right). \quad (3.98)$$

Compute the interaction matrix: By replacing the unit-vectors ${}^e\hat{\mathbf{u}}_{er}$ and ${}^e\hat{\mathbf{u}}_{et'}$ in the latter equation by (3.19) and (3.93), respectively, the time-derivative of RCM angular error is obtained as:

$$\dot{e}_{rcm1D} = - \underbrace{\left({}^e\mathbf{u}_{et'}^T \mathbf{L}_{u_{er}} + {}^e\mathbf{u}_{er}^T \mathbf{L}_{u_{et'}} \right)}_{\mathbf{L}_{e_{rcm1D}}} \underbrace{\begin{bmatrix} {}^e\mathbf{v}_e \\ {}^e\boldsymbol{\omega}_e \\ {}^e\mathbf{v}_e \end{bmatrix}}_{\mathbf{e}_{\mathbf{v}_e}}. \quad (3.99)$$

From curved tool to straight one: The previous equations are valid for curved tools. But they are also applicable for straight tools. Indeed, if the tool curvature is null ($\mathbf{C}_t(s_t) = \mathbf{0}$), which means that the tool is straight, then the unit-vector ${}^e\hat{\mathbf{u}}_{et'}$ (3.93) is

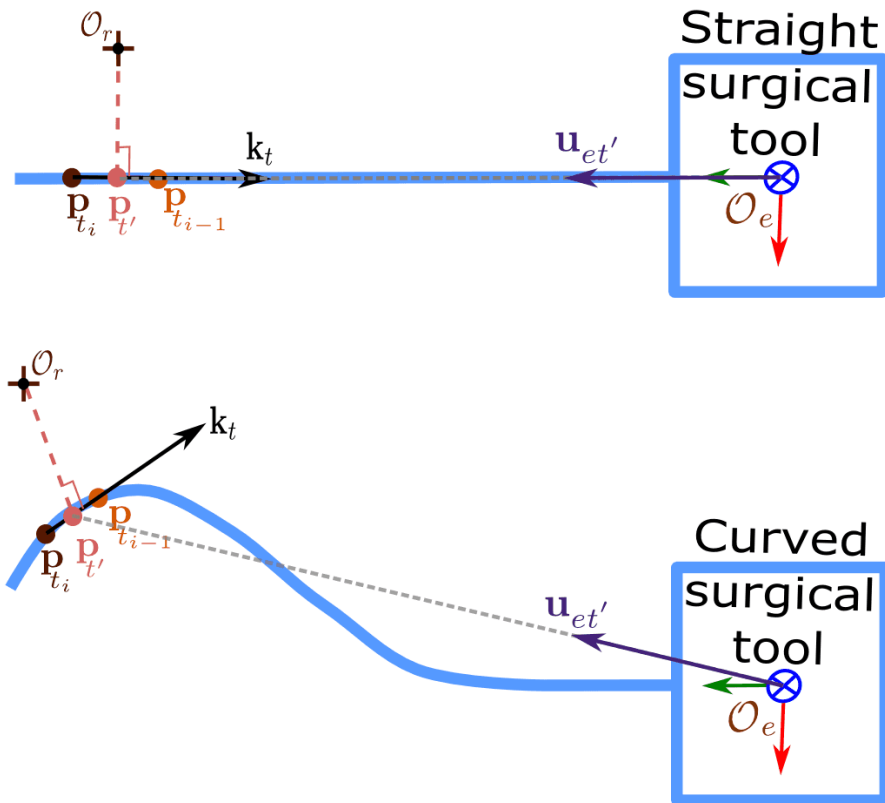


FIGURE 3.22: A comparison between the straight and curved tools.

redefined as:

$$\begin{aligned}
{}^e \dot{\mathbf{u}}_{et'} &= \frac{1}{\|{}^e \mathbf{e}t'\|} [\mathbf{I} - {}^e \mathbf{u}_{et'} {}^e \mathbf{u}_{et'}^T] {}^e \mathbf{k}_t {}^e \mathbf{k}_t^T {}^e \mathbf{v}_r \\
&= \frac{1}{\|{}^e \mathbf{e}t'\|} \left[{}^e \mathbf{k}_t {}^e \mathbf{k}_t^T {}^e \mathbf{v}_r - {}^e \mathbf{u}_{et'} \underbrace{{}^e \mathbf{u}_{et'}^T {}^e \mathbf{k}_t}_{=-1} {}^e \mathbf{k}_t^T {}^e \mathbf{v}_r \right] \\
&= \frac{1}{\|{}^e \mathbf{e}t'\|} [{}^e \mathbf{k}_t {}^e \mathbf{k}_t^T {}^e \mathbf{v}_r + {}^e \mathbf{u}_{et'} {}^e \mathbf{k}_t^T {}^e \mathbf{v}_r].
\end{aligned} \tag{3.100}$$

Since the tool is straight, then the vectors ${}^e \mathbf{k}_t$ and ${}^e \mathbf{u}_{et'}$ are parallel and in opposite direction (${}^e \mathbf{u}_{et'} = -{}^e \mathbf{k}_t$, see FIGURE 3.22). Thereby, the latter equation becomes equal to null, when replacing ${}^e \mathbf{u}_{et'} = -{}^e \mathbf{k}_t$. This implies also that the second term in the right hand side of $\dot{\mathbf{e}}_{rcm3D}$ (3.71) equals to null. The equation (3.71) is thus reduced and it becomes equal to equation (3.10). Similarly, the equation (3.98) is reduced and it becomes equivalent to equation (3.38).

3.2 Unilateral Constrained Motion

As explained previously, the RCM constraint imposes that the tool body should be coincident with the incision hole centre. If the incision hole is fixed in the world frame, then the tool motion is restricted along two axes (i.e., locally to the x - and z - axes of the incision frame, see the upper left zoom plot entitled "*Bilateral constraints*" in FIGURE 3.23). This figure shows a general scenario where the tool moves from its initial position toward the incision hole, after that the tool follows a 3D spiral path under the constraints imposed by the incision hole. The workspace inside the incision hole is represented by the blue triangle in FIGURE 3.23. A zoom was made on the incision hole in order to demonstrate the difference between the RCM and UCM movements.

The UCM movement releases the bilateral constraints on the tool motion into a unilateral constraint. The UCM constraint allows a limited linear motion along the restricted axes (i.e., the x - and z - axes of the incision frame), and the tool body can leave the incision centre point. Indeed, the linear motion is limited by the incision wall, which is represented by a horizontal line on the central zoom plot entitled "*Unilateral constraints*" at FIGURE 3.23.

Such a release is useful to gain more manoeuvrable space before the tool hits the incision wall. It is also an appropriate assumption for ear surgery, where the dimensions of the created tunnel by the standard mastoidectomy, or even the natural orifice of the external ear canal, are bigger than the surgical instrument diameter. In addition, the unilateral constraint has the advantage to potentially simplify the use of a highly curved tool during the surgery. Such a curved geometry provides the surgical tool with a higher dexterity, for instance, for avoiding obstacles as depicted at the plots on the right hand side of FIGURE 3.23 which are entitled "*Curved tool*" and "*Straight tool*".

³See sections 3.3 and 4.2 for more details about the simulator and the task priority controller, respectively.

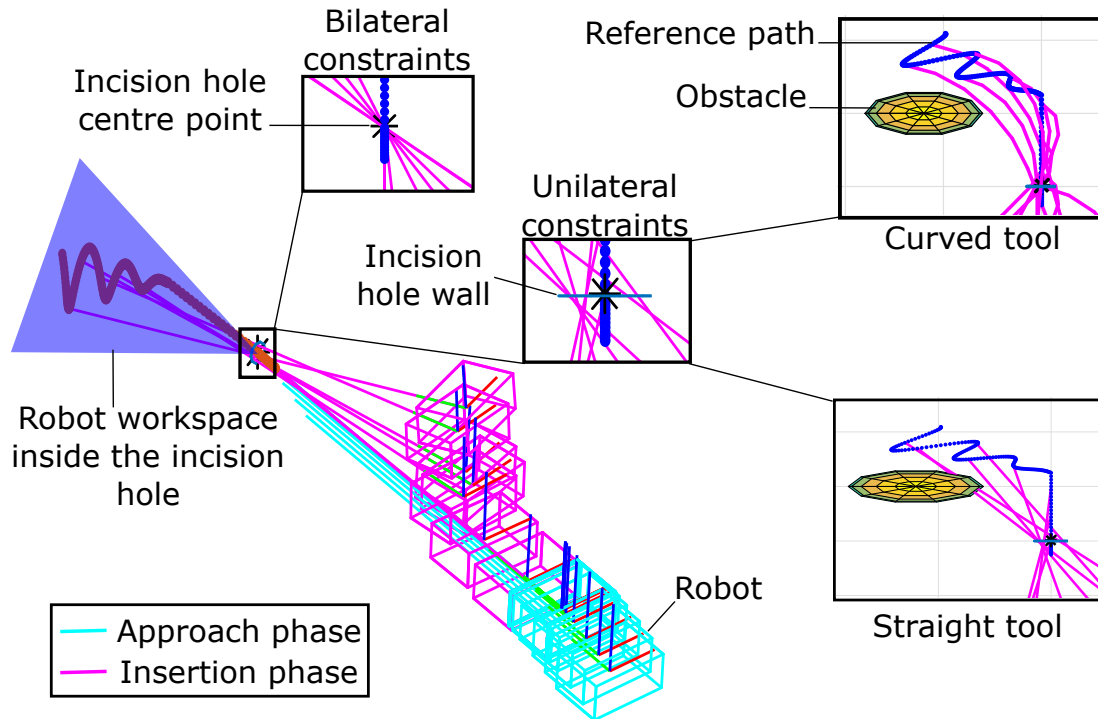


FIGURE 3.23: Simulated motion ³ for visualizing the difference between: i) bilateral and unilateral constraints, and ii) the usage of straight and curved tool.

3.2.1 Previous approaches

For solving the UCM movement, the system is considered as a non-linear optimization problem. With this assumption, the inverse problem admits either no solution, one solution or an infinite number of solutions. In the latter case, it is critical to select the optimal solution. Consequently, optimization techniques [Luenberger et al., 1984, Bertsekas, 1999] are suitable tools for imposing the required constraints and finding out the optimal solution. An instantaneous (or local) optimal solution is a convenient method for real-time application; since it needs small computation time. However, it does not guarantee the global optimal solution. Thereby, the global optimal control methods are better for off-line task planning; since they consume a large computation time.

Furthermore, the projection gradient technique [Nakamura et al., 1987, Siciliano, 1990] is a generic optimization technique which has the advantage to arrange different tasks in a hierarchical form. The authors in [Kanoun et al., 2011] used such a technique to formulate the inequality (unilateral) constraints in form of a Quadratic Programming (QP). The proposed convex function is constrained by an exterior penalty function. In the same way, the authors in [Flacco et al., 2015] developed the inequality problem as a convex QP problem which is conditioned by Karush-Kuhn-Tucker (KKT) criteria. These non-linear constrained optimization techniques are detailed in [Luenberger et al.,

1984, Bertsekas, 1999]. Such techniques are used for serial robot [Mansard and Khatib, 2008], humanoid robot [Kanoun et al., 2011] and snake-like robot [Flacco et al., 2015].

It is worth mentioning that non-medical applications (e.g., assembly manufacturing and fabrication) applied *compliant motion* control [De Schutter and Van Brussel, 1988, Kazerooni, 1989] in order to manipulate the robot end-effector in contact with its environment (environment interaction). Such a manipulation technique is needed when inserting a peg into a hole, polishing or grinding a surface, or following a contour or surface. This type of motion can be either passive or active. The passive type uses a mechanical (spring-damper) device which is added to the end-effector. However, the active type is basically achieved by a force-based feedback control [Lefebvre et al., 2005]. Such a controller can be obtained by various methods such as: hybrid force/position control [Chiaverini and Sciavicco, 1993], impedance or admittance control [Colbaugh et al., 1995]. Indeed, the impedance or admittance controls are based on the kinematic and dynamic models of the robot and the interaction with the environment. Both controllers are formulated by an equivalent mass-spring-damper system with adjustable parameters. However, the impedance control regulates the motion deviation by generating forces, while the admittance control regulates the interaction forces by imposing a deviation from the desired motion. These techniques are considered as an indirect force control because a force measurement is not applied. In opposition, the hybrid force/motion control is a sensor-based technique where a force/torque measurements are available to perform a direct force control.

The latter techniques are also applied in medical applications for defining the unilateral constraints. The term *virtual fixtures* is originally introduced by [Rosenberg, 1993] for applying the previous technique on a tele-operated robot. A comprehensive survey [Bowyer et al., 2014] was proposed to show the different techniques associated with the virtual fixtures in medical applications. The authors in [Bettini et al., 2004] applied the virtual fixtures method to constrain the robot motion in a certain direction by using an admittance control. This work was extended in [Kapoor et al., 2006] for performing incremental control on John Hopkins University (JHU) Steady Hand Robot by formulating the constrained motion as a weighted and a multi-objective optimization problem. The solution of such problem was determined by using the sequential QP method.

In brief, the unilateral constraint is an inequality problem, for instance, the distance between the tool body and the incision wall could vary from zero to a certain distance. The control of such a system is non-linear since the end-effector rotation matrix belongs to the special Euclidean group $SE(3)$ which is a non-linear space. Thus, the UCM movement could be considered as a non-linear problem under inequality constraints.

3.2.2 Proposed method

A simple solution is proposed in this part by formulating the unilateral constraint as an inequality of bilateral constraints which explained previously in Section 3.1. An admittance control is applied by placing a virtual spring between the tool body and the incision wall.

3.2.2.1 Rigid tool movement

The proposed solution in (3.94) and (3.99) describes the differential kinematics of the RCM angular error, $\dot{\mathbf{e}}_{rcm3D}$ and $\dot{\mathbf{e}}_{rcm1D}$ respectively. This description is useful to control either a straight tool or a curved one. To simplify the notation in this section, the general form of the differential RCM angular error is described as:

$$\dot{\mathbf{e}}_{rcm} = \mathbf{L}_{e_{rcm}} \mathbf{e}_{\mathbf{v}_e}. \quad (3.101)$$

A proportional controller is also proposed to reduce exponentially this error as:

$$\mathbf{L}_{e_{rcm}} \mathbf{e}_{\mathbf{v}_e} = -\lambda \mathbf{e}_{rcm}. \quad (3.102)$$

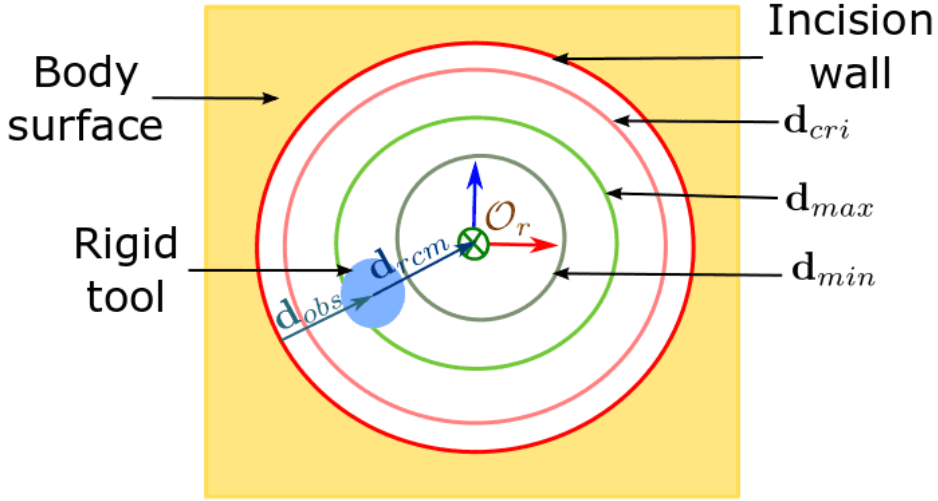


FIGURE 3.24: A geometric representation for the UCM concept.

UCM constraint based on the RCM angular error: The UCM task adds a virtual spring which is located between the tool body and the incision wall. It acts as a repulsive force to keep the tool body away from the incision wall. Therefore, the incision hole is divided into three main regions (FIGURE 3.24):

- i) a free region begins from the incision centre point O_r until a minimum distance (d_{min}). Within this region, the tool is free to move without any constraints and the virtual spring is deactivated.
- ii) a safe region begins from the minimum distance d_{min} until a maximum distance (d_{max}). Inside this region, the virtual spring is activated and its stiffness increases gradually until it reaches its maximum value at the border with the next region.
- iii) a critical region is bounded by a critical distance (d_{cri}) and the orifice wall. When the tool enters this region, the stiffness of virtual spring is the maximum in order to expel the tool from this region.

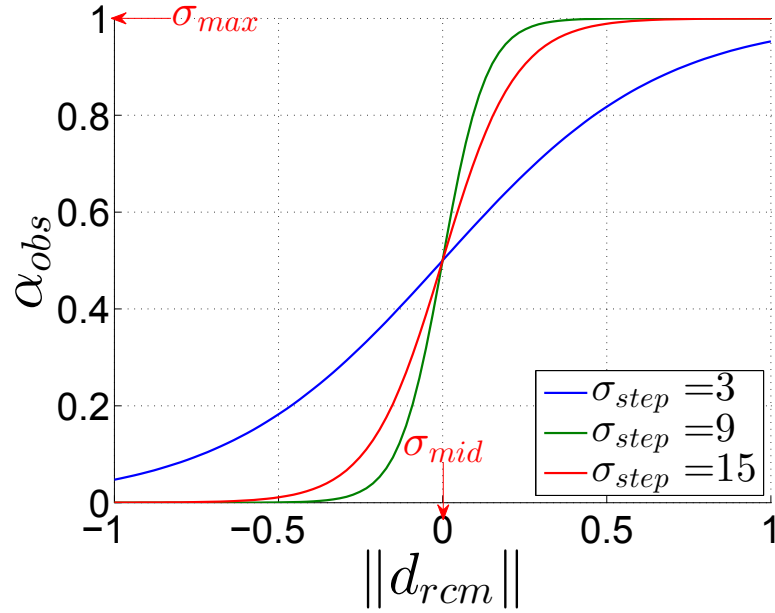


FIGURE 3.25: The sigmoid form of the virtual spring stiffness.

Such a behaviour is represented in a non-linear function (i.e., a sigmoid form as depicted in FIGURE 3.25) for obtaining a continuous differentiable characteristics. Thus the stiffness of the virtual spring (α_{obs}) is evaluated as:

$$\alpha_{obs} = \begin{cases} 0 & \|\mathbf{d}_{rcm}\| \leq d_{min} \\ \frac{\sigma_{max}}{1 + \exp(\sigma_{step}(\|\mathbf{d}_{rcm}\| - \sigma_{mid}))} & d_{min} < \|\mathbf{d}_{rcm}\| < d_{max} \\ \sigma_{max} & d_{max} \leq \|\mathbf{d}_{rcm}\| \leq d_{cri} \end{cases} . \quad (3.103)$$

In fact, the gain α_{obs} depends on the projection distance \mathbf{d}_{rcm} which is obtained as (3.6). This distance represents the linear error between the incision centre point and the tool body.

Control of UCM task: By placing the virtual spring α_{obs} in (3.102), it becomes in the following form:

$$\mathbf{L}_{e_{rcm}} \mathbf{}^e \underline{\mathbf{v}}_e = -\alpha_{obs} \lambda \mathbf{e}_{rcm}. \quad (3.104)$$

The control twist velocity is thus deduced as:

$$\mathbf{}^e \underline{\mathbf{v}}_e = -\alpha_{obs} \lambda \mathbf{L}_{e_{rcm}}^\dagger \mathbf{e}_{rcm}. \quad (3.105)$$

3.3 Numerical Simulator

An easy way to prove the concept of the proposed controller is achieved by implementing a simulator which is useful for i) visualizing the end-effector and the surgical tool movements, along side ii) the generated log files which contain important informations (e.g., the record of end-effector control velocities, the tool tip poses, etc.). In fact, the simulator allows concentrating on the fundamental developments in order to test the controller performances without including the experimental problems. Once the performances are satisfactory, the controller will be tested on a real robot ⁴.

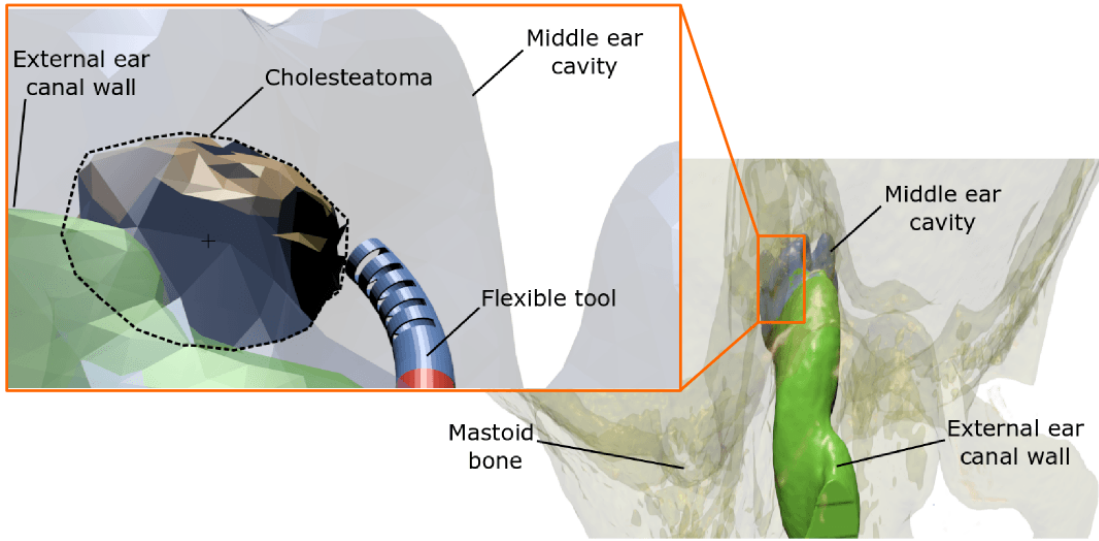


FIGURE 3.26: An example of realistic simulator, where the virtual scene is consists of: i) an auditory system with cholesteatoma which is created from DICOM images, and ii) a flexible surgical tool.

The simulator is done by a C++ program to implement the proposed controller. Indeed, the program encapsulates the different controllers (i.e., alignment controller, path following controller and task priority controller) ⁵ to deduce the control twist vector of end-effector. The simulator applies a numerical integration to calculate the new pose of the end-effector based on the control twist vector. Such a numerical integration is achieved by transforming the control twist vector into an exponential matrix and multiplying it by a sample time (T_e). Consequently, the applied velocities during the sample time are represented by the homogeneous matrix ($\Delta^e \mathbf{M}_e$) as:

$$\Delta^e \mathbf{M}_e = e^{\mathbf{B}},$$

$$\text{where } \mathbf{B} = T_e * \begin{bmatrix} [{}^e \omega_e]_{\times} & {}^e \mathbf{v}_e \\ \mathbf{0}_{1 \times 3} & 0 \end{bmatrix} \in \mathbb{R}^{4 \times 4}. \quad (3.106)$$

⁴See Section 4.4 for more details about the experimental validation which is conducted by a real robot.

⁵See Section 4.3 for more details about the simple simulator with the complete controller.

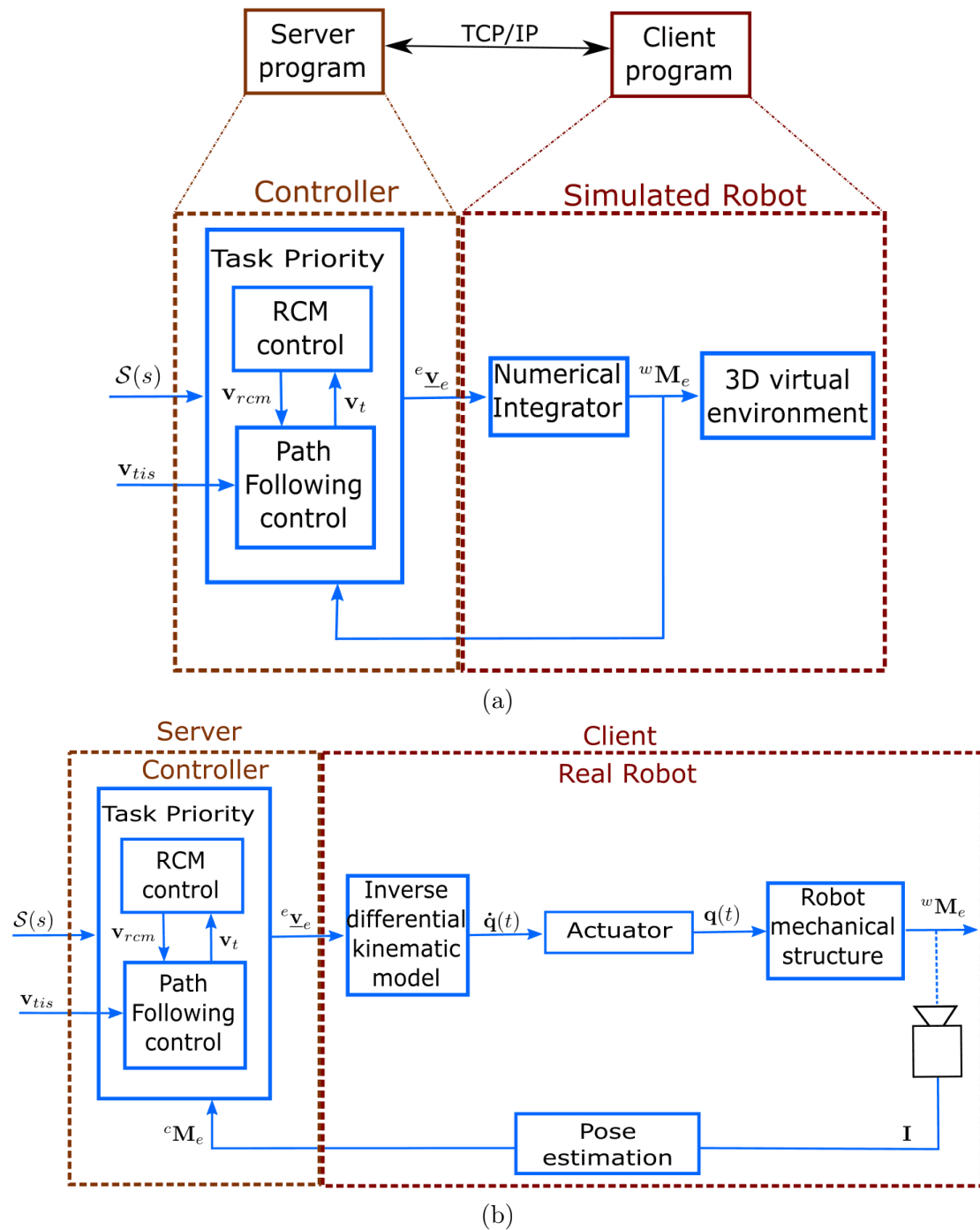


FIGURE 3.27: Block diagram of the client/server communication: (a) simulated robot, and (b) real robot.

The new pose of end-effector (${}^w\mathbf{M}_{e_{new}}$) is thus obtained by:

$${}^w\mathbf{M}_{e_{new}} = {}^w\mathbf{M}_{e_{old}} * \Delta^e\mathbf{M}_e \quad (3.107)$$

Where ${}^w\mathbf{M}_e = \begin{bmatrix} {}^w\mathbf{R}_e & {}^w\mathbf{p}_e \\ \mathbf{0}_{1 \times 3} & 1 \end{bmatrix}$ is the homogeneous matrix that describe the pose of end-effector frame (i.e., the rotation ${}^w\mathbf{R}_e$ and the position ${}^w\mathbf{p}_e$) with respect to the world frame. At the end of simulation, the log files are generated and a Matlab/Octave script is used to read these files and to visualize the output results (e.g., FIGURE 3.23).

Another option which is a realistic scene can be added to the simulator. This scene is conceived based on a numerical model which is created by the medical images of the auditory system (e.g., FIGURE 3.26). It is helpful to plan and to execute more realistic surgical gestures based on the anatomical structures. However, this optional realistic scene does not affect the controller performances.

The proposed simulator is divided into two programs (FIGURE 3.27(a)):

- i) the server program which includes the controller to deduce the end-effector twist velocity, and
- ii) the client program which moves the end-effector and the surgical tool within the scene/world. The client program can also be the code which implements the low-level controller of a real robot (FIGURE 3.27(b)).

For achieving such a decoupling between both the client and the server programs, a socket communication protocol (TCP/IP) was applied to these two programs. Such a protocol has the advantage of communication between both programs either in an offline mode (i.e., when both programs are sharing the resources of the same computer) or an online mode (i.e., when each program is running from two different computers but they are connected over the internet). However, the communication time and the synchronization between the client and the server programs are essential issues that should be considered.

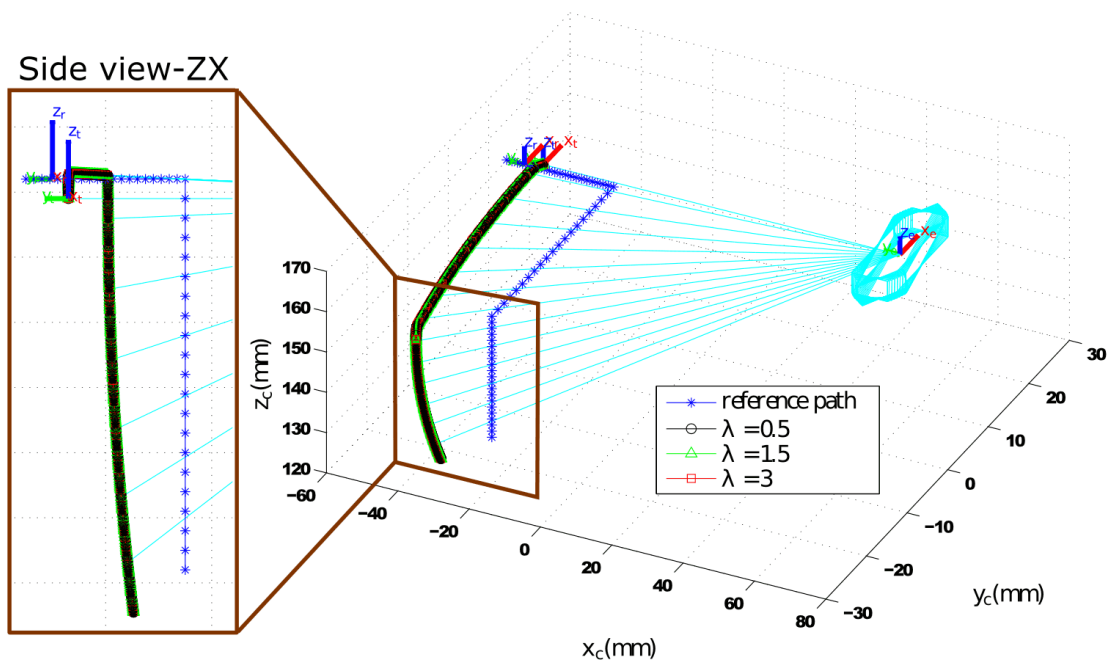
This section presents the simple simulator with a Matlab client which represents a virtual robot (FIGURE 3.27(a)). Such a client has the functions to: i) ensure the socket communication with the server, ii) integrate the command velocities to deduce the new pose of the end-effector and the tool, and iii) plot the output results.

3.3.1 Validation of RCM constraints

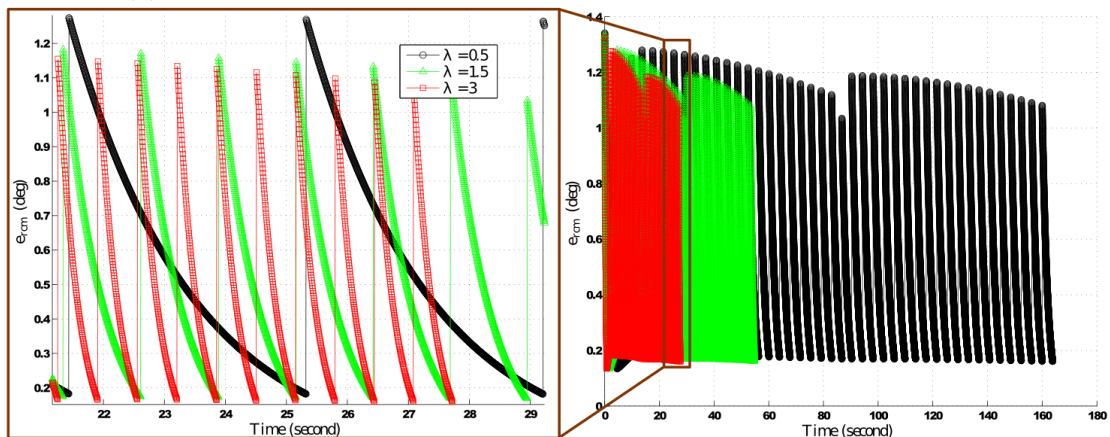
The objective of this part is testing the RCM alignment task only. The simulation scenario is artificially changing the pose of the trocar point along a pre-defined path, and then the RCM task should eliminate the misalignment angular error. The control twist velocity is thus deduced by equation (3.94) during the simulated motion. In fact, the pose of trocar point changes to the next one when the RCM linear error (3.6) is less than $0.25mm$. Such a strategy is hence a point-to-point tracking controller.

Straight tool with a straight path: The objective of this first trial is visualizing the effect of the gain λ on the RCM controller by increasing its value from 0.5, 1.5 to 3.

The position of trocar point changes in a linear path along the x-, y- and z-axes, respectively (FIGURE 3.28(a)). This figure shows the end-effector motion in the camera frame. It shows also the initial reference frames of the end-effector, the tool tip and the trocar point. We can observe that the end-effector does not move along the x-axis because the regulation task to reduce the linear distance between the tool tip and the trocar point is not activated. Thus, the control linear velocity of end-effector ${}^e\mathbf{v}_e$ is almost null, as shown in the upper graphs of FIGURES 3.28(c) and 3.28(d). However, the tool begun the alignment with the reference path (i.e., the linear part along the x-axis of the camera frame) by rotation about the x- and the z-axis of the end-effector frame, as depicted in



(a) The output motion of the tool to correct the RCM angular error



(b) The RCM angular error throughout the simulated motion

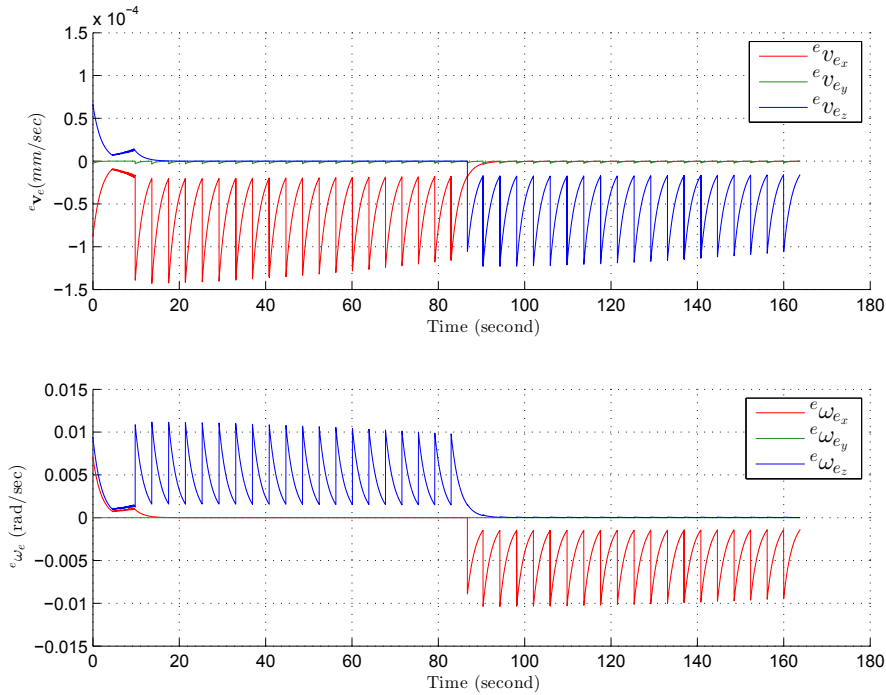
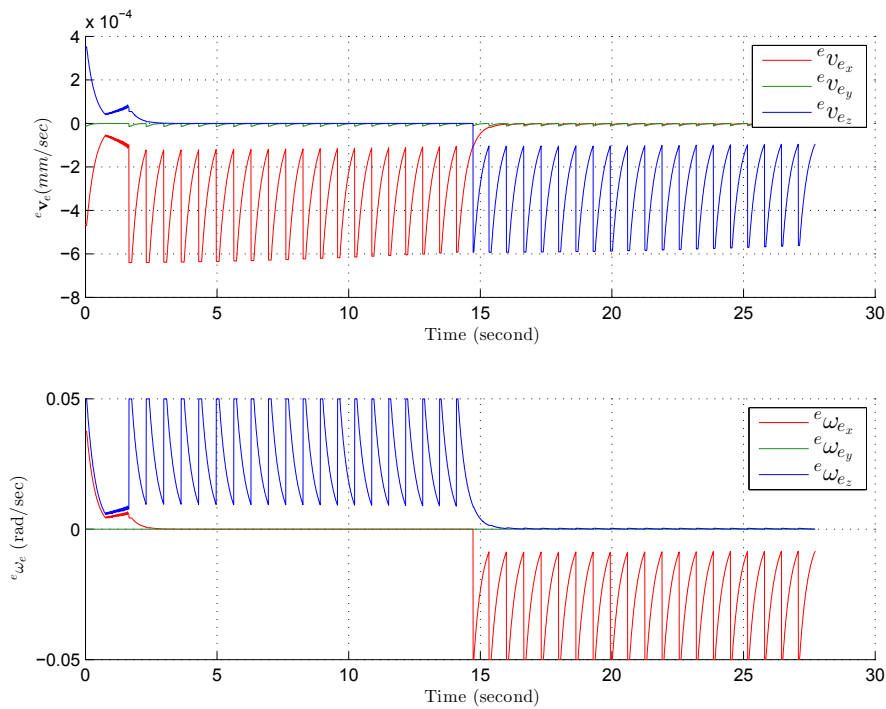
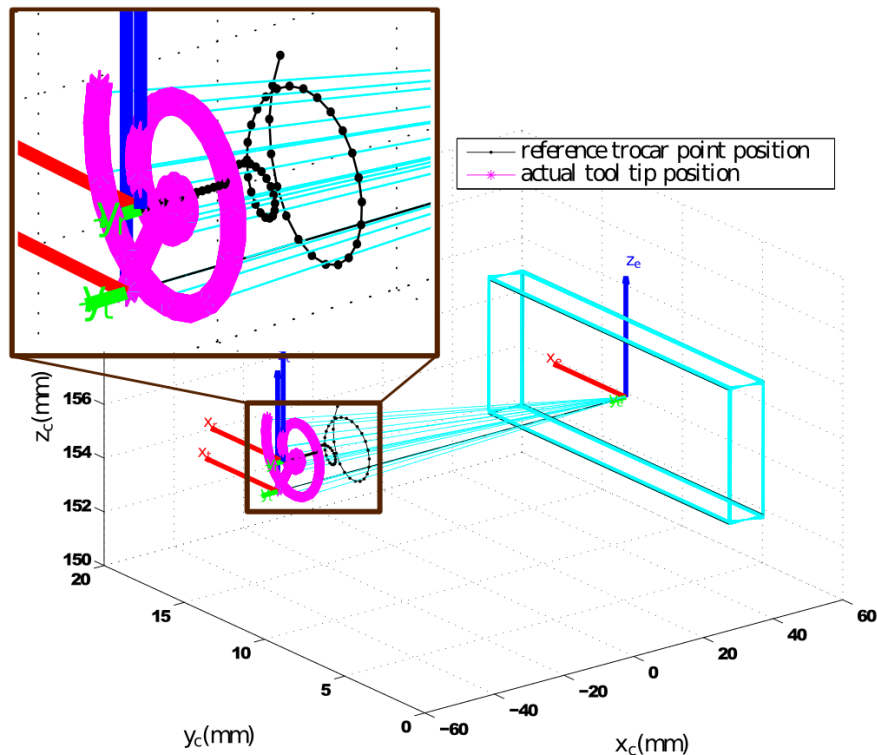
(c) The control twist vector of the end-effector when $\lambda = 0.5$ (d) The control twist vector of the end-effector when $\lambda = 3$

FIGURE 3.28: Testing only the RCM task with a straight tool by changing the position of the trocar point in a straight path. The test is repeated with three different values of λ .

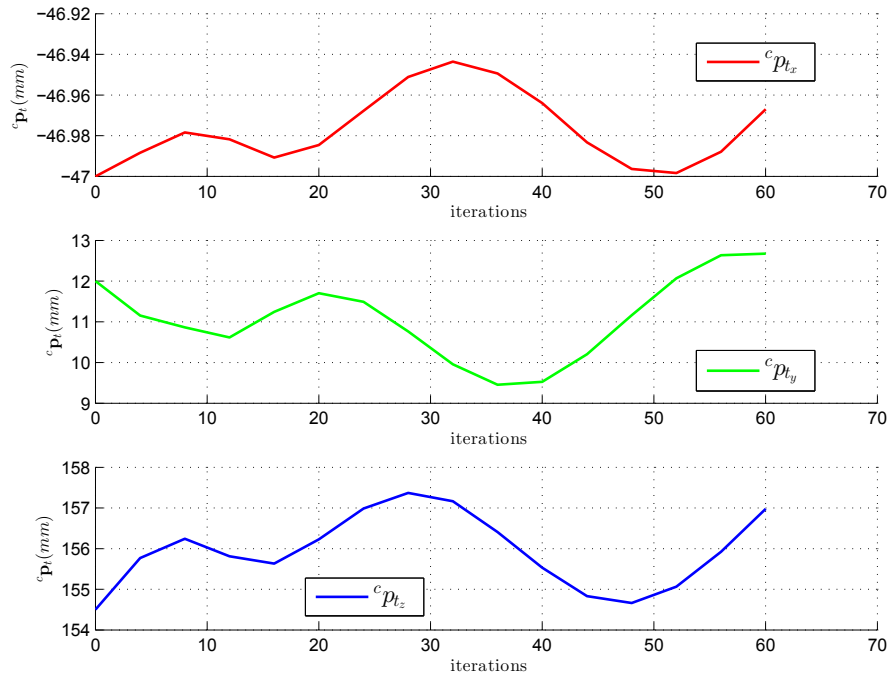
the first part of the lower graphs of FIGURES 3.28(c) and 3.28(d). Then, the tool rotates about the z-axis of the end-effector frame to track the trocar point along the y-axis of camera frame, as depicted in the second part of the lower graphs of FIGURES 3.28(c) and 3.28(d). The tool terminates by rotating about the x-axis of end-effector frame in order to track the trocar point along the z-axis of camera frame, as depicted in the third part of the lower graphs of FIGURES 3.28(c) and 3.28(d).

FIGURE 3.28(b) shows the Euclidean norm of the RCM angular error which determined as in equation (3.70). This error calculates the angle between both vectors ${}^e\mathbf{u}_{et'}$ and ${}^e\mathbf{u}_{er}$. The right graph in FIGURE 3.28(b) shows that a higher value of λ leads to a quicker convergence, where the total time to finish the path was 163 *seconds*, 54 *seconds* and 27 *seconds*, respectively for $\lambda = 0.5$, $\lambda = 1.5$ and $\lambda = 3$. In fact, the control twist vector of the end-effector is increased by augmenting the value of λ , as depicted in FIGURES 3.28(c) and 3.28(d). The oscillation form observed in the latter graphs represents the exponential convergence between two consecutive points on the reference path, as depicted in the left graph of FIGURE 3.28(b).

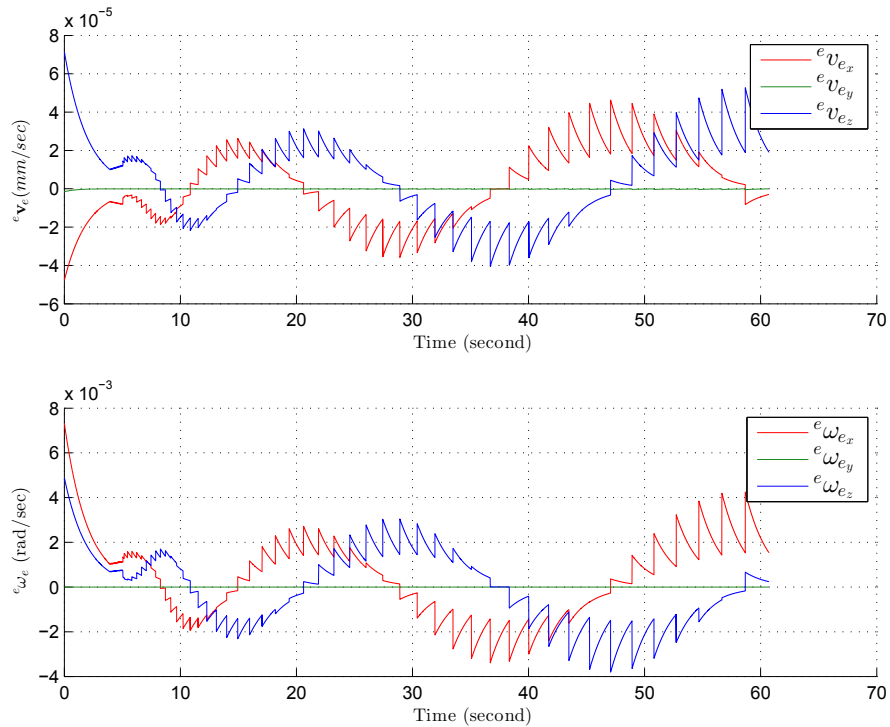
Straight tool with a spiral path: This second trial tests another path for the trocar point. A 3D spiral path is defined in the trocar point frame. In fact, the path is described by a line with starts from the initial position of the trocar point and advances along the negative direction of the y-axis, then the spiral height is also defined in the same direction,



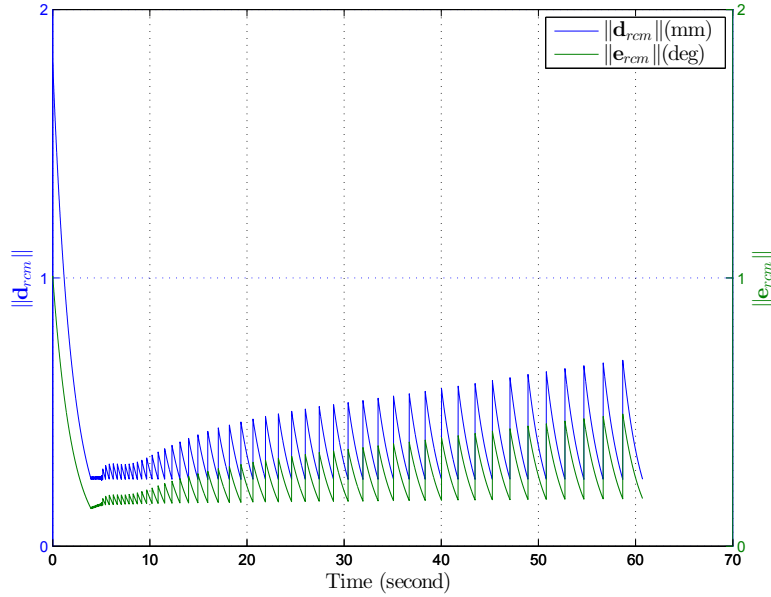
(a) The output motion of the tool to correct the RCM error



(b) The 3D position of the tool tip expressed in the camera frame



(c) The control twist vector of the end-effector



(d) The linear and angular errors of RCM task during the simulated motion

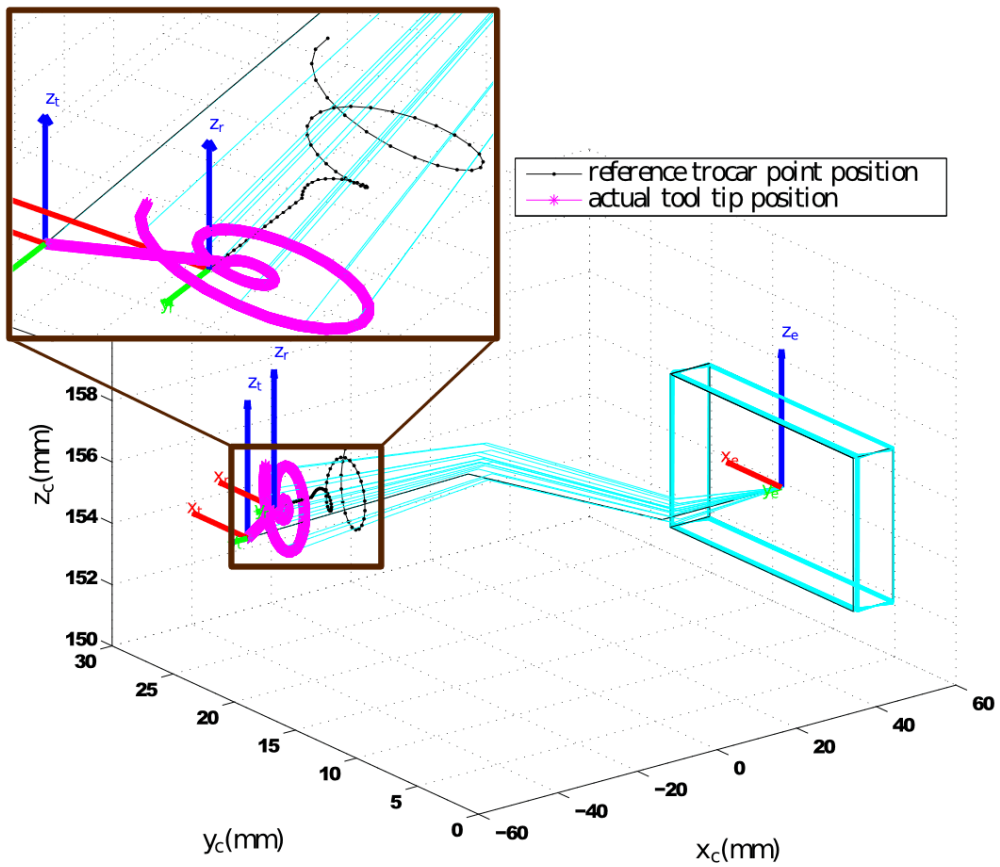
FIGURE 3.29: Testing only the RCM task with a straight tool by changing the position of the trocar point in a spiral path.

as depicted in FIGURE 3.29(a). This arrangement allows testing the projection of the trocar point along the tool body. Therefore, the tool rotation is observed about the x- and z-axes of the end-effector frame in order to reduce the RCM angular error (the lower graph in FIGURE 3.29(c)). The influence of such rotation is observed in FIGURE 3.29(b), where the y- and z-components of the tool tip change in a sine wave in order to track the trocar point.

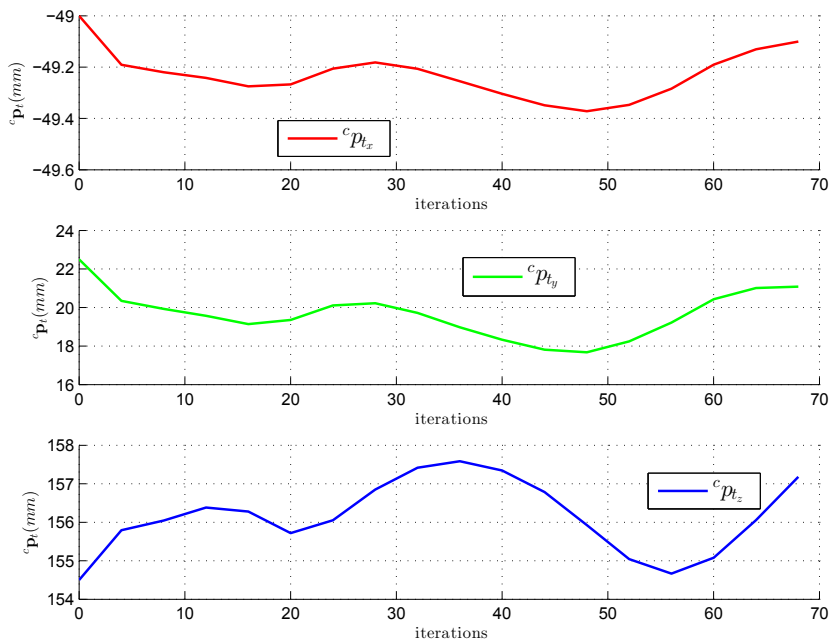
The linear displacement between the tool tip and the trocar point is neglected throughout this trial. Thus, the linear velocity of end-effector is almost null, as shown in the upper graph in FIGURE 3.29(c). It is also observed in FIGURE 3.29(b), where the x-component of the tool tip position is constant.

FIGURE 3.29(d) presents the RCM errors during the simulation. Indeed, the RCM linear error \mathbf{d}_{rcm} is determined by equation (3.6). When its Euclidean norm is equal or less than $0.25mm$, the trocar point changes its position to the next iteration on the reference path. However, the RCM angular error \mathbf{e}_{rcm} is evaluated by equation (3.70). The control twist vector of the end-effector is deduced based-on the \mathbf{e}_{rcm} as conducted in equation (3.95). The exponential convergences in FIGURE 3.29(d) is increased during the simulation because the arc length between the sampled point is not constant. However, the RCM controller converges to the stability and it eliminates the error \mathbf{e}_{rcm} .

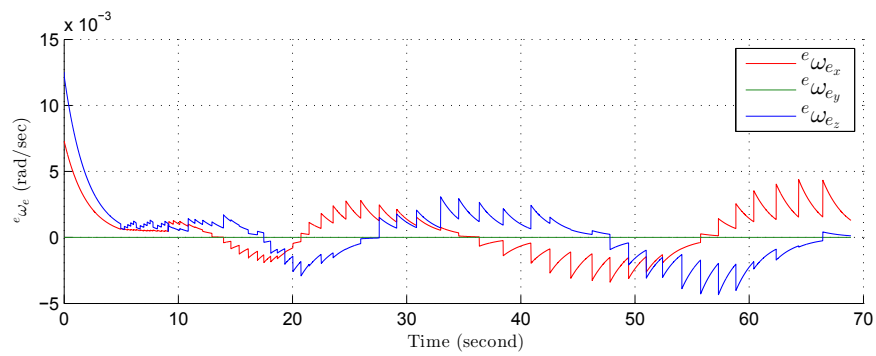
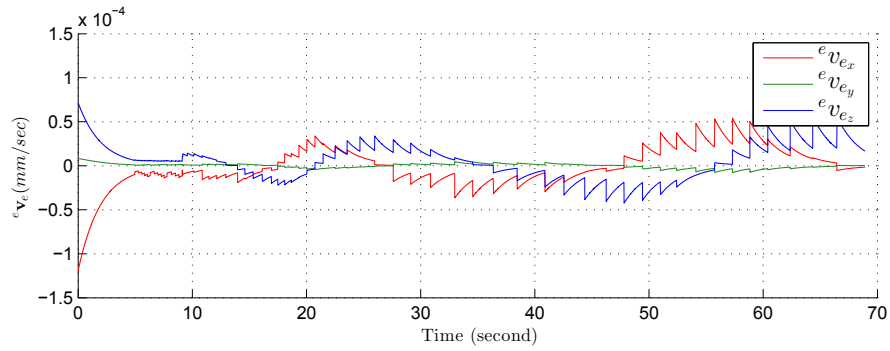
Piecewise straight tool with a spiral path: This trial tests the same path of the 3D spiral curve for the trocar point, but the tool geometry is formed with a combination



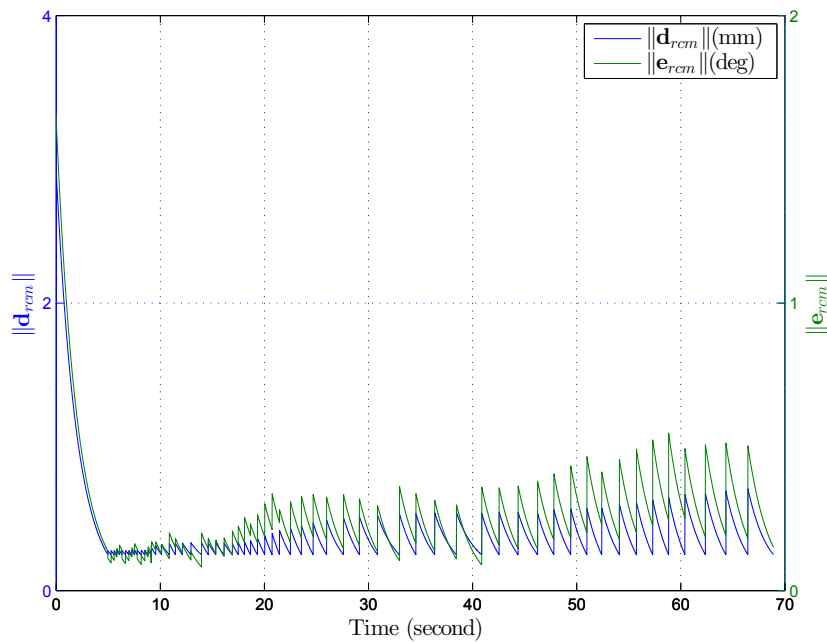
(a) The output motion of the tool to correct the RCM error



(b) The 3D position of the tool tip expressed in the camera frame



(c) The control twist vector of the end-effector

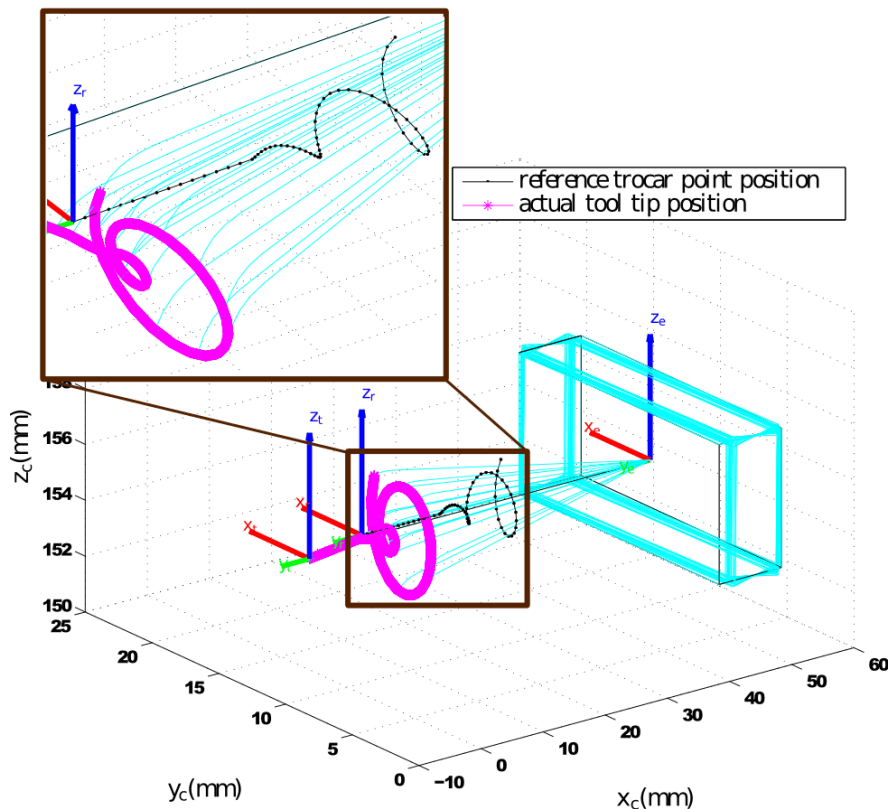


(d) The linear and angular errors of RCM task during the simulated motion

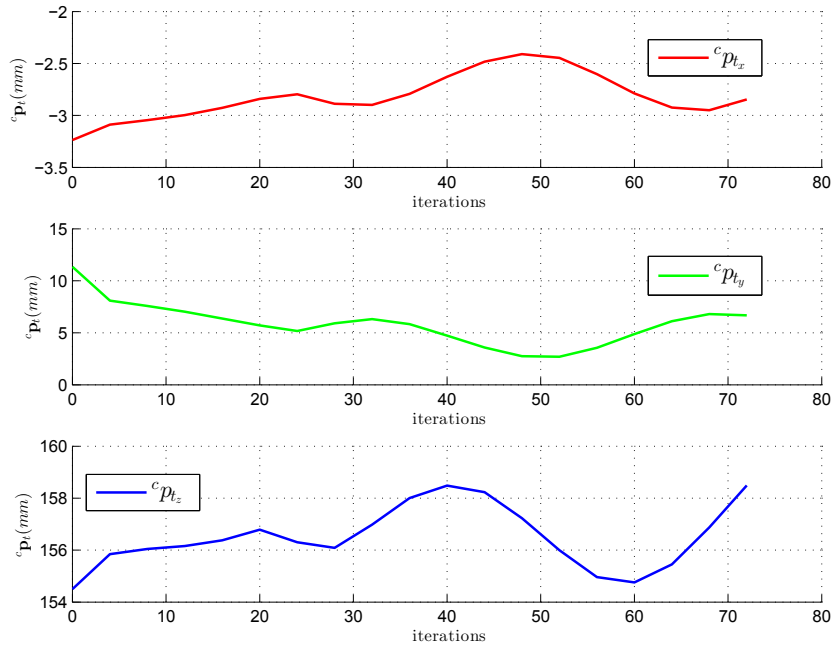
FIGURE 3.30: Testing only the RCM task with a piecewise straight tool in a spiral path.

of piecewise straight tool (FIGURE 3.30(a)). This trial tests only the RCM controller with a curved tool. As expected, the trocar point is projected correctly on the tool body. Thus, the tool rotates about the x- and y-axes of the end-effector (FIGURE 3.30(a)). The control angular velocity of the end-effector is shown in the lower graph of FIGURE 3.30(c), while the upper graph presents the control linear velocity of the end-effector which is approximately null because the distance error between the tool tip and the trocar point is neglected during this trial. Therefore, the position of the tool tip is constant along the x-component as depicted in FIGURES 3.30(a) and 3.30(b), while the position of the tool tip changes along the y- and z-components. The RCM task error is presented in FIGURE 3.30(d), where the error is reduced exponentially. The controller eliminates the initial angular error between the tool body and the trocar point. Then, the trocar point changes its position in a linear path. Therefore, the error in FIGURE 3.30(d) is relatively small. Afterwards, the error begins to become big because the distance between the sample points on the reference path is not constant. This distance is small at the base of spiral path, while it becomes larger at the end of the spiral path.

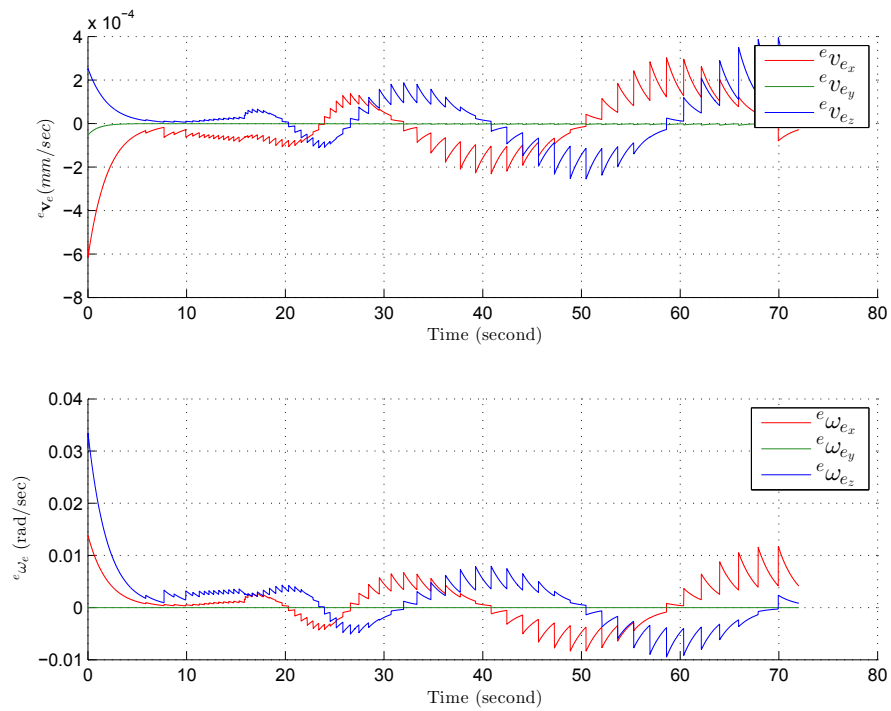
Curved circular tool with a spiral path: The final trial tested a curved tool which is formed by a combination of a linear segment at the base and a circular portion at the



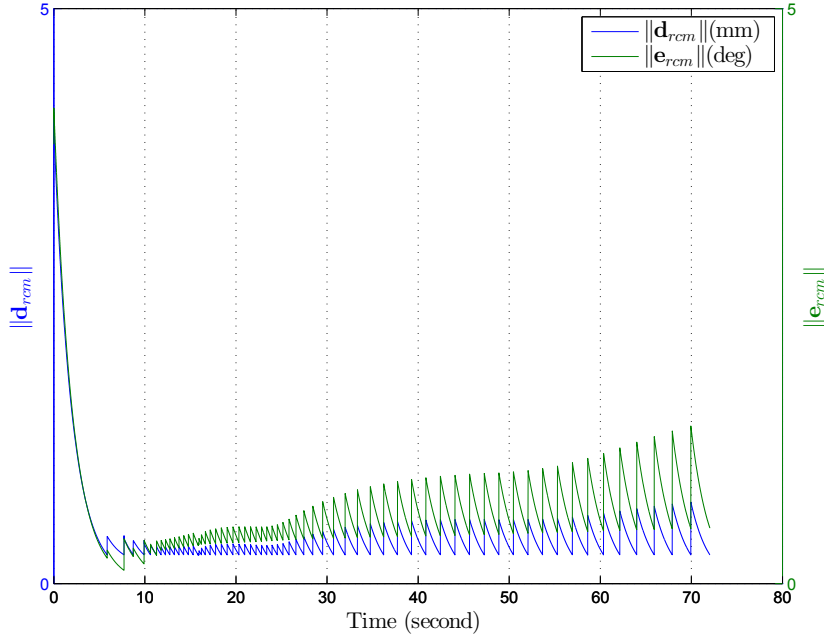
(a) The output motion of the tool to correct the RCM error



(b) The 3D position of tool tip expressed in the camera frame



(c) The control twist velocity of the end-effector



(d) The linear and angular errors of RCM task while the simulated motion

FIGURE 3.31: Testing only the RCM task with a curved circular tool in a spiral path.

distal end (FIGURES 3.31(a)). It is assessed to perform the spiral path as the previous trials. The controller successfully followed the trocar point.

Summary: The trials are performed with two types of paths: i) a 3D straight lines which are formed by a line along the x-, y- and z-axes (FIGURE 3.28(a)), and ii) a 3D spiral form (FIGURE 3.29(a)). These paths are executed with three different tool types: i) a straight tool (FIGURE 3.29(a)), ii) curved tool formed with a combination of straight segments (FIGURE 3.30(a)), and iii) curved tool formed by a portion of a circle (FIGURE 3.31(a)). The summary of these trials are presented in TABLE 3.1. During

Tool type	Path type	RCM linear error (<i>mm</i>)		RCM angular error (<i>deg</i>)	
		median	mean \pm STD	median	mean \pm STD
Straight tool	straight	0.64	0.75 \pm 0.16	0.44	0.51 \pm 0.29
	spiral	0.35	0.4 \pm 0.18	0.23	0.26 \pm 0.1
Piecewise straight tool	straight	0.58	0.71 \pm 0.42	0.38	0.47 \pm 0.3
	spiral	0.33	0.41 \pm 0.29	0.23	0.27 \pm 0.17
Curved circular tool	straight	0.6	0.83 \pm 0.54	0.37	0.52 \pm 0.55
	spiral	0.34	0.38 \pm 0.14	0.37	0.42 \pm 0.15

TABLE 3.1: summary of different trials done with constant gain coefficients (i.e., $\lambda = 0.5$ and $T_e = 0.005$ seconds, whereas STD error is the standard deviation error.

these simulations, the alignment scalar gain was constant $\lambda = 0.5$, and the sample time was also fixed to $T_e = 0.005$ *seconds*.

3.4 Conclusion

This chapter began by formulating a geometric method to describe the RCM task, afterward a brief introduction about the UCM task is presented. This constrained motion allows manipulating surgical tool through an entry point. Indeed, one of these two tasks will be chosen alongside the path following task in order to perform complex motions as will be explained in the next chapter. The projection gradient method will be used to ensure the hierarchical form between the different tasks.

The proposed controller is deployed with a rigid straight tool, but it can also handle a rigid curved tool. The controller cannot handle the situation where the tool curvature is higher than the regulating error. Such a challenging situation will be treated in the perspectives, alongside applying the proposed controller with a flexible tool.

Chapter 4

From Pre-operative images to Motion

Contents

4.1	3D path following controller	120
4.1.1	Background	121
4.1.2	Proposed method	122
4.1.3	Stability condition	132
4.2	Task priority controller	133
4.2.1	Following a path under RCM constraint	135
4.2.2	Following a path under UCM constraint	136
4.3	Numerical validation	138
4.3.1	3D path following controller	140
4.3.2	Task priority controller	144
4.4	Experimental validation	153
4.4.1	Trials with a parallel robot	153
4.4.2	Toward clinical trials	163
4.5	Conclusion	166

The main objective of this chapter is to present a task-space controller which guides a general purpose robot. Such a robot is commonly a redundant structure. The redundancy appears when the DOF of the required task is lower than those provided by the robot structure [Siciliano, 1990]. The required task could be any kinematic or dynamic goal. The advantage of redundancy appears to be useful for avoiding singularity, joints limits and workspace obstacles [Maciejewski and Klein, 1985]. It is also helpful for performing different surgical tasks simultaneously within the patient body. For instance, the surgeon needs to reach a specific region of interest, for scanning an organ or removing some tissues, while performing the RCM/UCM movement and avoiding the anatomical structures. Indeed, the complex surgical task is formed by assembling small tasks (i.e., the RCM/UCM movement task and the path following task). Therefore, a hierarchy

between these sub-tasks is useful to ensure that the secondary task does not influence the primary task. The task priority technique [Nakamura et al., 1987] allows setting a hierarchical form between different tasks.

Section 4.1 proposes a 3D path following scheme for a holonomic system which is characterized by a local frame in order to take advantage of the time-invariant controller. The proposed controller determines the tool tip velocity in the local frame of the reference curve (i.e., Frenet-Serret frame, for instance, FIGURE 4.1 shows the Frenet-Serret frame on a Lissajous path). The stability study of the latter method is also presented. Afterwards, Section 4.2 shows how to arrange the priority between the path following task and the RCM/UCM task. At the end, Sections 4.3 and 4.4 present the numerical and the experimental results of the proposed controller, respectively.

FIGURE 4.1: The progress of Frenet frame along a Lissajous curve ¹.

4.1 3D path following controller

In order to control the robot motion over a desired geometric curve in the Euclidean space, there are basically two controller categories for guiding the robot, either path following or trajectory tracking controllers. The dissimilarity between both controllers is the dependency on time [Gasparetto et al., 2015]. The trajectory controller is time-dependent, where the geometric curve is parametrized with time. On the contrary,

¹this figure contains an animated GIF. If your PDF viewer has the right plug-in to support animated GIF (e.g., Adobe reader), you can control the animation with the control panel below the figure.

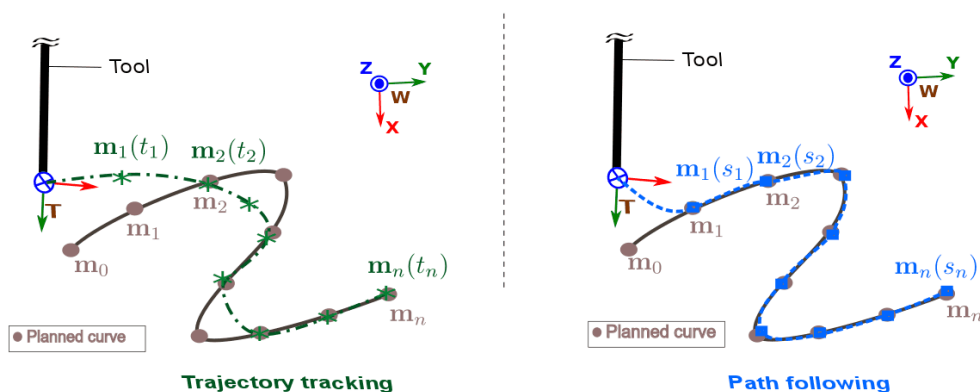


FIGURE 4.2: A comparison between the performance of a path following controller (the dash blue line on the right) and a trajectory tracking controller (the dash dotted green line on the left) for the same geometric curve (the continuous brown line).

the path controller is time-invariant, where the geometric curve is defined without any temporal constraints and it is commonly a function of its arc length.

This time restriction distinguishes the performances of both controllers (FIGURE 4.2), especially in the presence of perturbations and/or high curvature of the reference curve. On one hand, the trajectory controller accelerates and short-cuts the reference curve in order to reach the next point on the schedule. On the other hand, the path controller maintains the velocity tangent to the curve and it does not bypass the curve even if there is going to be a delay in reaching the next point. Consequently, the path following controller has better performances than the trajectory tracking controller in terms of geometric precision, and convergence to the reference curve in the presence of perturbations or lag conditions.

From the surgeon's viewpoint, the exact time to finish the curve is not an important factor. What really matters is that the instrument follows exactly the reference curve. In addition, the surgeon may need to modify the tool velocity independently from the curve shape, size or curvature. In fact, the tool velocity is certainly dependent on the tissue-tool interaction (tissue deformation) which may change due to the potential inhomogeneity of the infected tissue. In addition, the tool velocity profile may modify when the surgeon moves from one region of interest to another one for inspection and/or excision processes. For the above reasons, the path following is a good option for our applications; since it separates the geometric curve from the velocity profile.

4.1.1 Background

The majority of path following controllers, previously reported in the literature, were implemented for mobile robot applications. Such controllers had used various techniques for solving the path following issue with non-holonomic constraints, such as chain form [Samson, 1993], robust non-linear controller [Lapierre and Jouvencel, 2008], and back-stepping filter based on Lyapunov [Zhu and Huo, 2014]. These controllers are working

well with a non-holonomic system (i.e., ground, marine and air vehicles) in 2D and 3D spaces. However, a path following controller is not frequently applied to the medical applications. A 2D path following was deployed to guide a laser during larynx surgery [Seon et al., 2015]. The proposed controller in [Seon et al., 2015] is based on visual servoing technique. A unicycle non-holonomic model is applied for executing a visual path following controller with high frequency. Other 3D trajectory tracking and pose estimation methods were proposed in [Nageotte et al., 2006] for controlling an instrument to perform automatic suturing during laparoscopic surgery.

4.1.2 Proposed method

Problem statement: Before executing the desired motion, the reference geometric curve should be defined. Such a geometric curve is generally determined by a planning algorithm [Gasparetto et al., 2015] in order to avoid obstacles, and to generate the shortest distance between the initial and the target points. Alternatively, the surgeon may draw the desired curve on a tactile tablet². By the end of the planning phase, the geometric curve is defined as a set of points in the 3D Cartesian space (xyz -coordinates). The essential issue of a path following task is to minimize the projection distance (\mathbf{d}_{pf} , see FIGURE 4.3). The latter distance \mathbf{d}_{pf} is formed by projecting the origin point of tool tip frame (\mathcal{O}_t) onto the curve shape (\mathcal{S}_p), and the resultant projected point on the reference curve is (\mathbf{p}_p).

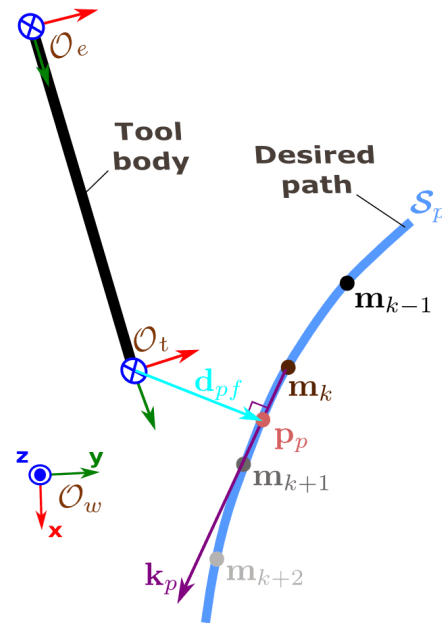


FIGURE 4.3: The concept of projecting the tool tip onto the geometric curve.

Problem Resolution: A geometrical curve could be represented either in an explicit form, an implicit form or a parametric form [Struik, 1988]. The explicit form is useful to plot graph; since the equation of independent variable is formed by the dependent ones (e.g., $y = mx + b$ for describing a straight line in \mathbb{R}^2). However, the implicit form is more useful than the explicit one because it groups all the variables on one side of equation (e.g., $f(x,y) = x^2 + y^2 = r^2$ for a circle in \mathbb{R}^2 , while a sphere in \mathbb{R}^3 $f(x,y,z) = x^2 + y^2 + z^2 = r^2$). A parametrized curve is more helpful than the implicit form to define a geometric curve or a path; since the coordinates of each point of the curve are defined as functions of one parameter. For instance, a parametrized spiral

² μ RALP (Micro-technologies and Systems for Robot-Assisted Laser Phonomicrosurgery). [online]. <http://www.microralp.eu/>

FIGURE 4.4: The progress of Frenet frame along a spiral curve ¹.

curve is defined as:

$$\mathcal{S}_p(c_p) = \begin{bmatrix} \mathcal{S}_{p_x}(c_p) \\ \mathcal{S}_{p_y}(c_p) \\ \mathcal{S}_{p_z}(c_p) \end{bmatrix} = \begin{bmatrix} r_s \cos(c_p) \\ h_s c_p \\ r_s \sin(c_p) \end{bmatrix} \quad (4.1)$$

whereby (r_s) is the maximum radius of spiral, (h_s) is the height of spiral in y -axis as shown in FIGURE 4.4, and (c_p) is the curve parameter.

A parametrized curve is generally defined as ($\mathcal{S}_p : I_p \rightarrow \mathbb{R}^n$) a function that maps an interval $I_p = (a, b)$ to the space \mathbb{R}^n [Carmo, 1976, Struik, 1988]. In order to have a smooth curve, it should be differentiable with respect to the curve parameter c_p . Thus, the corresponding point to $\frac{d\mathcal{S}_p}{dc_p} = \hat{\mathcal{S}}_p(c_p) \neq 0$ is called a regular point. Otherwise, the corresponding point to $\hat{\mathcal{S}}_p(c_p) = 0$ for $c_p \in I_p$ is called a singular point. Thereby, a regular parametrized differentiable curve is considered as a curve without singular points.

Arc length: The curve $\mathcal{S}_p(s_p)$ is commonly parametrized by its arc length (s_p). The arc length is expressed as the length of a segment between two consecutive points ($\hat{\mathcal{S}}_p(c_{p_i})$ and $\hat{\mathcal{S}}_p(c_{p_{i+1}})$) onto the geometric curve. If the curve is differentiable, its arc length is defined as:

$$s_p(c_p) = \int_{c_{p_0}}^{c_p} \|\hat{\mathcal{S}}_p(c_p)\| dc_p = \int_{c_{p_0}}^{c_p} \sqrt{\hat{\mathcal{S}}_p(c_p) \cdot \hat{\mathcal{S}}_p(c_p)} dc_p \quad (4.2)$$

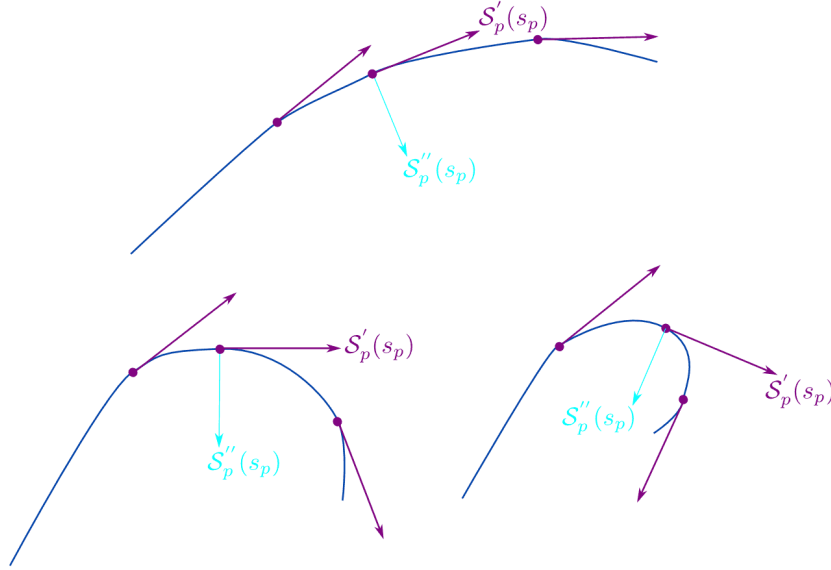


FIGURE 4.5: Examples of different curve types, and the corresponding unit tangent vectors and the principal normal vectors.

whereby $\left(\|\hat{\mathbf{S}}_p(c_p)\| = \sqrt{\hat{\mathbf{S}}_{p_x}(c_p)^2 + \hat{\mathbf{S}}_{p_y}(c_p)^2 + \hat{\mathbf{S}}_{p_z}(c_p)^2}\right)$ is the Euclidean norm of the vector $\hat{\mathbf{S}}_p(c_p)$.

Tangent vector: Since the curve $\mathbf{S}_p(s_p)$ is defined as a function of the arc length, the derivative of such a vector results into a tangent vector to the curve, and its unit-vector is determined as:

$$\mathbf{k}_p = \frac{d\mathbf{S}_p(s_p)}{ds_p} = \mathbf{S}'_p(s_p). \quad (4.3)$$

The rate of change of the unit tangent vector \mathbf{k}_p is the measure for the curve curvature ($C_p(s_p) = \|\mathbf{k}'_p(s_p)\|$). The curve curvature can thus calculated as [Kreyszig, 1991]:

$$C_p = \sqrt{\mathbf{S}''_p(s_p) \cdot \mathbf{S}''_p(s_p)}. \quad (4.4)$$

Normal vector: Since the vector \mathbf{k}_p is unit-vector, thereby the dot product by itself equals one ($\mathbf{k}_p \cdot \mathbf{k}_p = 1$). The derivative of latter expression with respect to the arc length, it becomes ($\mathbf{k}_p \cdot \mathbf{k}'_p = 0$) which means that the vector \mathbf{k}_p is perpendicular to the vector \mathbf{k}'_p (FIGURE 4.5). With the assumption that the vector \mathbf{k}'_p is not equal to zero, which implies the curvature is different from zero, its unit vector is called principal

normal vector (\mathbf{n}_p). It is thereby formulated as:

$$\mathbf{n}_p = \frac{\mathbf{k}'_p(s_p)}{\|\mathbf{k}'_p(s_p)\|} = \frac{\mathbf{k}'_p(s_p)}{C_p}. \quad (4.5)$$

Bi-normal vector: In order to form the Frenet frame, a third vector is defined by the cross-product between the two vectors \mathbf{k}_p and \mathbf{n}_p . The resultant vector (\mathbf{b}_p) is called bi-normal vector and it determined as:

$$\mathbf{b}_p = \mathbf{k}_p \times \mathbf{n}_p. \quad (4.6)$$

By defining the latter vector, the orthogonal basis of Frenet frame are formed by the three vector $\{\mathbf{k}_p, \mathbf{n}_p, \mathbf{b}_p\}$. The origin point of such frame is defined by projecting the tool tip frame onto the geometric curve.

Curve torsion: Another important feature is the curve torsion (τ_p) which measures how the curve winds out of the plane formed by \mathbf{k}_p and \mathbf{n}_p . By differentiating the bi-normal vector \mathbf{b}_p with respect to the arc length, the resultant has the following form:

$$\mathbf{b}'_p = \underbrace{\mathbf{k}'_p}_{=C_p \mathbf{n}_p} \times \mathbf{n}_p + \mathbf{k}_p \times \mathbf{n}'_p. \quad (4.7)$$

=0

Thus, the vector \mathbf{b}'_p is perpendicular to \mathbf{k}_p . the vector \mathbf{b}'_p is also perpendicular to \mathbf{b}_p ; since $\|\mathbf{b}_p\| = 1$. In addition, the vector \mathbf{b}'_p is parallel to \mathbf{n}_p , which implies ($\mathbf{b}'_p = \tau_p \mathbf{n}_p$). Thereby, the curve torsion is determined as [Kreyszig, 1991]:

$$\tau_p = -\mathbf{b}'_p{}^T \mathbf{n}_p. \quad (4.8)$$

Frenet frame: The Frenet-Serret formulas are defined as [Struik, 1988, Kreyszig, 1991]:

$$\begin{aligned} \mathbf{k}'_p &= \frac{d\mathbf{k}_p}{ds_p} = C_p \mathbf{n}_p \\ \mathbf{n}'_p &= \frac{d\mathbf{n}_p}{ds_p} = -C_p \mathbf{k}_p + \tau_p \mathbf{b}_p \\ \mathbf{b}'_p &= \frac{d\mathbf{b}_p}{ds_p} = -\tau_p \mathbf{n}_p, \end{aligned} \quad (4.9)$$

or in a matrix form as:

$$\begin{bmatrix} \mathbf{k}'_p \\ \mathbf{n}'_p \\ \mathbf{b}'_p \end{bmatrix} = \begin{bmatrix} 0 & C_p & 0 \\ -C_p & 0 & \tau_p \\ 0 & -\tau_p & 0 \end{bmatrix} \begin{bmatrix} \mathbf{k}_p \\ \mathbf{n}_p \\ \mathbf{b}_p \end{bmatrix}. \quad (4.10)$$

The previous equations characterize the Frenet frame along a regular parametrized differentiable curve. The evolution of Frenet frame along a spiral curve is shown in FIGURE 4.4. To plot this figure, the origin point of Frenet frame changes its location along the curve's sample points, and then the basis of frame are computed, as previously presented in equations (4.3).

Path following error: Back to the path following problem, the origin point of Frenet frame should be deduced by finding out the shortest distance between the tool tip frame and the reference curve. This problem is solved by projecting the tool tip \mathcal{O}_t onto the reference curve $\mathcal{S}_p(s_p)$. Suppose that the curve is sampled with n points ($\mathbf{m}_0 \cdots \mathbf{m}_n$). The first step to determine the projected point on the curve \mathbf{p}_p is calculating the shortest distance between the tool tip \mathcal{O}_t and the sampled points. Assume that the sample point \mathbf{m}_k is the closest point to the tool tip. Then the vector $\overrightarrow{\mathbf{m}_k \mathcal{O}_t}$ is required to be projected onto the tangential unit-vector \mathbf{k}_p , as depicted in FIGURE 4.6. Thus, the projection distance \mathbf{d}_{pf} can be determined as:

$$\mathbf{d}_{pf} = (\mathbf{I}_{3 \times 3} - \mathbf{k}_p \mathbf{k}_p^T) \overrightarrow{\mathbf{m}_k \mathcal{O}_t}. \quad (4.11)$$

Hence, a triangle is formed between the points $\{\mathbf{m}_k, \mathcal{O}_t, \mathbf{p}_p\}$. Since the vectors \mathbf{d}_{pf} and $\overrightarrow{\mathbf{m}_k \mathcal{O}_t}$ are known, then the vector $\overrightarrow{\mathbf{m}_k \mathbf{p}_p}$ is computed as:

$$\begin{aligned} \overrightarrow{\mathbf{m}_k \mathbf{p}_p} &= \overrightarrow{\mathbf{m}_k \mathcal{O}_t} + \mathbf{d}_{pf} \\ &= \mathbf{p}_p - \mathbf{m}_k. \end{aligned} \quad (4.12)$$

Consequently, the projected point \mathbf{p}_p is easily determined as:

$$\mathbf{p}_p = \mathbf{m}_k + \overrightarrow{\mathbf{m}_k \mathbf{p}_p}. \quad (4.13)$$

Since the the projected point \mathbf{p}_p is known, the projection distance \mathbf{d}_{pf} can be calculated as:

$$\mathbf{d}_{pf} = \mathcal{O}_t - \mathbf{p}_p. \quad (4.14)$$

This simple form of \mathbf{d}_{pf} allows to simplify the calculation of the differential kinematics.

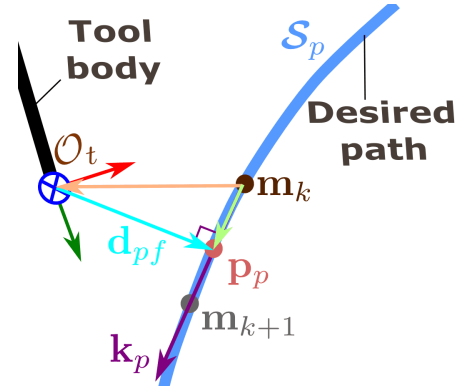


FIGURE 4.6: The concept of projecting the tool tip onto the geometric curve.

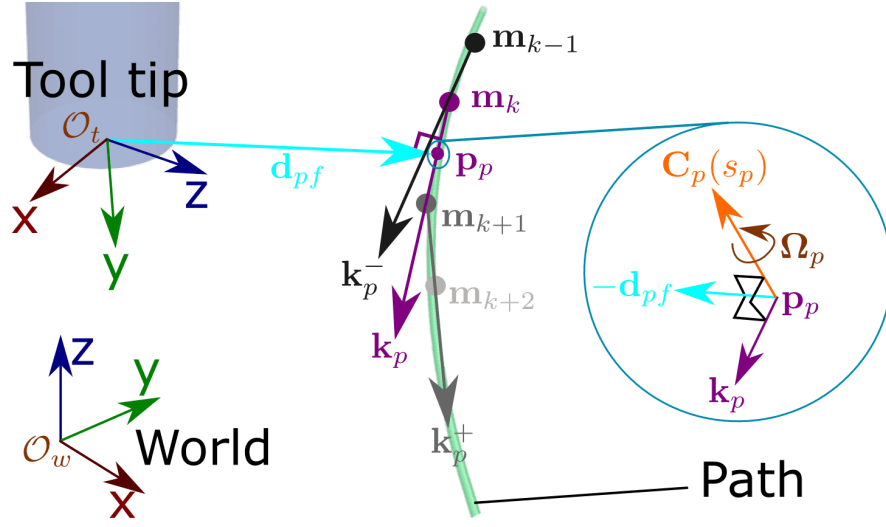


FIGURE 4.7: The different reference frames and notions deployed for describing the path following scheme.

Differential kinematics of path following error: The time-derivative of the projected distance \mathbf{d}_{pf} represents the required velocity for bringing back the tool tip to the reference path, and it is determined as:

$$\begin{aligned} \dot{\mathbf{d}}_{pf} &= \dot{O}_t - \dot{\mathbf{p}}_p \\ &= \mathbf{v}_t - \mathbf{v}_p. \end{aligned} \quad (4.15)$$

The velocity of the projected point along the reference path ($\mathbf{v}_p = \dot{s}_p \mathbf{k}_p$) could be represented as the multiplication between: i) the speed of projected point (\dot{s}_p) along the path which is also known as the curvilinear speed, and ii) the instantaneous tangential unit-vector \mathbf{k}_p .

In case that the parametric equation that describes the reference curve is unknown, for instance when the surgeon draws the reference curve on a tablet, the instantaneous unit-vector \mathbf{k}_p could be determined numerically. It can be estimated from two consecutive sample points (\mathbf{m}_k and \mathbf{m}_{k+1}) onto the reference curve (FIGURE 4.7) as:

$$\mathbf{k}_p = \frac{\mathbf{m}_{k+1} - \mathbf{m}_k}{\|\mathbf{m}_{k+1} - \mathbf{m}_k\|}. \quad (4.16)$$

The time-derivative of the unit-vector \mathbf{k}_p can also be obtained numerically as:

$$\begin{aligned} \dot{\mathbf{k}}_p &= \frac{d\mathbf{k}_p}{dt} = \frac{\partial \mathbf{k}_p}{\partial s_p} \frac{ds_p}{dt} \\ &= \frac{\mathbf{k}_p^+ - \mathbf{k}_p^-}{2 \Delta s_p} \dot{s}_p, \end{aligned} \quad (4.17)$$

$$\mathbf{k}_p^+ = \frac{\mathbf{m}_{i+2} - \mathbf{m}_{i+1}}{\|\mathbf{m}_{i+2} - \mathbf{m}_{i+1}\|}, \text{ and } \mathbf{k}_p^- = \frac{\mathbf{m}_i - \mathbf{m}_{i-1}}{\|\mathbf{m}_i - \mathbf{m}_{i-1}\|} \quad (4.18)$$

where ($\Delta s_p = s_{p_{k+1}} - s_{p_{k-1}}$) is the arclength between two consecutive sample points onto the reference curve, (\mathbf{k}_p^+) and (\mathbf{k}_p^-) are the previous and the next tangential vectors, respectively.

Recall that the Frenet frame is formed by the three basis $\{\mathbf{k}_p, \mathbf{n}_p, \mathbf{b}_p\}$. The vector \mathbf{d}_{pf} is collinear with the base \mathbf{n}_p , while the vector $\dot{\mathbf{k}}_p$ is in the same direction as the base \mathbf{n}_p . It implies that the vector $\dot{\mathbf{k}}_p$ is perpendicular to both vectors \mathbf{k}_p and \mathbf{b}_p . Another vector ($\boldsymbol{\Omega}_p$) is defined along the unit-vector \mathbf{b}_p (FIGURE 4.7) as:

$$\boldsymbol{\Omega}_p = \dot{s}_p \mathbf{C}_p(s_p). \quad (4.19)$$

In fact, the latter rotation vector is a geometric representation to determine the rate of change of the unit-vector \mathbf{k}_p in function of the path curvature $\mathbf{C}_p(s_p)$ and the curvilinear speed \dot{s}_p . Thus, the unit-vector $\dot{\mathbf{k}}_p$ is reformulated as:

$$\begin{aligned} \dot{\mathbf{k}}_p &= \boldsymbol{\Omega}_p \times \mathbf{k}_p \\ &= (\dot{s}_p \mathbf{C}_p(s_p)) \times \mathbf{k}_p. \end{aligned} \quad (4.20)$$

By replacing the unit-vector $\dot{\mathbf{k}}_p$ in (4.20) by that in (4.17), the resultant becomes equals to:

$$\frac{\mathbf{k}_p^+ - \mathbf{k}_p^-}{2 \Delta s_p} \dot{s}_p = \dot{s}_p (\mathbf{C}_p(s_p) \times \mathbf{k}_p). \quad (4.21)$$

Consequently, the path curvature $\mathbf{C}_p(s_p)$ is deduced analytically as:

$$\mathbf{C}_p(s_p) \cong -\mathbf{k}_p \times \frac{\mathbf{k}_p^+ - \mathbf{k}_p^-}{2 \Delta s_p}. \quad (4.22)$$

Since the projection distance \mathbf{d}_{pf} is perpendicular to the unit-vector \mathbf{k}_s , the dot product between these two vectors should be null ($\mathbf{d}_{pf}^T \mathbf{k}_p = 0$). The time-derivative of this dot product is concluded as:

$$\dot{\mathbf{d}}_{pf}^T \mathbf{k}_p + \mathbf{d}_{pf}^T \dot{\mathbf{k}}_p = 0. \quad (4.23)$$

For deducing the projected point speed \dot{s}_p , both sides of equation (4.15) are multiplied by the dot product of the unit-vector \mathbf{k}_p and the equation becomes as:

$$\dot{\mathbf{d}}_{pf}^T \mathbf{k}_p = \mathbf{v}_t^T \mathbf{k}_p - \dot{s}_p \underbrace{\mathbf{k}_p^T \mathbf{k}_p}_1. \quad (4.24)$$

By substituting the dot product $\dot{\mathbf{d}}_{pf}^T \mathbf{k}_p$ in (4.23) by that in (4.24), and by replacing the unit-vector $\dot{\mathbf{k}}_p$ in (4.23) by that in (4.20), the required curvilinear speed \dot{s}_p is calculated as:

$$\begin{aligned} [\dot{s}_p \mathbf{d}_{pf}^T (\mathbf{C}_p(s_p) \times \mathbf{k}_p)] + [\mathbf{v}_t^T \mathbf{k}_p - \dot{s}_p] &= 0 \\ \mathbf{v}_t^T \mathbf{k}_p &= \dot{s}_p [1 - \mathbf{d}_{pf}^T (\mathbf{C}_p(s_p) \times \mathbf{k}_p)] \end{aligned} \quad (4.25)$$

$$\dot{s}_p = \frac{\mathbf{v}_t^T \mathbf{k}_p}{1 - \mathbf{d}_{pf}^T (\mathbf{C}_p(s_p) \times \mathbf{k}_p)}. \quad (4.26)$$

Equation (4.26) represents the curvilinear speed \dot{s}_p along the reference path in terms of: i) the tool tip velocity \mathbf{v}_t , ii) the path curvature $\mathbf{C}_p(s_p)$, iii) the instantaneous tangential vector \mathbf{k}_p , and iv) the projection distance \mathbf{d}_{pf} . Back substituting (4.26) in (4.15), the time-derivative of the path following error becomes:

$$\dot{\mathbf{d}}_{pf} = \left(\mathbf{I}_{3 \times 3} - \frac{\mathbf{k}_p \mathbf{k}_p^T}{1 - \mathbf{d}_{pf}^T (\mathbf{C}_p(s_p) \times \mathbf{k}_p)} \right) \mathbf{v}_t. \quad (4.27)$$

The velocity profile of tool tip \mathbf{v}_t in the latter equation (4.27) is free to be chosen and independently from the path parameters. Thereby, the problem now is to choose the adequate controller which deduces the tool tip velocity to minimize the projected distance \mathbf{d}_{pf} .

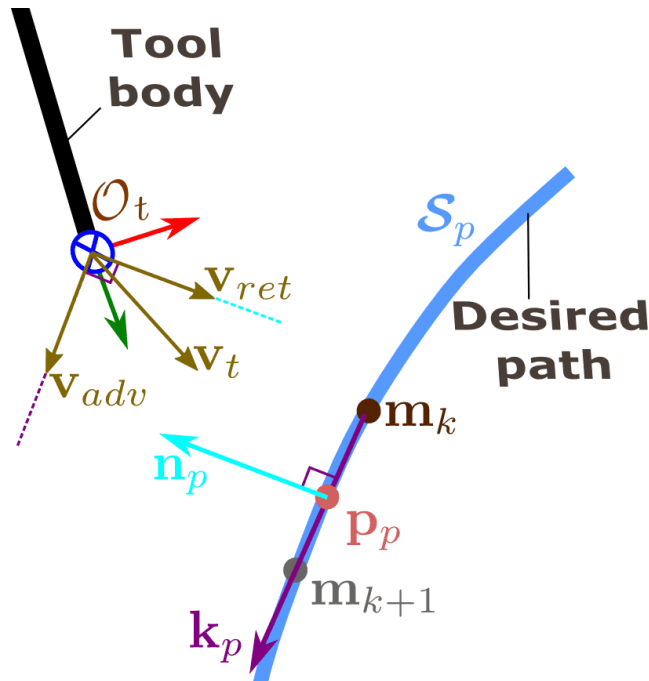


FIGURE 4.8: The geometric concept of the path following controller.

Control of path following error: An intuitive solution (4.28) is to decompose the resultant linear velocity of tool tip into two components (FIGURE 4.8): i) the required velocity to advance the tool along the path (\mathbf{v}_{adv}), and ii) the necessary velocity to bring

back the tool onto the path (\mathbf{v}_{ret}) when the tool is deviated from the path. Such a solution is represented as:

$$\mathbf{v}_t = \underbrace{\alpha \mathbf{k}_p}_{\mathbf{v}_{adv}} + \underbrace{\beta \mathbf{d}_{pf}}_{\mathbf{v}_{ret}}. \quad (4.28)$$

whereby (β) is a negative gain for returning to the path (see Section 4.1.3), and (α) is a positive gain for advancing along the path.

The weighting coefficients (α and β) provide a priority choice between the two velocity components. The choice of such weighting coefficients affects the system performance and its stability.

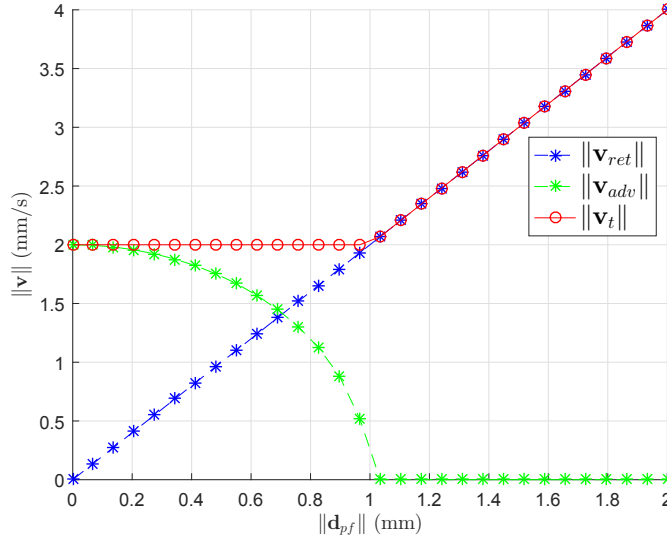


FIGURE 4.9: The influence of the path following error \mathbf{d}_{pf} on the control velocity of the tool tip \mathbf{v}_t , while using the gains choice (4.30).

Choice of weighting coefficients: A possible option to determine the value of α and β is to impose a constant speed for the tool tip ($\|\mathbf{v}_t\| = v_{tis}$). This speed v_{tis} depends on the interaction between the tool (i.e., cutting or imaging tool) and the tissue. Hence, equation (4.28) is reformulated as:

$$\|\mathbf{v}_t\|^2 = \alpha^2 \underbrace{\|\mathbf{k}_p\|^2}_{=1} + \beta^2 \underbrace{\|\mathbf{d}_{pf}\|^2}_{=\|\mathbf{v}_{ret}\|^2} = v_{tis}^2. \quad (4.29)$$

The tool velocity along the tissue v_{tis} is defined by the surgeon, while the gain parameters are formulated in function of this velocity v_{tis} . A first option is defined as:

$$if \begin{cases} \|\mathbf{v}_{ret}\|^2 < v_{tis}^2, & \begin{cases} \beta = constant \\ \alpha = \sqrt{v_{tis}^2 - \|\mathbf{v}_{ret}\|^2} \end{cases} \\ \|\mathbf{v}_{ret}\|^2 > v_{tis}^2, & \begin{cases} \beta = constant \\ \alpha = 0 \end{cases} \end{cases} \quad (4.30)$$

This first option is represented graphically in FIGURE 4.9. In case that the tool is not far from the desired path, the first condition in (4.30) is chosen in order to advance along the path and to regulate the tool deviation from the reference path. In fact, the $\|\mathbf{v}_{adv}\|$ is reducing when the $\|\mathbf{d}_{pf}\|$ is increasing, and the $\|\mathbf{v}_{ret}\|$ is also increasing (FIGURE 4.9). On the opposite, the second condition in (4.30) is chosen where the priority is returning the tool tip to the reference path and the tool can not advance along the path.

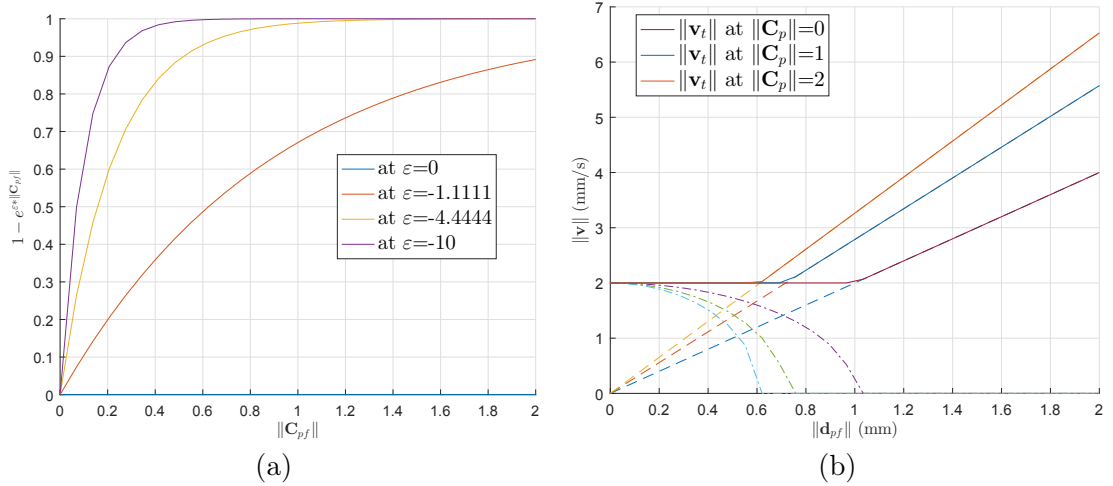


FIGURE 4.10: (a) The controller sensitivity to the path curvature, (b) the influence of the path following error \mathbf{d}_{pf} and the path curvature \mathbf{C}_p on the control velocity of the tool tip \mathbf{v}_t , while using the gains choice (4.32).

An alternative option is choosing the gain coefficient β in function of the path curvature. This second option increase exponentially the gain β when the path curvature increases. It is formulated as:

$$\beta = \beta' \left[1 + \left(1 - e^{\varepsilon\|\mathbf{C}_p(s_p)\|} \right) \right] \quad (4.31)$$

where (β') is a negative gain for returning to path, and (ε) is a negative gain for sensing the amount of curvature.

When the path curvature is null (i.e., a straight path), the term $e^{\varepsilon\|\mathbf{C}_p(s_p)\|}$ tends to be one, and the term $(1 - e^{\varepsilon\|\mathbf{C}_p(s_p)\|})$ becomes null. On the opposite, when the path

curvature is big, the term $e^{\varepsilon\|\mathbf{C}_p(s_p)\|}$ tends to be zero, and the term $(1 - e^{\varepsilon\|\mathbf{C}_p(s_p)\|})$ goes to one. FIGURE 4.10(a) shows the output of the term $(1 - e^{\varepsilon\|\mathbf{C}_p(s_p)\|})$ when reducing the gain ε . Such a reduction of the gain ε will increase the gain β in order to return faster to the reference path.

However, the path curvature may change its direction along the path. Thus, a sign function is added to the latter equation in order to detect the variation of the curvature direction, and it becomes equal to:

$$\begin{aligned} \beta &= \beta' \left[1 + \text{sign}(\mathbf{d}_{pf}^T (\mathbf{C}_p(s_p) \times \mathbf{k}_p)) (1 - e^{\varepsilon\|\mathbf{C}_p(s_p)\|}) \right] \\ \alpha &= \begin{cases} \sqrt{v_{tis}^2 - \|\mathbf{v}_{ret}\|^2}, & \|\mathbf{v}_{ret}\|^2 < v_{tis}^2 \\ 0, & \|\mathbf{v}_{ret}\|^2 > v_{tis}^2 \end{cases} \end{aligned} \quad (4.32)$$

This second option allows the controller adapting automatically the variation of the path curvature. FIGURE 4.10(b) shows the controller output which changes according to the path curvature.

4.1.3 Stability condition

Since the path following task is a non-linear problem, the stability condition is studied based on Lyapunov stability [Khalil, 1996]. Let us consider the following Lyapunov candidate:

$$V = \frac{1}{2} \mathbf{d}_{pf}^T \mathbf{d}_{pf} \Rightarrow \begin{cases} V > 0 \text{ when } \mathbf{d}_{pf} \neq \mathbf{0} \\ V = 0 \text{ when } \mathbf{d}_{pf} = \mathbf{0} \end{cases} \quad (4.33)$$

The time-derivative of a Lyapunov function (4.33) should be a negative scalar (in case $\mathbf{d}_{pf} \neq \mathbf{0}$) and null (in case $\mathbf{d}_{pf} = \mathbf{0}$) in order to ensure the system stability. Therefore, the necessary condition for V to be a well-formed Lyapunov function is:

$$\begin{cases} \dot{V} < 0 \text{ when } \mathbf{d}_{pf} \neq \mathbf{0} \\ \dot{V} = 0 \text{ when } \mathbf{d}_{pf} = \mathbf{0} \end{cases} \quad (4.34)$$

where $\dot{V} = \frac{1}{2} (\mathbf{d}_{pf}^T \dot{\mathbf{d}}_{pf} + \dot{\mathbf{d}}_{pf}^T \mathbf{d}_{pf}) = \mathbf{d}_{pf}^T \dot{\mathbf{d}}_{pf}$.

By applying the control tool tip velocity (4.28) on the path following kinematics (4.27), the resultant velocity of the projected distance is modified to:

$$\dot{\mathbf{d}}_{pf} = \left(\alpha \mathbf{k}_p - \frac{\alpha \mathbf{k}_p \overbrace{\mathbf{k}_p^T \mathbf{k}_p}^{=1}}{1 - \mathbf{d}_{pf}^T (\mathbf{C}_p(s_p) \times \mathbf{k}_p)} \right) + \left(\beta \mathbf{d}_{pf} - \frac{\beta \mathbf{k}_p \overbrace{\mathbf{k}_p^T \mathbf{d}_{pf}}^{=0}}{1 - \mathbf{d}_{pf}^T (\mathbf{C}_p(s_p) \times \mathbf{k}_p)} \right) \quad (4.35)$$

$$\dot{\mathbf{d}}_{pf} = \alpha \left[1 - \frac{1}{1 - \mathbf{d}_{pf}^T (\mathbf{C}_p(s_p) \times \mathbf{k}_p)} \right] \mathbf{k}_p + \beta \mathbf{d}_{pf}. \quad (4.36)$$

Back substituting (4.36) in (4.34) to verify the system stability, the time-derivative of Lyapunov function becomes:

$$\dot{V} = \alpha \left[1 - \frac{1}{1 - \mathbf{d}_{pf}^T (\mathbf{C}_p(s_p) \times \mathbf{k}_p)} \right] \underbrace{\mathbf{d}_{pf}^T \mathbf{k}_p}_{=0} + \beta \mathbf{d}_{pf}^T \mathbf{d}_{pf}. \quad (4.37)$$

Thereby, the \dot{V} is reduced as, thanks to the orthogonality property between the two vectors \mathbf{d}_{pf} and \mathbf{k}_p :

$$\dot{V} = \beta \mathbf{d}_{pf}^T \mathbf{d}_{pf} = 2\beta V. \quad (4.38)$$

For achieving an asymptotic convergence, the coefficient β should be a negative scalar in order to satisfy the necessary condition. In that case, equation (4.38) expresses an exponential stability. However, the coefficient α should be positive. It does not affect the system stability but rather it changes its performance. An experimental assessment is performed in Section 4.3.1 to show the influence of the ratio between these coefficients.

4.2 Task priority controller

During a surgical intervention, it is required to accomplish a global task by performing multiple subtasks simultaneously. Let consider a subtask ($\dot{\mathbf{e}}_i \in \mathbb{R}^{m_i}$) given by:

$$\dot{\mathbf{e}}_i = \mathbf{L}_i {}^e \underline{\mathbf{v}}_e, \quad \text{where } i=1,2,\dots,j \quad (4.39)$$

whereby (${}^e \underline{\mathbf{v}}_e \in se(3)$) is the control vector which is required to be computed, and ($\mathbf{L}_i \in \mathbb{R}^{m_i \times n}$) is the interaction matrix which describes the i^{th} subtask. Indeed, the interaction matrix \mathbf{L}_i is a function which describes how the control vector ${}^e \underline{\mathbf{v}}_e$ will modify the error $\dot{\mathbf{e}}_i$.

For instance, the visual servoing control [Hutchinson et al., 1996, Chaumette and Hutchinson, 2006] assumes that the vector $\mathbf{e}_1 = f({}^w \mathbf{M}_e(t))$ is the error between the measured features (i.e., a visual features extracted from an image) and the desired ones. This error is in function of the end-effector's pose ${}^w \mathbf{M}_e(t) \in SE(3)$ expressed in the world frame. The vector $\dot{\mathbf{e}}_1$ is the time variation of the error \mathbf{e}_1 . If it is required to ensure an exponential decrease of the error (i.e., $\dot{\mathbf{e}}_1 = -b\mathbf{e}_1$), the solution is ${}^e \underline{\mathbf{v}}_e = -b\mathbf{L}_1^\dagger \mathbf{e}_1$. This inverse solution is the control velocity of the end-effector in order to decrease the error towards zero.

Generally, the inverse solution of a task is not guaranteed because the interaction matrix \mathbf{L}_1 is a non-linear function, its dimensions can be different from square, and its rank could be locally deficient. Thereby, an approximation is done thanks to the least-square solution (${}^e \underline{\mathbf{v}}_e = \mathbf{L}_1^\dagger \dot{\mathbf{e}}_1$), where The estimated \mathbf{L}_1^\dagger is achieved by the psuedo-inverse. In other words, if the exact solution does not exist, the solution will minimize

$\|{}^e\mathbf{v}_e - \mathbf{L}_1^\dagger \dot{\mathbf{e}}_1\|$. Such a solution was extended to include additional subtasks by applying the projection gradient technique which its general form given by [Nakamura et al., 1987]:

$${}^e\mathbf{v}_e = \mathbf{L}_1^\dagger \dot{\mathbf{e}}_1 + (\mathbf{I} - \mathbf{L}_1^\dagger \mathbf{L}_1) \mathbf{z}_1 \quad (4.40)$$

where (\mathbf{z}_1) is an additional vector to be optimized, (\mathbf{L}_1^\dagger) is the estimated inverse of the interaction matrix \mathbf{L}_1 . The second part in the right hand side of (4.40) is a homogeneous solution that is done by the projector operator $(\mathbf{I} - \mathbf{L}_1^\dagger \mathbf{L}_1)$. Such an operator allows to map a second subtask $\dot{\mathbf{e}}_2$ into the *null-space* (or *Kernel*) of the first one. Such a subspace contains all solutions to $\mathbf{L}_1 {}^e\mathbf{v}_e = \mathbf{0}$.

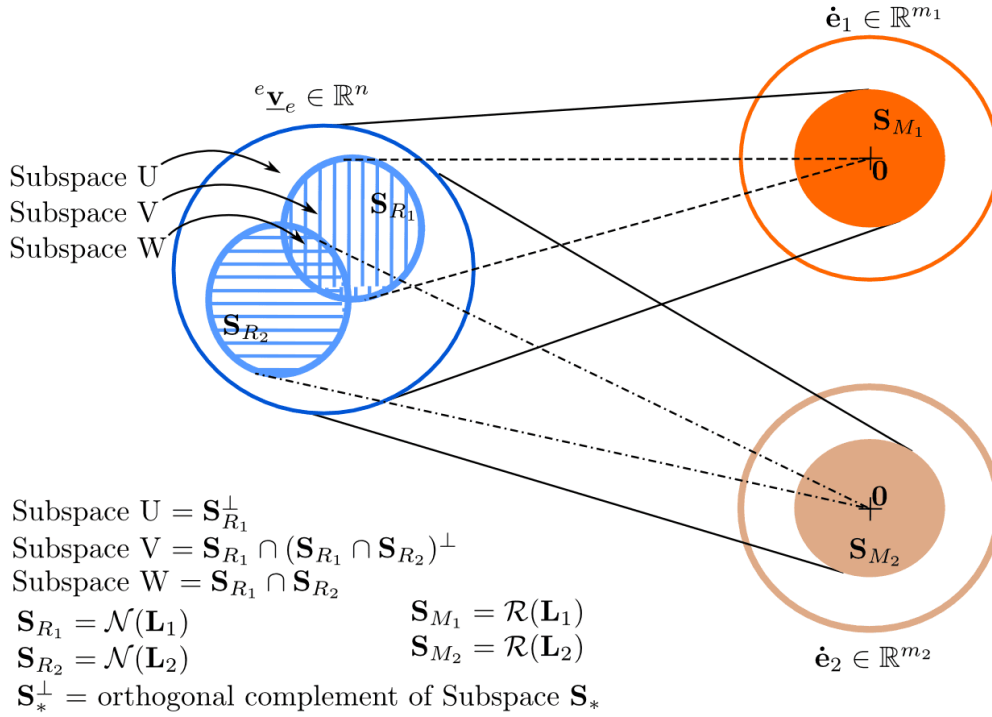


FIGURE 4.11: The difference spaces of the projection gradient.

Let defines a range space (or manipulable space) of the interaction matrix as $\mathcal{R}(\mathbf{L}_i)$, and a null space (or redundant space) as $\mathcal{N}(\mathbf{L}_i)$ [Hanafusa et al., 1981, Nakamura et al., 1987]. The manipulable space is considered as space which collects all combinations of the manipulator variable $\dot{\mathbf{e}}_i$. These combinations can be produced by different values of ${}^e\mathbf{v}_e$ which belongs to the range of \mathbf{L}_i . The redundant space is considered as space which contains the remaining DOF which are not used by the manipulator to accomplish the desired task. These two spaces are shown in FIGURE 4.11, where the subspaces $\mathbf{S}_{M_1} = \mathcal{R}(\mathbf{L}_1)$ and $\mathbf{S}_{M_2} = \mathcal{R}(\mathbf{L}_2)$ are the manipulable spaces of the first and second tasks, respectively, while the subspaces $\mathbf{S}_{R_1} = \mathcal{N}(\mathbf{L}_1)$ and $\mathbf{S}_{R_2} = \mathcal{N}(\mathbf{L}_2)$ are the redundant spaces of the first and second tasks, respectively. The subspace U is $\mathbf{S}_{R_1}^\perp$ which means

the orthogonal complement of subspace \mathbf{S}_{R_1} . It also indicates the contribution of ${}^e \underline{\mathbf{v}}_e$ to the first manipulator variable $\dot{\mathbf{e}}_1$. This contribution is represented by the first term in the right hand side of equation (4.40). The subspace V is $\mathbf{S}_{R_1} \cap (\mathbf{S}_{R_1} \cap \mathbf{S}_{R_2})^\perp$ which can contribute the the second manipulator variable $\dot{\mathbf{e}}_2$ without disturbing the first one \mathbf{b}_1 . It is defined by the second term in the right hand side of equation (4.40). The subspace W is $\mathbf{S}_{R_1} \cap \mathbf{S}_{R_2}$ which means the remaining DOF and can be applied for performing the third task $\dot{\mathbf{e}}_3$, if it is required. It is defined as the second term in the right hand side of equation (4.42).

The vector \mathbf{z}_1 in (4.40) could be any criteria (a secondary task) needed to be added to the first task. This additional task will not affect the first one since it is located in the null-space of the first task. If the secondary task is defined as $\mathbf{b}_2 = \mathbf{L}_2 {}^e \underline{\mathbf{v}}_e$, the equation (4.40) is injected in the latter expression, the resultant becomes as:

$$\begin{aligned} \dot{\mathbf{e}}_2 &= \mathbf{L}_2 \left(\mathbf{L}_1^\dagger \dot{\mathbf{e}}_1 + (\mathbf{I} - \mathbf{L}_1^\dagger \mathbf{L}_1) \mathbf{z}_1 \right) \\ &= \mathbf{L}_2 \mathbf{L}_1^\dagger \dot{\mathbf{e}}_1 + \underbrace{\mathbf{L}_2 (\mathbf{I} - \mathbf{L}_1^\dagger \mathbf{L}_1)}_{\tilde{\mathbf{L}}_2} \mathbf{z}_1. \end{aligned} \quad (4.41)$$

Hence, the vector \mathbf{z}_1 is deduced from the previous equation as:

$$\mathbf{z}_1 = \tilde{\mathbf{L}}_2^\dagger (\dot{\mathbf{e}}_2 - \mathbf{L}_2 \mathbf{L}_1^\dagger \dot{\mathbf{e}}_1) + (\mathbf{I} - \tilde{\mathbf{L}}_2^\dagger \tilde{\mathbf{L}}_2) \mathbf{z}_2 \quad (4.42)$$

whereby (\mathbf{z}_2) is another criteria vector which is projected in the null-space of the secondary task. By replacing (4.42) in (4.40), the general projection gradient form is redefined as:

$$\begin{aligned} {}^e \underline{\mathbf{v}}_e &= \mathbf{L}_1^\dagger \dot{\mathbf{e}}_1 + (\mathbf{I} - \mathbf{L}_1^\dagger \mathbf{L}_1) \left(\tilde{\mathbf{L}}_2^\dagger (\dot{\mathbf{e}}_2 - \mathbf{L}_2 \mathbf{L}_1^\dagger \dot{\mathbf{e}}_1) + (\mathbf{I} - \tilde{\mathbf{L}}_2^\dagger \tilde{\mathbf{L}}_2) \mathbf{z}_2 \right) \\ &= \mathbf{L}_1^\dagger \dot{\mathbf{e}}_1 + (\mathbf{I} - \mathbf{L}_1^\dagger \mathbf{L}_1) \tilde{\mathbf{L}}_2^\dagger (\dot{\mathbf{e}}_2 - \mathbf{L}_2 \mathbf{L}_1^\dagger \dot{\mathbf{e}}_1) + (\mathbf{I} - \mathbf{L}_1^\dagger \mathbf{L}_1) (\mathbf{I} - \tilde{\mathbf{L}}_2^\dagger \tilde{\mathbf{L}}_2) \mathbf{z}_2. \end{aligned} \quad (4.43)$$

A third task could be introduced in the third term on the right hand side of (4.43), and a recursive form could be obtained. The second term of (4.43) is simplified as [Maciejewski and Klein, 1985]:

$${}^e \underline{\mathbf{v}}_e = \mathbf{L}_1^\dagger \dot{\mathbf{e}}_1 + \tilde{\mathbf{L}}_2^\dagger (\dot{\mathbf{e}}_2 - \mathbf{L}_2 \mathbf{L}_1^\dagger \dot{\mathbf{e}}_1). \quad (4.44)$$

The equation (4.44) shows the solution of ${}^e \underline{\mathbf{v}}_e$ to satisfy both tasks $\dot{\mathbf{e}}_1$ and $\dot{\mathbf{e}}_2$ in a hierarchical form. In fact, the first task consumes some of the robot DOFs, and the remaining DOFs of the robot are used by the second task.

4.2.1 Following a path under RCM constraint

Recall that the RCM task was defined in (3.94) and (3.99), $\dot{\mathbf{e}}_{rcm3D}$ and \dot{e}_{rcm1D} respectively. These equations describe the differential kinematics of the RCM angular error ³.

They are also valid to control either a straight tool or a curved one. Thus, the simplify notation of RCM task is:

$$\dot{\mathbf{e}}_{rcm} = \mathbf{L}_{e_{rcm}} \mathbf{e}_{\mathbf{v}_e}. \quad (4.45)$$

This equation is considered as the first task with the highest priority. In order to ensure an exponential decreasing of the RCM error, a proportional controller is formed as:

$$\underbrace{-\lambda \mathbf{e}_{rcm}}_{\dot{\mathbf{e}}_1} = \underbrace{\mathbf{L}_{e_{rcm}}}_{\mathbf{L}_1} \mathbf{e}_{\mathbf{v}_e}. \quad (4.46)$$

The secondary task in the hierarchy is the path following task. The control velocity of the tool tip was defined in (4.28). Such a velocity can be represented with respect to any desired frame. By selecting the end-effector frame, the tool tip linear velocity is related to the twist velocity of the end-effector as:

$$\mathbf{e}_{\mathbf{v}_t} = \underbrace{[\mathbf{I} \quad -[{}^e\mathbf{et}]_{\times}]}_{\mathbf{L}_{e_{pf}}} \underbrace{\begin{bmatrix} \mathbf{e}_{\mathbf{v}_e} \\ \mathbf{e}_{\omega_e} \end{bmatrix}}_{\mathbf{e}_{\mathbf{v}_e}}, \quad (4.47)$$

$$\underbrace{\mathbf{e}_{\mathbf{v}_t}}_{\dot{\mathbf{e}}_2} = \underbrace{\mathbf{L}_{e_{PF}}}_{\mathbf{L}_2} \mathbf{e}_{\mathbf{v}_e} \quad (4.48)$$

whereby ($\mathbf{e}_{\mathbf{v}_t}$) is the linear velocity of the tool tip expressed in the end-effector frame, and ($\mathbf{L}_{e_{pf}}$) is the interaction matrix of the path following task.

By placing the equations (4.46) and (4.48) in equation (4.44), the control twist vector of the end-effector is deduced as:

$$\mathbf{e}_{\mathbf{v}_e} = -\lambda \mathbf{L}_{e_{rcm}}^{\dagger} \mathbf{e}_{rcm} + \tilde{\mathbf{L}}_{e_{pf}}^{\dagger} \left(\mathbf{e}_{\mathbf{v}_t} + \lambda \mathbf{L}_{e_{pf}} \mathbf{L}_{e_{rcm}}^{\dagger} \mathbf{e}_{rcm} \right) \quad (4.49)$$

whereby $\tilde{\mathbf{L}}_{e_{pf}} = \mathbf{L}_{e_{pf}} \left(\mathbf{I} - \mathbf{L}_{e_{rcm}}^{\dagger} \mathbf{L}_{e_{rcm}} \right)$. Equation (4.49) computes the control twist vector in order to achieve the path following task under the RCM constraint.

4.2.2 Following a path under UCM constraint

Recall that the UCM task was defined in (3.104) as:

$$\underbrace{-\alpha_{obs} \lambda \mathbf{e}_{rcm}}_{\dot{\mathbf{e}}_1} = \underbrace{\mathbf{L}_{e_{rcm}}}_{\mathbf{L}_1} \mathbf{e}_{\mathbf{v}_e}. \quad (4.50)$$

whereby (α_{obs}) is the stiffness of the virtual spring (3.103) which is located between the tool body and the incision wall.

³See Section 3.1.2 for more details about the bilateral constraints.

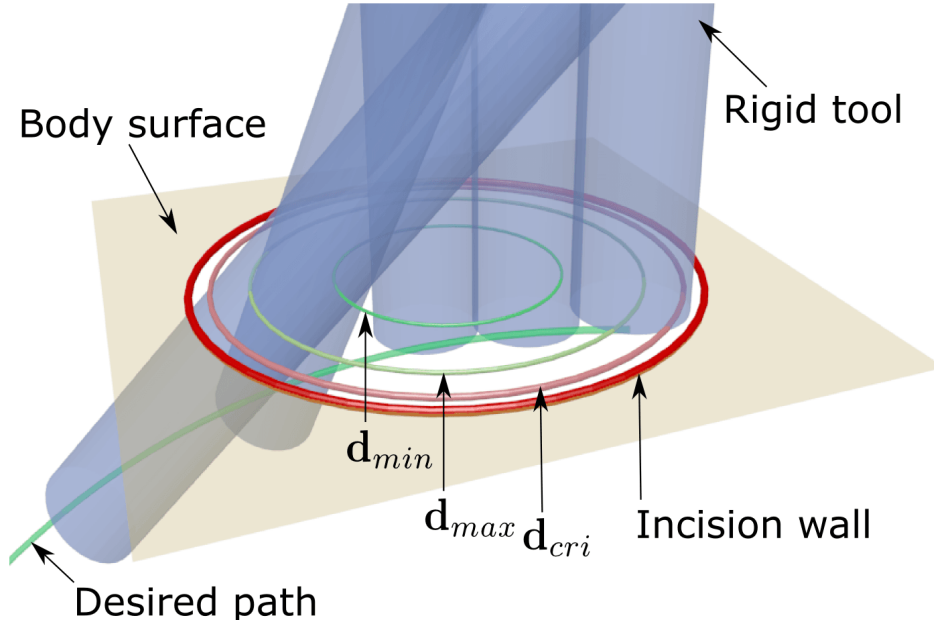


FIGURE 4.12: The UCM movement of the tool to follow the desired path.

The gain α_{obs} depends on the linear error between the incision centre point and the tool body. This error is represented by the projection distance (\mathbf{d}_{rcm}) which is obtained as:

$$\mathbf{d}_{rcm} = (\mathbf{I}_{3 \times 3} - {}^e \mathbf{u}_{et'} {}^e \mathbf{u}_{et'}^T) {}^e \mathbf{er}. \quad (4.51)$$

Besides that, the distance between the incision wall to the incision centre point is characterized by three distant spaces (FIGURE 3.24): i) a minimum distance (d_{min}), ii) a maximum distance (d_{max}), and iii) a critical distance (d_{cri}).

The strategy to achieve the UCM task alongside the path following task is done by switching the priority between both tasks (4.50) and (4.48), respectively. Such a hierarchy is defined in term of the tool position within the incision hole. Therefore, the incision hole is divided into two main regions: i) the safe region begins from the incision centre point until the critical distance, and ii) critical region is bounded between the critical distance and the orifice wall.

Case: tool within the safe region The tool is free to move within this region, when the norm of projected distance $\|\mathbf{d}_{rcm}\|$ is smaller than the critical distance d_{cri} . During this situation, the path following task (4.48) has the highest priority and the secondary task is the UCM task (4.50). Therefore, the end-effector twist vector is defined as the general form of projection gradient method (4.44):

$${}^e \underline{\mathbf{v}}_e = \mathbf{L}_{ePF}^\dagger {}^e \mathbf{v}_t + \tilde{\mathbf{L}}_{eRCM}^\dagger \left(-\alpha_{obs} \lambda \mathbf{e}_{rcm} - \mathbf{L}_{eRCM} \mathbf{L}_{ePF}^\dagger {}^e \mathbf{v}_t \right) \quad (4.52)$$

whereby $\tilde{\mathbf{L}}_{e_{RCM}} = \mathbf{L}_{e_{RCM}} (\mathbf{I} - \mathbf{L}_{PF}^\dagger \mathbf{L}_{PF})$.

Case: tool within the critical region When the norm of projected distance $\|\mathbf{d}_{rcm}\|$ is bigger than the critical distance d_{cri} , the tool is forced to get back into the safe region. In this situation, the UCM task becomes the first priority and the path following has a lower priority. Consequently, the end-effector twist vector is refined as:

$${}^e \underline{\mathbf{v}}_e = -\alpha_{obs} \lambda \mathbf{L}_{e_{RCM}}^\dagger \mathbf{e}_{rcm} + \tilde{\mathbf{L}}_{PF}^\dagger \left({}^e \mathbf{v}_t + \alpha_{obs} \lambda \mathbf{L}_{PF} \mathbf{L}_{e_{RCM}}^\dagger \mathbf{e}_{rcm} \right). \quad (4.53)$$

4.3 Numerical validation

The results obtained in this part are performed with the simulator which is presented in Section 3.3. The scenario of the tool motion is generally divided into two phases:

- i) *Approach phase* starts when the tool is located outside the incision hole. During this phase, the tool should approach the incision hole and align the tool pose with respect to that of the incision hole.
- ii) *Insertion phase* begins when the tool passes the external surface of incision hole. During this phase, the tool should maintain the RCM/UCM constraints and it should follow the reference path within the patient's body.

The flowchart of the complete controller which performs the proposed scenario is shown in FIGURE 4.13. It is also valid to control the proposed simulator as well as a real robot⁴. However, the only difference between both setups (i.e., the simulator and the robot) is the usage of a camera (i.e., the second block in FIGURE 4.13). Therefore, a virtual camera is added to the simulator.

The user starts the program by initializing the different gain parameters (i.e., λ for the alignment task (4.46), γ for the approach task (4.55), and v_{tis} , β' and ϵ for the path following task (4.32)). In fact, the tasks are arranged during the approach phase as: i) the alignment task (4.46) with the highest priority, and ii) the secondary task is reducing the distance error (4.54) between the initial position of the tool tip frame \mathbf{o}_t and that of trocar point frame \mathbf{o}_r . Such an error is regulated by a simple proportional controller as:

$$\mathbf{e}_{app} = {}^e \mathbf{tr} = {}^e \mathbf{r} - {}^e \mathbf{t} \quad (4.54)$$

$$-\gamma \mathbf{e}_{app} = \underbrace{[\mathbf{I} \quad -[{}^e \mathbf{r}]_\times]}_{\mathbf{L}_{e_{app}}} \underbrace{\begin{bmatrix} {}^e \mathbf{v}_e \\ {}^e \omega_e \end{bmatrix}}_{{}^e \underline{\mathbf{v}}_e} \quad (4.55)$$

whereby (γ) is a positive gain factor which affects the approaching velocity, and ($\mathbf{L}_{e_{app}}$) is the interaction matrix of the approaching task.

⁴See the next Section 4.4 for more details about the experimental validation.

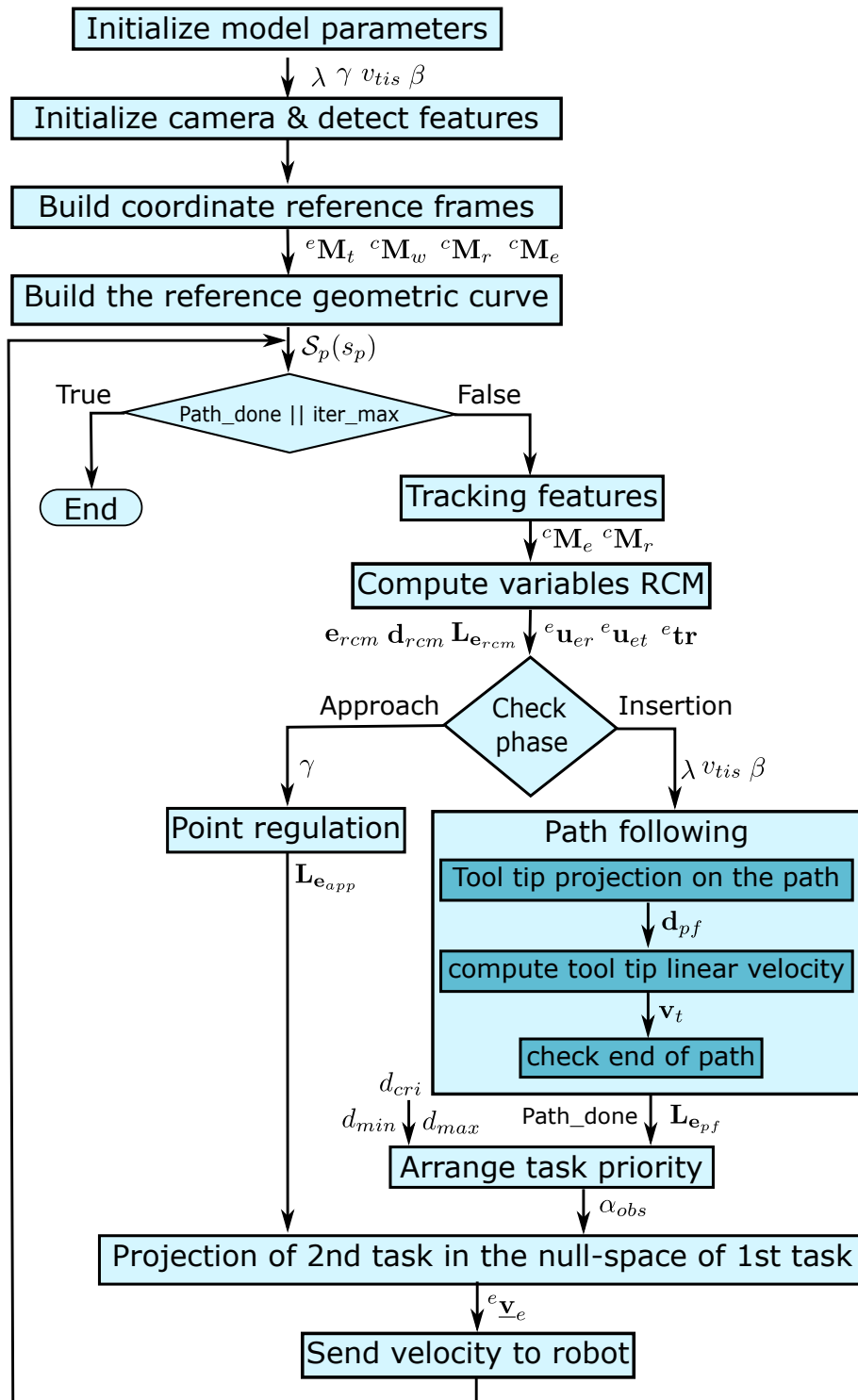


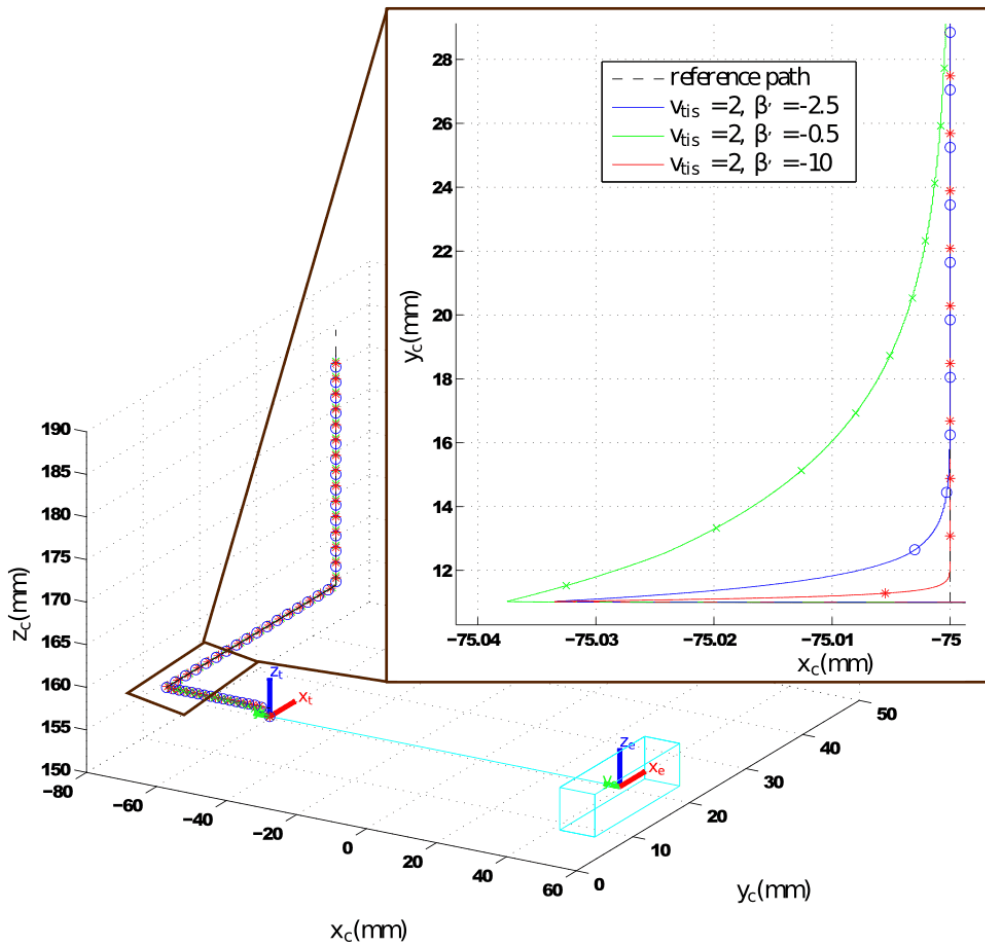
FIGURE 4.13: Flowchart of the simulator to execute the desired path under the RCM/UCM constraints.

During the insertion phase, the task priority controller acts as explained previously in Section 4.2. The aim of this part is identifying the strategy to choose the gain parameters.

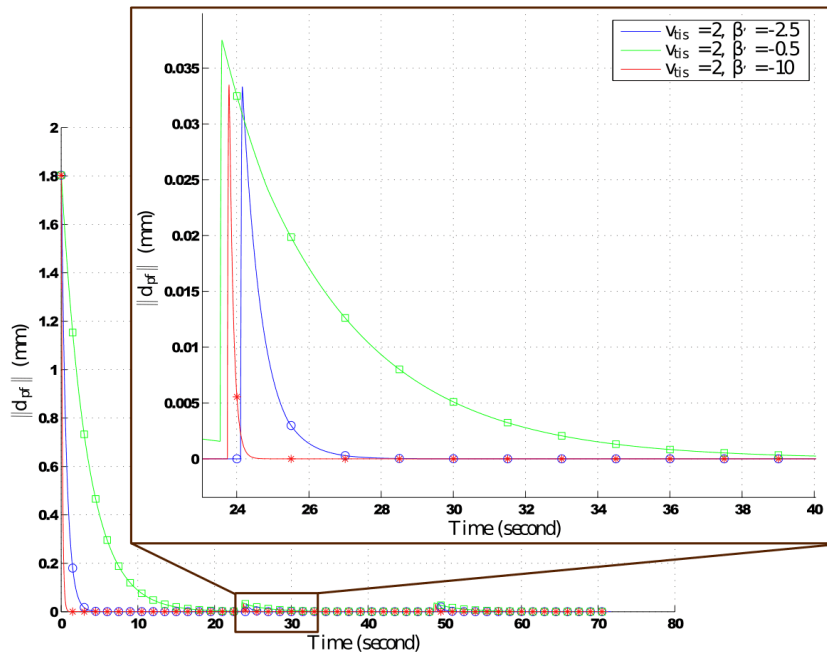
4.3.1 3D path following controller

The path following task was explained in Section 4.1.2. The proposed controller in equation (4.32) has two variables which are: i) the desired velocity along the path v_{tis} , and ii) the gain coefficient for returning to the path β' . These variables are free to be chosen by the user. The objective of this part is to show the effect of these variables on the system performance.

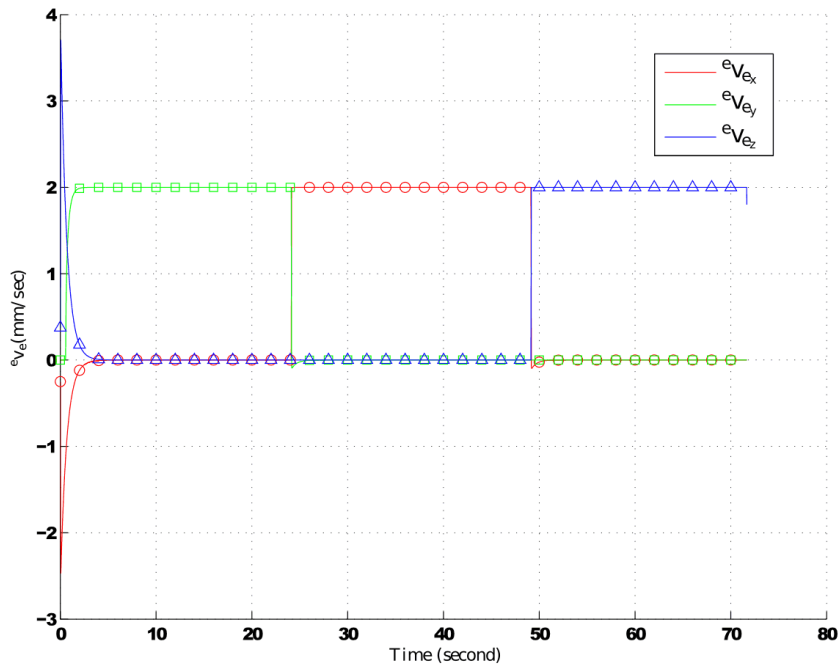
Straight tool follows a straight path: To better understand the choice of these variables (i.e., v_{tis} and β'), FIGURE 4.14 visualizes the choice effect. A step input for the controller is performed by defining a simple linear curve that translates in the plans XY , YZ and XZ , respectively (FIGURE 4.14(a)). This graph shows the reference path



(a) the simulated motion in the 3D space



(b) the path following error $\|\mathbf{d}_{pf}\|$ during the simulated motion



(c) The control linear velocity of the end-effector when $\beta' = -2.5$ and $v_{tis} = 2\text{mm/s}$

FIGURE 4.14: A straight path done by a straight tool when changing the value of β' from -0.5 to -10 .

and the tool tip motion expressed in the camera frame. It shows also the initial frame of the end-effector and that of the tool tip.

FIGURE 4.14(c) presents the control velocity which is applied to the end-effector in order to follow the desired path. In the beginning, the tool regulates the errors along the x- and the z-axes, then it follows the path along the y-axis. After that its velocity along the x-axis is active, while the velocity along the y-axis is deactivated. In the end, the tool velocity along the z-axis reaches the desired velocity to finish the reference path.

Effect of β' : As proved in Section 4.1.3, β' should be a negative scalar to achieve the system stability. The influence of β' is shown in FIGURE 4.14(b) by varying its value from -0.5 to -10 , while the others weighting factors kept constant (i.e., $v_{tis} = 2\text{mm/s}$ and $\epsilon = -1$). By reducing β' , the system reaches quickly the stability point, as depicted in FIGURE 4.14(b). This graph shows that the path following error $\|\mathbf{d}_{pf}\|$ is reduced exponentially as designed. It is difficult for the controller to predict a pointed corner (i.e., discontinuous path). Therefore, two peaks are observed in the error plot, where a zoom is made on one of these two peaks as presented in FIGURE 4.14(b). To eliminate such a peak, the pointed corner should be smoothed by adding a fillet to the corner. It means that the path should be continuous in order to remove the error's peaks.

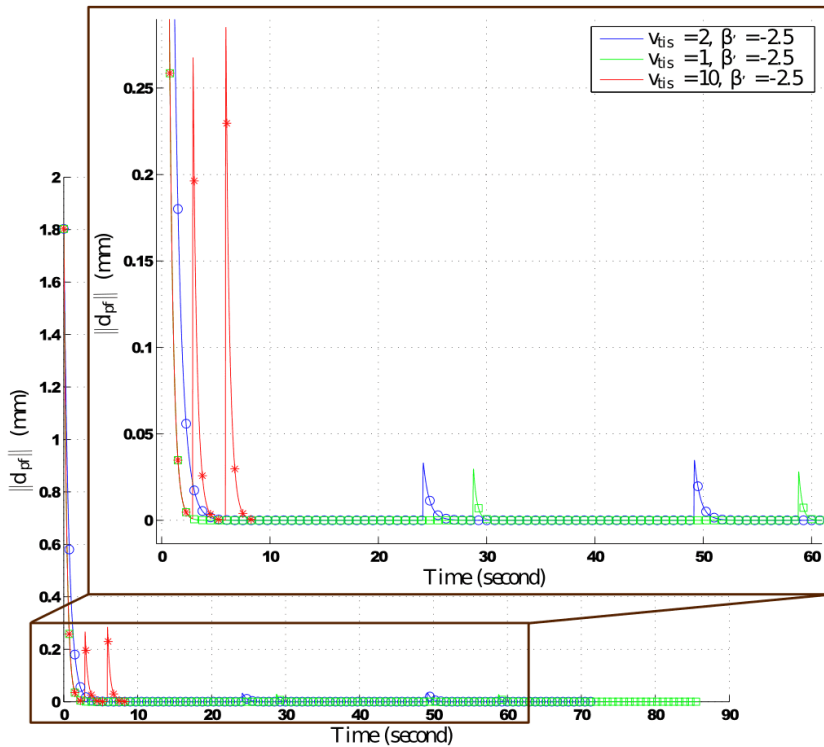
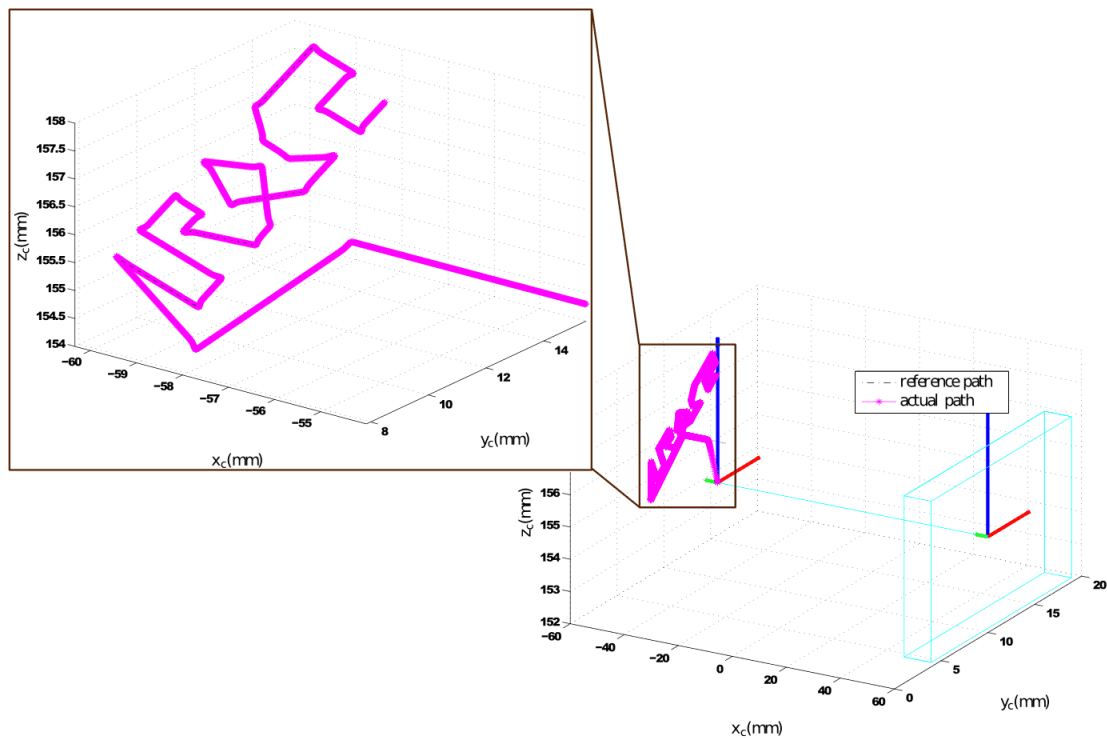


FIGURE 4.15: The path following error during the simulated motion of the linear path while changing the value of v_{tis} .

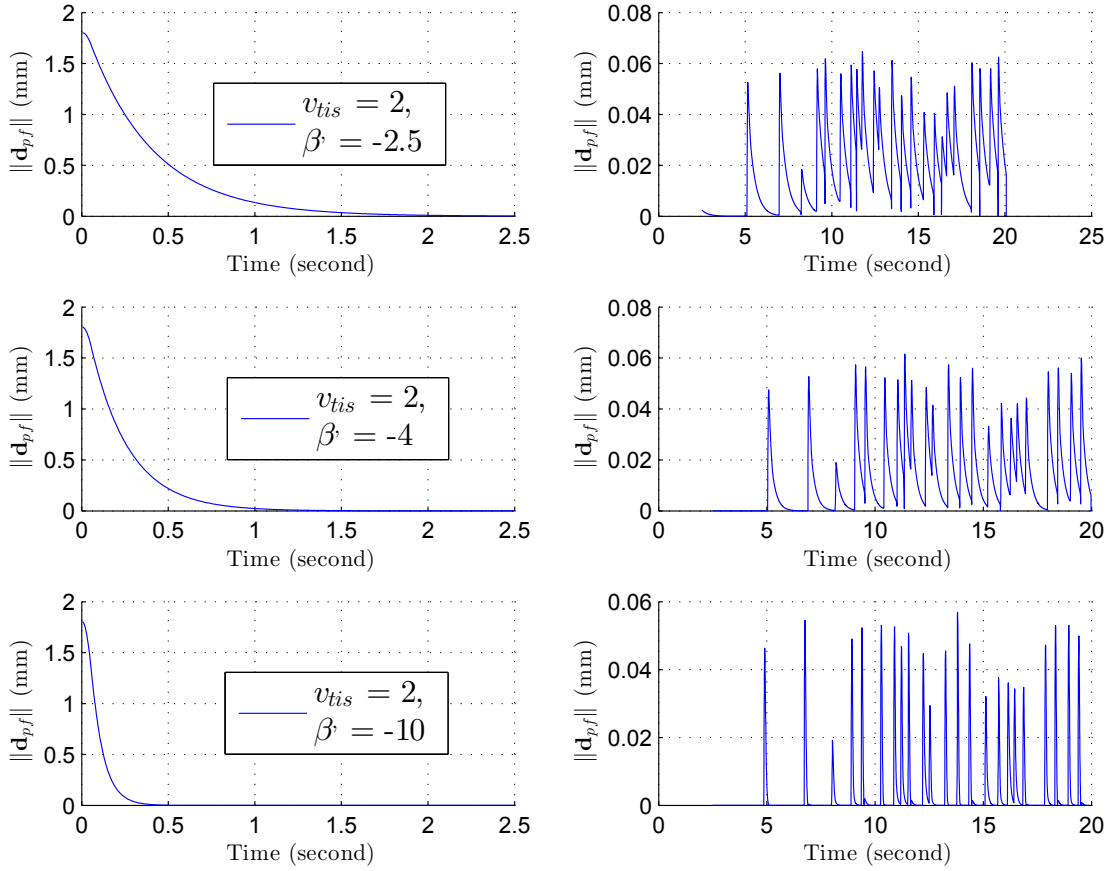
Effect of v_{tis} : The influence of v_{tis} is presented in FIGURE 4.15 by changing its value from 1 to 4mm/s, while the others weighting factors kept constant (i.e., $\beta' = -2.5$ and $\epsilon = -1$). If v_{tis} is high, the system will finish the reference path quickly but the path following error will be larger. On the contrary, when v_{tis} is small, an additional perturbation may add to the system due to the dry friction between the robot joints but the robot will be more precise. Thereby, there is a compromise to choose the gain values in order to obtain the desired performances. The value of β' should be greater than v_{tis} in order to ensure that the returning component has a greater priority than the advance component.

Straight tool follows a "UROCS" path: The last trial consists of following a path with sharp edges (FIGURE 4.16) which is considered as a more complex path compared to the previous trial. This trial tests a reference path which is defined as the word "UROCS" on an inclined plan, as depicted in FIGURE 4.16(a). In fact, this trial is repeated three times by varying β' from -2 , -4 , to -10 , while the other gain parameters remain constant (i.e., $v_{tis} = 2\text{mm/s}$, $\epsilon = -1$). The zoom plot in FIGURE 4.16(a) shows the output results when $\beta' = -10$.

FIGURE 4.16(b) shows the path following error \mathbf{d}_{pf} for the three configurations. The figure is divided into two columns as: i) the left one is a zoom on the error \mathbf{d}_{pf} during the initial stage where the tool approaches the path and it advances along the



(a) the simulated motion of the end-effector in the 3D space



(b) the path following error $\|\mathbf{d}_{pf}\|$ during the simulation

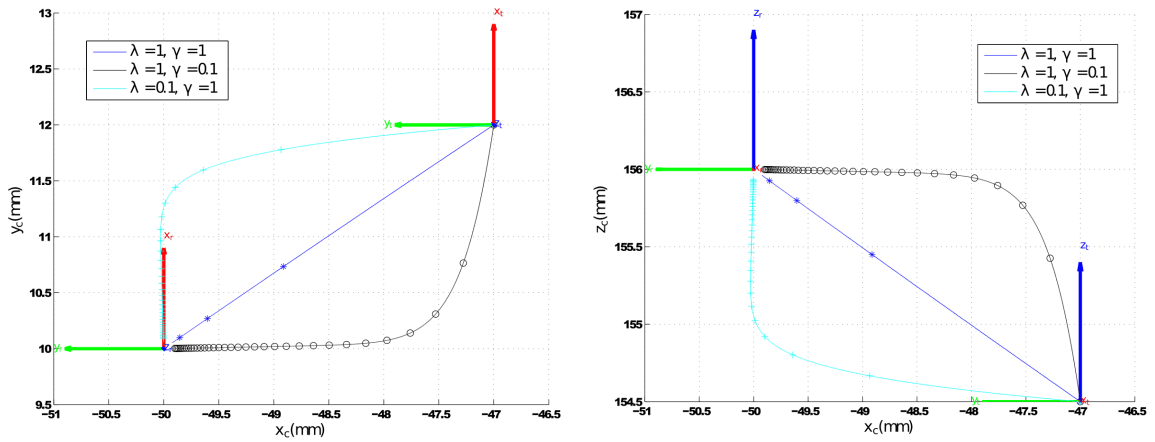
FIGURE 4.16: A "UROCS" path done by a straight tool, while changing the value of β' from -2 to -10 .

first linear path, and ii) the right one is a zoom on the error \mathbf{d}_{pf} during the rest of the "UROCS" path. The left column of FIGURE 4.16(b) shows how the error is reduced exponentially. The error is also reduced faster when the β' is bigger. The right column of FIGURE 4.16(b) shows the peaks which result from the pointed corner since the reference path is formed by a combination of line segments. The mean error of the path following is reduced during the three configurations from $0.05mm$, $0.03mm$ to $0.01mm$, respectively. The standard deviation is also reduced from $0.18mm$, $0.15mm$, to $0.11mm$.

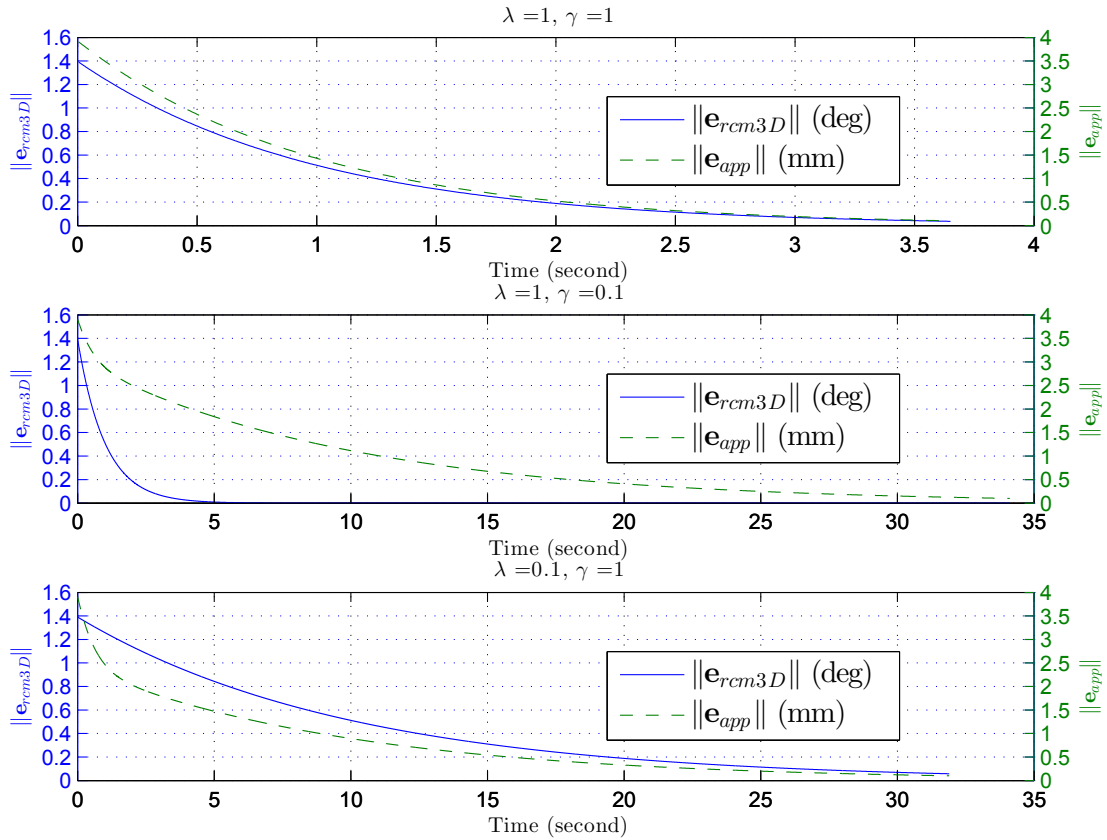
During all simulations, the sample time was constant $T_e = 0.005second$ (i.e., $200Hz$).

4.3.2 Task priority controller

The aim of this part is to test the complete controller which combines the path following task with either the RCM or the UCM tasks. This controller was presented in Section 4.2.



(a) the top view of the simulated motion (b) the side view of the simulated motion



(c) The RCM angular error \mathbf{e}_{rcm3D} and the approach error \mathbf{e}_{app} during the simulation

FIGURE 4.17: The controller performances during the approach phase while varying the values of λ and γ .

Approach phase: During this phase, it is required to achieve two tasks: i) the alignment task (4.46) in order to correct the angular error \mathbf{e}_{rcm3D} , and ii) the approach task (4.54) for eliminating the error \mathbf{e}_{app} between the initial position of the tool tip and the incision point. Moreover, the tasks priority throughout this phase is arranged in the same order as mentioned respectively. Therefore, the gain parameters λ and γ , in equations (4.46) and (4.54) respectively, effect the system performances (FIGURE 4.17).

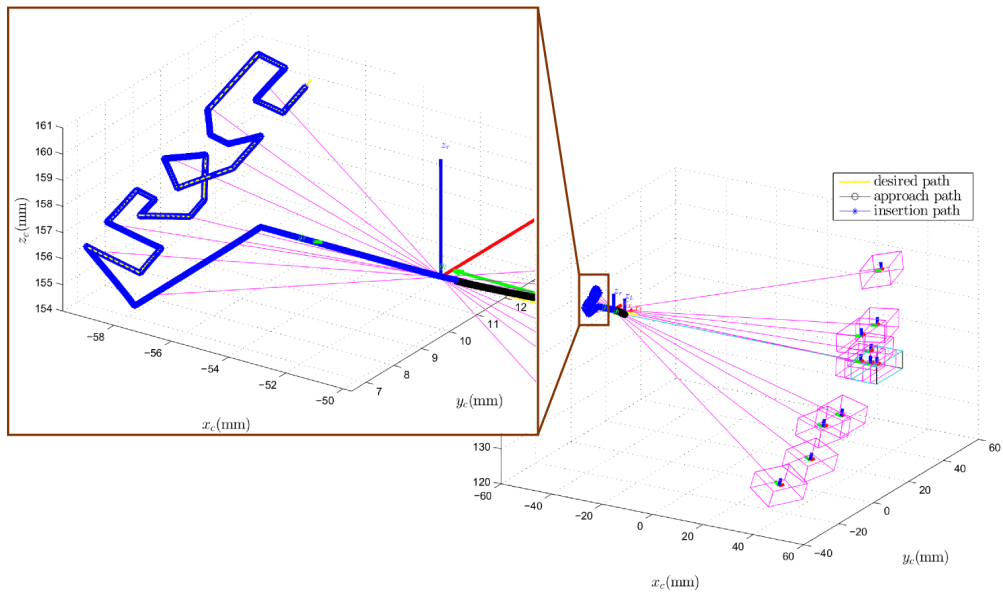
The blue star line in FIGURE 4.17(a) and (b) shows the system behaviour when the two parameters are equal (i.e., $\lambda = \gamma = 1$). The upper graph in FIGURE 4.17(c) shows the errors \mathbf{e}_{rcm3D} and \mathbf{e}_{app} . When the value of λ is greater than γ (i.e., black round line in FIGURE 4.17(a) and (b)), the system tends to reduce the alignment task error \mathbf{e}_{rcm} faster than the approach task error \mathbf{e}_{app} . This behaviour is observed in the middle graph in FIGURE 4.17(c) where the approach error took more time, compared to the upper graph in the same figure, in order to be eliminated. In opposition, when γ is greater than λ , the approach task converges faster than the alignment task (plus line in FIGURE 4.17(a) and (b)). The lower graph in FIGURE 4.17(c) demonstrates that the RCM angular error \mathbf{e}_{rcm3D} consumed more time, compared to the upper graph in the same figure, in order to be eliminated.

Therefore, it is recommended to chose the gain λ bigger than the gain γ in order to ensure that the RCM task has priority over the approach task. The approach error is also used to switch between the approach and the insertion phases. When the error $\mathbf{e}_{app} = 0.1mm$, the controller switches to the insertion phase.

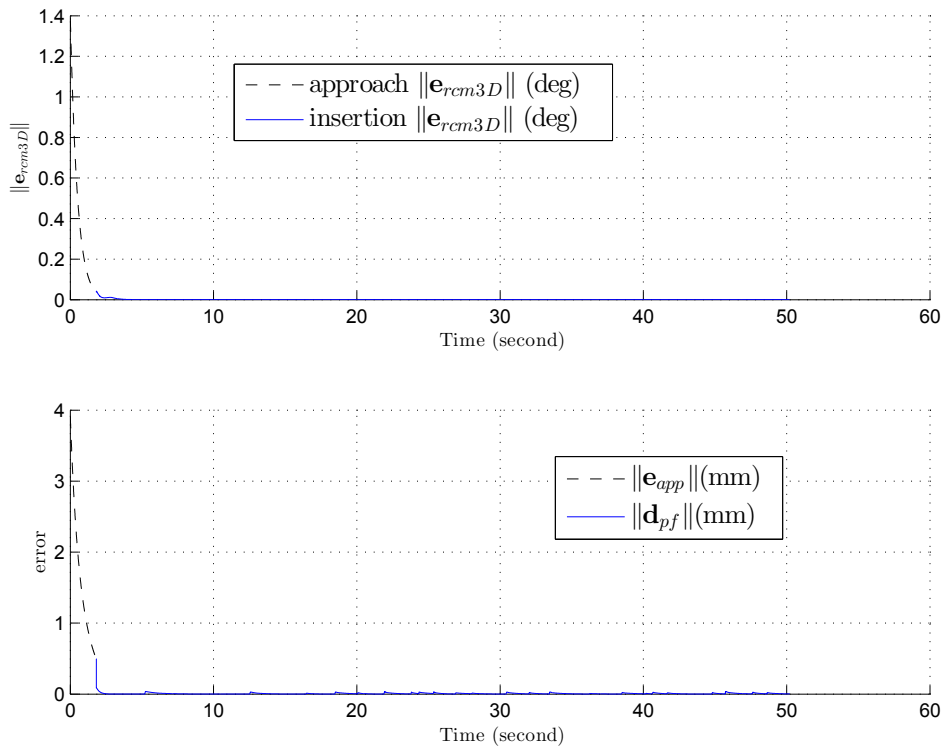
Insertion phase: During this phase, it is needed to achieve two tasks: i) the path following task (4.48) in order to eliminate the error \mathbf{d}_{pf} , and ii) the alignment task with respect to the incision hole which can be done either by the RCM task (4.46) or the UCM task (4.50). Thus, the path following gain parameters (i.e., v_{tis} , β' and ϵ in equation (4.32)), alongside the alignment task parameters (i.e., λ and α_{obs} in equations (4.46) and (4.50)) have their impact on the system performances.

RCM movement with a straight tool: This trial performs the complete scenario, where the tool is initially placed far from the incision hole. Then the tool approaches to the centre point of the incision hole (4.54), while the tool aligns its pose with that of the incision hole (4.46). After that the tool should follow the reference path (4.48) under the RCM constraint (4.46). Throughout the insertion phase, the RCM task has the highest priority while the path following is the secondary task. Indeed, a straight tool is used to follow the "uRoCS" path as depicted in FIGURE 4.18(a). This plot shows also how the tool body stayed on the centre point of the incision hole while the tool tip reaches the distal target points.

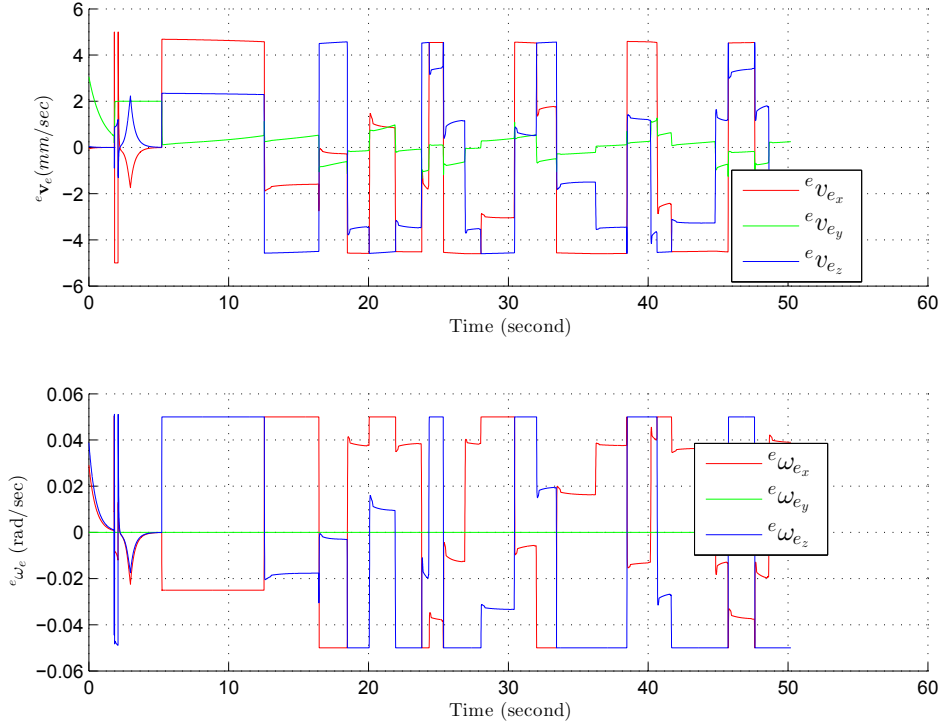
Throughout the approach phase, the angular RCM error \mathbf{e}_{rcm} and the approach error \mathbf{e}_{app} are depicted as a black dash line in the upper and the lower graphs in FIGURE 4.18(b), respectively. As expected, the alignment error \mathbf{e}_{rcm} is exponentially reduced (see the upper graph in FIGURE 4.18(b)). In addition, the approach error switches the controller to the insertion phase, when $\mathbf{e}_{app} = 0.5mm$ (see the lower graph in FIGURE 4.18(b)).



(a) a global view on the end-effector motion with a zoom on the reference path and the actual path which is done by the tool tip



(b) the angular RCM error task \mathbf{e}_{rcm3D} alongside the path following error \mathbf{d}_{pf} and the approach error \mathbf{e}_{app}



(c) the control twist velocity of the end-effector

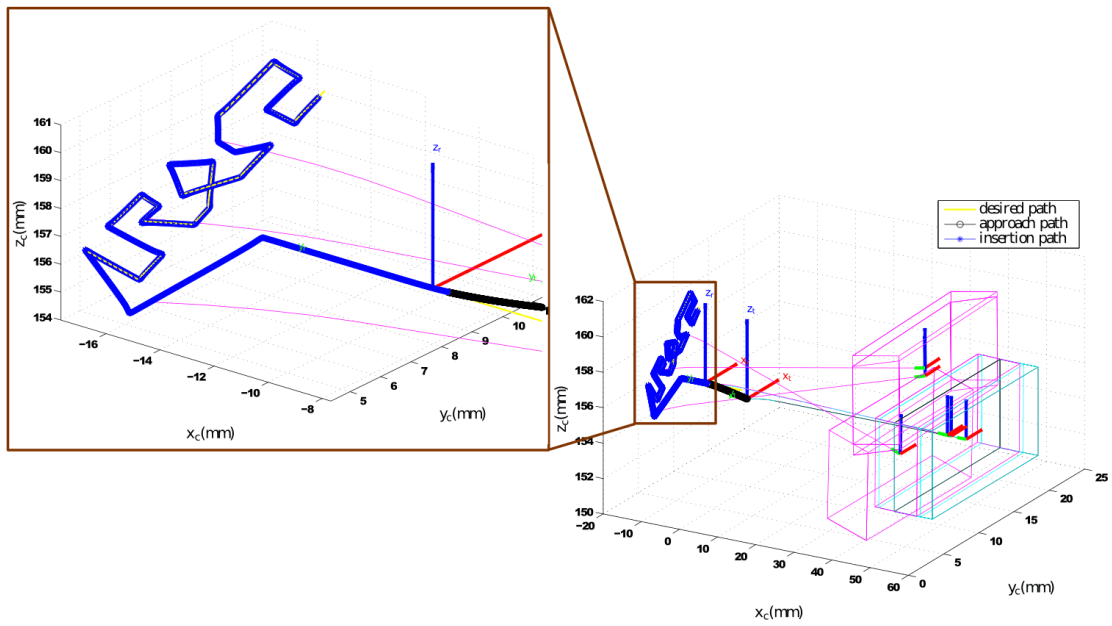
FIGURE 4.18: The trial of the path following task with the RCM task while using a straight tool.

During the insertion phase, the RCM error \mathbf{e}_{rcm} and the path following error \mathbf{d}_{pf} are illustrated as a blue continuous line in the upper and the lower graphs in FIGURE 4.18(b), respectively. As expected, the RCM error \mathbf{e}_{rcm} remains constant at zero. In fact, some numerical noise is measured as $0.001 \pm 0.002^\circ$ (the mean error plus or minus the standard deviation error). The path following error was also small through this phase, where the mean and the standard deviation errors were $0.007 \pm 0.01mm$.

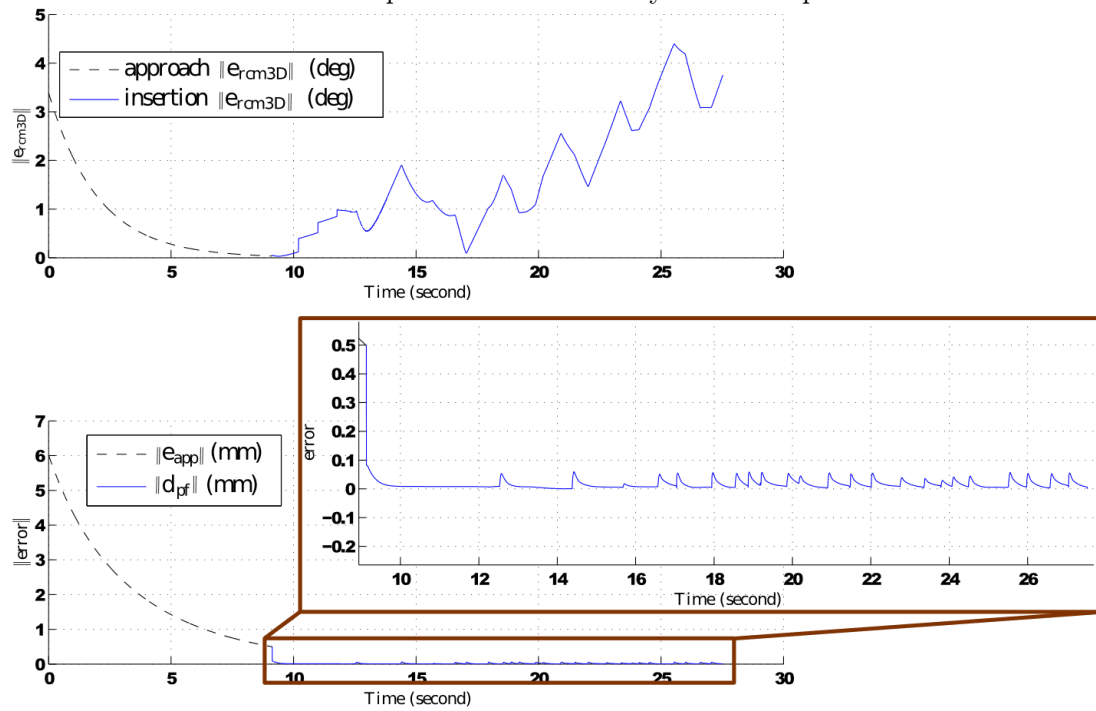
The gain parameters was chosen as $\lambda = 2$, $\gamma = 1$, $v_{tis} = 2mm/s$, $\epsilon = -1$, $\beta' = -4$ and $T_e = 0.005s$. The control twist velocity is also presented in FIGURE 4.18(b).

RCM movement with a curved tool: This trial repeats the previous trial but it uses a circular tool as depicted in FIGURE 4.19(a). During the approach phase, the task priority controller arranges the RCM task (4.46) as the highest priority and the approach task (4.54) as the secondary priority. The angular RCM error \mathbf{e}_{rcm3D} and the approach error \mathbf{e}_{app} are reduced exponentially as expected (see the black dash lines in the upper and the lower graphs in FIGURE 4.19(b), respectively).

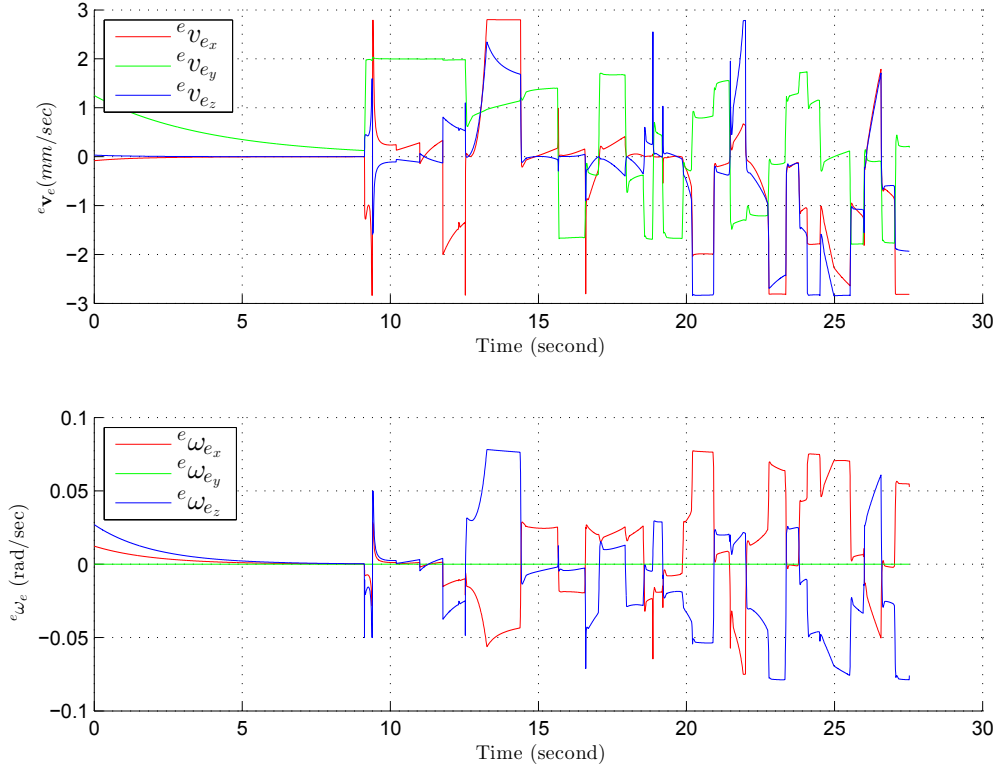
Through the insertion phase, the controller has encountered difficulties to achieve the global objective by arranging the RCM task (4.46) as the highest priority and the path following task (4.48) as the secondary priority. Indeed, the RCM task added too



(a) a global view on the end-effector motion with a zoom on the reference path and the actual path which is done by the tool tip



(b) the angular RCM error task e_{rcm3D} alongside the path following error d_{pf} and the approach error e_{app}



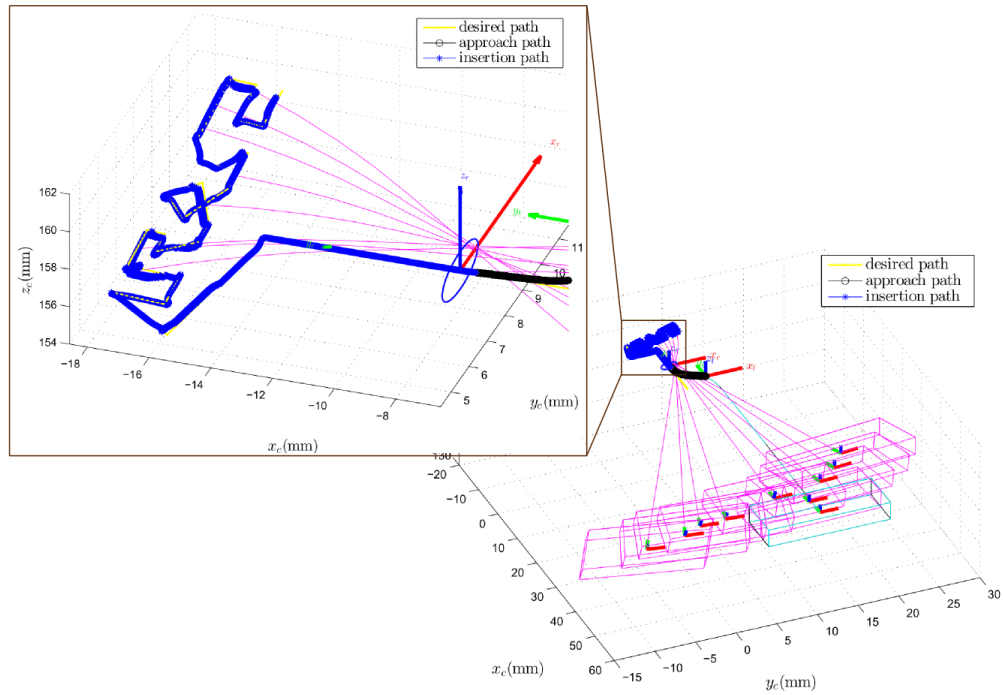
(c) the control twist velocity of the end-effector

FIGURE 4.19: The trial of path following task with the RCM task while using a circular tool.

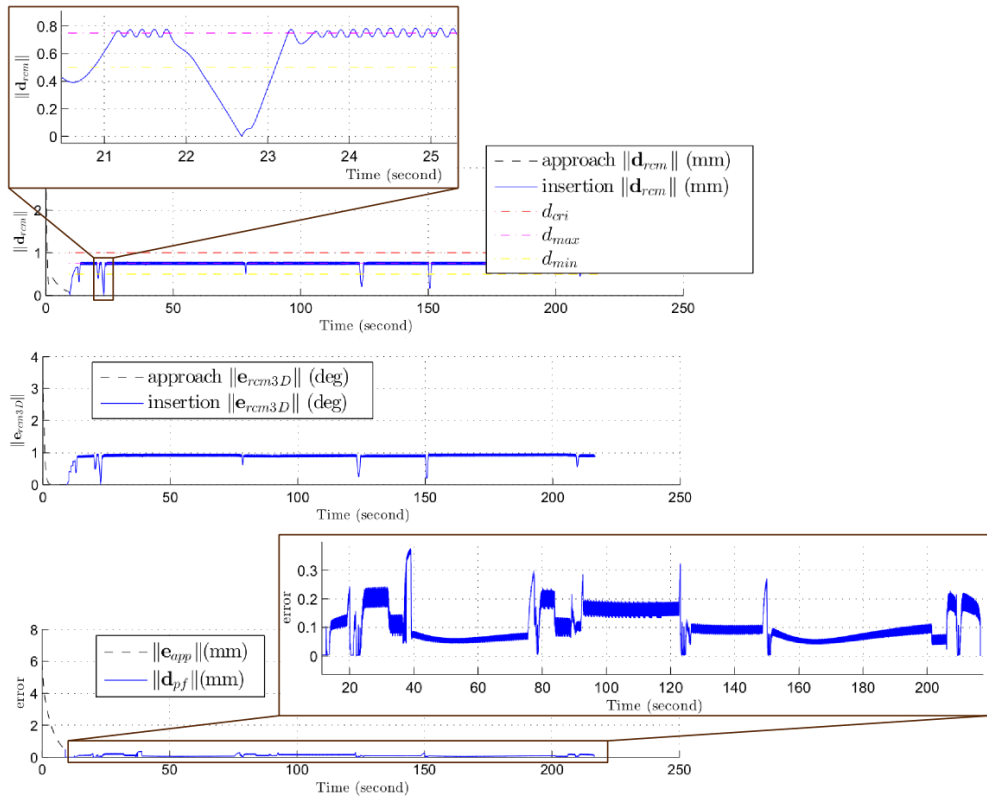
may constraints on the curved tool. Besides that, the controller cannot find out the optimal solution to satisfy both the RCM task and the path following task. Thereby, the hierarchical form is changed to consider the path following task as the highest priority and the RCM task as the secondary task. Consequently, the path following error \mathbf{d}_{pf} was small during this phase, where its mean error and its standard deviation were $0.016 \pm 0.017mm$ and (see the blue continuous line in the lower graph in FIGURE 4.19(b)).

In opposition, the RCM error \mathbf{e}_{rcm3D} was big, where its mean error and its standard deviation were $1.68 \pm 1.15^\circ$ (see the blue continuous line in the upper graph in FIGURE 4.19(b)). The gain parameters were $\lambda = 0.5$, $\gamma = 0.25$, $T_e = 0.005s$, $v_{tis} = 2mm/s$, $\epsilon = -1$ and $\beta' = -4$. FIGURE 4.19(c) presents the control twist velocity of end-effector.

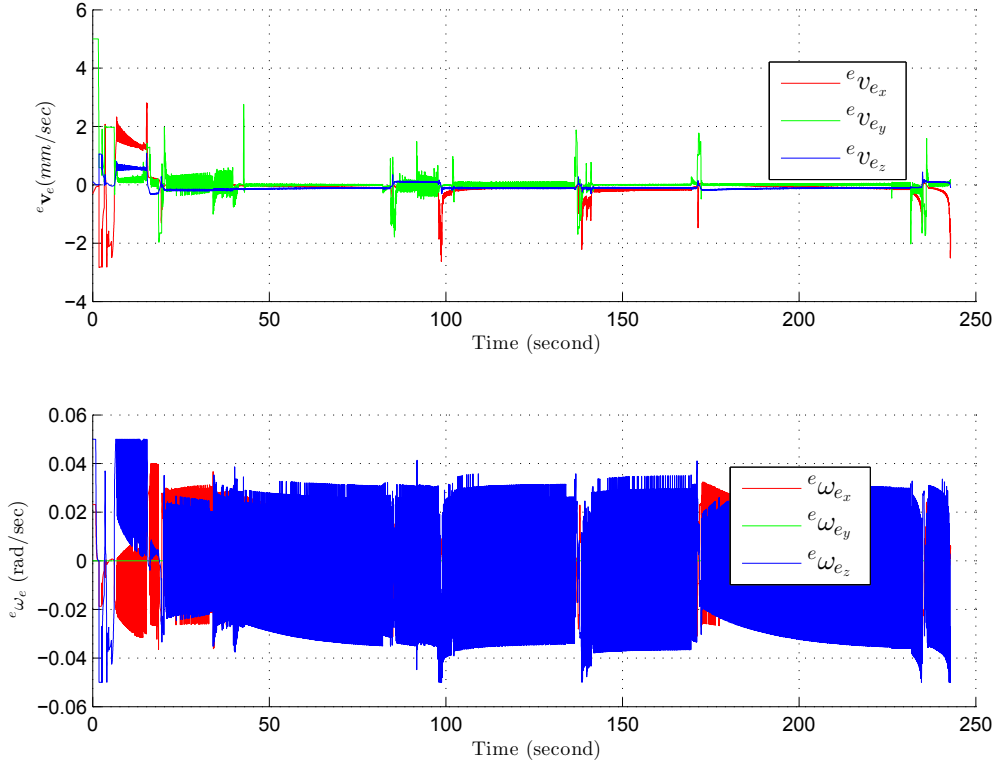
UCM movement with a curved tool: This trial uses the circular tool as the previous trial but it applies the UCM constraint. Through the approach phase, the task priority controller is similar to the previous trial. Indeed, it sets the highest priority for the alignment task (4.46), while the second priority for the approach task (4.54).



(a) A global view on the end-effector motion with a zoom on the reference path and the actual path which is done by the tool tip



(b) the linear RCM error task \mathbf{d}_{rcm} alongside the angular RCM error task \mathbf{e}_{rcm3D} , the path following error \mathbf{d}_{pf} and the approach error \mathbf{e}_{app}



(c) the control twist velocity of the end-effector

FIGURE 4.20: The trial of the path following task with the UCM task while using a circular tool.

During the insertion phase, it is required to execute the UCM task. Thus the incision hole is divided into three distances: i) the minimum distance d_{min} where a safe region is defined from this distance until the centre point of the incision hole, ii) the maximum distance d_{max} where a critical region is described between this distance and the d_{min} , and iii) the critical distance d_{cri} where a dangerous region is characterized between this distance and the incision wall. These regions are used to select the tasks hierarchy and the stiffness of the virtual spring α_{obs} . The zoom plot in FIGURE 4.20(a) represents the critical distance d_{cri} by a circle on the XZ-plan of the incision hole frame. Throughout the simulation, the tool body does not violate the incision wall and the tool laid on the incision wall to reach the distal target points.

The controller arranges the tasks according to the projected distance of the incision hole's centre point onto the tool body \mathbf{d}_{rcm} . If the Euclidean norm of the projected distance $\|\mathbf{d}_{rcm}\|$ is smaller than the $d_{min} = 0.5mm$, then the tool body is located in the safe region where the controller executes only the path following task (4.48). When the tool stands in the critical region (i.e., $d_{min} \leq \|\mathbf{d}_{rcm}\| < d_{max}$, where $d_{max} = 0.75mm$), the controller arranges the path following task as the highest priority and the UCM task (4.50) as the secondary priority. When the tool is located in the dangerous region (i.e.,

$d_{max} \leq \|\mathbf{d}_{rcm}\| \leq d_{cri}$, where $d_{cri} = 1mm$), the controller changes the priority by putting the UCM task as the first priority and the path following task as the second task.

This switching between the tasks priority generates an oscillation around the d_{max} level as depicted in the upper and the middle graphs of FIGURE 4.20(b). This oscillation is also observed in the control twist velocity in FIGURE 4.20(c). However, the tool tip is successfully finished the reference path. The path following error \mathbf{d}_{pf} is presented in the lower graph of FIGURE 4.20(b), where its mean error and its standard deviation are measured as $0.1 \pm 0.05mm$. This error \mathbf{d}_{pf} is bigger than that of the previous trial. Despite that the angular RCM error is smaller than the previous trial, where its mean and its standard deviation during this trial was $0.89 \pm 0.11^\circ$.

Note that the values of gain parameters were $\lambda = 2$, $\gamma = 0.25$, $T_e = 0.005s$, $v_{tis} = 2mm/second$, $\epsilon = -1$ and $\beta' = -8$.

4.4 Experimental validation

Before the intervention begins a CAS (Computer Assistant Surgery) software which will co-operating with the surgeon to decide the best strategy for reaching the region of interest within the patient's body. These pre-operative decisions are taken with the help of a planning software which creates a numerical model based on the pre-operative medical images. Besides that, the planning software assists to identify the optimal path/trajectory (e.g., [Gerber et al., 2014, Gasparetto et al., 2015]). Such an advanced planning software will be discussed in the perspectives; since the objective of this part is validating the control laws which guides a real robot throughout the intervention. Thereby, the different reference paths are defined by simple geometrical curves as spiral or a combination of straight lines.

During the intra-operative phase, a navigation software starts collecting information regarding the robot internal state (i.e., the pose of its end-effector with respect to its base) and its relative pose with respect to the targeted anatomical structure. The relative pose of the robot's end-effector is a very important information during this phase. The visual servoing control approaches [Chaumette and Hutchinson, 2006, Azizian et al., 2014] are convenient methods to guide the manipulator pose; since they mimic the perception sense of the surgeon. Such methods use a real-time imaging (e.g., conventional endoscope, optical coherence tomography or ultrasound) to detect, track and guide the instrument (e.g., [Krupa et al., 2002, Voros et al., 2007]).

This section evaluates the proposed controller during the navigation phase in order to guide a real robot for following a reference path under the constraint of RCM or UCM.

4.4.1 Trials with a parallel robot

This part evaluates the proposed approaches in order to follow a pre-defined 3D path besides that it maintains either the constraints of RCM or UCM. In addition, this part assesses the proposed control laws without the clinical environment.

The trials in this part were done by using a parallel robot of type 3PPSR. Indeed, this tripod robot is actuated by six DC continuous motors which control the six prismatic

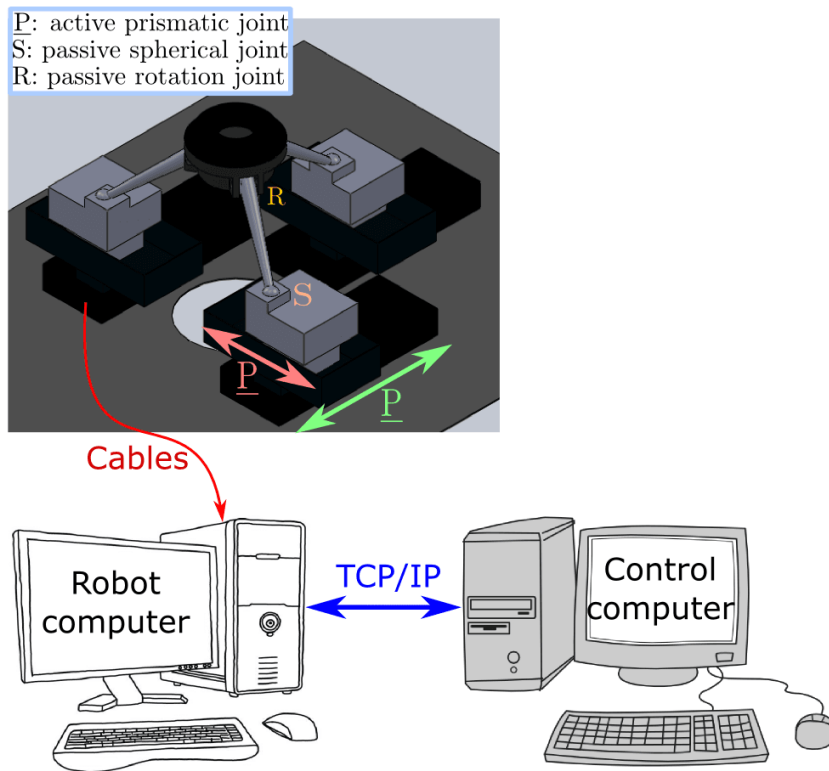


FIGURE 4.21: Conceptual scheme of the parallel robot.

joints as depicted in FIGURE 4.21, while the other joints are passive (i.e., the spherical and rotation joints). The 6-DOF parallel robot is also characterized with the following features⁵: translation ranges $(T_x, T_y, T_z)_{max} = (50mm, 100mm, 12.7mm)$ and rotation ranges $(R_x, R_y, R_z)_{max} = (10^\circ, 10^\circ, 10^\circ)$, a linear resolution of $0.2\mu m$ (repeatability of $\pm 0.5\mu m$) and an angular resolution of 0.0005° (repeatability of $\pm 0.0011^\circ$).

The robot's end-effector carries the tool adaptor which holds a standard surgical tool. The surgical tool (FIGURE 4.22) could be either: i) a straight tool where its diameter varies from $2.4mm$ at its base to $0.5mm$ at its distal tip, ii) a curved tool formed by a piecewise straight segments where its diameter varies from $2.5mm$ at its base to $1.75mm$ at its distal tip, or iii) a curved tool formed by a portion of a circle where its radius is around $83.5mm$ and the tool diameter is $1mm$.

The low-level control of robot (i.e., inner PID loop, static and differential kinematic models) is done by a PLC (Programmable Logic Controller) which communicates with a computer (a 2.33-GHz Xeon Intel CPU with a Windows distribution). The higher level control of robot (i.e., the task priority, the RCM/UCM movement and the path following controllers) is done on another computer (a 3.20-GHz i5 core Intel CPU with a Linux

⁵Addition information about the PI parallel robot *SpaceFAB SF-3000 BS* is available online. <https://www.physikinstrumente.com/en/products/parallel-kinematic-hexapods/hexapods-with-motor-screw-drives/sf-3000-bs-spacefab-1204400/>

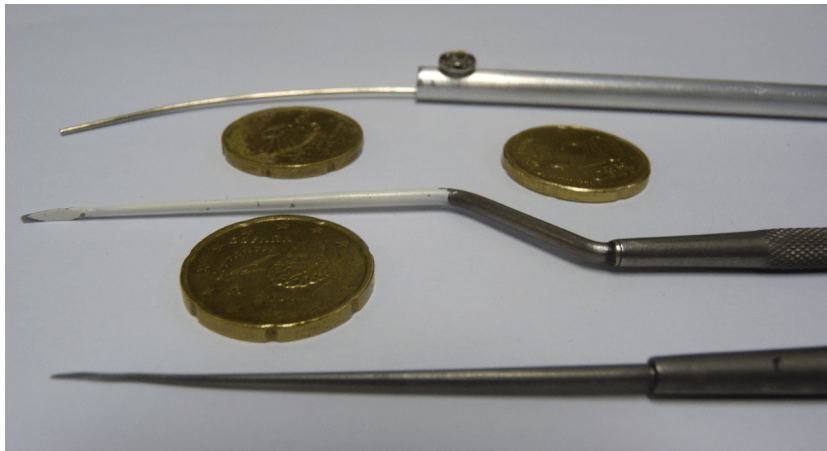


FIGURE 4.22: The different tool types, where a straight tool is located on the bottom, a piecewise straight tool is located in the middle, and a circular shape tool is located on the top.

distribution) which sends the twist control velocity to the robot computer via a TCP/IP communication protocol (FIGURE 4.21).

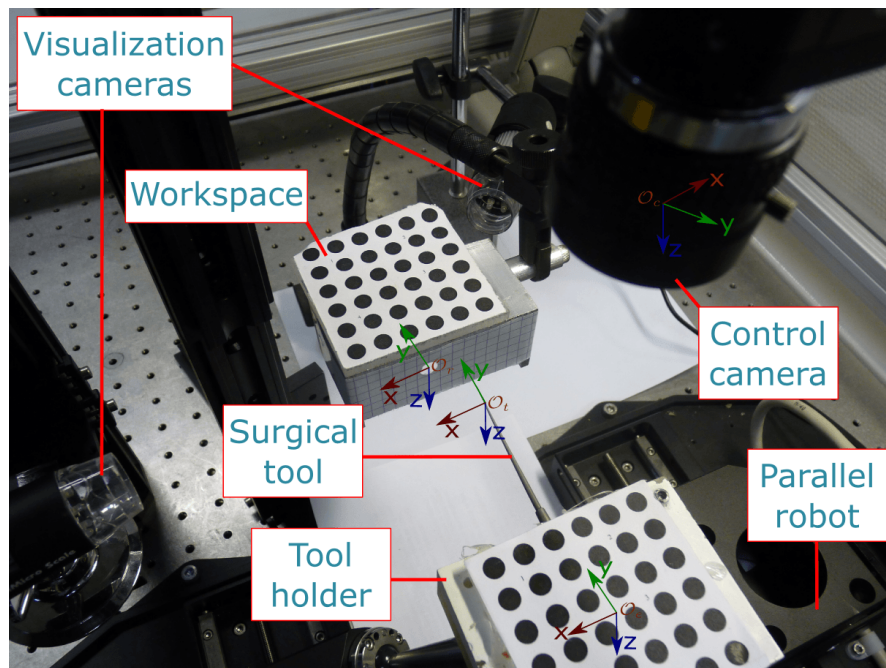


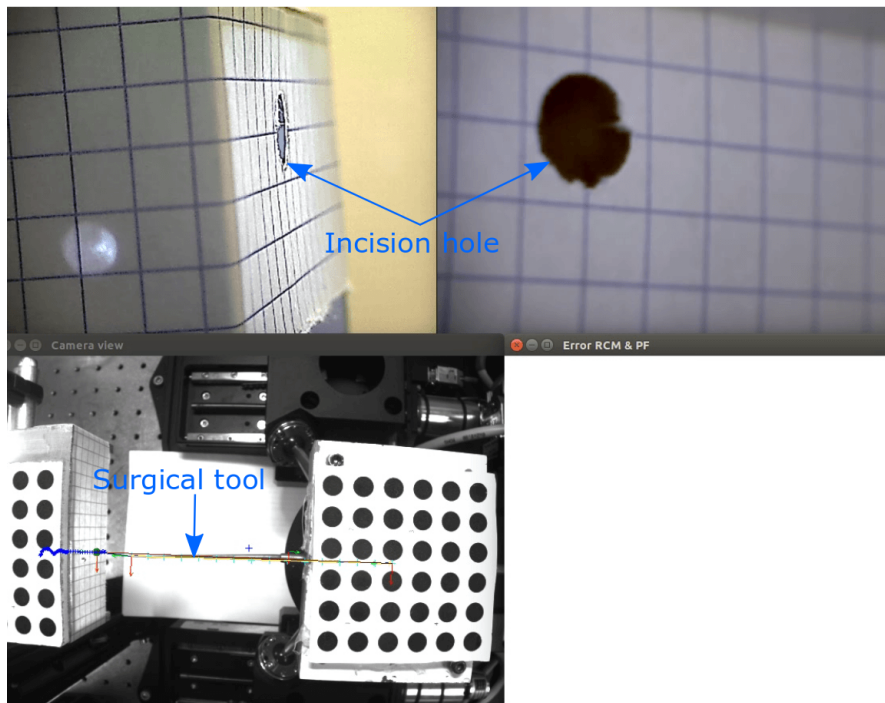
FIGURE 4.23: The experimental setup with the different coordinate frames of the end-effector, tool tip, incision hole and camera.

Besides that, the high level control computer is used to communicate with a monocular camera for tracking and estimating the pose of end-effector in real-time (FIGURE 4.23). Thus, the off-line camera calibration must be done as the first step in order to estimate the camera parameters (i.e., intrinsic and extrinsic parameters). Such a procedure could be done with the help of ViSP (Visual Servoing Platform ⁶) library [Marchand et al., 2005] or Matlab camera calibration toolbox ⁷. It is important to well calibrate the exteroceptive sensor (i.e., the camera); since its error will influence the controller performances. In fact, the calibration errors will be added to the external perturbations that act on the system, and the controller should overcome these perturbations. In other words, if the camera calibration is not good, the pose estimation of the target object in the camera frame (i.e., the pose of end-effector and that of incision hole) will not be precise. If the calibration errors are relatively small, the controller could converge to the stability. On the opposite, if the calibration error is relatively big, it will be difficult for the controller to compensate these errors.

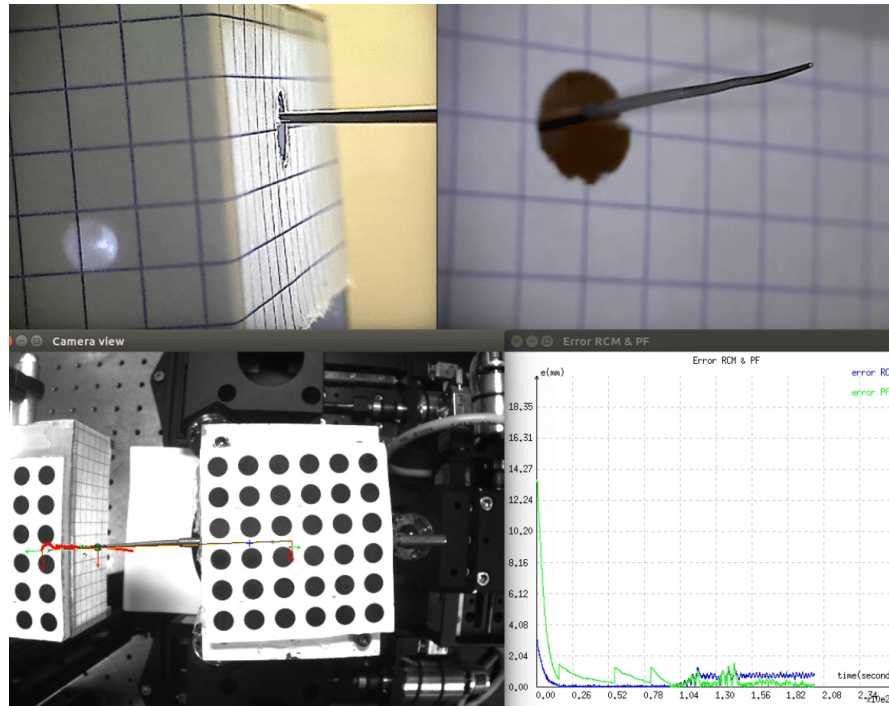
After the calibration step is done, the primary images are acquired by the control camera to extract the visual features of the target objects. This process allows estimating the initial pose of the end-effector and that of the incision hole in the camera frame. In fact, Dementhon algorithm [Dementhon and Davis, 1995] is used to estimate the

⁶ViSP library is available online. <https://visp.inria.fr/>

⁷Camera calibration toolbox for Matlab is available online. http://www.vision.caltech.edu/bouguetj/calib_doc/



(a) screen shot at the beginning of approach phase



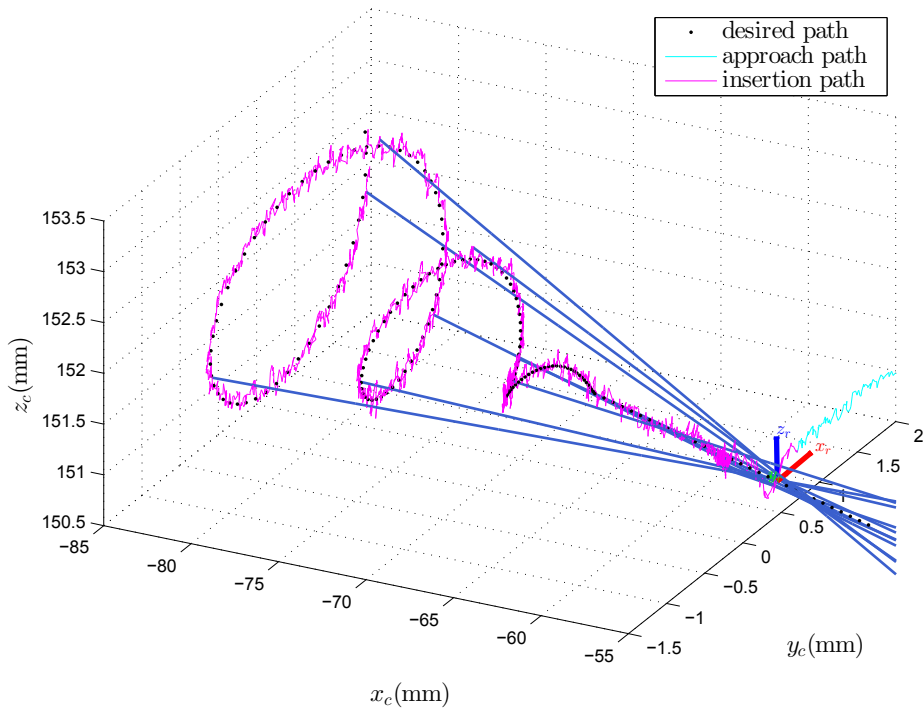
(b) screen shot at the end of insertion phase

FIGURE 4.24: Screen shot of the control computer, where the upper two windows are the images acquired by the visualization cameras, the lower left window is the images acquired by the control camera, and the lower right window is displaying the instantaneous errors of both RCM and path following tasks.

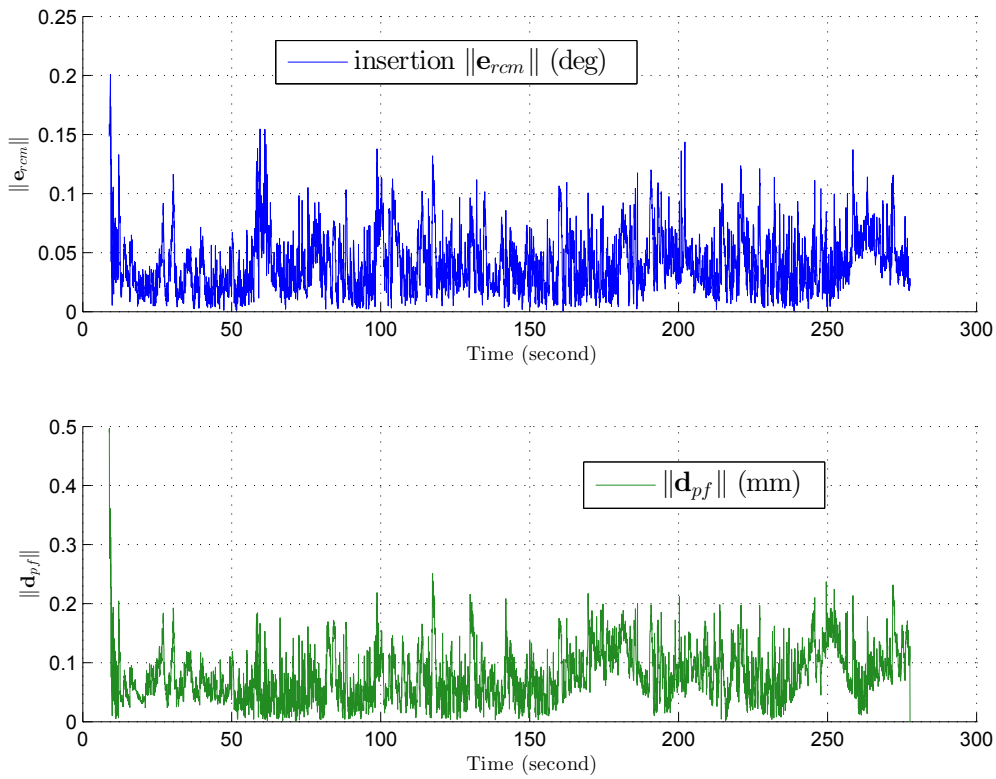
instantaneous pose of the extracted features with respect to the camera frame (using a single camera). This algorithm is robust for estimating the pose of an object but it required at least four features to deduce the pose. Thereby, a circular pattern is used to detect and track the incision point as presented in FIGURE 4.23. The wall of incision hole is formed by a piece of paper in order to verify that the tool body does not hit and tear the incision wall.

The complete experimental setup with the parallel robot is presented in FIGURE 4.23, where two additional cameras are added in order to observe the incision wall. However, these visualization cameras are not contributing in the control loop. They are only displaying the acquired images on the screen of the control computer, as shown in FIGURE 4.24. Another circular pattern is fixed on the tool holder in order to detect and track the end-effector pose. Besides that, the tool tip pose is easily deduced since the tool is rigid and its geometry is known. Thus the homogeneous transformation between the end-effector and the tool tip is fixed.

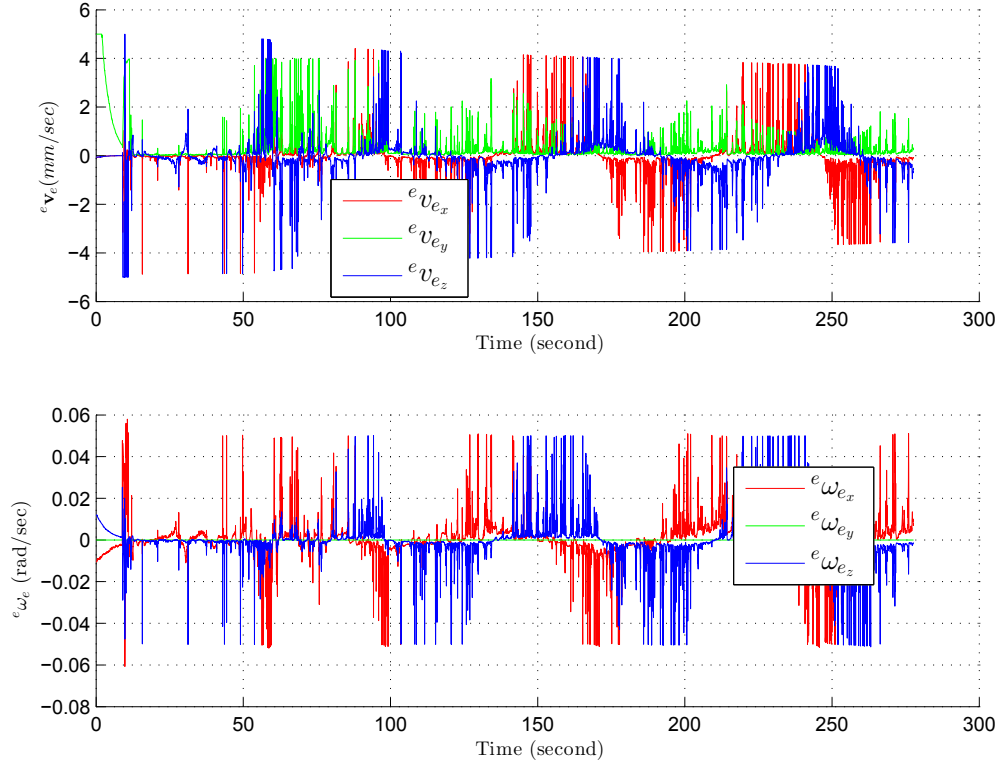
Straight tool follows a path under the RCM constraint: FIGURE 4.24 shows the screen shot of the control computer while executing the first trial which tests a straight



(a) a zoom view on the reference path and the actual path which is done by the tool tip



(b) the angular RCM error task \mathbf{e}_{rcm3D} and the path following error \mathbf{d}_{pf} during the insertion phase



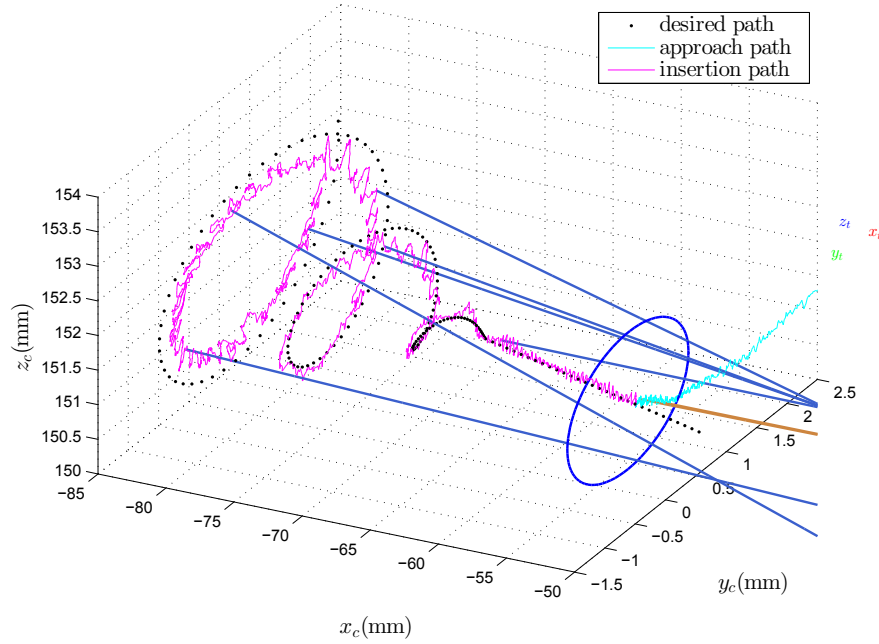
(c) the control twist velocity of the end-effector

FIGURE 4.25: The trial of path following task with the RCM task while using a straight tool.

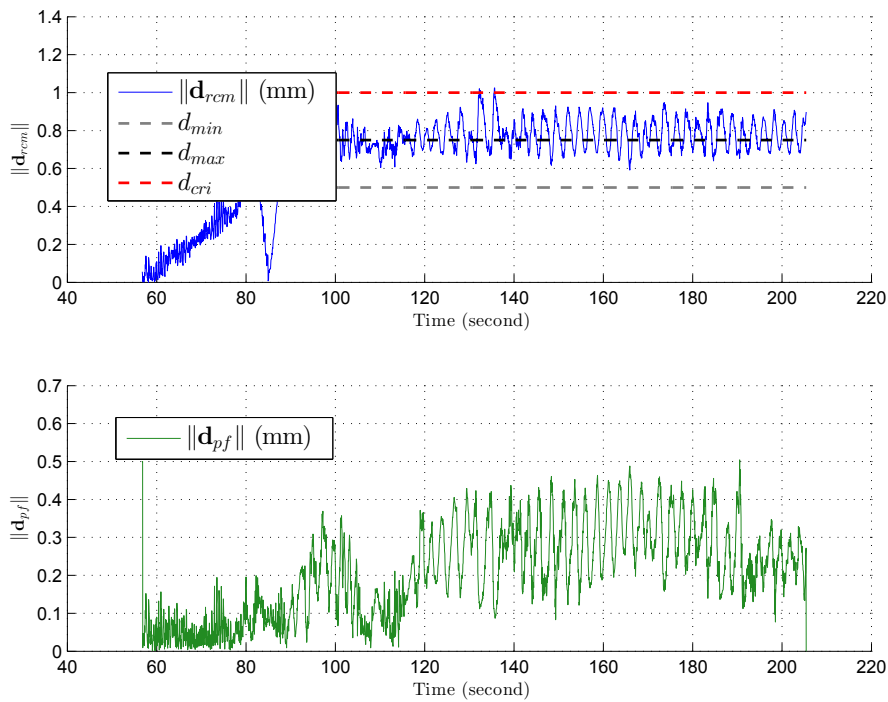
tool for following a spiral path under the RCM constraint. FIGURE 4.25(a) shows the motion of tool tip during the approach and the insertion phases. During the approach phase, the task priority controller sets the alignment task (4.46) as the highest priority and the approach task (4.54) as the secondary one.

During the insertion phase, the controller arranges the RCM task (4.46) as the first task, and the secondary one is the path following task (4.47). The angular RCM error e_{rcm3D} during this phase was measured as $0.05 \pm 0.03^\circ$, its mean value plus or minus its standard deviation, while the path following error \mathbf{d}_{pf} was also measured as $0.08 \pm 0.04mm$. The errors evaluation during the trial is presented in FIGURE 4.25(b), while the control twist velocity of end-effector is present in FIGURE 4.25(c). The values of gain parameters were $\lambda = 0.8$, $\gamma = 0.25$, $T_e = 0.05s$, $v_{tis} = 2mm/second$ and $\beta' = -4$.

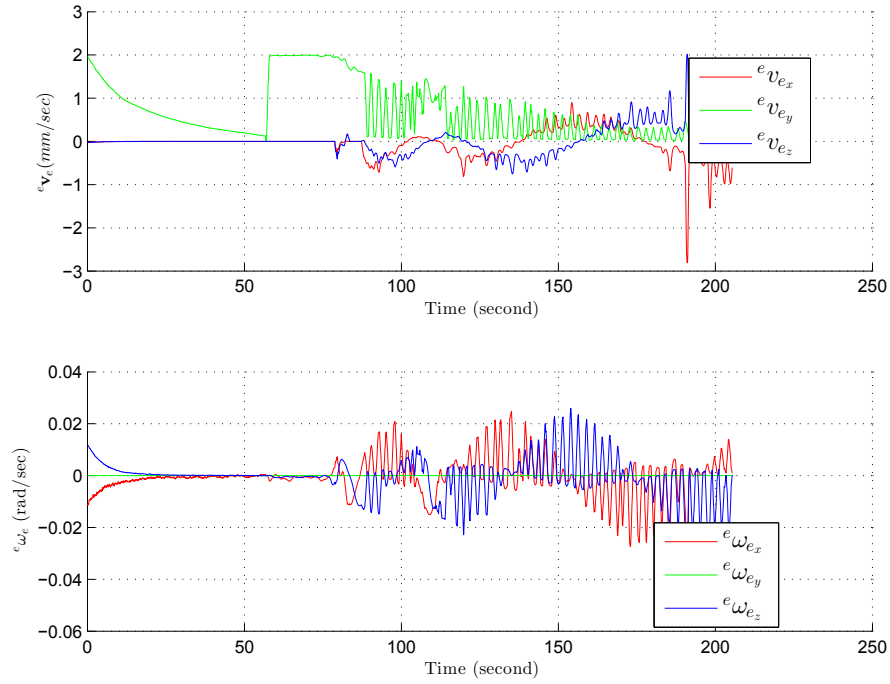
Straight tool follows a path under the UCM constraint: This trial uses a straight tool for following a spiral path with UCM constraint. FIGURE 4.26(a) shows the motion of end-effector. The tool body stays within the incision hole (FIGURE 4.26(a)). This behaviour is also observed in the lateral alignment error \mathbf{d}_{rcm} (the upper left plot in FIGURE 4.26(b)), where its value is bounded between d_{min} et d_{cri} . Indeed, the measured



(a) a zoom view on the reference path and the actual path which is done by the tool tip



(b) the lateral alignment task error \mathbf{d}_{rcm} and the path following error \mathbf{d}_{pf} during the insertion phase

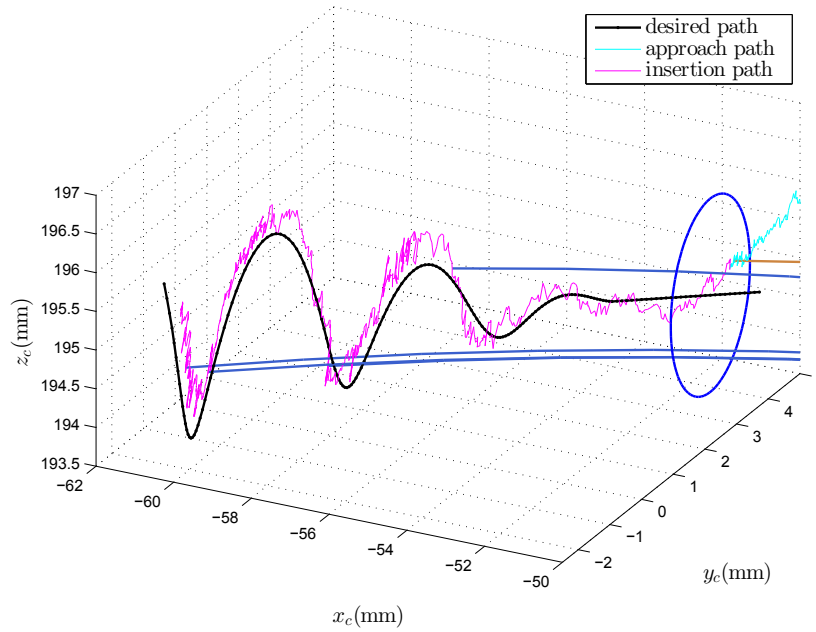


(c) the control twist velocity of the end-effector

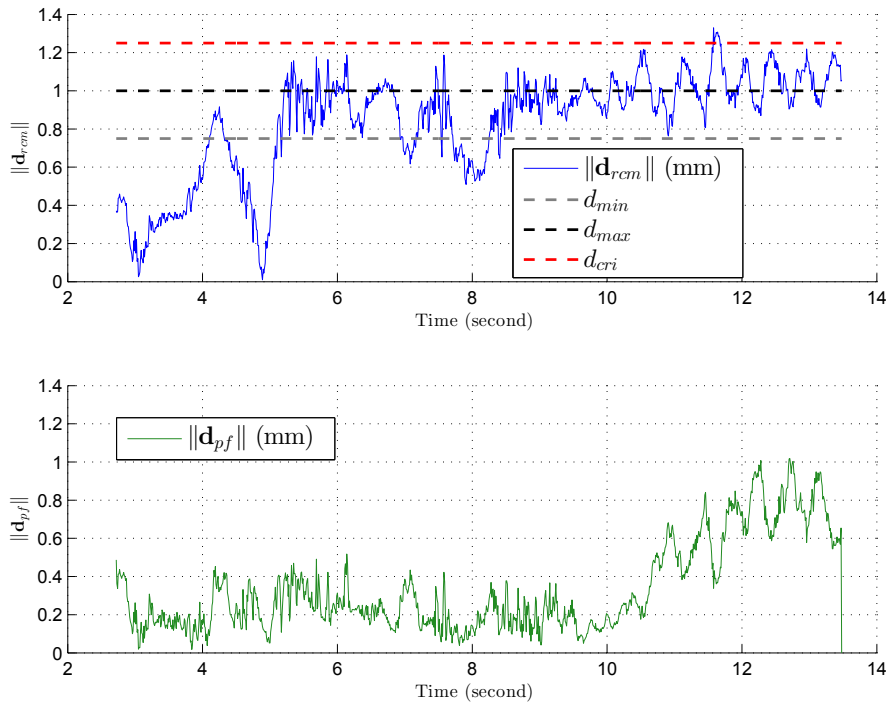
FIGURE 4.26: The trial of path following task with the UCM task while using a straight tool.

value of \mathbf{d}_{rcm} during the insertion phase $0.67 \pm 0.23mm$ and its median value as $0.73mm$, while the boundaries are defined as $d_{min} = 0.5mm$, $d_{max} = 0.75mm$ and $d_{cri} = 1mm$. Moreover, the measured path following error \mathbf{d}_{pf} was $0.208 \pm 0.12mm$ and its median value $0.207mm$. In fact, the lateral alignment error is coupled with the path following error, where the oscillation of \mathbf{d}_{rcm} error around the boundary d_{max} causes the \mathbf{d}_{pf} to oscillate. Indeed, these oscillations are resulted from the virtual spring which pushes the tool body in order to return to the safe region. These results are produced with the gains values of $\lambda = 0.8$, $v_{tis} = 2mm/second$, $\beta = 4$ and $T_e = 0.05second$.

Curved tool follows a path with UCM constraint: This trial uses the same controller to guide a curved tool. The output results are presented in FIGURE 4.27(a). The spiral reference path is tested as the previous trial but it is rotated about the z-axis. FIGURE 4.27(b) presents the tool motion errors, where the lateral alignment error \mathbf{d}_{rcm} was measured as $0.83 \pm 0.28mm$ and its median value was $0.92mm$. Moreover, the path following error \mathbf{d}_{pf} was measured as $0.33 \pm 0.24mm$ and its median value was $0.24mm$. These results are produced with the gains values of $v_{tis} = 2 mm/second$, $\beta = 3$ and $T_e = 0.01 second$.



(a) a zoom view on the reference path and the actual path which is done by the tool tip



(b) the lateral alignment task error \mathbf{d}_{rem} and the path following error \mathbf{d}_{pf} during the insertion phase

FIGURE 4.27: The trial of the path following task with the UCM task while using a curved tool.

4.4.2 Toward clinical trials

This part conducts the trials on a serial robot within ARTORG Centre. The robotic system of ARTORG was explained previously in Section 2.2. In brief, the system is dedicated to cochlear implantation. It consists of a serial robot [Bell et al., 2012], and a stereo camera for tracking the motion of the patient and the robot (FIGURE 4.28). It is also certified by the CE (Conformité Européene) and it is adapted for clinical trials.

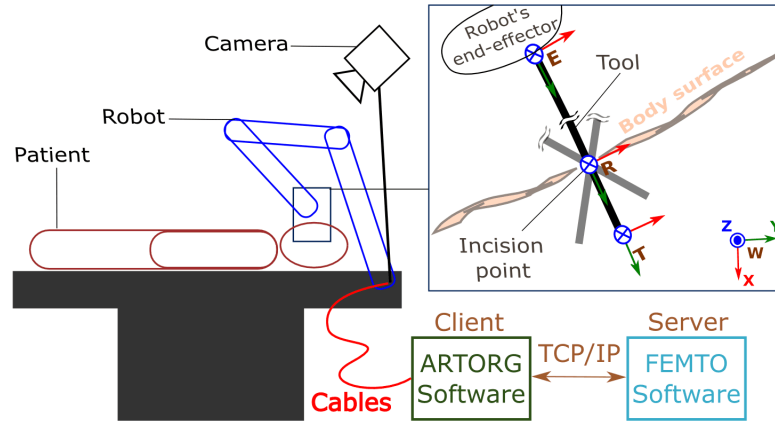


FIGURE 4.28: Conceptual scheme of the serial robot within the operation room.

The experimental work in this part has the objective to validate the FEMTO software controller on the ARTORG robotic system (FIGURE 4.28). Therefore, a first step was testing the TCP/IP communication protocol between FEMTO software and ARTORG software by adding a C++ class to the latter software. Afterwards, some basic tests (i.e., linear motion along the xyz -axes) were done in open-loop to ensure that the control twist velocity sent by the FEMTO software, it is received by the ARTORG software and it is executed by the serial robot.

Straight tool follows a path: The objective of this trial is testing the path following controller without any constraints on the tool motion. Such a trial is done by milling an artificial bone, as shown the final result in FIGURE 4.29. This figure presents also the serial robot which holds a driller. A marker is fixed above the driller tool in order to estimate the pose of the end-effector and that of the tool tip in the camera frame. Another marker is fixed on the artificial bone in order to determine the relative pose of the end-effector with respect to the "patient".

The milling process simulates the ablation action around a facial nerve which is defined as a sine wave. Indeed, the bone surface is coated with a green color, and then the driller bur begins by removing a small layer on the upper side of the facial nerve. After that, the driller leaves $2mm$ along the z -direction which represents the nerve thickness, and then it begins to drill the lower side of the nerve in order to isolate it.

The actual path done by the tool tip during this trial is shown in FIGURE 4.30(a). The error of path following task \mathbf{d}_{pf} during the motion is presented in FIGURE 4.30(b),

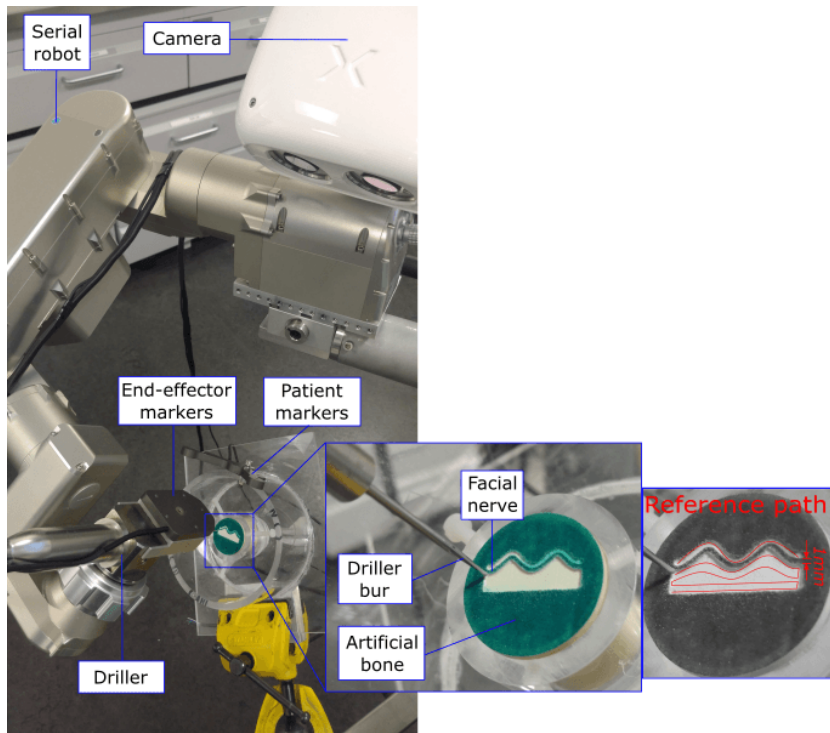
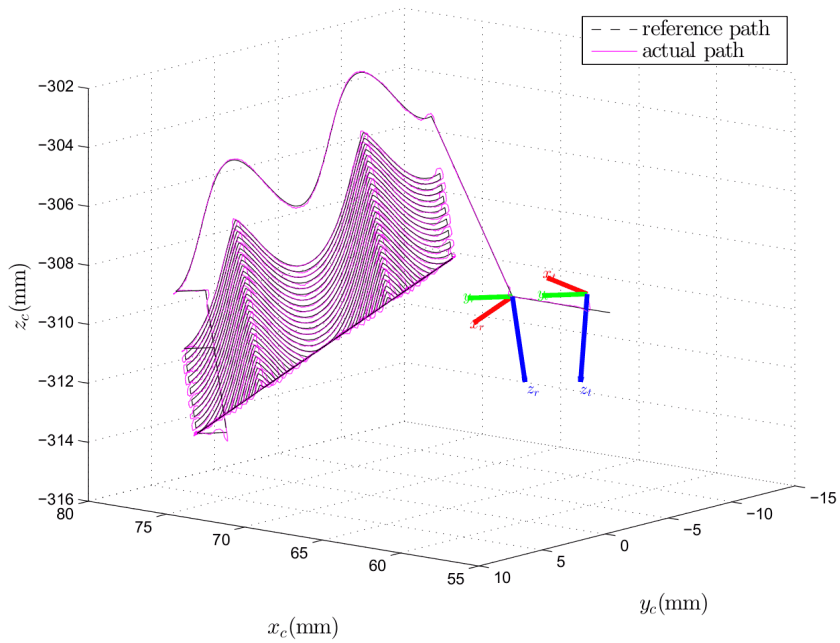
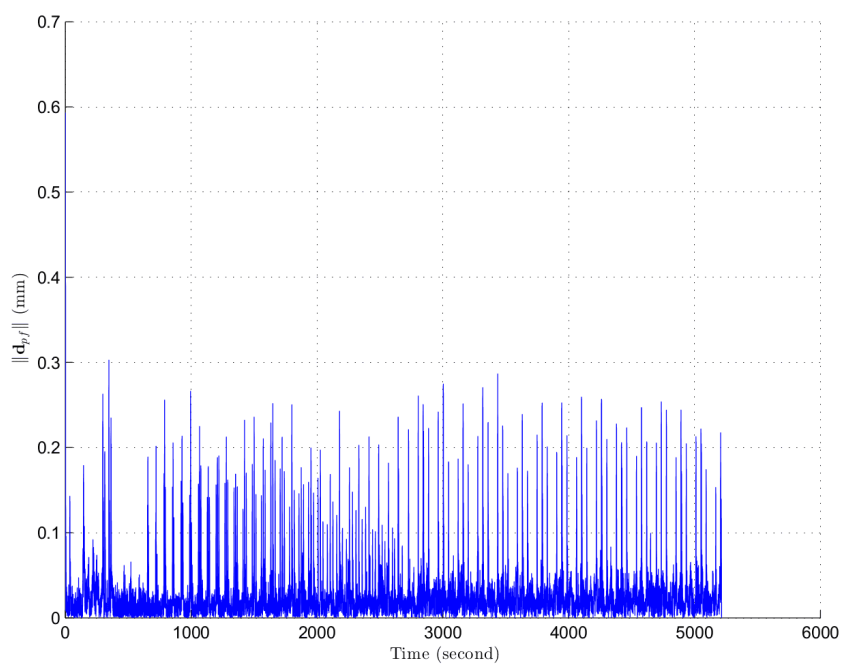


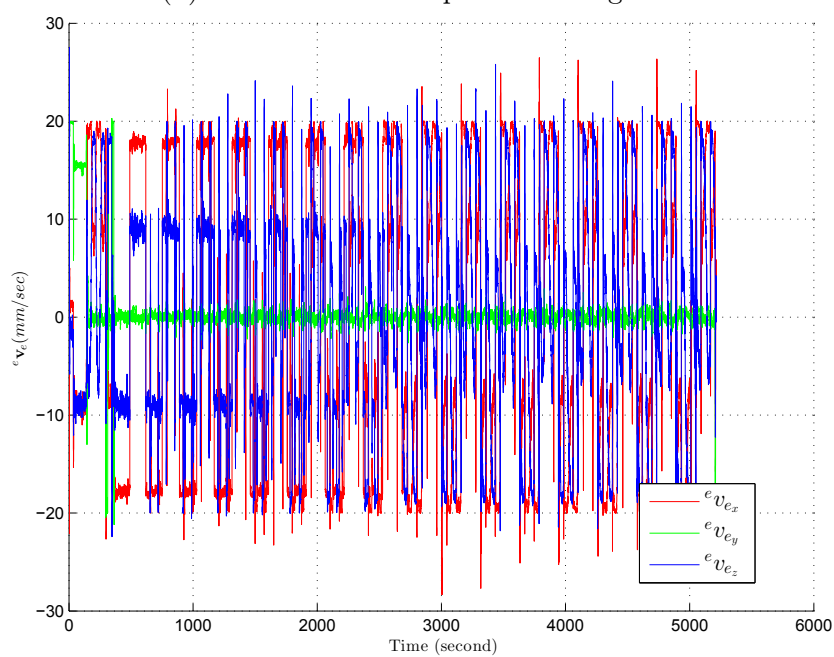
FIGURE 4.29: The experimental setup with the robotic system of ARTORG.



(a) the position of tool tip with respect to the reference path



(b) the linear error of path following task



(c) the command twist velocity of end-effector

FIGURE 4.30: The trial of path following task with the RCM task while using a straight tool.

where the measured error \mathbf{d}_{pf} throughout this trial equals $0.018mm$ and $0.03 \pm 0.039mm$ for its median value and its mean value plus or minus its standard deviation, respectively. FIGURE 4.30(c) shows the control twist velocity of end-effector, where the linear velocity of the end-effector has a rectangular wave form. Since the reference path is defined as a sine wave, then the time-derivative of this path becomes a rectangular wave which represents the control velocity.

4.5 Conclusion

The chapter began by presenting the path following task. It described the advantage of applying such a controller. Afterwards, the chapter proposed two types of controller to reduce the path following error (i.e., controllers in (4.30) and (4.32)). The second controller (4.32) can anticipate the path curvature because it is formulated in function of the path curvature and the path following error. Thereby, the controller (4.32) is used during the simulation and the experimental validation. However, a comparison should be performed between these two controllers. This track will be studied in the future.

The projection gradient technique was also presented in this chapter. It allows arranging the different tasks (i.e., the path following task alongside the RCM/UCM task) in a hierarchical form. It was difficult for a curved tool to follow a reference path under the RCM constraint, where the RCM task is defined as the highest priority and the path following task is considered as the secondary one. However, the controller overcomes the previous difficulty by inverting the priority of the tasks.

The proposed solution to achieve the unilateral constraint is indeed a simple one. It is required for the perspectives to add a damper to the controller and to consider more complex situations. For instance, the incision orifice could have an irregular shape at the surface plan. Besides that, the orifice constraints would be more complex by adding the internal walls of the orifice. Thereby, it would be useful to check the collision of the complex orifice geometry and the tool body.

Table 4.1 summarized the different trials which were conducted either by the simulator, the parallel robot or the serial robot.

	Geometric solution		Numerical solution		
		Straight tool	Straight tool	Segments tool	Circular tool
PF task		▲ ● ■		▲	▲
RCM task	3D	▲	▲	▲	▲
PF+RCM tasks	3D	▲	▲ ●	▲	▲
PF+UCM tasks	3D		▲ ●	▲	▲

TABLE 4.1: Summary of different trials done. The following symbols mean that a trial was performed on: (▲) the simulator, (●) the parallel robot, and (■) the serial robot. The abbreviations stand for: (PF) Path Following, (RCM) Remote Centre of Motion, and (UCM) Unilateral Central Motion.

General Conclusion and Perspectives

Contents

General Conclusion	167
Perspectives	169

General Conclusion

Cholesteatoma surgery is a difficult intervention compared to other middle ear procedures (e.g., stapedectomy or cochlear implantation) since the surgery should:

- i) drill the mastoid bone in order to reach the middle ear without causing any damage to the important anatomical structures (e.g., facial nerve, chorda tympani or carotid artery),
- ii) remove all cholesteatoma cells from the middle ear cavity to avoid that small residual cells expand again,
- iii) reconstruct the ear functionality that was affected due to the cholesteatoma.

The design of a minimally invasive surgical robotic system for a cholesteatoma intervention is not an easy task, and it requires further developments in terms of clinical and engineering technologies. The system should help the surgeon to achieve the above-mentioned objectives. The thesis started with a focus on the clinical aspects of cholesteatoma disease and the robotic systems dedicated to otological surgeries. This review showed also the requirements and specifications for designing and implementing a robotic system to deal with the cholesteatoma surgery.

Important aspects such as an innovative medical imaging system allowing an accurate detection of the cholesteatoma and a flexible micro-manipulator within the middle ear are not deepened during this thesis. These topics are vast domains of research and they require too much time of investigation and developments. Besides that, these advanced topics will enhance the surgical outputs but they are not the basic bricks to implement the required robotic system. The fundamental work is the ability to guide a standard/-commercial surgical tools for performing a complex surgical task. For instance, this task could be: i) milling a mastoid bone in order to reach the middle ear cavity, ii) scanning

a region of interest, or iii) ablating soft tissues. The ability to model these movements geometrically and then implement an adequate controller for releasing some constraints on the mechanical design. For instance, the RCM movement was originally achieved by a complex kinematic structure and a simple controller. Now, a complex controller can perform the RCM movement with a simple mechanical structure. Thus, the thesis focuses on the control aspect to guide the standard surgical tools, as a first step toward the cholesteatoma robotic system.

A complex surgical task is divided into sub-tasks in order to simplify the whole problem into small ones. A basic task is to follow a reference curve defined by the surgeon. Thereby, a first contribution is the proposition of a path following controller. A geometrical method was presented to describe how a tool tip can follow the desired path. In fact, the surgeon defines the required tool velocity which depends on the tool-tissue interaction. Then the controller adapts the tool velocity to maintain the required velocity and to follow the reference path independently from its shape, curvature or size.

Another basic task is to preserve the incision walls. Therefore, some constraints should be imposed on the tool's movement in order to prevent the patient's head damage. A second contribution was proposed to satisfy this requirement by formulating of a UCM (Unilaterally Constrained Motion) controller. A geometrical description is given to demonstrate such a constrained motion. It is applicable when the diameter of the entry orifice is bigger than the tool diameter (i.e., a standard mastoidectomy incision or the external ear canal). Throughout a UCM movement, the proposed controller guides a tool to follow a reference path without any problem until the tool gets closer to the incision wall, then the controller applies a virtual spring to keep the tool away from the incision wall. In the future, it will be needed to add a virtual damper in order to reduce the repulsive behaviour of the controller. Besides that, it will be required to consider the entry orifice with an irregular form.

A final task is imposing more constraints on the tool motion by reducing the diameter of the entry orifice until it becomes slightly bigger than the tool diameter. Consequently, a third contribution is an RCM (Remote Centre of Motion) controller. A geometric method is used to describe the RCM constraint. It is helpful besides the path following controller in order to become minimally invasive during the intervention. It can be applied to reduce the incision hole created by a mastoidectomy procedure into a conical shape tunnel. Such a tunnel has a small diameter at the external surface of the mastoid bone, and the tunnel diameter expands gradually until the bigger diameter at the tunnel base. For the perspectives, it will have to extend this controller in order to become more generic by guiding a bendable tool. It will also require proposing a robust method for choosing the optimal gain parameters which are used for the different task (i.e., the path following task and the RCM/UCM tasks).

A simulator was implemented as a first step in order to validate the proposed controller. This simulator was helpful at the beginning of the fundamental development because it allows testing the controller without the experimental problems. Once, the

controller performances are validated on the simulator, the controller was assessed on a parallel robot at FEMTO-ST, and then with a serial robot at ARTORG.

Perspectives

There are various tracks to follow-up our work. A first track could be helpful during the pre-operative phase is performing an automatic segmentation of auditory system (e.g., a review on the segmentation method of medical image [Pham et al., 2000b]). The advantages of the automated segmentation are: i) the creation of a surface model of auditory system based on the pre-operative medical images, and ii) the reduction of the planning phase time. Indeed, the planning software is an important issue to be subjected to further researches in the future. It will assist the surgeon in determining i) the optimal access tunnel to reach the middle ear cavity, and ii) the optimal strategy to remove the infected cells. The automatic detection of cholesteatoma from the pre-operative images is another challenging problem.

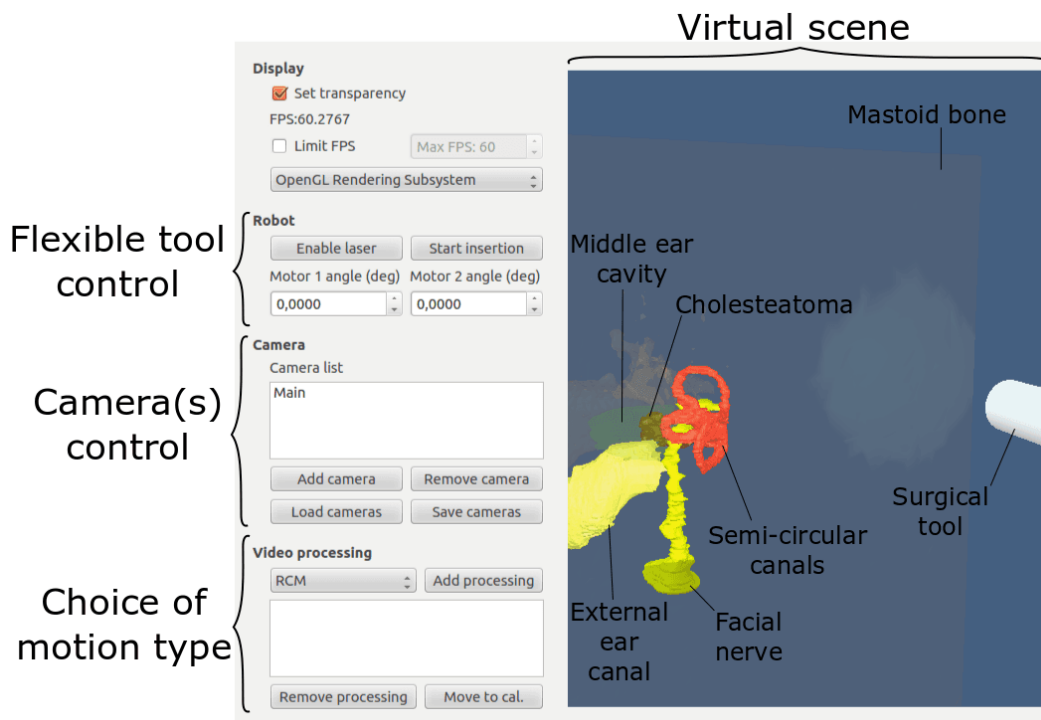


FIGURE 1: The window of the proposed realistic simulator with the different options.

Based on the numerical model of an auditory system, a realistic simulator could be implemented (FIGURE 1). The advantages of the simulator are: i) the planning of realistic surgical gestures, ii) the testing of the proposed control laws, and iii) the testing of the bendable tool different configurations. The last point will be discussed later in this section. Indeed, the actual way to conceive the virtual scene requires an expert for

performing a manual segmentation. It is also complicated for transforming the MRI or CT images into a compatible format which is readable by a C++ library. Thereby, an easier way could be found for generating the virtual scene in a 3D graphical application.

An advanced level of such simulator could be improved in order to implement a surgical training platform based on the virtual reality. The advanced simulator could also be equipped with a master console which would be helpful for the real robotic system as well. A feature as a master console allows a tele-operation between the surgeon and the slave robot. It is also suitable to integrate a haptic feedback (e.g., [Okamura, 2004, Bolopion and Régnier, 2013]) which is similar to the touch sense. Besides that, the robotic system could be more co-operative by adding the augmented reality feature (e.g., [Shuhaiber, 2004, Van Krevelen and Poelman, 2010, Lanchon et al., 2016]). Such a feature helps the surgeon during the operation by superimposing a graphical illustration on the user's view of the real world. Still, the previous features consume time and the real problem is how to turn it in real-time.

Detecting the cholesteatoma cells during the intra-operative stage is another challenging problem. The OCT and ultrasound imaging techniques are promising methods to detect the infected cells as they provide a 3D image of the scene. However, a clinical study is required to compare the performances of the different imaging methods. The way is open to find out an alternative for distinguishing between the healthy and infected cells based on other techniques, for instance, the electrical properties of cholesteatoma cells. Such a technique is applied before for detecting the facial nerve during a cochlear implantation [Ansó et al., 2014].

After the detection of infected cells, they should be removed. Therefore, the design of an ablation tool is an important issue. Applying an ultrasound as an ablation tool is a good solution; since the same tool can also be used as an imaging tool. This solution also reduces the number of tools used during the operation. Still, it is required further investigations: i) to reduce the probe diameter which is adequate with the dimensions of middle ear cavity (e.g., [Torbatian et al., 2009]), and ii) to find out the right frequencies for the removal and the detection of cholesteatoma cells. Other ablation tool types are open for discussion, for instance, a tool based on MEMS technology. FIGURE 2 shows an example of an ablation tool dedicated to remove the big debris of cholesteatoma. It is mainly composed of: i) a pre-deformed elastic tube which changes its curvature when it translates through the base tube, and ii) a suction/irrigation tube where a cutter is fixed at its tip. Such a design is not easy for fabrication and assembly.

This design leads us to another important topic which is the design of a bendable tool. The required micro-bendable tool allows: i) holding the different tool types (i.e., imaging and ablation tools), and ii) improving the robot dexterity within confined spaces. As a result, an optimization study should be performed to identify exactly the important parameters as, the optimal diameter, curvature and number of sections. This study should be done independently with no reliance on the choice of actuation source.

The realistic simulator will be useful for this study because it permits testing various configurations of the flexible structure based on real values (i.e., the numerical models obtained from various patients). For instance, a first trial may begin by testing an

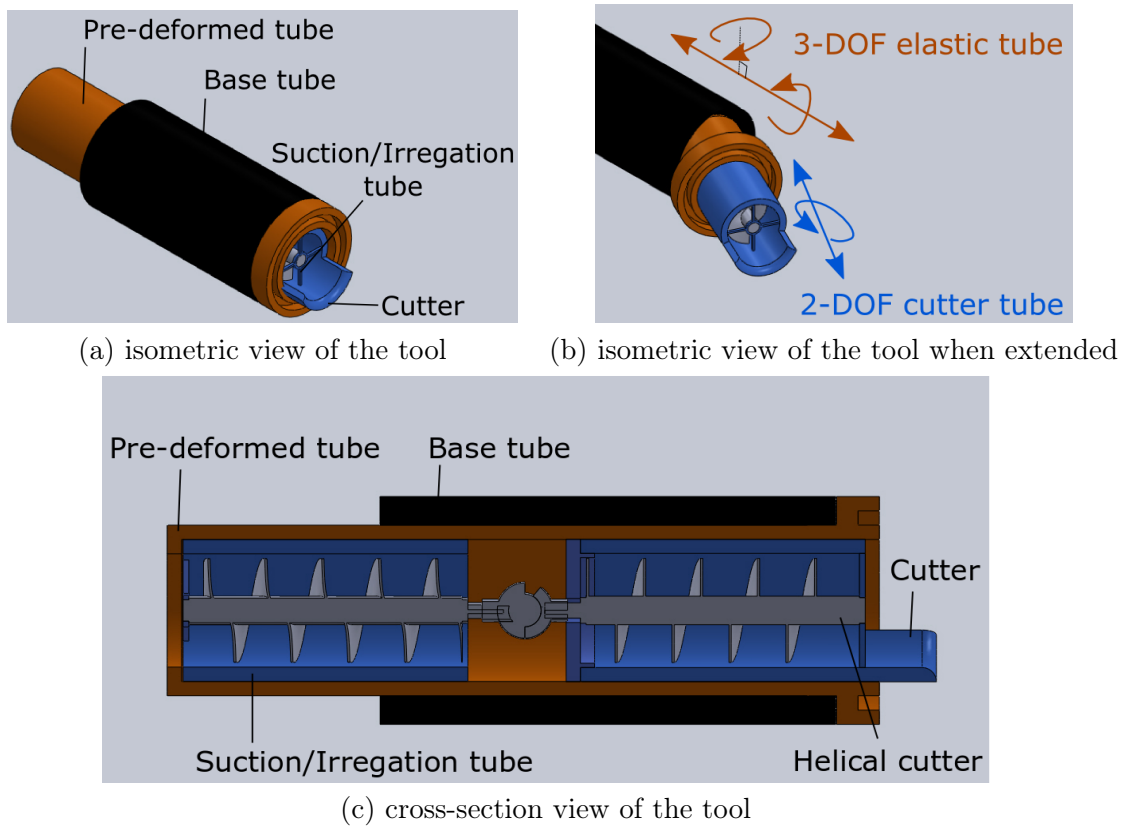


FIGURE 2: A tool concept for cholesteatoma removal based on concentric tube principle.

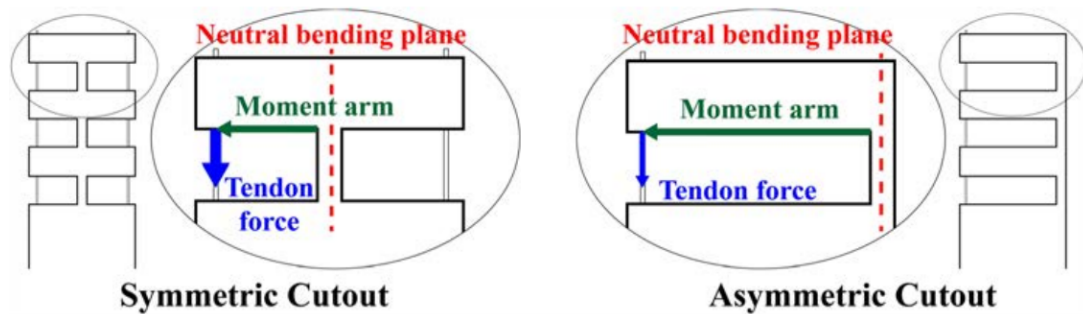


FIGURE 3: A comparison between the symmetric and the asymmetric cutouts [Swaney et al., 2017].

elastic section to reach some regions inside the middle ear cavity of a specific model, where the tool path from the entry point to the desired regions should be constant during the trials. Afterwards, the test is repeated with different values of section length and diameter while observing which combination of these parameters results in minimal

hits with the critical anatomical structures. Additional sections could be added to find out the optimal combination.

After the optimal parameters of bendable tool are defined, the choice of actuation source must be done. A first track was proposed in [Swaney et al., 2017, Fichera et al., 2017] for a cable-driven bendable tool which consists of creating an asymmetric cutouts in an elastic tube (FIGURE 3). Such a solution is a good candidate compared to symmetric cutouts because it allows reducing: i) the actuation force since its moment arm is long (FIGURE 3), and ii) the number of actuated cable for liberating more space within the tube cavity.

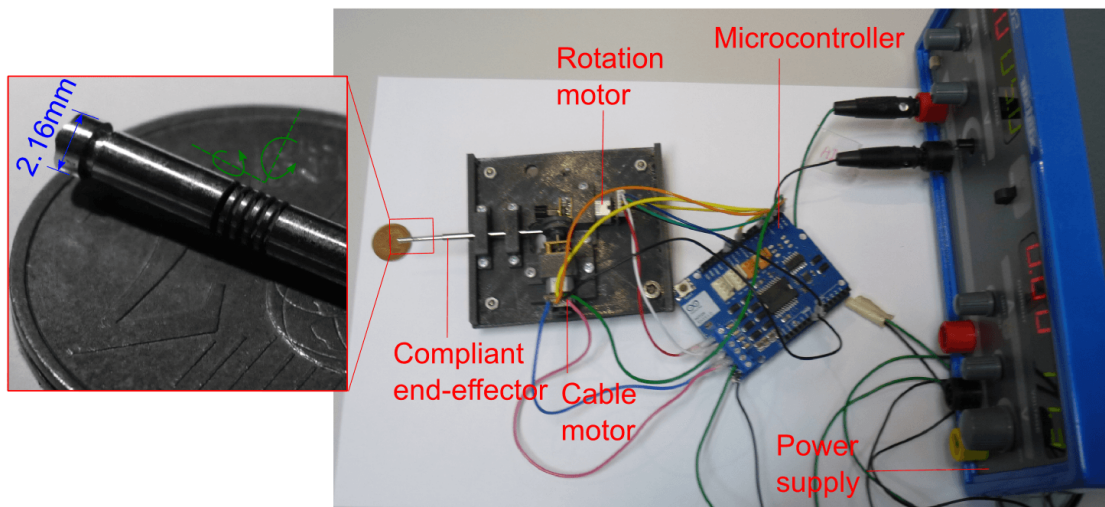


FIGURE 4: First prototype of bendable tool based on the model of [Swaney et al., 2017]

FIGURE 4 shows a reproduction of the model proposed in [Swaney et al., 2017] which allows a better understanding of the mathematical model. This first prototype is composed of a bendable tube of Nitinol which has rectangular cutouts for making the tube deflect easily from one side. One DC motor is used to pull the cable for deflecting the tube while a second DC motor is applied for rotating the tube about its central axis.

The cutout shape could also be modified for reaching a maximum deflection. FIGURE 5 proposes an extension of the previous concept which makes the cutout as a pyramid with a filleted peak. The distal end of this first stage bendable tool contents a small orifice for passing through a secondary bendable tool.

This secondary stage could be actuated by another type of actuation source for achieving a hybrid concept, for instance, EAP or a magnetic field. However, it is challenging to integrate this secondary stage due to the tiny dimensions of middle ear cavity and the miniaturization constraints. Therefore, it requires more detailed study with the miniaturization techniques for the development of micro- and/or nano-robots [Dong and Nelson, 2007, Nelson et al., 2010] which should improve the biopsy and the therapy of auditory system disorders and diseases.

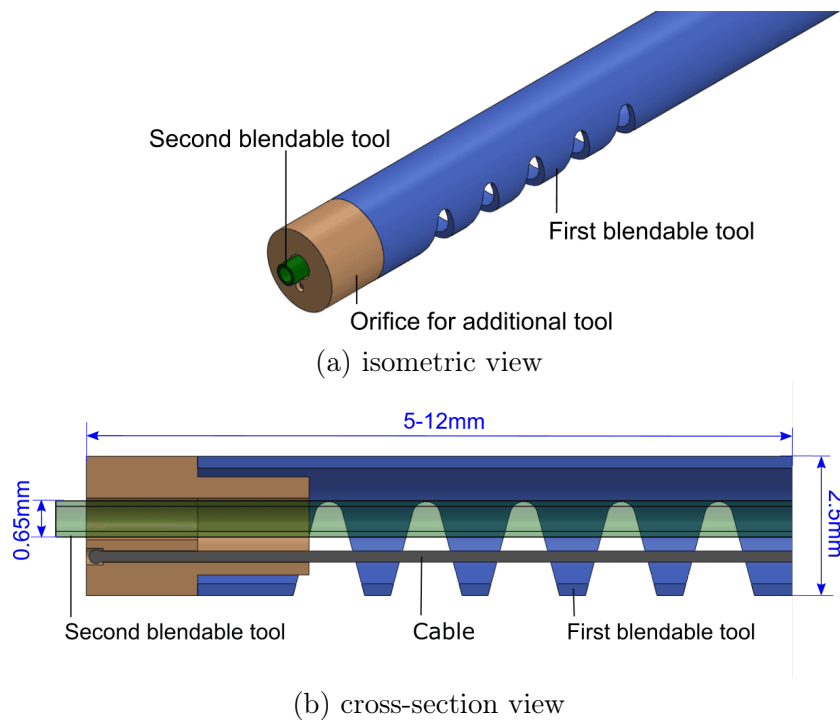


FIGURE 5: A secondary concept of the bendable tool.

Finally, the perspectives could be summarized as:

- **Short term:**

- i) consider an irregular form of the incision hole and include a virtual damper to the UCM controller,
- ii) implementing a robust controller,
- iii) propose a robust method for the choice of the gain parameters,
- iv) extend the path following controller with that of the RCM/UCM to guide a bendable tool.

- **Long term:**

- i) implement a realistic simulator with a planning software,
- ii) medical imaging tool for detecting the cholesteatoma cells through the intervention,
- iii) innovative ablation tool for the large debris and the residual small cells,
- iv) flexible manipulator: detecting, tracking, modelling and controlling,
- v) mechatronics device for an easy and fast exchange between the different tool types,
- vi) a detailed study about the danger that could occur during the operation due to the usage of the proposed system.

Bibliography

- [Abdala and Keefe, 2012] Abdala, C. and Keefe, D. H. (2012). Morphological and functional ear development. In *Human Auditory Development*, pages 19–59. Springer. [16](#)
- [Aghakhani et al., 2013] Aghakhani, N., Geravand, M., Shahriari, N., Vendittelli, M., and Oriolo, G. (2013). Task control with remote center of motion constraint for minimally invasive robotic surgery. In *IEEE International Conference on Robotics and Automation (ICRA)*, pages 5807–5812. [67](#)
- [Alper, 2004] Alper, C. M. (2004). *Advanced therapy in otitis media*. PMPH-USA. [17](#), [18](#), [19](#), [25](#), [27](#)
- [Ansó et al., 2014] Ansó, J., Stahl, C., Gerber, N., Williamson, T., Gavaghan, K., Rösler, K. M., Caversaccio, M.-D., Weber, S., and Bell, B. (2014). Feasibility of using emg for early detection of the facial nerve during robotic direct cochlear access. *Otology & Neurotology*, 35(3):545–554. [46](#), [170](#)
- [Aquino et al., 2011] Aquino, J. E. A. P. d., Cruz Filho, N. A., and Aquino, J. N. P. d. (2011). Epidemiology of middle ear and mastoid cholesteatomas: study of 1146 cases. *Brazilian journal of otorhinolaryngology*, 77(3):341–347. [20](#)
- [Awad et al., 2012] Awad, T., Moharram, H., Shaltout, O., Asker, D., and Youssef, M. (2012). Applications of ultrasound in analysis, processing and quality control of food: A review. *Food Research International*, 48(2):410–427. [23](#)
- [Ayache et al., 2008] Ayache, S., Tramier, B., and Strunski, V. (2008). Otoendoscopy in cholesteatoma surgery of the middle ear: what benefits can be expected? *Otology & Neurotology*, 29(8):1085–1090. [21](#)
- [Azimian et al., 2010] Azimian, H., Patel, R. V., and Naish, M. D. (2010). On constrained manipulation in robotics-assisted minimally invasive surgery. In *IEEE RAS and EMBS International Conference on Biomedical Robotics and Biomechanics (BioRob)*, pages 650–655. [67](#), [70](#)

- [Azizian et al., 2014] Azizian, M., Khoshnam, M., Najmaei, N., and Patel, R. V. (2014). Visual servoing in medical robotics: a survey. part i: endoscopic and direct vision imaging—techniques and applications. *The International Journal of Medical Robotics and Computer Assisted Surgery*, 10(3):263–274. [153](#)
- [Badr-el Dine, 2002] Badr-el Dine, M. (2002). Value of ear endoscopy in cholesteatoma surgery. *Otology & neurotology*, 23(5):631–635. [21](#)
- [Badr-El-Dine et al., 2013] Badr-El-Dine, M., James, A. L., Panetti, G., Marchioni, D., Presutti, L., and Nogueira, J. F. (2013). Instrumentation and technologies in endoscopic ear surgery. *Otolaryngologic Clinics of North America*, 46(2):211–225. [vi](#), [29](#)
- [Barbé et al., 2007] Barbé, L., Bayle, B., de Mathelin, M., and Gangi, A. (2007). In vivo model estimation and haptic characterization of needle insertions. *The International Journal of Robotics Research*, 26(11-12):1283–1301. [40](#)
- [Baron et al., 2010] Baron, S., Eilers, H., Munske, B., Toennies, J., Balachandran, R., Labadie, R., Ortmaier, T., and Webster III, R. (2010). Percutaneous inner-ear access via an image-guided industrial robot system. *Proceedings of the Institution of Mechanical Engineers, Part H: Journal of Engineering in Medicine*, 224(5):633–649. [43](#), [44](#), [47](#), [62](#)
- [Bell et al., 2013] Bell, B., Gerber, N., Williamson, T., Gavaghan, K., Wimmer, W., Caversaccio, M., and Weber, S. (2013). In vitro accuracy evaluation of image-guided robot system for direct cochlear access. *Otology & Neurotology*, 34(7):1284–1290. [46](#)
- [Bell et al., 2012] Bell, B., Stieger, C., Gerber, N., Arnold, A., Nauer, C., Hamacher, V., Kompis, M., Nolte, L., Caversaccio, M., and Weber, S. (2012). A self-developed and constructed robot for minimally invasive cochlear implantation. *Acta oto-laryngologica*, 132(4):355–360. [vi](#), [37](#), [39](#), [44](#), [45](#), [163](#)
- [Bertsekas, 1999] Bertsekas, D. P. (1999). *Nonlinear programming*. Athena scientific Belmont. [100](#), [101](#)
- [Bettini et al., 2004] Bettini, A., Marayong, P., Lang, S., Okamura, A. M., and Hager, G. D. (2004). Vision-assisted control for manipulation using virtual fixtures. *IEEE Transactions on Robotics*, 20(6):953–966. [101](#)
- [Boctor et al., 2004] Boctor, E. M., Webster III, R. J., Mathieu, H., Okamura, A. M., and Fichtinger, G. (2004). Virtual remote center of motion control for needle placement robots. *Computer Aided Surgery*, 9(5):175–183. [vii](#), [67](#), [68](#), [70](#)
- [Bolopion and Régnier, 2013] Bolopion, A. and Régnier, S. (2013). A review of haptic feedback teleoperation systems for micromanipulation and microassembly. *IEEE Transactions on automation science and engineering*, 10(3):496–502. [40](#), [170](#)

- [Bordure et al., 2009] Bordure, P., Bailleul, S., Malard, O., and Wagner, R. (2009). Otite chronique cholestéatomateuse. aspects cliniques et thérapeutiques. [18](#), [19](#), [28](#)
- [Bordure et al., 2005] Bordure, P., Robier, A., and Malard, O. (2005). *Chirurgie otologique et otoneurologique*. Elsevier Masson. [vi](#), [21](#), [25](#), [26](#)
- [Bowyer et al., 2014] Bowyer, S. A., Davies, B. L., and y Baena, F. R. (2014). Active constraints/virtual fixtures: A survey. *IEEE Transactions on Robotics*, 30(1):138–157. [101](#)
- [Bradley et al., 2013] Bradley, J. A., Jiang, N., Levy, L. L., Richards-Kortum, R., Sikora, A., and Smouha, E. E. (2013). High-resolution microendoscope images of middle ear cholesteatoma and surrounding tissue: Evaluation of interobserver concordance. *Otolaryngology–Head and Neck Surgery*, 149(2 suppl):P100. [24](#)
- [Brett et al., 1995] Brett, P., Baker, D., Reyes, L., and Blanshard, J. (1995). An automatic technique for micro-drilling a stapedotomy in the flexible stapes footplate. *Proceedings of the Institution of Mechanical Engineers, Part H: Journal of Engineering in Medicine*, 209(4):255–262. [42](#), [62](#)
- [Brett et al., 2007] Brett, P., Taylor, R., Proops, D., Coulson, C., Reid, A., and Griffiths, M. (2007). A surgical robot for cochleostomy. In *Engineering in Medicine and Biology Society, 2007. EMBS 2007. 29th Annual International Conference of the IEEE*, pages 1229–1232. IEEE. [42](#), [62](#)
- [Brezinski et al., 1997] Brezinski, M. E., Tearney, G. J., Weissman, N., Boppart, S., Bouma, B., Hee, M., Weyman, A., Swanson, E., Southern, J., and Fujimoto, J. (1997). Assessing atherosclerotic plaque morphology: comparison of optical coherence tomography and high frequency intravascular ultrasound. *Heart*, 77(5):397–403. [24](#)
- [Brown et al., 2009] Brown, J. A., Torbatian, Z., Adamson, R. B., Van Wijhe, R., Pennings, R. J., Lockwood, G. R., and Bance, M. L. (2009). High-frequency ex vivo ultrasound imaging of the auditory system. *Ultrasound in medicine & biology*, 35(11):1899–1907. [23](#), [55](#)
- [Budenz et al., 2007] Budenz, D. L., Anderson, D. R., Varma, R., Schuman, J., Cantor, L., Savell, J., Greenfield, D. S., Patella, V. M., Quigley, H. A., and Tielsch, J. (2007). Determinants of normal retinal nerve fiber layer thickness measured by stratus oct. *Ophthalmology*, 114(6):1046–1052. [24](#)
- [Burgner et al., 2013] Burgner, J., Gilbert, H. B., and Webster, R. J. (2013). On the computational design of concentric tube robots: Incorporating volume-based objectives. In *IEEE International Conference on Robotics and Automation (ICRA)*, pages 1193–1198. [58](#)
- [Burgner et al., 2011] Burgner, J., Swaney, P. J., Rucker, D. C., Gilbert, H. B., Nill, S. T., Russell, P. T., Weaver, K. D., and Webster, R. (2011). A bimanual teleoperated

- system for endonasal skull base surgery. In *IEEE/RSJ International Conference on Intelligent Robots and Systems (IROS)*, pages 2517–2523. vi, 37, 52
- [Burgner-Kahrs et al., 2015] Burgner-Kahrs, J., Rucker, D. C., and Choset, H. (2015). Continuum robots for medical applications: A survey. *IEEE Transactions on Robotics*, 31(6):1261–1280. 36, 52, 57
- [Burkhardt et al., 2012] Burkhardt, A., Walther, J., Cimalla, P., Mehner, M., and Koch, E. (2012). Endoscopic optical coherence tomography device for forward imaging with broad field of view. *Journal of biomedical optics*, 17(7):071302–071302. 24
- [Caffier et al., 2008] Caffier, P. P., Marzahn, U., Franke, A., Sudhoff, H., Jovanovic, S., Haisch, A., and Sedlmaier, B. (2008). Laser-assisted cholesteatoma surgery: technical aspects, in vitro implementation and challenge of selective cell destruction. *European Archives of Oto-Rhino-Laryngology*, 265(10):1179–1188. 29
- [Camarillo et al., 2008] Camarillo, D. B., Milne, C. F., Carlson, C. R., Zinn, M. R., and Salisbury, J. K. (2008). Mechanics modeling of tendon-driven continuum manipulators. *IEEE Transactions on Robotics*, 24(6):1262–1273. 38, 53, 57, 58
- [Carmena et al., 2003] Carmena, J. M., Lebedev, M. A., Crist, R. E., O’Doherty, J. E., Santucci, D. M., Dimitrov, D. F., Patil, P. G., Henriquez, C. S., and Nicolelis, M. A. (2003). Learning to control a brain–machine interface for reaching and grasping by primates. *PLoS biology*, 1(2):e42. 40
- [Carmo, 1976] Carmo, M. P. D. (1976). *Differential geometry of curves and surfaces*. Prentice Hall. 123
- [Carpi and Pappone, 2009] Carpi, F. and Pappone, C. (2009). Stereotaxis niobe® magnetic navigation system for endocardial catheter ablation and gastrointestinal capsule endoscopy. *Expert Review of Medical Devices*, 6(5):487–498. vi, 37, 38, 57, 58
- [Chaumette and Hutchinson, 2006] Chaumette, F. and Hutchinson, S. (2006). Visual servo control. i. basic approaches. *IEEE Robotics & Automation Magazine*, 13(4):82–90. 60, 133, 153
- [Chen et al., 2008] Chen, G., Pham, M. T., and Redarce, T. (2008). Sensor-based guidance control of a continuum robot for a semi-autonomous colonoscopy. *Robotics and autonomous systems*, 57(6):712–722. 57
- [Chiaverini and Sciavicco, 1993] Chiaverini, S. and Sciavicco, L. (1993). The parallel approach to force/position control of robotic manipulators. *IEEE Transactions on Robotics and Automation*, 9(4):361–373. 101
- [Chikhaoui, 2016] Chikhaoui, M. T. (2016). *Nouveaux concepts de robots à tubes concentriques à micro-actionneurs à base de polymères électro-actifs*. PhD thesis, Université de Franche-Comté. 57

- [Clark et al., 2012] Clark, J. R., Leon, L., Warren, F. M., and Abbott, J. J. (2012). Magnetic guidance of cochlear implants: proof-of-concept and initial feasibility study. *Journal of Medical Devices*, 6(3). [42](#), [57](#), [58](#), [62](#)
- [Cleary and Peters, 2010] Cleary, K. and Peters, T. M. (2010). Image-guided interventions: technology review and clinical applications. *Annual review of biomedical engineering*, 12:119–142. [35](#), [59](#)
- [Colbaugh et al., 1995] Colbaugh, R., Seraji, H., and Glass, K. (1995). Adaptive compliant motion control for dexterous manipulators. *The International journal of robotics research*, 14(3):270–280. [101](#)
- [Dahroug et al., 2016] Dahroug, B., Tamadazte, B., and Andreff, N. (2016). 3d path following with remote center of motion constraints. In *13th International Conference on Informatics in Control, Automation and Robotics (ICINCO)*, volume 1, pages 84–91. [38](#), [72](#)
- [Dahroug et al., 2017a] Dahroug, B., Tamadazte, B., and Andreff, N. (2017a). Task controller for performing remote centre of motion. *430:117–132*. [86](#)
- [Dahroug et al., 2017b] Dahroug, B., Tamadazte, B., and Andreff, N. (2017b). Visual servoing controller for time-invariant 3d path following with remote centre of motion constraint. In *IEEE International Conference on Robotics and Automation (ICRA)*, pages 3612–3618. [80](#)
- [Dahroug et al., 2018] Dahroug, B., Tamadazte, B., Weber, S., Tavernier, L., and Andreff, N. (2018). Review on otological robotic systems: Toward micro-robot assisted system for cholesteatoma surgery. *IEEE Reviews in Biomedical Engineering*. [42](#)
- [Dalvand and Shirinzadeh, 2012] Dalvand, M. M. and Shirinzadeh, B. (2012). Remote centre-of-motion control algorithms of 6-rrcr parallel robot assisted surgery system (pramiss). In *IEEE International Conference on Robotics and Automation (ICRA)*, pages 3401–3406. [63](#), [66](#)
- [Danilchenko et al., 2011] Danilchenko, A., Balachandran, R., Toennies, J. L., Baron, S., Munske, B., Fitzpatrick, J. M., Withrow, T. J., Webster III, R. J., and Labadie, R. F. (2011). Robotic mastoidectomy. *Otology & neurotology: official publication of the American Otological Society, American Neurotology Society [and] European Academy of Otology and Neurotology*, 32(1):11–16. [vii](#), [47](#), [48](#), [62](#)
- [Davies, 2000] Davies, B. (2000). A review of robotics in surgery. *Proceedings of the Institution of Mechanical Engineers, Part H: Journal of Engineering in Medicine*, 214(1):129–140. [38](#)
- [De Foer et al., 2015] De Foer, B., Nicolay, S., Vercruyssen, J.-P., Offeciers, E., Casselman, J. W., and Pouillon, M. (2015). Imaging of cholesteatoma. In *Temporal Bone Imaging*, pages 69–87. Springer. [21](#)

- [De Schutter and Van Brussel, 1988] De Schutter, J. and Van Brussel, H. (1988). Compliant robot motion ii. a control approach based on external control loops. *The International Journal of Robotics Research*, 7(4):18–33. [101](#)
- [De Volder and Reynaerts, 2010] De Volder, M. and Reynaerts, D. (2010). Pneumatic and hydraulic microactuators: a review. *Journal of Micromechanics and microengineering*, 20(4):043001. [57](#)
- [Dementhon and Davis, 1995] Dementhon, D. F. and Davis, L. S. (1995). Model-based object pose in 25 lines of code. *International journal of computer vision*, 15(1-2):123–141. [156](#)
- [Dillon et al., 2014] Dillon, N. P., Balachandran, R., dit Falisse, A. M., Wanna, G. B., Labadie, R. F., Withrow, T. J., Fitzpatrick, J. M., and Webster, R. J. (2014). Preliminary testing of a compact bone-attached robot for otologic surgery. In *SPIE Medical Imaging*, volume 9036. International Society for Optics and Photonics. [vii](#), [47](#), [48](#), [62](#)
- [Djalilian et al., 2008] Djalilian, H. R., Ridgway, J., Tam, M., Sepehr, A., Chen, Z., and Wong, B. J. (2008). Imaging the human tympanic membrane using optical coherence tomography in vivo. *Otology & neurotology: official publication of the American Otological Society, American Neurotology Society [and] European Academy of Otology and Neurotology*, 29(8):1091–1094. [25](#)
- [Djalilian et al., 2010] Djalilian, H. R., Rubinstein, M., Wu, E. C., Naemi, K., Zardouz, S., Karimi, K., and Wong, B. J. (2010). Optical coherence tomography of cholesteatoma. *Otology & neurotology: official publication of the American Otological Society, American Neurotology Society [and] European Academy of Otology and Neurotology*, 31(6):932–935. [vi](#), [25](#), [39](#)
- [Djurhuus et al., 2010] Djurhuus, B. D., Faber, C. E., and Skytthe, A. (2010). Decreasing incidence rate for surgically treated middle ear cholesteatoma in denmark 1977–2007. *Dan Med Bull*, 57(10):A4186. [20](#)
- [Djurhuus et al., 2015] Djurhuus, B. D., Skytthe, A., Christensen, K., and Faber, C. E. (2015). Cholesteatoma in danish children—a national study of changes in the incidence rate over 34 years. *International journal of pediatric otorhinolaryngology*, 79(2):127–130. [20](#)
- [Dogangil et al., 2009] Dogangil, G., Davies, B., and y Baena, F. R. (2009). A review of medical robotics for minimally invasive soft tissue surgery. *Proceedings of the Institution of Mechanical Engineers, Part H: Journal of Engineering in Medicine*, 224(5):653–679. [38](#)
- [Dong and Nelson, 2007] Dong, L. and Nelson, B. J. (2007). Tutorial-robotics in the small part ii: nanorobotics. *IEEE Robotics & Automation Magazine*, 14(3):111–121. [172](#)

- [Donoghue et al., 2007] Donoghue, J. P., Nurmikko, A., Black, M., and Hochberg, L. R. (2007). Assistive technology and robotic control using motor cortex ensemble-based neural interface systems in humans with tetraplegia. *The Journal of physiology*, 579(3):603–611. [40](#)
- [Dupont et al., 2010] Dupont, P. E., Lock, J., Itkowitz, B., and Butler, E. (2010). Design and control of concentric-tube robots. *IEEE Transactions on Robotics*, 26(2):209–225. [38](#)
- [Entsfellner et al., 2013] Entsfellner, K., Tauber, R., Roppenecker, D. B., Gumprecht, J. D., Strauss, G., and Lueth, T. (2013). Development of universal gripping adapters: Sterile coupling of medical devices and robots using robotic fingers. In *IEEE/ASME International Conference on Advanced Intelligent Mechatronics (AIM)*, pages 1464–1469. IEEE. [51](#), [62](#), [64](#)
- [Faraz and Payandeh, 1997] Faraz, A. and Payandeh, S. (1997). Synthesis and workspace study of endoscopic extenders with flexible stem. *Journal of mechanical design*, 119(3):412–414. [56](#)
- [Fei et al., 2001] Fei, B., Ng, W. S., Chauhan, S., and Kwok, C. K. (2001). The safety issues of medical robotics. *Reliability Engineering & System Safety*, 73(2):183–192. [41](#)
- [Fenster et al., 2001] Fenster, A., Downey, D. B., and Cardinal, H. N. (2001). Three-dimensional ultrasound imaging. *Physics in medicine and biology*, 46(5):R67. [23](#)
- [Fercher, 1996] Fercher, A. F. (1996). Optical coherence tomography. *Journal of Biomedical Optics*, 1(2):157–173. [24](#)
- [Fercher et al., 2003] Fercher, A. F., Drexler, W., Hitzenberger, C. K., and Lasser, T. (2003). Optical coherence tomography-principles and applications. *Reports on progress in physics*, 66(2):239. [24](#)
- [Fichera et al., 2017] Fichera, L., Dillon, N. P., Zhang, D., Godage, I. S., Siebold, M. A., Hartley, B. I., Noble, J. H., Russell, P. T., Labadie, R. F., and Webster, R. J. (2017). Through the eustachian tube and beyond: A new miniature robotic endoscope to see into the middle ear. *IEEE Robotics and Automation Letters*, 2(3):1488–1494. [39](#), [51](#), [56](#), [62](#), [172](#)
- [Fiedler et al., 2013] Fiedler, T., Boeger, D., Buentzel, J., Esser, D., Hoffmann, K., Jecker, P., Mueller, A., Radtke, G., Häfke, D., Bitter, T., et al. (2013). Middle ear surgery in thuringia, germany: a population-based regional study on epidemiology and outcome. *Otology & Neurotology*, 34(5):890–897. [20](#)
- [Flacco et al., 2015] Flacco, F., De Luca, A., and Khatib, O. (2015). Control of redundant robots under hard joint constraints: Saturation in the null space. *IEEE Transactions on Robotics*, 31(3):637–654. [100](#), [101](#)

- [Fleming et al., 2008] Fleming, I., Balicki, M., Koo, J., Iordachita, I., Mitchell, B., Handa, J., Hager, G., and Taylor, R. (2008). Cooperative robot assistant for retinal microsurgery. In *International conference on medical image computing and computer-assisted intervention*, pages 543–550. Springer. [63](#)
- [Frickmann and Zautner, 2012] Frickmann, H. and Zautner, A. E. (2012). Cholesteatoma— a potential consequence of chronic middle ear inflammation. *Otolaryngology*, 5(1). [22](#)
- [Funda et al., 1996] Funda, J., Taylor, R. H., Eldridge, B., Gomory, S., and Gruben, K. G. (1996). Constrained cartesian motion control for teleoperated surgical robots. *IEEE Transactions on Robotics and Automation*, 12(3):453–465. [67](#)
- [Gasparetto et al., 2015] Gasparetto, A., Boscariol, P., Lanzutti, A., and Vidoni, R. (2015). Path planning and trajectory planning algorithms: A general overview. In *Motion and Operation Planning of Robotic Systems*, pages 3–27. Springer. [120](#), [122](#), [153](#)
- [Gerber et al., 2014] Gerber, N., Bell, B., Gavaghan, K., Weisstanner, C., Caversaccio, M., and Weber, S. (2014). Surgical planning tool for robotically assisted hearing aid implantation. *International journal of computer assisted radiology and surgery*, 9(1):11–20. [35](#), [39](#), [44](#), [153](#)
- [Gilbert et al., 2016] Gilbert, H. B., Rucker, D. C., and Webster III, R. J. (2016). Concentric tube robots: The state of the art and future directions. In *Robotics Research*, pages 253–269. Springer. [58](#)
- [Gora et al., 2017] Gora, M. J., Suter, M. J., Tearney, G. J., and Li, X. (2017). Endoscopic optical coherence tomography: technologies and clinical applications. *Biomedical Optics Express*, 8(5):2405–2444. [24](#)
- [Gosline et al., 2012] Gosline, A. H., Vasilyev, N. V., Veeramani, A., Wu, M., Schmitz, G., Chen, R., Arabagi, V., del Nido, P. J., and Dupont, P. E. (2012). Metal mems tools for beating-heart tissue removal. In *2012 IEEE International Conference on Robotics and Automation (ICRA)*, pages 1921–1926. IEEE. [vi](#), [vii](#), [30](#), [52](#), [53](#), [56](#)
- [Gray, 1918] Gray, H. (1918). *Anatomy of the human body*. Lea & Febiger. [10](#)
- [Greigarn and Çavuşoğlu, 2014] Greigarn, T. and Çavuşoğlu, M. C. (2014). Task-space motion planning of mri-actuated catheters for catheter ablation of atrial fibrillation. In *Intelligent Robots and Systems (IROS 2014), 2014 IEEE/RSJ International Conference on*, pages 3476–3482. [59](#)
- [Gu et al., 2016] Gu, G.-Y., Zhu, L.-M., Su, C.-Y., Ding, H., and Fatikow, S. (2016). Modeling and control of piezo-actuated nanopositioning stages: a survey. *IEEE Transactions on Automation Science and Engineering*, 13(1):313–332. [57](#)

- [Haar and Coussios, 2007] Haar, G. t. and Coussios, C. (2007). High intensity focused ultrasound: physical principles and devices. *International Journal of Hyperthermia*, 23(2):89–104. [23](#)
- [Hamilton, 2005] Hamilton, J. W. (2005). Efficacy of the ktp laser in the treatment of middle ear cholesteatoma. *Otology & Neurotology*, 26(2):135–139. [29](#)
- [Hanafusa et al., 1981] Hanafusa, H., Yoshikawa, T., and Nakamura, Y. (1981). Analysis and control of articulated robot arms with redundancy. *IFAC Proceedings Volumes*, 14(2):1927–1932. [134](#)
- [Hanna et al., 2014] Hanna, B., Kivekäs, I., Wu, Y.-H., Guo, L. J., Lin, H., Guidi, J., and Poe, D. (2014). Minimally invasive functional approach for cholesteatoma surgery. *The Laryngoscope*, 124(10):2386–2392. [21](#)
- [He et al., 2015] He, X., van Geirt, V., Gehlbach, P., Taylor, R., and Iordachita, I. (2015). Iris: Integrated robotic intraocular snake. In *IEEE International Conference on Robotics and Automation (ICRA)*, pages 1764–1769. [51](#), [58](#)
- [Heermann et al., 2002] Heermann, R., Hauger, C., Issing, P., and Lenarz, T. (2002). Application of optical coherence tomography (oct) in middle ear surgery. *Laryngo-rhino-otologie*, 81(6):400–405. [25](#)
- [Hildmann and Sudhoff, 2006] Hildmann, H. and Sudhoff, H. (2006). *Middle ear surgery*. Springer Science & Business Media. [vi](#), [25](#), [26](#), [27](#), [28](#)
- [Hogben, 2006] Hogben, L. (2006). *Handbook of linear algebra*. CRC Press. [76](#)
- [Howe and Matsuoka, 1999] Howe, R. D. and Matsuoka, Y. (1999). Robotics for surgery. *Annual Review of Biomedical Engineering*, 1(1):211–240. [40](#)
- [Hussong et al., 2008] Hussong, A., Rau, T., Eilers, H., Baron, S., Heimann, B., Leinung, M., Lenarz, T., and Majdani, O. (2008). Conception and design of an automated insertion tool for cochlear implants. In *30th Annual International Conference of the IEEE Engineering in Medicine and Biology Society*, pages 5593–5596. IEEE. [vi](#), [43](#), [44](#)
- [Hutchinson et al., 1996] Hutchinson, S., Hager, G. D., and Corke, P. I. (1996). A tutorial on visual servo control. *IEEE Transactions on Robotics and Automation*, 12(5):651–670. [60](#), [133](#)
- [Ida et al., 2012] Ida, Y., Sugita, N., Ueta, T., Tamaki, Y., Tanimoto, K., and Mitsuishi, M. (2012). Microsurgical robotic system for vitreoretinal surgery. *International journal of computer assisted radiology and surgery*, 7(1):27–34. [38](#), [63](#)
- [Ikuta et al., 2006] Ikuta, K., Ichikawa, H., Suzuki, K., and Yajima, D. (2006). Multi-degree of freedom hydraulic pressure driven safety active catheter. In *IEEE International Conference on Robotics and Automation*, pages 4161–4166. [57](#)

- [Jang et al., 2002] Jang, I.-K., Bouma, B. E., Kang, D.-H., Park, S.-J., Park, S.-W., Seung, K.-B., Choi, K.-B., Shishkov, M., Schlendorf, K., Pomerantsev, E., et al. (2002). Visualization of coronary atherosclerotic plaques in patients using optical coherence tomography: comparison with intravascular ultrasound. *Journal of the American College of Cardiology*, 39(4):604–609. [24](#)
- [Jani et al., 2014] Jani, J. M., Leary, M., Subic, A., and Gibson, M. A. (2014). A review of shape memory alloy research, applications and opportunities. *Materials & Design*, 56:1078–1113. [57](#)
- [Kanoun et al., 2011] Kanoun, O., Lamiroux, F., and Wieber, P.-B. (2011). Kinematic control of redundant manipulators: Generalizing the task-priority framework to inequality task. *IEEE Transactions on Robotics*, 27(4):785–792. [100](#), [101](#)
- [Kapoor et al., 2006] Kapoor, A., Li, M., and Taylor, R. H. (2006). Constrained control for surgical assistant robots. In *IEEE International Conference on Robotics and Automation (ICRA)*, pages 231–236. [101](#)
- [Karhuketo et al., 1988] Karhuketo, T., Dastidar, P., Laasonen, E., Sipilä, M., and Puhakka, H. (1988). Visualization of the middle ear with high resolution computed tomography and superfine fiberoptic videomicroendoscopy. *European archives of oto-rhino-laryngology*, 255(6):277–280. [21](#)
- [Kazerooni, 1989] Kazerooni, H. (1989). On the robot compliant motion control. *Journal of dynamic systems, measurement, and control*, 111(3):416–425. [101](#)
- [Kemppainen et al., 1999] Kemppainen, H. O., Puhakka, H. J., Laippala, P. J., Sipilä, M. M., Manninen, M. P., and Karma, P. H. (1999). Epidemiology and aetiology of middle ear cholesteatoma. *Acta oto-laryngologica*, 119(5):568–572. [20](#)
- [Kettenbach et al., 2008] Kettenbach, J., Kronreif, G., Melzer, A., Fichtinger, G., Stoianovici, D., and Cleary, K. (2008). Ultrasound-, ct-and mr-guided robot-assisted interventions. In *Image Processing in Radiology*, pages 393–409. Springer. [40](#)
- [Khalil, 1996] Khalil, H. K. (1996). Lyapunov stability. In *The control handbook*, chapter 56, pages 889–894. CRC press. [132](#)
- [Khalil and Dombre, 2002] Khalil, W. and Dombre, E. (2002). *Modelisation, identification and control of robots*. Butterworth-Heinemann. [38](#)
- [Kim et al., 2014] Kim, J.-S., Lee, D.-Y., Kim, K., Kang, S., and Cho, K.-J. (2014). Toward a solution to the snapping problem in a concentric-tube continuum robot: Grooved tubes with anisotropy. In *IEEE International Conference on Robotics and Automation (ICRA)*, pages 5871–5876. [58](#)

- [Klenzner et al., 2009] Klenzner, T., Ngan, C. C., Knapp, F. B., Knoop, H., Kromeier, J., Aschendorff, A., Papastathopoulos, E., Raczkowski, J., Wörn, H., and Schipper, J. (2009). New strategies for high precision surgery of the temporal bone using a robotic approach for cochlear implantation. *European archives of oto-rhino-laryngology*, 266(7):955–960. [42](#), [62](#)
- [Korb et al., 2005] Korb, W., Kornfeld, M., Birkfellner, W., Boesecke, R., Figl, M., Fuerst, M., Kettenbach, J., Vogler, A., Hassfeld, S., and Kornreif, G. (2005). Risk analysis and safety assessment in surgical robotics: A case study on a biopsy robot. *Minimally Invasive Therapy & Allied Technologies*, 14(1):23–31. [41](#)
- [Kösling and Bootz, 2001] Kösling, S. and Bootz, F. (2001). Ct and mr imaging after middle ear surgery. *European journal of radiology*, 40(2):113–118. [21](#), [54](#)
- [Kratchman et al., 2011] Kratchman, L. B., Blachon, G. S., Withrow, T. J., Balachandran, R., Labadie, R. F., and Webster, R. J. (2011). Design of a bone-attached parallel robot for percutaneous cochlear implantation. *IEEE Transactions on Biomedical Engineering*, 58(10):2904–2910. [vii](#), [46](#), [47](#), [62](#)
- [Kreyszig, 1991] Kreyszig, E. (1991). *Differential geometry*. Dover. [124](#), [125](#)
- [Krulvitch et al., 1996] Krulvitch, P., Lee, A. P., Ramsey, P. B., Trevino, J. C., Hamilton, J., and Northrup, M. A. (1996). Thin film shape memory alloy microactuators. *Journal of Microelectromechanical Systems*, 5(4):270–282. [57](#)
- [Krupa et al., 2002] Krupa, A., Doignon, C., Gangloff, J., and De Mathelin, M. (2002). Combined image-based and depth visual servoing applied to robotized laparoscopic surgery. In *IEEE/RSJ International Conference on Intelligent Robots and Systems*, volume 1, pages 323–329. [153](#)
- [Kuo et al., 2012] Kuo, C.-H., Dai, J. S., and Dasgupta, P. (2012). Kinematic design considerations for minimally invasive surgical robots: an overview. *The International Journal of Medical Robotics and Computer Assisted Surgery*, 8(2):127–145. [38](#), [66](#)
- [Labadie et al., 2009] Labadie, R. F., Mitchell, J., Balachandran, R., and Fitzpatrick, J. M. (2009). Customized, rapid-production microstereotactic table for surgical targeting: description of concept and in vitro validation. *International journal of computer assisted radiology and surgery*, 4(3):273–280. [vii](#), [47](#)
- [Lademann et al., 2007] Lademann, J., Otberg, N., Richter, H., Meyer, L., Audring, H., Teichmann, A., Thomas, S., Knüttel, A., and Sterry, W. (2007). Application of optical non-invasive methods in skin physiology: a comparison of laser scanning microscopy and optical coherent tomography with histological analysis. *Skin Research and Technology*, 13(2):119–132. [24](#)
- [Lanchon et al., 2016] Lanchon, C., Custillon, G., Moreau-Gaudry, A., Descotes, J.-L., Long, J.-A., Fiard, G., and Voros, S. (2016). Augmented reality using transurethral

- ultrasound for laparoscopic radical prostatectomy: Preclinical evaluation. *The Journal of urology*, 196(1):244–250. [170](#)
- [Lapierre and Jouvencel, 2008] Lapierre, L. and Jouvencel, B. (2008). Robust nonlinear path-following control of an auv. *IEEE Journal of Oceanic Engineering*, 33(2):89–102. [121](#)
- [Lay, 2012] Lay, D. C. (2012). *Linear algebra and its applications*. Addison Wesley, Boston. [77](#)
- [Lefebvre et al., 2005] Lefebvre, T., Xiao, J., Bruyninckx, H., and De Gerssem, G. (2005). Active compliant motion: a survey. *Advanced Robotics*, 19(5):479–499. [101](#)
- [Legent et al., 1968] Legent, F., Perlemuter, L., and Vandenbrouck, C. (1968). *Cahiers d’anatomie ORL*. Masson. [6](#), [7](#), [11](#), [13](#), [16](#)
- [Leinung et al., 2007] Leinung, M., Baron, S., Eilers, H., Heimann, B., Bartling, S., Heermann, R., Lenarz, T., Majdani, O., and CURAC, G. (2007). Robotic-guided minimally-invasive cochleostomy: first results. *GMS CURAC*, 2. [vi](#), [43](#), [44](#)
- [Lesinski and Giesken, 2008] Lesinski, S. G. and Giesken, K. (2008). Optical fiber for co2 laser otosclerosis surgery. *Otolaryngology–Head and Neck Surgery*, 139(2 suppl):P57–P57. [29](#)
- [Levy et al., 2013] Levy, L. L., Jiang, N., Smouha, E., Richards-Kortum, R., and Sikora, A. G. (2013). Optical imaging with a high-resolution microendoscope to identify cholesteatoma of the middle ear. *The Laryngoscope*, 123(4):1016–1020. [vi](#), [24](#), [55](#)
- [Lim et al., 2011] Lim, H., Han, J.-M., Hong, J., Yi, B.-J., Lee, S. H., Jeong, J. H., Matsumoto, N., Oka, M., Komune, S., and Hashizume, M. (2011). Image-guided robotic mastoidectomy using human-robot collaboration control. In *International Conference on Mechatronics and Automation (ICMA)*, pages 549–554. IEEE. [vii](#), [48](#), [62](#)
- [Liu et al., 2014] Liu, W. P., Azizian, M., Sorger, J., Taylor, R. H., Reilly, B. K., Cleary, K., and Preciado, D. (2014). Cadaveric feasibility study of da vinci si-assisted cochlear implant with augmented visual navigation for otologic surgery. *JAMA Otolaryngology–Head & Neck Surgery*, 140(3):208–214. [vi](#), [42](#), [43](#), [62](#)
- [Loeve et al., 2010] Loeve, A., Breedveld, P., and Dankelman, J. (2010). Scopes too flexible... and too stiff. *IEEE pulse*, 1(3):26–41. [38](#)
- [Luenberger et al., 1984] Luenberger, D. G., Ye, Y., et al. (1984). *Linear and nonlinear programming*, volume 2. Springer. [100](#), [101](#)
- [Maciejewski and Klein, 1985] Maciejewski, A. A. and Klein, C. A. (1985). Obstacle avoidance for kinematically redundant manipulators in dynamically varying environments. *The international journal of robotics research*, 4(3):109–117. [56](#), [65](#), [119](#), [135](#)

- [Maier et al., 2011] Maier, T., Strauss, G., Bauer, F., Grasser, A., Hata, N., and Lueth, T. C. (2011). Distance measurement in middle ear surgery using a telemanipulator. In *Medical Image Computing and Computer-Assisted Intervention–MICCAI*, pages 41–48. Springer. [50](#), [62](#)
- [Maier et al., 2010] Maier, T., Strauss, G., Hofer, M., Kraus, T., Runge, A., Stenzel, R., Gumprecht, J., Berger, T., Dietz, A., and Lueth, T. C. (2010). A new micromanipulator system for middle ear surgery. In *IEEE International Conference on Robotics and Automation (ICRA)*, pages 1568–1573. IEEE. [vii](#), [50](#)
- [Majdani et al., 2009] Majdani, O., Rau, T. S., Baron, S., Eilers, H., Baier, C., Heimann, B., Ortmaier, T., Bartling, S., Lenarz, T., and Leinung, M. (2009). A robot-guided minimally invasive approach for cochlear implant surgery: preliminary results of a temporal bone study. *International journal of computer assisted radiology and surgery*, 4(5):475–486. [43](#)
- [Mansard and Khatib, 2008] Mansard, N. and Khatib, O. (2008). Continuous control law from unilateral constraints. In *IEEE International Conference on Robotics and Automation (ICRA)*, pages 3359–3364. [101](#)
- [Marchand et al., 2005] Marchand, E., Spindler, F., and Chaumette, F. (2005). Visp for visual servoing: a generic software platform with a wide class of robot control skills. *IEEE Robotics and Automation Magazine*, 12(4):40–52. [156](#)
- [Marchioni et al., 2011] Marchioni, D., Molteni, G., and Presutti, L. (2011). Endoscopic anatomy of the middle ear. *Indian Journal of Otolaryngology and Head & Neck Surgery*, 63(2):101–113. [21](#)
- [Marinho et al., 2014] Marinho, M. M., Bernardes, M. C., and Bó, A. P. (2014). A programmable remote center-of-motion controller for minimally invasive surgery using the dual quaternion framework. In *5th IEEE RAS & EMBS International Conference on Biomedical Robotics and Biomechatronics*, pages 339–344. [67](#)
- [Martin and Clark, 1997] Martin, F. N. and Clark, J. G. (1997). *Introduction to audiology*. Allyn and Bacon Boston. [7](#), [9](#), [11](#), [13](#), [16](#), [17](#)
- [Maurin et al., 2004] Maurin, B., Piccin, O., Bayle, B., Gangloff, J., de Mathelin, M., Soler, L., and Gangi, A. (2004). A new robotic system for ct-guided percutaneous procedures with haptic feedback. In *International Congress Series*, volume 1268, pages 515–520. Elsevier. [54](#), [59](#)
- [Mayer et al., 2004] Mayer, H., Nagy, I., and Knoll, A. (2004). Kinematics and modelling of a system for robotic surgery. In *On Advances in Robot Kinematics*, pages 181–190. Springer. [67](#), [68](#)
- [McJunkin and Chole, 2014] McJunkin, J. and Chole, R. (2014). Clinical utility of mri for cholesteatoma recurrence. *Current Surgery Reports*, 2(8):1–7. [21](#), [54](#)

- [Millan et al., 2004] Millan, J. R., Renkens, F., Mourino, J., and Gerstner, W. (2004). Noninvasive brain-actuated control of a mobile robot by human eeg. *IEEE Transactions on biomedical Engineering*, 51(6):1026–1033. [40](#)
- [Miroir et al., 2010] Miroir, M., Nguyen, Y., Szewczyk, J., Mazalaigue, S., Ferrary, E., Sterkers, O., and Grayeli, A. B. (2010). Robotol: from design to evaluation of a robot for middle ear surgery. In *IEEE/RSJ International Conference on Intelligent Robots and Systems (IROS)*, pages 850–856. IEEE. [vii](#), [39](#), [49](#), [56](#), [64](#)
- [Miroir et al., 2008] Miroir, M., Szewczyk, J., Nguyen, Y., Mazalaigue, S., and Sterkers, O. (2008). Design of a robotic system for minimally invasive surgery of the middle ear. In *2nd IEEE RAS & EMBS International Conference on Biomedical Robotics and Biomechanics. BioRob 2008.*, pages 747–752. IEEE. [49](#)
- [Mitra and Acharya, 2007] Mitra, S. and Acharya, T. (2007). Gesture recognition: A survey. *IEEE Transactions on Systems, Man, and Cybernetics, Part C (Applications and Reviews)*, 37(3):311–324. [40](#)
- [Muldoon et al., 2007] Muldoon, T. J., Pierce, M. C., Nida, D. L., Williams, M. D., Gillenwater, A., and Richards-Kortum, R. (2007). Subcellular-resolution molecular imaging within living tissue by fiber microendoscopy. *Optics express*, 15(25):16413–16423. [24](#)
- [Nageotte et al., 2006] Nageotte, F., Zanne, P., Doignon, C., and de Mathelin, M. (2006). Visual servoing-based endoscopic path following for robot-assisted laparoscopic surgery. In *IEEE/RSJ International Conference on Intelligent Robots and Systems*, pages 2364–2369. [122](#)
- [Nakamura et al., 1987] Nakamura, Y., Hanafusa, H., and Yoshikawa, T. (1987). Task-priority based redundancy control of robot manipulators. *The International Journal of Robotics Research*, 6(2):3–15. [65](#), [100](#), [120](#), [134](#)
- [Nathoo et al., 2005] Nathoo, N., Çavusoglu, M. C., Vogelbaum, M. A., and Barnett, G. H. (2005). In touch with robotics: neurosurgery for the future. *Neurosurgery*, 56(3):421–433. [40](#)
- [Nelson et al., 2010] Nelson, B. J., Kaliakatsos, I. K., and Abbott, J. J. (2010). Microrobots for minimally invasive medicine. *Annual review of biomedical engineering*, 12:55–85. [172](#)
- [Nguyen et al., 2012a] Nguyen, C. T., Jung, W., Kim, J., Chaney, E. J., Novak, M., Stewart, C. N., and Boppart, S. A. (2012a). Noninvasive in vivo optical detection of biofilm in the human middle ear. *Proceedings of the National Academy of Sciences*, 109(24):9529–9534. [25](#)
- [Nguyen et al., 2012b] Nguyen, Y., Miroir, M., Kazmitcheff, G., Ferrary, E., Sterkers, O., and Grayeli, A. B. (2012b). From conception to application of a tele-operated assistance robot for middle ear surgery. *Surgical innovation*, 19(3):241–251. [49](#), [62](#)

- [Nissen and Yock, 2001] Nissen, S. E. and Yock, P. (2001). Intravascular ultrasound. *Circulation*, 103(4):604–616. [23](#)
- [Noble et al., 2009] Noble, J. H., Dawant, B. M., Warren, F. M., and Labadie, R. F. (2009). Automatic identification and 3-d rendering of temporal bone anatomy. *Otology & neurotology: official publication of the American Otological Society, American Neurotology Society [and] European Academy of Otology and Neurotology*, 30(4):436. [46](#)
- [Noble et al., 2008] Noble, J. H., Warren, F. M., Labadie, R. F., and Dawant, B. M. (2008). Automatic segmentation of the facial nerve and chorda tympani in ct images using spatially dependent feature values. *Medical physics*, 35(12):5375–5384. [46](#)
- [Okamura, 2004] Okamura, A. M. (2004). Methods for haptic feedback in teleoperated robot-assisted surgery. *Industrial Robot: An International Journal*, 31(6):499–508. [170](#)
- [Olds et al., 2014] Olds, K. C., Chalasani, P., Pacheco-Lopez, P., Iordachita, I., Akst, L. M., and Taylor, R. H. (2014). Preliminary evaluation of a new microsurgical robotic system for head and neck surgery. In *Intelligent Robots and Systems (IROS 2014), 2014 IEEE/RSJ International Conference on*, pages 1276–1281. IEEE. [51](#)
- [Olszewska et al., 2004] Olszewska, E., Wagner, M., Bernal-Sprekelsen, M., Ebmeyer, J., Dazert, S., Hildmann, H., and Sudhoff, H. (2004). Etiopathogenesis of cholesteatoma. *European Archives of Oto-Rhino-Laryngology and Head & Neck*, 261(1):6–24. [17](#), [18](#), [19](#)
- [Orosco et al., 2013] Orosco, R. K., Tsien, R. Y., and Nguyen, Q. T. (2013). Fluorescence imaging in surgery. *IEEE reviews in biomedical engineering*, 6:178–187. [24](#)
- [Osa et al., 2010] Osa, T., Staub, C., and Knoll, A. (2010). Framework of automatic robot surgery system using visual servoing. In *IEEE/RSJ International Conference on Intelligent Robots and Systems (IROS)*, pages 1837–1842. [38](#), [63](#), [66](#), [68](#), [70](#)
- [Patwari et al., 2000] Patwari, P., Weissman, N. J., Boppart, S. A., Jesser, C., Stamper, D., Fujimoto, J. G., and Brezinski, M. E. (2000). Assessment of coronary plaque with optical coherence tomography and high-frequency ultrasound. *The American journal of cardiology*, 85(5):641–644. [24](#)
- [Peters, 2006] Peters, T. M. (2006). Image-guidance for surgical procedures. *Physics in medicine and biology*, 51(14):R505. [35](#), [59](#)
- [Pham et al., 2015] Pham, C. D., Coutinho, F., Leite, A. C., Lizarralde, F., From, P. J., and Johansson, R. (2015). Analysis of a moving remote center of motion for robotics-assisted minimally invasive surgery. In *IEEE/RSJ International Conference on Intelligent Robots and Systems (IROS)*, pages 1440–1446. [67](#)
- [Pham et al., 2000a] Pham, D. L., Xu, C., and Prince, J. L. (2000a). Current methods in medical image segmentation. *Annual review of biomedical engineering*, 2(1):315–337. [35](#)

- [Pham et al., 2000b] Pham, D. L., Xu, C., and Prince, J. L. (2000b). Current methods in medical image segmentation. *Annual review of biomedical engineering*, 2(1):315–337. [169](#)
- [Pile and Simaan, 2014] Pile, J. and Simaan, N. (2014). Modeling, design, and evaluation of a parallel robot for cochlear implant surgery. *IEEE/ASME Transactions on Mechatronics*, 19(6):1746–1755. [42](#), [62](#)
- [Pitris et al., 2011] Pitris, C., Saunders, K. T., Fujimoto, J. G., and Brezinski, M. E. (2011). High-resolution imaging of the middle ear with optical coherence tomography: a feasibility study. *Archives of Otolaryngology–Head & Neck Surgery*, 127(6):637–642. [25](#)
- [Pott et al., 2005] Pott, P. P., Scharf, H.-P., and Schwarz, M. L. (2005). Today’s state of the art in surgical robotics. *Computer Aided Surgery*, 10(2):101–132. [38](#)
- [Rautaray and Agrawal, 2012] Rautaray, S. S. and Agrawal, A. (2012). Vision based hand gesture recognition for human computer interaction: a survey. *Artificial Intelligence Review*, 43(1):1–54. [40](#)
- [Riga et al., 2011] Riga, C. V., Bicknell, C. D., Hamady, M. S., and Cheshire, N. J. (2011). Evaluation of robotic endovascular catheters for arch vessel cannulation. *Journal of vascular surgery*, 54(3):799–809. [53](#)
- [Rosenberg, 1993] Rosenberg, L. B. (1993). Virtual fixtures: Perceptual tools for telerobotic manipulation. In *IEEE Virtual Reality Annual International Symposium*, pages 76–82. [101](#)
- [Rothbaum et al., 2002] Rothbaum, D. L., Roy, J., Stoianovici, D., Berkelman, P., Hager, G. D., Taylor, R. H., Whitcomb, L. L., Francis, H. W., and Niparko, J. K. (2002). Robot-assisted stapedotomy: micropick fenestration of the stapes footplate. *Otolaryngology–Head and Neck Surgery*, 127(5):417–426. [32](#), [42](#), [62](#)
- [Sajjadi, 2013] Sajjadi, H. (2013). Endoscopic middle ear and mastoid surgery for cholesteatoma. *Iranian journal of otorhinolaryngology*, 25(71):63–70. [21](#), [54](#)
- [Salami et al., 2009] Salami, A., Dellepiane, M., Proto, E., and Mora, R. (2009). Piezosurgery in otologic surgery: four years of experience. *Otolaryngology–Head and Neck Surgery*, 140(3):412–418. [30](#)
- [Samson, 1993] Samson, C. (1993). Control of chained systems application to path following and time-varying point-stabilization of mobile robots. *IEEE Transactions on Automatic Control*, 40(1):64–77. [121](#)
- [Schenck, 1992] Schenck, J. F. (1992). Health and physiological effects of human exposure to whole-body four-tesla magnetic fields during mri. *Annals of the New York Academy of Sciences*, 649(1):285–301. [58](#)

- [Seon et al., 2015] Seon, J.-A., Tamadazte, B., and Andreff, N. (2015). Decoupling path following and velocity profile in vision-guided laser steering. *IEEE Transactions on Robotics*, 31(2):280–289. [122](#)
- [Sergeev et al., 1997] Sergeev, A., Gelikonov, V., Gelikonov, G., Feldchtein, F., Kuranov, R., Gladkova, N., Shakhova, N., Snopova, L., Shakhov, A., Kuznetzova, I., et al. (1997). In vivo endoscopic oct imaging of precancer and cancer states of human mucosa. *Optics express*, 1(13):432–440. [24](#)
- [Sheehy et al., 1977] Sheehy, J. L., Brackmann, D. E., and Graham, M. D. (1977). Cholesteatoma surgery: Residual and recurrent disease a review of 1,024 cases. *Annals of Otology, Rhinology & Laryngology*, 86(4):451–462. [20](#)
- [Shoa et al., 2008] Shoa, T., Madden, J. D., Fekri, N., Munce, N. R., and Yang, V. X. (2008). Conducting polymer based active catheter for minimally invasive interventions inside arteries. In *Engineering in Medicine and Biology Society, 2008. EMBS 2008. 30th Annual International Conference of the IEEE*, pages 2063–2066. IEEE. [38](#), [57](#)
- [Shuhaiber, 2004] Shuhaiber, J. H. (2004). Augmented reality in surgery. *Archives of surgery*, 139(2):170–174. [170](#)
- [Siciliano, 1990] Siciliano, B. (1990). Kinematic control of redundant robot manipulators: A tutorial. *Journal of Intelligent and Robotic Systems*, 3(3):201–212. [56](#), [65](#), [100](#), [119](#)
- [Siciliano and Khatib, 2008] Siciliano, B. and Khatib, O. (2008). *Springer handbook of robotics*. Springer Science & Business Media. [38](#)
- [Silverman, 2009] Silverman, R. H. (2009). High-resolution ultrasound imaging of the eye—a review. *Clinical & experimental ophthalmology*, 37(1):54–67. [23](#)
- [Spong et al., 2006] Spong, M. W., Hutchinson, S., and Vidyasagar, M. (2006). *Robot modeling and control*, volume 3. Wiley New York. [38](#)
- [Strang et al., 1993] Strang, G., Strang, G., Strang, G., and Strang, G. (1993). *Introduction to linear algebra*, volume 3. Wellesley-Cambridge Press Wellesley, MA. [76](#), [77](#)
- [Struik, 1988] Struik, D. J. (1988). *Lectures on Classical Differential Geometry*. Dover Publications, second edition. [122](#), [123](#), [125](#)
- [Subhash et al., 2012] Subhash, H. M., Nguyen-Huynh, A., Wang, R. K., Jacques, S. L., Choudhury, N., and Nuttall, A. L. (2012). Feasibility of spectral-domain phase-sensitive optical coherence tomography for middle ear vibrometry. *Journal of biomedical optics*, 17(6):0605051–0605053. [25](#)

- [Swaney et al., 2012] Swaney, P. J., Croom, J. M., Burgner, J., Gilbert, H. B., Rucker, D. C., Webster, R. J., Weaver, K. D., and Russell, P. T. (2012). Design of a quadra-manual robot for single-nostril skull base surgery. In *ASME 2012 5th Annual Dynamic Systems and Control Conference joint with the JSME 2012 11th Motion and Vibration Conference*, volume 3, pages 387–393. [vii](#), [52](#), [62](#), [64](#)
- [Swaney et al., 2017] Swaney, P. J., York, P. A., Gilbert, H. B., Burgner-Kahrs, J., and Webster, R. J. (2017). Design, fabrication, and testing of a needle-sized wrist for surgical instruments. *Journal of medical devices*, 11(1):014501. [x](#), [171](#), [172](#)
- [Tabrizi et al., 2017] Tabrizi, P. R., Monfaredi, R., Liu, W. P., Taylor, R. H., Cleary, K., and Preciado, D. (2017). Robotic otology. In *Atlas of Head and Neck Robotic Surgery*, pages 161–174. Springer. [42](#)
- [Taylor et al., 1995] Taylor, R. H., Funda, J., Grossman, D. D., Karidis, J. P., and LaRose, D. A. (1995). Remote center-of-motion robot for surgery. US Patent 5,397,323. [vii](#), [66](#)
- [Taylor and Stoianovici, 2003] Taylor, R. H. and Stoianovici, D. (2003). Medical robotics in computer-integrated surgery. *IEEE Transactions on Robotics and Automation*, 19(5):765–781. [38](#)
- [Thomassin et al., 1993] Thomassin, J. M., Korchia, D., and Doris, J. M. D. (1993). Endoscopic-guided otosurgery in the prevention of residual cholesteatomas. *The Laryngoscope*, 103(8):939–943. [21](#)
- [Torbatian et al., 2009] Torbatian, Z., Adamson, R., van Wijhe, R., Pennings, R., Bance, M., and Brown, J. (2009). Imaging the auditory system: A new application of high-frequency ultrasound. In *Ultrasonics Symposium (IUS), 2009 IEEE International*, pages 236–239. IEEE. [24](#), [55](#), [170](#)
- [Tran et al., 2004] Tran, P. H., Mukai, D. S., Brenner, M., and Chen, Z. (2004). In vivo endoscopic optical coherence tomography by use of a rotational microelectromechanical system probe. *Optics letters*, 29(11):1236–1238. [24](#)
- [Van Krevelen and Poelman, 2010] Van Krevelen, D. and Poelman, R. (2010). A survey of augmented reality technologies, applications and limitations. *International Journal of Virtual Reality*, 9(2):1. [170](#)
- [Vercruyssen et al., 2006] Vercruyssen, J.-P., De Foer, B., Pouillon, M., Somers, T., Caselman, J., and Offeciers, E. (2006). The value of diffusion-weighted mr imaging in the diagnosis of primary acquired and residual cholesteatoma: a surgical verified study of 100 patients. *European radiology*, 16(7):1461–1467. [v](#), [22](#), [23](#)
- [Vitiello et al., 2013] Vitiello, V., Lee, S.-L., Cundy, T. P., and Yang, G.-Z. (2013). Emerging robotic platforms for minimally invasive surgery. *IEEE Reviews in Biomedical Engineering*, 6:111–126. [36](#), [38](#)

- [Vitrani et al., 2005] Vitrani, M.-A., Morel, G., and Ortmaier, T. (2005). Automatic guidance of a surgical instrument with ultrasound based visual servoing. In *IEEE International Conference on Robotics and Automation (ICRA)*, pages 508–513. [60](#)
- [Voros et al., 2007] Voros, S., Long, J.-A., and Cinquin, P. (2007). Automatic detection of instruments in laparoscopic images: A first step towards high-level command of robotic endoscopic holders. *The International Journal of Robotics Research*, 26(11-12):1173–1190. [153](#)
- [Walker, 2013] Walker, I. D. (2013). Continuous backbone “continuum” robot manipulators. *ISRN Robotics*, 2013. [52](#)
- [Weber et al., 2017] Weber, S., Gavaghan, K., Wimmer, W., Williamson, T., Gerber, N., Anso, J., Bell, B., Feldmann, A., Rathgeb, C., Matulic, M., et al. (2017). Instrument flight to the inner ear. *Science robotics*, 2(4):eaal4916. [36](#), [62](#)
- [Webster and Jones, 2010] Webster, R. J. and Jones, B. A. (2010). Design and kinematic modeling of constant curvature continuum robots: A review. *The International Journal of Robotics Research*. [38](#), [52](#), [57](#)
- [Williamson et al.,] Williamson, T. M., Bell, B. J., Gerber, N., Salas, L., Zysset, P., Caversaccio, M., and Weber, S. Estimation of tool pose based on force–density correlation during robotic drilling. [44](#)
- [Xu and Zheng, 2012] Xu, K. and Zheng, X. (2012). Configuration comparison for surgical robotic systems using a single access port and continuum mechanisms. In *IEEE International Conference on Robotics and Automation (ICRA)*, pages 3367–3374. [58](#)
- [Yokoyama et al., 2003] Yokoyama, K., Handa, H., Isozumi, T., Fukase, Y., Kaneko, K., Kanehiro, F., Kawai, Y., Tomita, F., and Hirukawa, H. (2003). Cooperative works by a human and a humanoid robot. In *IEEE International Conference on Robotics and Automation (ICRA)*, volume 3, pages 2985–2991. [40](#)
- [York et al., 2015] York, P. A., Swaney, P. J., Gilbert, H. B., and Webster, R. J. (2015). A wrist for needle-sized surgical robots. In *IEEE International Conference on Robotics and Automation (ICRA)*, pages 1776–1781. [51](#), [58](#)
- [Zhang et al., 2008] Zhang, J., Wei, W., Manolidis, S., Roland Jr, J. T., and Simaan, N. (2008). Path planning and workspace determination for robot-assisted insertion of steerable electrode arrays for cochlear implant surgery. In *Medical Image Computing and Computer-Assisted Intervention. MICCAI 2008. 30th Annual International Conference of the IEEE*, pages 692–700. Springer. [44](#)
- [Zhang et al., 2006] Zhang, J., Xu, K., Simaan, N., and Manolidis, S. (2006). A pilot study of robot-assisted cochlear implant surgery using steerable electrode arrays. In *Medical Image Computing and Computer-Assisted Intervention–MICCAI 2006*, pages 33–40. Springer. [44](#)

- [Zhang et al., 2014] Zhang, Y., Pfeiffer, T., Weller, M., Wieser, W., Huber, R., Raczkowski, J., Schipper, J., Wörn, H., and Klenzner, T. (2014). Optical coherence tomography guided laser cochleostomy: Towards the accuracy on tens of micrometer scale. *BioMed research international*, 2014. [vi](#), [45](#), [46](#), [59](#)
- [Zhang and Worn, 2014] Zhang, Y. and Worn, H. (2014). Optical coherence tomography as highly accurate optical tracking system. In *IEEE/ASME International Conference on Advanced Intelligent Mechatronics (AIM)*, pages 1145–1150. [vi](#), [45](#), [46](#), [62](#)
- [Zhu and Huo, 2014] Zhu, B. and Huo, W. (2014). 3-d path-following control for a model-scaled autonomous helicopter. *IEEE Transactions on Control Systems Technology*, 22(5):1927–1934. [121](#)

This document contains 214 references.

Résumé :

Cholestéatome est une maladie affectant l'oreille moyenne qui peut potentiellement conduire à de graves complications (par exemple, surdit e or paralysie faciale) en l'absence de traitement. Actuellement, le seul traitement efficace de cette maladie, est une intervention chirurgicale. Cependant, une telle m ethode est invasive et induit une forte incidence de cholest eato me r esiduel. Par cons equent, le patient peut subir plus d'une intervention chirurgicale (souvent deux, ou voire plus). Ainsi, un syst eme robotique original a  et e propos e afin d' eliminer cette incidence en enlevant efficacement toutes les cellules infect ees d es la premi ere intervention chirurgicale, et surtout permettre une intervention la moins invasive possible. Ce manuscrit traite des diff erents d efis auxquels il faut r epondre pour d evelopper de nouvelles proc edures chirurgicales tout en s'inspirant des approches de micro-robotique. Il est  egalement une question de la d efinition d'un cahier des charges n ecessaire  a la mise en  oeuvre d'un syst eme micro-robotique efficace et s ur qui contribue  a une meilleure chirurgie du cholest eato me. De plus, ce document traite du d eveloppement de lois de commande d ed ees  a ce type de chirurgie mini-invasive. En effet, ces lois permettent de contr oler les mouvements d'un instrument rigide (droit ou courb e) en tenant compte de contraintes anatomiques (par exemple, le trou d'incision, le nerf facial et les osselets), et d'effectuer une t ache secondaire telle qu'un suivi de chemin (correspondant aux t aches clinique comme r esection ou balayage de surface). Une forme hi erarchique est  egalement appliqu ee dans l'espace Cart esien (ou l'espace des t aches) afin de conserver la priorit e entre les diff erentes t aches. Ce contr oleur est une couche modulaire qui peut  tre ajout ee  a diff erentes structures robotiques. Le contr oleur propos e a montr e de bons r esultats en termes de pr ecision apr es une validation exp erimentale sur des robots parall ele et s eriel.

Mots-cl es : Micro-robotique m edicale, M ecatronique, Commande de robot, Suivi de chemin, Mouvement sous contrainte, Asservissement visuel

Abstract:

Cholesteatoma is a disease affecting the middle ear, which can potentially lead to serious complications (e.g., hearing loss or facial nerve paralysis) in the absence of treatment. The only treatment in the current medical practice is a surgical intervention. However, such a method is invasive and induces a high incidence of residual cholesteatoma. Therefore, the patient may end up being exposed to more than one surgical operation (often two, or even more). Thus, a novel robotic system has been proposed to eliminate this incidence by removing in efficient manners all the infected cells from the first surgery, and especially achieve a minimally invasive surgery. This manuscript shows the different challenges which have to be tackled for developing new surgical procedures while taking inspiration from micro-robotic approaches. It is also a question of defining the requirements and the specifications necessary for implementing an efficient and safe mirco-robotic system for a better cholesteatoma surgery. In addition, this manuscript clarifies the development of control laws attributed to such type of minimally invasive surgeries. As a matter of fact, these laws contribute in controlling the motion of a rigid tool (either straight or curved) under the anatomical constraints (e.g., the incision hole, the facial nerve and the ossicles), and performing a secondary task such as following a path (corresponding to clinical tasks as resection or scanning). A hierarchical form is also applied in the Cartesian space (or task-space) in order to maintain the priority among the various tasks. This controller is a modular layer which can be added to different robotics structures. The proposed controller has shown good results in terms of accuracy after experimental validation on parallel and serial robots.

Keywords: Medical micro-robotics, Mechatronics, Robot control, Path following, Constrained motion, Visual servoing

The logo for SPIM (School of Doctoral Studies) features a stylized 'S' followed by the letters 'PIM' in a bold, sans-serif font. A horizontal bar is positioned to the left of the 'S'.

■  cole doctorale SPIM 16 route de Gray F - 25030 Besan on cedex

■ t el. +33 (0)3 81 66 66 02 ■ ed-spim@univ-fcomte.fr ■ www.ed-spim.univ-fcomte.fr

The logo for the University of Franche-Comt e (UFC) consists of the letters 'UFC' in a large, bold, serif font. Below it, the words 'UNIVERSIT E DE FRANCHE-COMT E' are written in a smaller, sans-serif font. A vertical bar is positioned to the left of the 'U'.

